Université Paris-Sud
Centre Scientifique d'Orsay

THESE

Présenté pour obtenir
Le grade de **Docteur en Sciences**
Spécialité: Physique de la Matière condensée

par

CLAUDIA OJEDA-ARISTIZABAL

Laboratoire de Physique des Solides, groupe de Physique Mésoscopique

Transport quantique dans le graphène

Quantum transport in graphene

Soutenue le 18 Novembre 2010 devant la commission d'examen:

Président	Christian Glattli
Rapporteurs	Marc Sanquer
	Thomas Ihn
Examinateurs	Dominique Mailli
	Sophie Guéron
	Hélène Bouchiat

.

Remerciements

Je voudrais remercier Hélène Bouchiat, Sophie Guéron et Meydi Ferrier qui ont encadré cette thèse avec beaucoup de soin et de dévouement. Merci à Hélène pour avoir été toujours disponible pour répondre à mes questions à tout moment tant sur le versant théorique qu'expérimental. Sa disponibilité et présence permanente ont été très rassurantes et agréables pendant ma thèse. La générosité vis-à-vis du temps que Helene a consacré à moi et a tous les thésards, est une qualité que j'ai grandement apprecié et admire. Son attitude positive, sa motivation et sa façon d'encadrer le groupe Méso ont été très formateur et m'ont inspiré pendant mes trois années de thèse.

Sophie (comme Helene et Meydi) a été présente pendant la fabrication des échantillons, la mesure et l'interprétation des données. Les quiz oraux qu'elle me faisait passer de temps en temps, ont amélioré ma compréhension de la physique et du montage expérimental (elle a su faire revivre un stress oublie à l'école primaire !). J'ai appris beaucoup de Sophie sur la physique grâce à ses explications et aux discussions qu'elle incitait souvent dans le groupe sur un certain phénomène ou une certaine théorie. J'ai appris de Sophie à approcher la physique expérimentale de façon pratique, à comprendre le sens de chaque étape et à interpréter mes donnees au moment de la mesure. Elle m'a appris à présenter mes résultats de façon claire et concise. L'attitude joyeuse de Sophie et son énergie ont été très motivantes pendant ma thèse.

Merci à Meydi pour son accueil chaleureux quand je venais voir le groupe les premières fois avant de commencer ma thèse. Ses explications détaillées et son attitude aimable m'ont beaucoup motive à faire une thèse expérimentale dans le groupe. L'expertise de Meydi sur la physique expérimentale a été de grande importance pendant ma thèse. Meydi a pris beaucoup de son temps pour m'enseigner à utiliser les diffèrent appareils. Il a été le premier à me montrer la fabrication des échantillons de graphène avec la technique d'exfoliation. Son attitude sympathique quand je commençais ma thèse a été rassurante et motivante. Je remercie Meydi pour avoir toujours été disponible pendant ma thèse pour répondre à mes questions.

Je voudrais remercier aussi Miguel Monteverde qui est arrivé au cours de ma deuxième année de thèse. Son expérience de la physique expérimentale m'a permis d'apprendre énormément. Son attitude toujours gentille et accueillante a fait de ma collaboration avec lui une expérience très agréable. J'appréciais discuter à tout moment avec lui, sur la physique ou sur n'importe quel sujet, c'était un plaisir de pouvoir discuter avec Miguel dans ma langue maternelle. J'admirais sa patience, son enthousiasme ainsi que sa disponibilité pour chaque membre du groupe.

J'ai eu la chance que Julien Basset arrive au group Méso pendant ma deuxième année de thèse. Julien est devenu un de mes meilleurs amis en France. Je le remercie pour son soutien constant, pour avoir fait du bureau qu'on partageait un endroit agréable, ou il y avait la place pour des discussions sur la physique et aussi pour des petits cours de français.

Je voudrais remercier Alik Kasumov. L'expertise d'Alik a été de grande importance pour la fabrication des échantillons, ce qui nous a permis de faire plusieurs expériences. J'ai apprécié son attitude toujours

aimable. Je remercie également Rafael Weil pour son aide avec la fabrication des échantillons et sa disponibilité. Merci aussi à Richard Deblock pour le temps qu'il consacrait chaque fois pour me donner des conseils pour mes présentations orales ; j'appréciais ses commentaires toujours précis et justes. Je tiens à remercier Alexei Chapelianski ; mes discussions avec lui ont été en plusieurs occasions fructueuses dans la compréhension de certains phénomènes. Alexei rendait l'ambiance du groupe agréable et joyeuse. J'ai apprécié d'Alexei sa disponibilité et son intérêt aux différents projets du groupe. Je remercie aussi Francesca Chiodi et Bastien Dassonneville avec qui j'ai eu l'occasion de discuter de physique et passer de moments agréables pendant ma thèse.

Je remercie Jean Nöel Fuchs avec qui j'ai découvert la physique du graphène. J'ai apprecie de Jean Noel ses explications toujours pédagogiques.

Merci à mes amis espagnoles du laboratoire, Rafael, Francisco, Rodrigo et Almudena avec qui j'ai pu partager plusieures fois une pause agréable au laboratoire. Merci à tout le personnel administrative, spécialement a Silvie Falcinelli, Marie France Cozic et Marie France Mariotto.

Je tiens à remercier Michel Héritier qui a soutenu ma candidature pour une bourse d'accueil de l'Université de Paris-XI dédiée aux étudiants étrangers. Ceci m'a permis de faire le Mastère de Physique de la Matière Condensée. Les conseils de M. Héritier au moment du choix d'un sujet de thèse ont été d'énorme importance pour moi ainsi que son soutien dans ma recherche d'un financement. Les discussions que j'ai eues avec M. Héritier pendant mon année de DEA m'ont permis d'apprendre beaucoup de physique de la matière condensée.

Je remercie de façon spéciale Professeur Alain Bérard, qui m'a accueilli dans son groupe pour un stage en physique théorique la première fois que je suis venue en France. M. Bérard m'a appris des concepts fondamentaux de la physique pendant mes 6 mois de stage. J'ai été inspire par son enthousiasme pour la physique théorique et par ses cours clairs et motivants. L'accueil chaleureux de sa famille, leur soutien et la présence inconditionnelle de M Bérard ont marqué mon séjour en France.

Le soutien de mes parents et de ma sœur a été très précieux. Je ne trouve pas de mots pour les remercier de leur compréhension, leur patience, leur mots de soutien pendant mon année de DEA et mes trois années de thèse. Gracias a Chigui por toda la motivacion que nos brindaste desde pequenas a Diani y a mi hacia la ciencia, gracias por tu apoyo cuando las dos decidimos hacer una carrera en ciencias, gracias por tu constante dedicacion, por tu sabiduria y por tu cariño, por haber sido un modelo inspirador para Diani y para mi. Gracias Mami por tu apoyo, tu infinita dedicacion, tus correos tan bonitos durante estos anos, por haber aceptado con cariño la distancia, por haber sido un modelo de constancia y tenacidad y por tu infinito amor. Gracias Diani por tu apoyo, por tu compania durante la redaccion y por tu ejemplo de motivacion.

Je tiens à remercier mes amis qui m'ont permis de passer des moments inoubliables en France. En particulier Keyan, Juliana, Raphael, Quentin, Guilia, Mathilde, Camille et Marie Pierre.

Mon expérience pendant ma thèse n'aurait pas été le même sans le soutien de Damien. Merci de tes conseils, du temps que t'as passe à m'écouter, de ta patience et de ta générosité.

Table des matières

Chapitre 1

Introduction (français)

Cette thèse étudie le transport électronique dans le graphène, le crystal monoatomique de carbone où les électrons se déplacent comme si ils étaient sans masse. Les expériences faites dans cette thèse peuvent être classifiées en deux régimes, un régime macroscopique où la longueur de cohérence de phase L_ϕ est plus petite que la taille de l'échantillon L, $L_\phi < L$ et un régime mésoscopique où les paquets d'onde des électrons interfèrent, $(L_\phi > L)$.

Avant d'introduire les expériences faites dans ces deux régimes différents, je vais présenter de façon courte la physique du graphène et de la bicouche de graphène, deux matériels qui ont comme base un réseau hexagonal d'atomes de carbone et qui donnent accès à deux physiques très différentes.

L'existence d'un crystal bidimensionnel comme le graphène était impensable il y a 70 ans. Selon Peirls et Landau c'était impossible avoir un ordre cristallographique à longue portée à une ou deux dimensions. Cet argument était basé sur l'approximation harmonique dans le cas Peierls et sur la théorie des transitions de phase de deuxième ordre dans le cas de Landau. La théorie a été étendue plus tard par Mermin [80] qui a mit l'argument de Peierls et Landau sur une base plus rigoureuse en prenant compte plusieurs types d'interactions entre particules. L'impossibilité d'un ordre à longue distance est liée aux fluctuations thermiques. A basse dimension les fluctuations thermiques donnent lieu à un terme divergeant qui fait que le déplacement des atomes est de l'ordre de la distance inter-atomique ce qui rend les cristaux à deux dimensions instables. Le graphène habitant dans un monde à trois dimensions, les fluctuations thermiques sont dissipées dans la troisième direction ce qui le fait stable. Ce-ci ne contredit pas la conclusion de Peierls et Landau qui se base sur un crystal bidimensionnel habitant dans un monde à 2 dimensions. Mais cette stabilité a un coût. Le graphène se déforme hors son plan ce qui fait qu'il n'est pas complément plat. Les ondulations observées dans le graphène ont une hauteur d'environ un nanomètre et une dimension latérale de l'ordre de la dizaine de nanomètres. Remarquablement les déformations transversales de la feuille de graphène sont douces et se produisent sans que la feuille se casse et sans que des défauts n'y apparaissent.

Le graphène est construit à partir du carbone, qui est fait de 6 protons, 6 neutrons et 6 électrons. Dans l'état de plus basse énergie, les 6 électrons sont dans la configuration $1s^2 2s^2 2p^2$. Deux électrons remplissent l'orbital $1s$ qui est près du noyau et non significatif pour les réactions chimiques et 4 électrons remplissent les orbitales extérieures $2s$ et $2p$. Trois de ces électrons forment une liaison forte covalente σ avec les atomes de carbone voisins et l'électron restant forme une liaison π. Il y a donc 1 électron π par atome responsable des propriétés de transport électronique à basses énergies, et 3 électrons σ qui forment des bandes d'énergie loin du niveau de Fermi. Ces électrons π dans le graphène ont un comportement très particulier lié à la structure hexagonale dans laquelle les atomes de carbone s'arrangent (voir figure 2.1). Cette structure n'est pas un réseau de Bravais car les atomes dans le crystal ne sont pas équivalents, ils ne voient pas le même environnement. Les atomes dans le graphène sont ainsi classifiés en atomes de type A et atomes de type B. Les atomes de type A ont un plus proche voisin au nord et deux dans le sud, leur

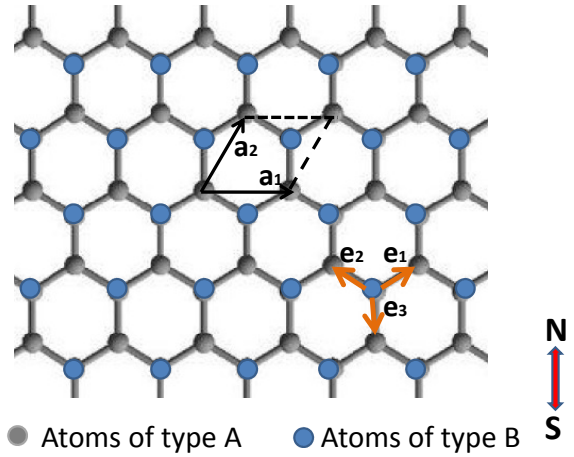

FIGURE 1.1 – Structure en nid d'abeille du graphène. Les vecteurs $\mathbf{a_1}$ and $\mathbf{a_2}$ forment la maille élémentaire du réseau triangulaire de Bravais avec deux atomes A and B par maille. $\mathbf{e_1}$, $\mathbf{e_2}$ and $\mathbf{e_3}$ déterminent les plus proches voisins des atomes de type B.

positions étant déterminées par les vecteurs $\mathbf{e}_1$, $\mathbf{e}_2$ and $\mathbf{e}_3$ comme est montré dans la figure 2.1,

$$\mathbf{e}_1 = \frac{a}{2}\left(\sqrt{3}\mathbf{e}_x + \mathbf{e}_y\right) \tag{1.1}$$

$$\mathbf{e}_2 = \frac{a}{2}\left(-\sqrt{3}\mathbf{e}_x + \mathbf{e}_y\right) \tag{1.2}$$

$$\mathbf{e}_3 = -a\mathbf{e}_y. \tag{1.3}$$

Le réseau hexagonal peut être pourtant décomposé dans un réseau parallépipedique de Bravais avec une base de deux atomes par maille (A et B) comme c'est montré dans la figure 2.1. Les vecteurs de maille s'écrivent :

$$\mathbf{a_1} = \sqrt{3}a\mathbf{e_x} \qquad \mathbf{a_2} = \frac{\sqrt{3}a}{2}\left(\mathbf{e_x} + \sqrt{3}\mathbf{e_y}\right)$$

où $a \approx 0.14nm$ est la distance entre plus proches voisins. Les vecteurs de maille du réseau réciproque sont

$$\mathbf{a_1^*} = \frac{2\pi}{\sqrt{3}a}\left(\mathbf{e_x} - \frac{\mathbf{e_y}}{\sqrt{3}}\right) \qquad \mathbf{a_2^*} = \frac{4\pi}{\sqrt{3}a}\mathbf{e_y}$$

La première zone de Brillouin a une forme hexagonale (voir figure 2.2) avec deux points inéquivalents K et K' qui ne peuvent pas être liés par des vecteurs du réseau réciproque. Ils sont associés aux vecteurs $\mathbf{K}$ et $\mathbf{K}'$. Les points équivalents à K et K' sont obtenus à partir de K et K' en faisant une translation du vecteur dans l'espace réciproque $G = \gamma_1\mathbf{e_1^*} + \gamma_2\mathbf{e_2^*}$ avec γ_1 et γ_2 des nombres entiers.

$$\mathbf{K}^{\pm} = \pm\frac{4\pi}{3\sqrt{3}a}\mathbf{e_x}$$

Les propriétés électroniques les plus importantes du graphène peuvent être obtenues à partir de l'approximation de liaisons fortes. Wallace [75] a calculé pour la première fois la structure de bande du

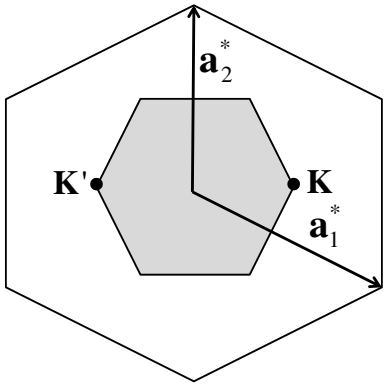

FIGURE 1.2 – Première zone de Brillouin avec les points cristallographiquement inéquivalents **K** et **K′**.

graphène en 1947 en démontrant le comportement semi-métallique inhabituel de ce matériau. Le Hamiltonien dans l'approximation des liaisons fortes qui considère des électrons qui sautent aux sites voisins s'écrit [76] :

$$H = -t \sum_{i \in A} \sum_{j=1}^{3} \left(a^{+}_{\mathbf{R_i}} b_{\mathbf{R_i}+\mathbf{e_j}} + b^{+}_{\mathbf{R_i}+\mathbf{e_j}} a_{\mathbf{R_i}} \right) \tag{1.4}$$

où $a_{\mathbf{R_i}}$ ($a^{+}_{\mathbf{R_i}}$) annihile (crée) un electron au vecteur $\mathbf{R_i}$ du sous-réseau A and $b_{\mathbf{R_i}+\mathbf{e_j}}$ ($b^{+}_{\mathbf{R_i}+\mathbf{e_j}}$) annihile (crée) un électron du sous-réseau B au vecteur $\mathbf{R_i} + \mathbf{e_j}$. $\mathbf{e}_j$ désigne les plus proches voisins (2.1, 2.2 et 2.3 pour les atomes de type B) et $t \approx 2.7eV$ est l'énergie de saut au plus proche voisin qui vient du recouvrement entre fonctions d'onde des sites voisins. Le saut entre deuxièmes plus proches voisins n'est pas considéré car le recouvrement entre leur fonctions d'onde est $t' \approx 0.1eV$, ce qui affecte la relation de dispersion seulement à des énergies de l'ordre de $100meV$.

La diagonalisation de ce Hamiltonien donne la relation de dispersion suivante :

$$\epsilon_{\mathbf{q}} = \pm \sqrt{\left(\sum_j \cos(\mathbf{q} \cdot \mathbf{e}_j) \right)^2 + \left(\sum_j \sin(\mathbf{q} \cdot \mathbf{e}_j) \right)^2} \tag{1.5}$$

les signes positif et negatif correspond à la bande d'électrons et des trous, qui sont représentés dans la figure 2.3. Elles se touchent aux points **K** et **K′** appelés points de Dirac. Le gap entre la bande de valence et la bande de conduction est donc nul. De plus, comme il y a autant d'électrons que d'atomes de carbone, la bande de valence est pleine et la bande de conduction est vide, ce qui fait que le niveau de Fermi tombe juste au point de contact entre les deux bandes à énergie nulle.

Quand on ne considère que des excitations à basse énergie ($E < t \approx 2.7eV$) le Hamiltonien 2.4 dans l'espace de Fourier peut être développé autour de K et K', en obtenant un Hamiltonien de la forme

$$H^{eff}_{\alpha=\pm} = \alpha \hbar v_F \kappa \cdot \sigma,$$

où κ est le vecteur d'onde et σ les matrices de Pauli. Ce Hamiltonien est le celui d'une particule relativiste sans masse, ce qui révèle le caractère relativiste des électrons dans le graphène. Il y a deux Hamiltoniens effectifs ($\alpha = +$ et $\alpha = -$) correspondant aux points K et K'. La relation de dispersion associée à chaque

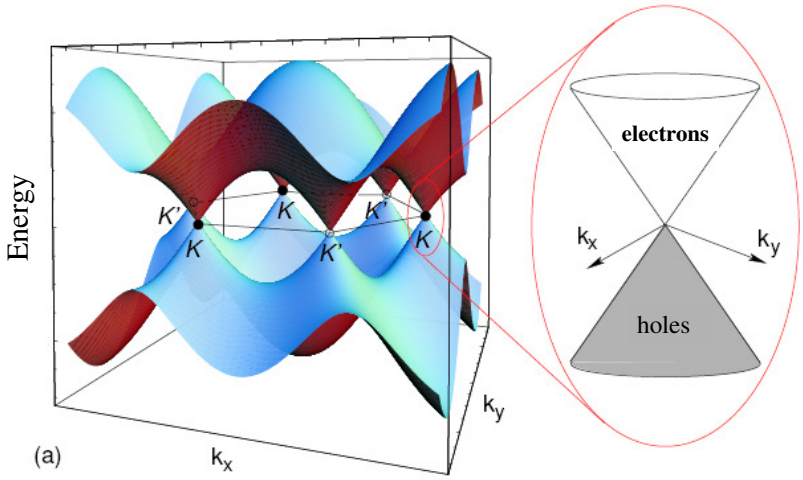

FIGURE 1.3 – Structure de bandes du graphène déduite en considérant seulement le saut aux sites voisins. La bande d'électrons et la bande de trous se touchent aux points de Dirac K and K'. Le zoom montre la relation de dispersion à basses énergies. (D'après [76]).

un de ces Hamiltoniens est linéaire, comme est représenté dans le zoom de la figure 2.3,

$$\epsilon_\alpha(\kappa) = \pm\frac{3}{2}ta|\kappa| = \pm\hbar v_F|\kappa| \tag{1.6}$$

où v_F est la vitesse de Fermi, la vitesse de groupe des électrons près de la surface de Fermi

$$v_F = \frac{3ta}{2\hbar} \approx 1 \times 10^6 m/s. \tag{1.7}$$

Toutes les particularités du graphène sont liées à sa structure des bandes. Les caractéristiques les plus importantes peuvent être résumées comme :

1. La bande de valence et la bande de conduction se touchent à énergie nulle en deux points K et K' qui sont appelés vallées et qui sont cristallographiquement inéquivalents. L'inéquivalence des points K et K' n'est pas lié à la présence de deux types d'atomes A et B par maille mais plutôt au réseau de Bravais. Le graphène est donc un semi-conducteur à gap nul avec deux vallées. Il peut être aussi considéré comme un métal dans lequel la bande de valence et de conduction forment une seule grande band mais dont la densité d'états est nulle au niveau de Fermi.
2. Près du niveau de Fermi la relation de dispersion des électrons est comme celle des Fermions de Dirac sans masse, $\epsilon = \pm\sqrt{p^2c^{*2} + m^{*2}c^{*2}} = \pm pc^*$ avec une masse effective nulle $m^* = 0$ et une vitesse $c^* = \sqrt{3}ta/2\hbar$ qui est lié à la constant de réseau $a \approx 0.25nm$ et l'enérgie de saut $t \approx 3eV$. La vitesse de groupe des électrons dans le graphène c^* est 300 fois plus petite que la vitesse de la lumière.
3. Près du niveau de Fermi, il y a une symétrie entre la bande de valance et la bande de conduction. Elle est appelée symétrie électron-trou.

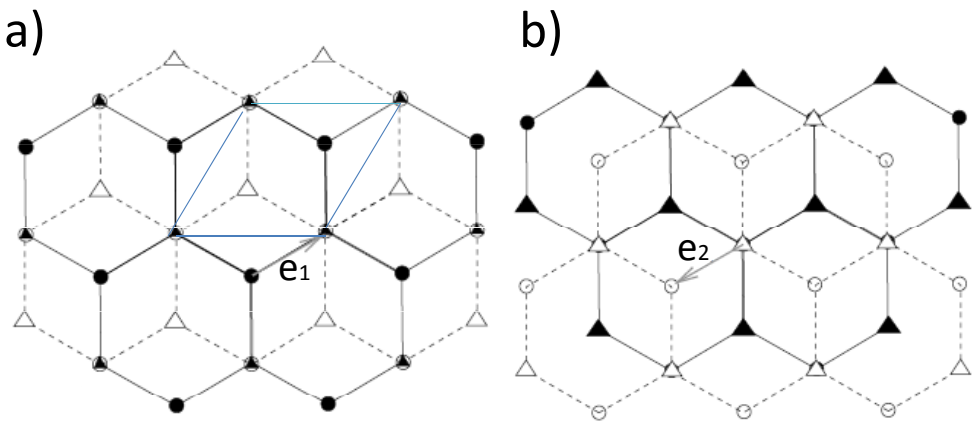

FIGURE 1.4 – Les deux possibilités pour l'empilement de deux couches de graphène. Noire représente la couche en dessous et blanc la couche en dessus. Les cercles représentent les atomes de type A, et les triangles les atomes de type B. En a) la couche de en dessus est translaté de $\mathbf{e_1}$ par rapport à la couche de en dessous. En b) la couche de en dessus est translaté de $\mathbf{e_2}$. La maille élémentaire est représenté en a). La bicouche de graphène a 4 atomes par maille. (D'après [76]).

L'étude du graphène nous amène facilement à la bicouche de graphène qui est aussi un matériel très intéressant. C'est le seul matériel où les propriétés semi-conductrices peuvent être contrôlées par un effet de champ. La bicouche de graphène a un gap (contrairement à la monocouche) qui peut être modulé en appliquant un voltage bias entre les deux couches de graphène, mais surtout la bicouche de graphène donne accès à une physique très différente par rapport à celle du monolayer, avec une relation de dispersion qui est quadratique et non pas linéaire, un facteur de diffusion différent, une densité d'états différente et une quantification des niveaux d'énergie différente en présence d'un champ magnétique.

La bicouche de graphène consiste de deux couches empilées de graphène séparées de $d \approx 2.4a = 0.34nm$. Les couches sont translatées l'une par rapport à l'autre de $\mathbf{e_1}$ ou $\mathbf{e_2}$ (2.1 et 2.2), comme s'est vu dans la figure 2.4 La structure des bandes de la bicouche peut être déduite en utilisant un Hamiltonien dans l'approximation des liaisons fortes comme a été fait pour le graphène, [77],

$$\begin{aligned} H &= -\gamma_0 \sum_{<i,j>m} \left(a^+_{m,i} b_{m,j} + h.c. \right) \\ &- \gamma_1 \sum_j \left(a^+_{1,j} a_{2,j} + h.c. \right) \\ &- \gamma_3 \sum_j \left(a^+_{1,j} b_{2,j} + a^+_{2,j} b_{1,j} + h.c. \right) \\ &- \gamma_4 \sum_j \left(b^+_{1,j} b_{2,j} + h.c. \right) \end{aligned}$$

où $a_{m,i}$ annihile an eléctron de type A sur la couche $m = 1, 2$ dans le site $\mathbf{R}_i$ et $b_{m,j}$ annihile un eléctron de

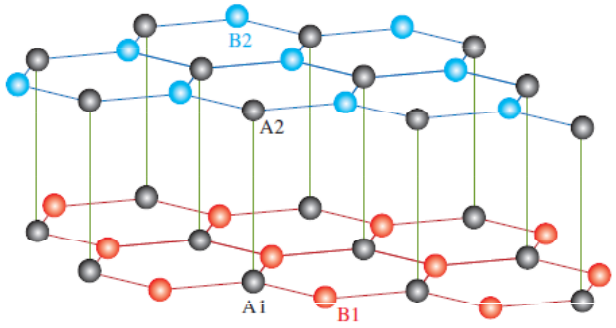

FIGURE 1.5 – Réseau cristallin de la bicouche. Les cercles foncés représentent les atomes de type A et les cercles claires les atomes de type B. D'après [77].

type B dans le site $\mathbf{R}_j$ avec j le plus proche voisin de i. γ_0 est l'énergie de saut dans une couche $t \approx 2.8eV$, $\gamma_1 = t_\perp \approx 0.35eV$ est l'energie de saut entre l'atome A_1 et l'atome A_2 (voir figure 2.5), $\gamma_3 \approx 0.3eV$ est l'énergie de saut entre l'atome A_1 et l'atome B_2 (ou l'atome A_2 et l'atome B_1) et $\gamma_4 \approx 0.2eV$ est l'énergie de saut entre B_1 et B_2. Dans l'espace de Fourier à basse énergie, le vecteur d'onde $\mathbf{q}$ peut être développé autour de $\pm\mathbf{K}$ comme dans la monocouche, ce qui donne le Hamiltonien effective suivant

$$H^{eff} = \begin{pmatrix} -V & \hbar v_F k & 0 & 3\gamma_3 a k^* \\ \hbar v_F k^* & -V & \gamma_1 & 0 \\ 0 & \gamma_1 & V & \hbar v_F k \\ 3\gamma_3 a_k & 0 & \hbar v_F k^* & V \end{pmatrix} \tag{1.8}$$

où $k = k_x + ik_y$ est un nombre complexe et V est la moitié du potentiel appliqué entre les deux couches. Si le potentiel appliqué entre les deux couches est nul, $V = 0$ et $\gamma_3, v_F k << \gamma_1$, les états de haute énergie peuvent être éliminés de façon perturbatrice et le Hamiltonien effective se réduit à :

$$H^{eff} = \begin{pmatrix} 0 & \frac{\hbar^2 v_F^2 k^2}{\gamma_1} + 3\gamma_3 a k^* \\ \frac{\hbar^2 v_F^2 k^{*2}}{\gamma_1} + 3\gamma_3 a k & 0 \end{pmatrix} \tag{1.9}$$

Si $\gamma_3 = 0$ le Hamiltonien effective 2.12 a les valeurs propres

$$\epsilon_{k,\pm} \approx \pm \frac{\hbar^2 v_F^2 k^2}{t_\perp} = \pm \frac{\hbar^2 k^2}{2m^*},$$

avec $m^* \approx 0.054 m_e$. Cette relation de dispersion corresponde à deux bandes paraboliques qui se touchent à $\epsilon = 0$ comme c'est montré dans la figure 2.6. Deux bandes additionnel commencent à $\pm t_\perp$. Quand $\gamma_3 \neq 0$ le spectre est différent à basse énergie. En lieu de deux bandes qui se touchent à $k = 0$, il y a quatre cônes de Dirac à $k = 0$ et à trois points équivalents avec un moment finie. Une tension appliquée entre les deux couches induit un gap qui dépend de la tension appliquée.

Les différences et similitudes principales entre la structure de bandes de la bicouche et de la monocouche de graphène peuvent être résumées comme :

1. Dans la bicouche de graphène, la bande de valence et la bande de conduction se touchent entre elles à énergie nulle comme pour la monocouche.

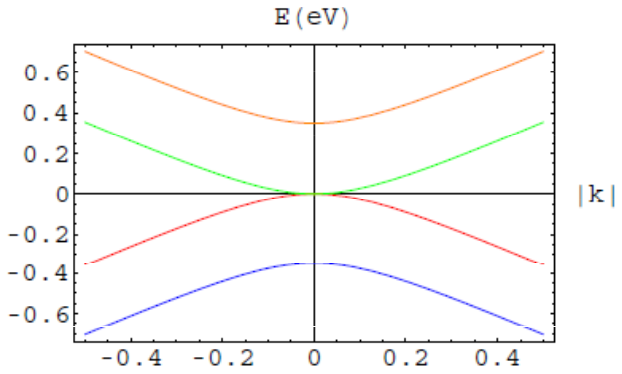

FIGURE 1.6 – Structure des bandes de la bicouche de graphène quand $V = 0$. Il y a deux bandes qui commencent à $\epsilon = 0$ et deux bandes additionnelles à $\pm t_\perp$

2. Dans l'approximation $\gamma_3 = 0$ (en négligeant le saut entre les atomes A_1 et B_2 (figure 2.5)), la relation de dispersion de la bicouche est quadratique et non pas linéaire comme est le cas dans la monocouche.
3. Dans la bicouche la bande de valence et la bande de conduction sont aussi symétriques mais elles se touchent dans un seul point $k = 0$ contrairement à la monocouche (dans l'approximation $\gamma_3 = 0$).
4. La bicouche de graphène ouvre la possibilité d'un semi-conducteur à gap accordable.

La densité d'états et le coefficient de diffusion ont aussi une forme très différente dans ces deux systèmes. La densité d'états $\rho(E_F)$ compte le nombre d'états per unité d'aire $\mathscr{A}$ dans les alentours du niveau de Fermi. Elle peut être calculé à partir du nombre d'états N sous E_F,

$$\rho(E_F) = \frac{1}{\mathscr{A}} \frac{\partial N}{\partial E}$$

avec

$$N_c = g \sum_{\substack{\mathbf{k} \\ k \leq k_F}} \approx g\mathscr{A} \int_{k \leq k_F} \frac{d^2k}{(2\pi)^2} = \frac{g\mathscr{A}}{4\pi^2} 2\pi \int_0^{k_F} dk k = \frac{g\mathscr{A}}{4\pi} k_F^2$$

cette expression compte pour n'importe quel système bidimensionnel (g est la dégénérescence due aux degrés de libertés internes). Dans le cas de la monocouche et de la bicouche on a respectivement

$$E_{ML} = \hbar v_F k_F \qquad E_{BL} = \frac{\hbar^2 k_F^2}{2m^*}$$

donc $k_F^2 = E_{ML}^2/\hbar^2 v_F^2$ pour la monocouche et $k_F^2 = E_{BL} 2m^*/\hbar^2$ pour la bicouche, ce qui donne

$$\rho(E_F)_{ML} = \frac{2E_F}{\pi \hbar^2 v_F^2} \qquad et \qquad \rho(E_F)_{BL} = \frac{2m^*}{\pi \hbar^2} \tag{1.10}$$

où on a prit $g = 4$ pour le monocouche et le bicouche (dégénérescence de spin et de vallée). La densité d'états est linéaire en énergie pour la monocouche et c'est une constante pour la bicouche, comme pour la plupart des systèmes bidimensionnels.

Le coefficient de diffusion peut être écrit en termes du libre parcours moyen, $D = v_F l_e/d$ avec d la dimension du système, ou en terme de la densité d'états,

$$D = \frac{\sigma}{e^2 \rho(E_F)}$$

On trouve expérimentalement que la conductivité σ est proportionnel à k_F^2 pour la monocouche et la bicouche [1]. Donc

$$\sigma_{ML} \propto E_F^2 \quad , \quad \sigma_{BL} \propto E_F$$

et

$$D_{ML} \propto E_F \propto k_F \quad , \quad D_{BL} \propto E_F \propto k_F^2.$$

Le coefficient de diffusion a donc une dépendance différente en le vecteur d'onde pour la monocouche et la bicouche due à la densité d'états différents de ces deux systèmes.

Une autre différence remarquable entre la monocouche et la bicouche repose sur la vitesse de Fermi. Pour des particules massives la vitesse de Fermi change avec l'énergie, comme c'est le cas pour la bicouche

$$v_{BL} = \frac{\hbar k}{m^*} = \sqrt{\frac{2E}{m^*}}.$$

Dans la monocouche dans autre côté, les électrons ont toujours la même vitesse peu importe leur énergie ou moment,

$$v_{ML} \approx 1 \times 10^6 m/s.$$

En présence d'un champ magnétique, la quantification des niveaux d'énergie est différente pour la monocouche et pour la bicouche. Elle a une dépendance en $\sqrt{n}$ pour la monocouche et en n pour la bicouche,

$$\begin{aligned} E_{ML} &= v_F \sqrt{2\hbar e B n} \\ E_{BL} &= \hbar \omega_c n \end{aligned}$$

avec $\omega_c = eB/m^*$.

Maintenant qu'on a resumé les différentes propriétés de transport de la monocouche et la bicouche, on peut procéder à la description de différentes expériences réalisées au cours de cette thèse. Comme a été mentionné au début, ces expériences peuvent être classifiées dans un régime macroscopique et un régime mésoscopique. L'expérience faite dans le régime macroscopique correspond à des mesures de magnétorésistance à des temperatures $\geq 1K$ telles que les echantillons ne sont pas cohérents quantiquement. Elles sont été faites dans la monocouche et la bicouche [86] et elles nous ont donné des informations sur le type d'impuretés qui limitent le transport dans le graphène, un sujet assez controversé dans ce moment.

La figure 1.7 montre la magnétorésistance à deux fils mesuré pour la monocouche et la bicouche. A partir de ces mesures on a pu extraire le rapport entre les deux temps caractéristiques de transport du système. Le temps de transport, qui détermine la relaxation du courant et qui apparaît dans l'expression de conductivité de Drude, et le temps élastique, qui est le temps de vie d'un état électronique.

Le temps de transport τ_{tr} a été déduit à partir de la magnétorésistance à bas champ magnétique (figure 1.7), qui a une dépendance quadratique avec le champ magnétique et τ_{tr},

$$\rho \propto (\omega_c \tau_{tr})^2.$$

Le temps élastique a été déduit des oscillations de Shubnikov-de Haas à plus forts champs magnétiques, ou la résistivité à deux points s'écrit

$$\rho \propto \exp\left(-\frac{\pi}{\omega_c \tau_e}\right) \cos\left(\frac{E_F}{\hbar \omega_c}\right)$$

1. Plus précisément la conductivité a la forme $\approx \ln^2(k)$ comme on verra dans le chapitre 3

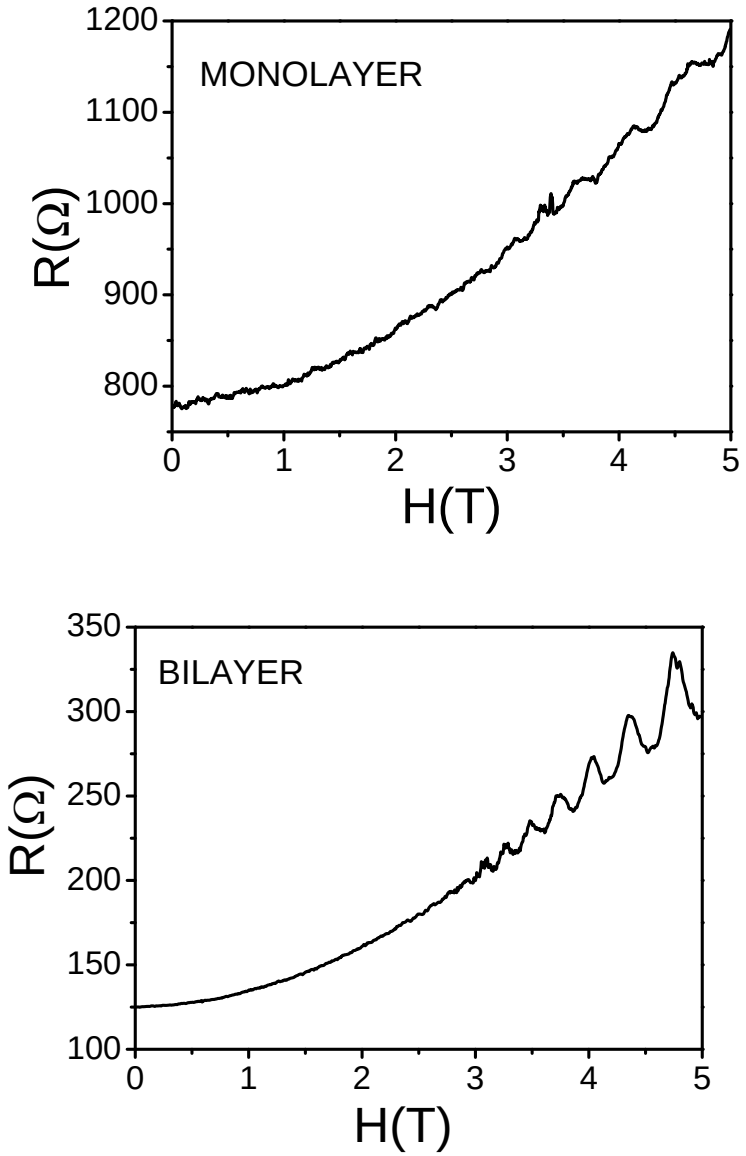

FIGURE 1.7 – Mesures de magnétorésistance pour la monocouche (haut) et la bicouche (bas) en dehors du point de Dirac. La résistance de contact a été soustraite dans le deux cas.

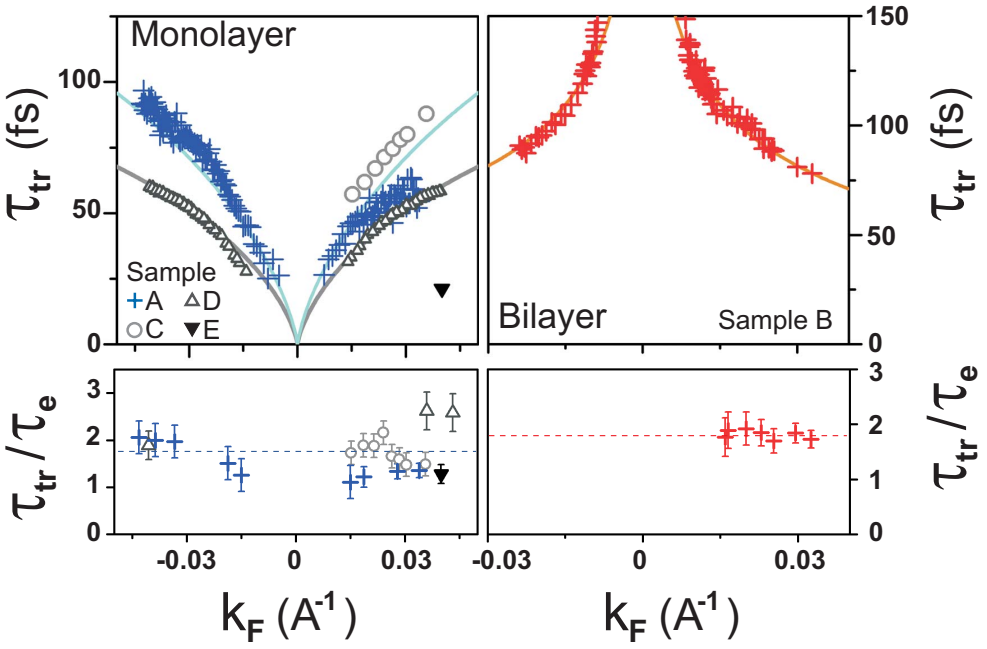

FIGURE 1.8 – Dépendance en k_F du τ_{tr} et du rapport τ_{tr}/τ_e. La figure de gauche montre des donnés provenant des monocouches mesurés au groupe de Physique Mésoscopique (A et C) et au CEA Saclay par Keyan Bennaceur (D et E). La figure de droit montre des données provenant de la bicouche. Les lignes continues correspondent au modèle théorique qui considère un particule de Dirac qui se diffuse sur une impureté forte de courte portée. Le rapport τ_{tr}/τ_e est près de 1.8 pour toutes les échantillons qu'on a étudié, comme c'est indiqué par les lignes pointillés.

Dans le cas de la monocouche ω_c depénd de k_F ($\omega_c = eB/(E/v_F^2)$), donc pour déduire τ_{tr}, k_F est déduit d'abord à partir de la période des oscillations de Shubnikov de Haas. τ_e est déduit de l'amortissement exponentiel des oscillations avec le champ magnétique.

Une avantage remarquable de cette méthode pour déduire les temps caractéristiques repose sur le fait que la résistance de contact n'intervient pas dans le calcul. Les calculs de τ_e et τ_{tr} et leur lien avec la nature des impuretés dans le graphène a été fait par Miguel Monteverde.

On a trouvé une dépendance différente de ces temps en k_F pour la monocouche et la bicouche comme est montré dans la figure 1.8. Ceci montre que la physique de ces deux systèmes est assez différente. On a trouvé aussi un rapport $\tau_{tr}/\tau_e \approx 1.8$, ce qui est signature d'une diffusion de courte portée (comme cela est expliqué au début du chapitre 3). Les lignes continues correspondent à un modèle qui considère la diffusion d'une particule de Dirac (sans masse dans le cas de la monocouche et massive pour la bicouche) sur une impureté forte de courte portée. Le modèle explique très bien nos résultats en indiquant que le mécanisme principal de diffusion dans nos échantillons est des défauts neutres, dont l'énergie est comparable à la largeur de bande $\approx eV$ et de courte portée ($R < \lambda_F$). Des possibles candidats en étant des lacunes ou des adatomes.

Dans le régime mésoscopique on s'est intéressé aux fluctuations universelles de la conductance et à l'effet de proximité avec un supraconducteur. Les fluctuations universelles de la conductance sont la signature la plus importante du transport cohérent dans un système. Dans un système cohérent, la conductance fluctue en fonction d'un paramètre externe comme le champ magnétique, l'énergie de Fermi ou le désordre. Quand on fait varier le champ magnétique traversant l'échantillon, l'énergie de Fermi ou le désordre, la phase entre deux trajectoires électroniques qui interférent est modifié ce qui se traduit par une variation de la conductance. Les fluctuations sont censées à être reproductibles et universelles avec une amplitude

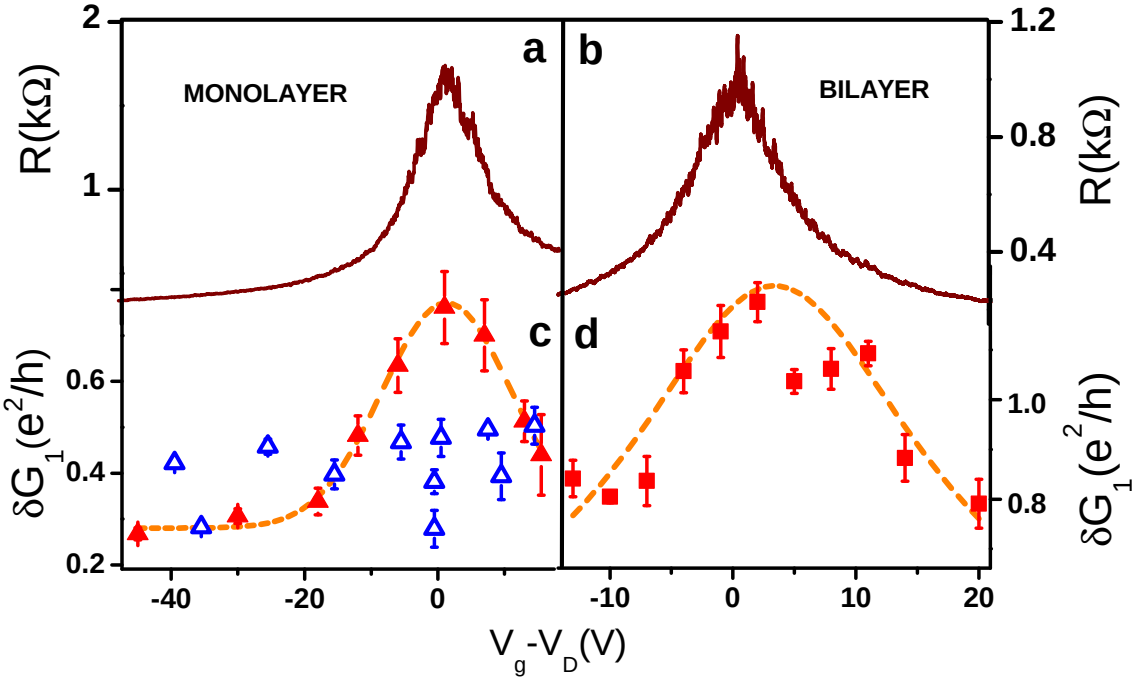

FIGURE 1.9 – L'amplitude des fluctuations de la conductance est comparée à la résistance en fonction de la tension de grille. Les fluctuations en fonction de la tension de grille (symboles pleines) sont plus grandes près du point de Dirac pour la monocouche et la bicouche (figures c) et d)). Les bares d'erreur sont la déviation standard de la différence entre deux balayages. L'amplitude des fluctuations en fonction de la tension de grille V_g change de façon similaire à la résistance. Les fluctuations en fonction du champ magnétique (triangles vides) ne changent pas énormément avec la tension de grille.

qui ne dépend pas du désordre ou de la taille de l'échantillon. Elles sont aussi ergodiques, les fluctuations en fonction de l'énergie de Fermi, du champ magnétique ou du désordre sont prédites avoir la même amplitude. Leur fonction de corrélation fait intervenir l'énergie de Thouless pour les fluctuations en fonction de l'énergie, $E_{Th} = \hbar D/L^2_{min}$ (avec D le coefficient de diffusion et $L_{min} = min(L, L_T, L_\phi)$ la longueur caracteristique sur laquelle ont lieu les interferences quantiques), et elle suit ϕ_0/S pour les fluctuations en fonction du champ magnétique. (ϕ_0 est le quantum de flux et S la surface de l'échantillon perpendiculaire au champ magnétique parcourue par les trajectoires cohérentes). Dans nos expériences sur la monocouche et la bicouche [87], on a trouvé que les fluctuations de la conductance étaient non-ergodiques. L'amplitude des fluctuations en fonction de l'énergie de Fermi dépend de l'énergie de Fermi alors que les fluctuations en fonction du champ magnétique n'en dépendent pas, comme c'est montré dans la figure 1.9

On a trouvé également que l'énergie de corrélation des fluctuations en fonction de l'énergie de Fermi correspond bien à l'énergie de Thouless et que le champ magnétique de corrélation des fluctuations en fonction du champ magnétique est en accord avec ϕ_0/S comme c'est prédit par la théorie pour les systèmes diffusifs (voir figure 1.10)

On a étudié aussi la conductance de deuxième ordre en fonction du champ magnétique. Il correspond au terme non linéaire qui apparaît dans la relation I-V, $I = G_1V + G_2V^2$. Ce terme est différent de zéro dans un échantillon mésoscopique quand la symétrie par inversion spatiale est absente, ce qui est le cas du graphène grâce aux impuretés. La présence d'un champ magnétique fait que les dipôles qui se forment autour des impuretés (qui sont liés à la tension de polarisation imposée), tournent dans une direction

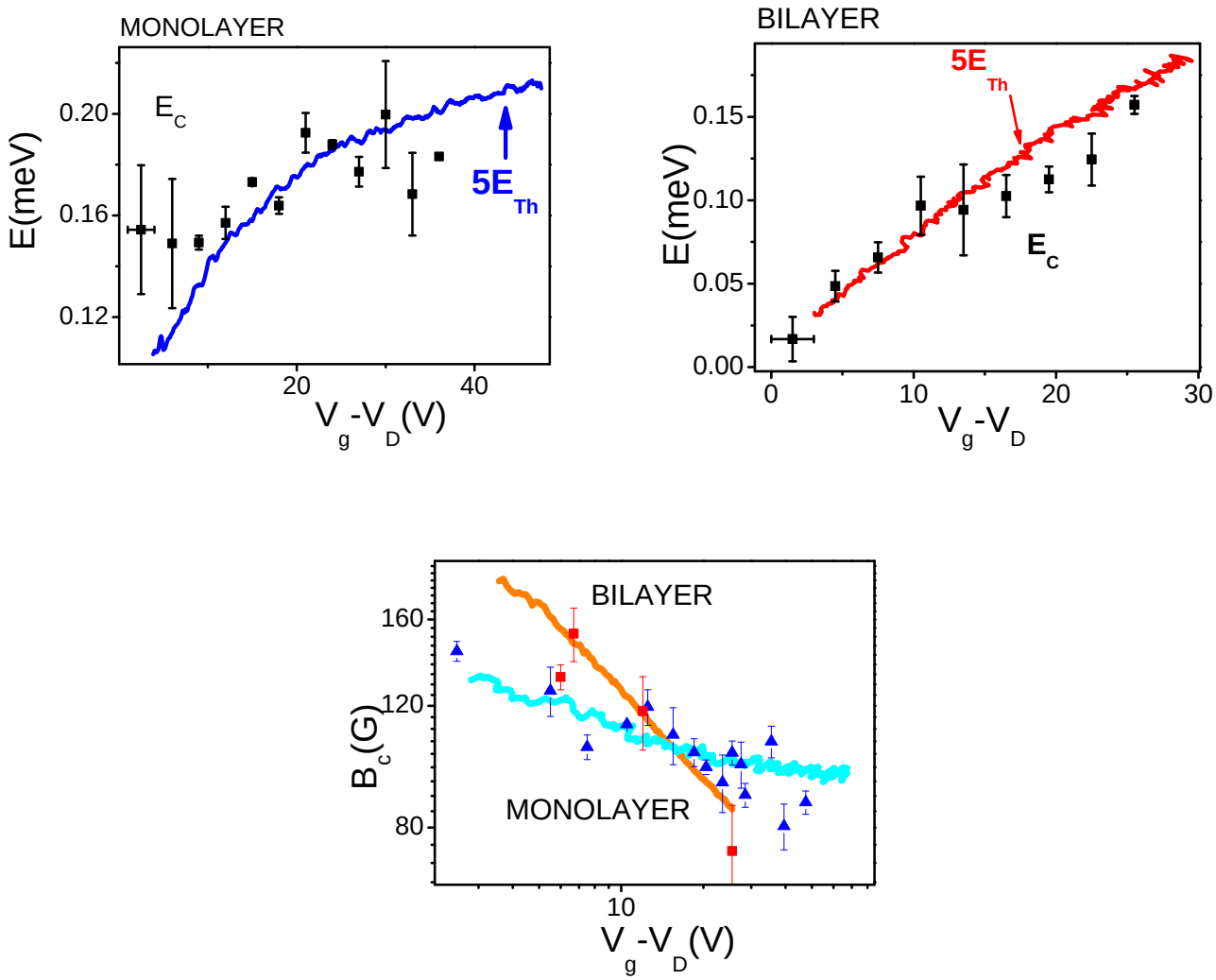

FIGURE 1.10 – Haut : Energie de corrélation des fluctuations de la conductance dans la monocouche et la bicouche. Les points représentent les énergies de corrélation extraits des donnés. La ligne continue représente $5E_{Th}$. Bas : champ magnétique de corrélation pour la monocouche (triangles) et la bicouche (carrés). Les lignes continues sont $B_\Phi = 6\Phi_0/(L_T L)$ pour la monocouche et $B_\Phi = 4\Phi_0/(L_T L)$ pour la bicouche.

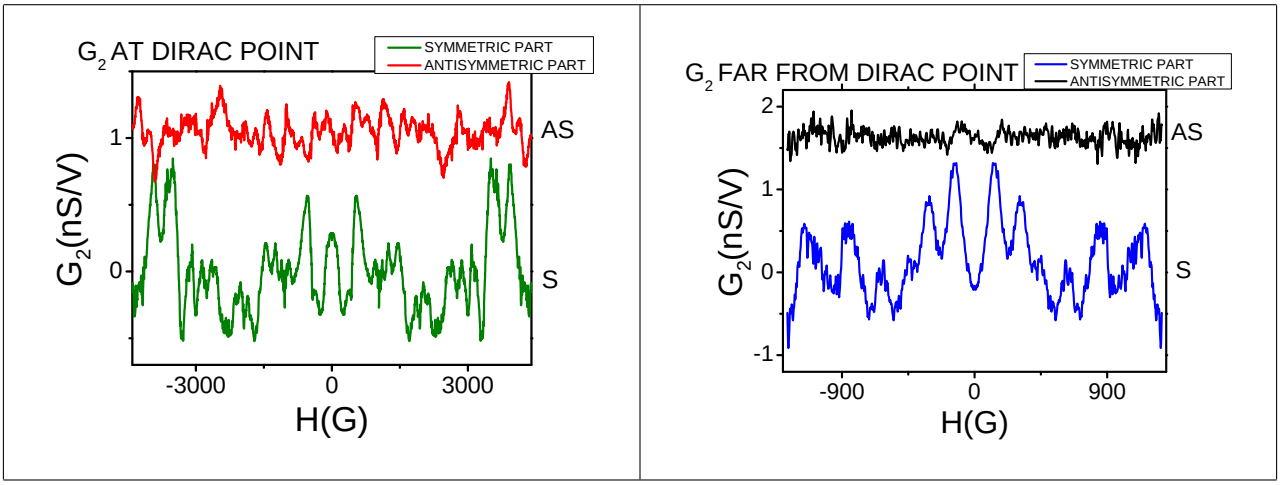

FIGURE 1.11 – G_2^{AS} et G_2^S près et loin du point de Dirac. Les courbes ont été décalés pour clarté.

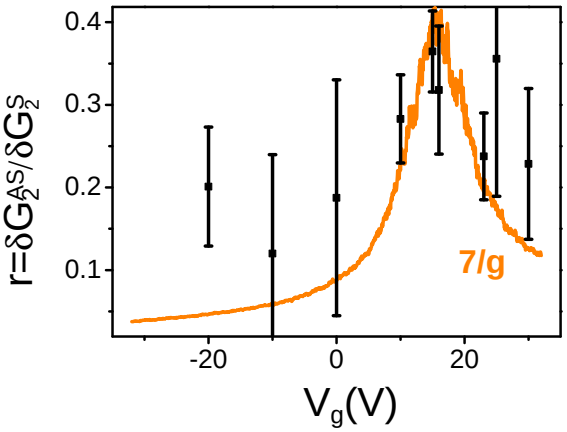

FIGURE 1.12 – Le rapport $r = \delta G_2^{AS}/\delta G_2^S$ extrait des donnés et comparé à $7/g$ (continuous line)

différente dépendant du signe du champ magnétique. La densité électronique gagne donc une composante impaire avec le champ magnétique qui change localement le potentiel. En conséquence, la conductance G_2 qui dépend du potentiel local (comme est montré dans le chapitre 4) acquiert une composante impaire en champ magnétique (contrairement à la conductance linéaire G_1 qui est symétrique en champ magnétique et qui suit les relations de Onsager). La figure 1.11 montre la partie symétrique et la partie antisymétrique de la conductance de second ordre G_2 de la monocouche près et loin du point de Dirac. On voit que l'amplitude de la partie antisymétrique est plus importante dans le premier cas. La figure 1.12 montre le rapport entre la partie antisymétrique de la variance de G_2 et la partie symétrique à différents tensions de grille. La théorie pour les systèmes diffusifs prédit que ce rapport doit suivre γ/g avec g la conductance adimensionnelle et γ une constante qui quantifie l'interaction entre les électrons ($\gamma = 0$ si il n'y a pas d'interaction $\gamma = 1$ si l'interaction est forte). On a pu calculer γ pour le graphène dans les différents dopages explorés avec la tension de grille (comme est expliqué dans le chapitre 4) et on a trouvé que $\gamma \approx 1$ dans toute la gamme de tension de grille explorée. La rapport $r = \delta G_2^{AS}/\delta G_2^S$ trouvé expérimentalement suit bien $1/g$ avec un facteur 7 qu'on attribue au rapport d'aspect de l'échantillon. Ceci constitue la première mesure de la conductance de deuxième ordre dans un échantillon mésoscopique diffusif .

Une deuxième expérience faite dans le régime mésoscopique a été l'induction d'un supercourant dans le graphène par effet de proximité. On s'attend à ce que la supraconductivité par effet de proximité dans le graphène soit modifiée par rapport à celle d'un matériau classique à cause de sa structure électronique où les bandes de valence et de conduction se touchent en un point à demi remplissage. Ceci fait que le processus qui rend possible le passage de paires de Cooper à travers le graphène, appelé réflexion d'Andreev, se passe différemment. Dans le graphène l'électron et le trou qui forment la paire d'Andreev peuvent appartenir à des bandes différentes. Ce phénomène, qui est censé à avoir une signature expérimentale a été exploré par plusieurs groupes sans que aucun signe ait été observé. Ceci est du aux poches d'électrons et trous qui se forment dans l'échantillon quand on est près du point de Dirac dont l'énergie est donc mal définie à l'échelle du gap supraconducteur.

Dans notre expérience on n'a pas vu une signature sur l'effet de proximité lié à la structure de bandes du graphène, mais on a pu induire la supraconductivité dans ce matériel de façon progressive [88]. En faisant plusieurs étapes de recuits sur l'échantillon, qui consistait en une feuille de graphène avec deux électrodes supra, on a réussi a augmenter progressivement le coefficient de transmission entre les électrodes et le graphène en ayant à la fin un supercourant traversant le graphène. La figure 1.13 montre l'évolution de la résistance en fonction de la tension de grille après les différents recuits. Chaque recuit consistait d'un fort courant (de $\approx 3mA$ à $\approx 11mA$) qui traversait l'échantillon pendant quelques dizaines de seconds. On voit sur la figure qu'après le deuxième recuit le point de Dirac se déplace à une tension de grille dont on a plus accès, et qu'après les différents recuits la résistance de l'échantillon baisse. En étant celle-ci une mesure à deux contacts on a conclu que la résistance de contact baisse après chaque recuit. Les fluctuations qu'on observe sur les premières courbes sont reproductibles et correspondent à des fluctuations universelles de la conductance. Dans la deuxième figure on voit l'évolution de la résistance différentielle après les différents recuits. La résistance baisse et des anomalies liées à des réflexions d'Andreev apparaissent après le premier et le deuxième recuit. Après le troisième recuit on observe une résistance nulle à tension nulle qui apparait. La figure 1.14 montre le supercourant induit modulé par un champ magnétique. Il a la forme d'un spectre de diffraction de Fraunhoffer, qui est caractéristique d'une jonction rectangulaire supra-métal normal-supra. Le fit de cette dépendance du supercourant avec le champ magnétique en tenant compte de la taille de l'échantillon, nous a confirmé que le supercourant observé venait d'un vrai effet de proximité induit sur le graphène et non pas de grains supraconducteurs qui auraient pu migrer pendant le recuit.

On s'est intéressé aussi à la supraconductivité de proximité dans le graphène induit par des nanoparticules superconductrices. Feigel'man *et al.* [47] ont montré que couvrir le graphène avec des îlots superconducteurs peut induire un état supraconducteur macroscopique dans le graphène avec une température critique de l'ordre du Kelvin pour une certaine distance entre les îlots. Le graphène, en ayant un coefficient de diffusion important ($D \geq 10^2 cm^2/s$) et une densité électronique faible ($10^{12}/cm^2$), n'est pas susceptible à un effet de proximité inverse puisque $\Delta_0 \geq G_{graph}\delta$ (Δ_0 est le gap supraconducteur des nanoparticules et δ l'espacement entre niveaux, $\delta \approx 1/L^2$).

Une image optique d'un des échantillons analysés, fabriqué par Alik Kasumov est montrée dans la figure 1.15. Une feuille de graphène est couverte avec des nanoparicules d'Indium de taille $\approx 5nm$ et espacés de $\approx 50nm$. Une mesure à deux points faite avec des électrodes en Pd/Ag déposés précédemment au dépôt des nanoparticules nous a révélé que en baisant la température, l'échantillon devient isolant, comme le montre la figure 1.16. La conductance suit une loi d'activation $G \propto \exp(-E_{act}/K_B T)$ avec une énergie d'activation $E_{act} = 0.2meV$ qui est proche du gap supraconducteur de l'Indium et aussi du gap spectral E_g prédit par Feigel'man, comme on verra dans le chapitre 5. On a observé que la conductance différentielle présente un gap qui a tendance à se fermer avec le champ magnétique et aussi en appliquant une tension de grille, comme c'est montré dans la figure 1.17.

Cette expérience nous a questionné s'il serait possible induire une transition métal-isolant dans le graphène en changeant la concentration des porteurs de charge avec la tension de grille, ou encore mieux une transition isolant-supraconducteur. Deux dimensions est la dimension critique pour la localisation et la supraconductivité, comme cela a été observé expérimentalement par plusieurs groupes qui ont étudié des filmes minces supraconductrices qui deviennent isolants quand on réduit l'épaisseur des filmes ou en

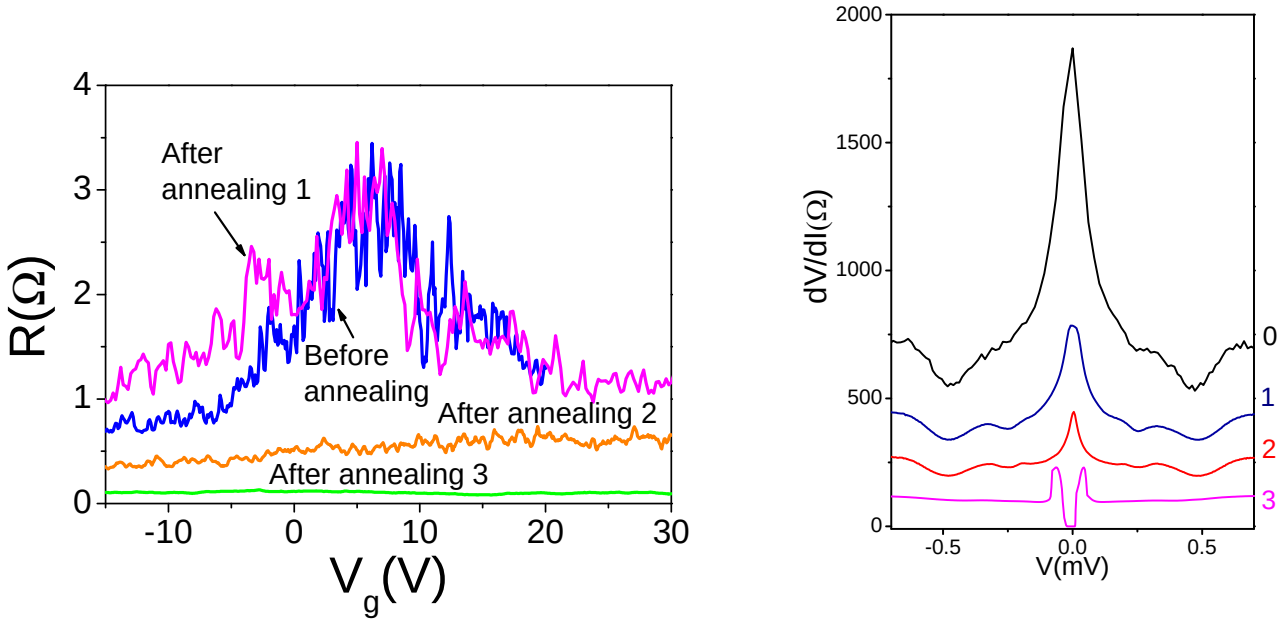

FIGURE 1.13 – Gauche : Résistance vs V_g après les différentes étapes de recuit (les courbes n'ont pas été décalés verticalement). Après le dernier recuit un supercourant a été induit dans le graphène. (Cette courbe a été mesurée avec un champ magnétique de $200G$ qui détruit l'effet de proximité, on mesure donc la résistance intrinsèque de l'échantillon). Droit : résistance différentielle en fonction de la tension de polarisation après les différents recuits.

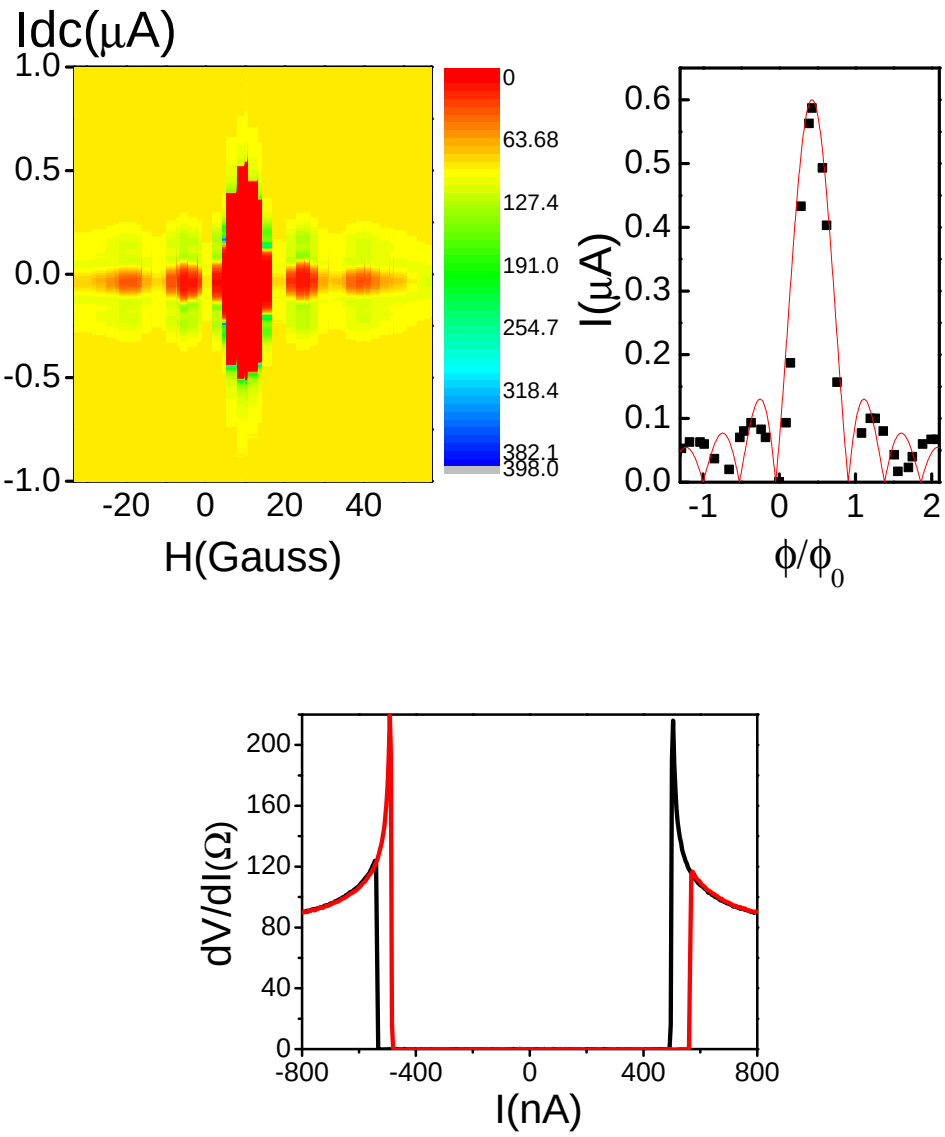

FIGURE 1.14 – Haut : Plot couleur de la résistance différentielle représentant la modulation du courant de switch par le champ magnétique (orange représente résistance nulle). La forme de cette figure est connue comme patron de diffraction de Franhouffer en analogie avec l'optique. Son origine est expliqué au début du chapitre 5. Bas : conductance différentielle. Un supercourant de $550nA$ a été induit dans le graphène lors du dernier recuit.

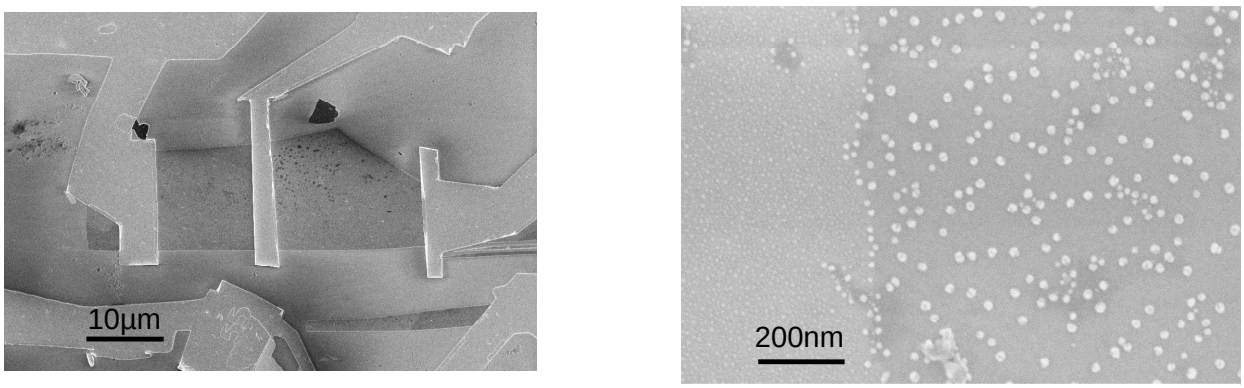

FIGURE 1.15 – Gauche : Image MEB de l'échantillon avant le dépôt des nanoparticules d'Indium. Droit : Zoom sur une région après le dépôt des nanoparticules. Les nanoparticules formées sont plus grandes sur le graphène que sur le substrat.

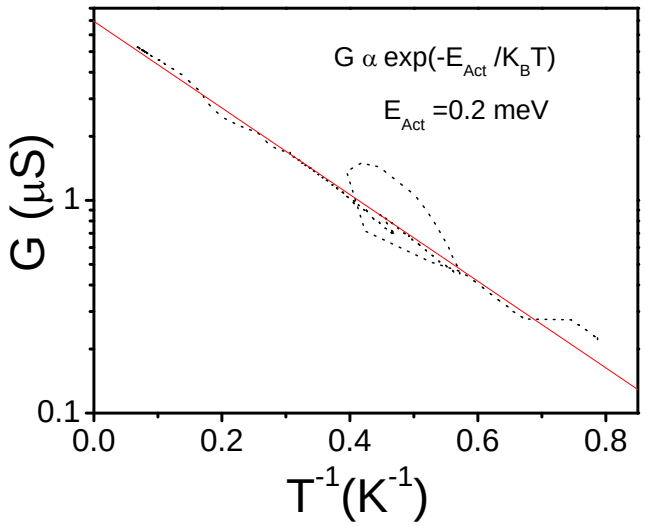

FIGURE 1.16 – Dépendance en température de la conductance en échelle log, elle suit une loi d'activation thermique avec une énergie d'activation de $0.2meV$

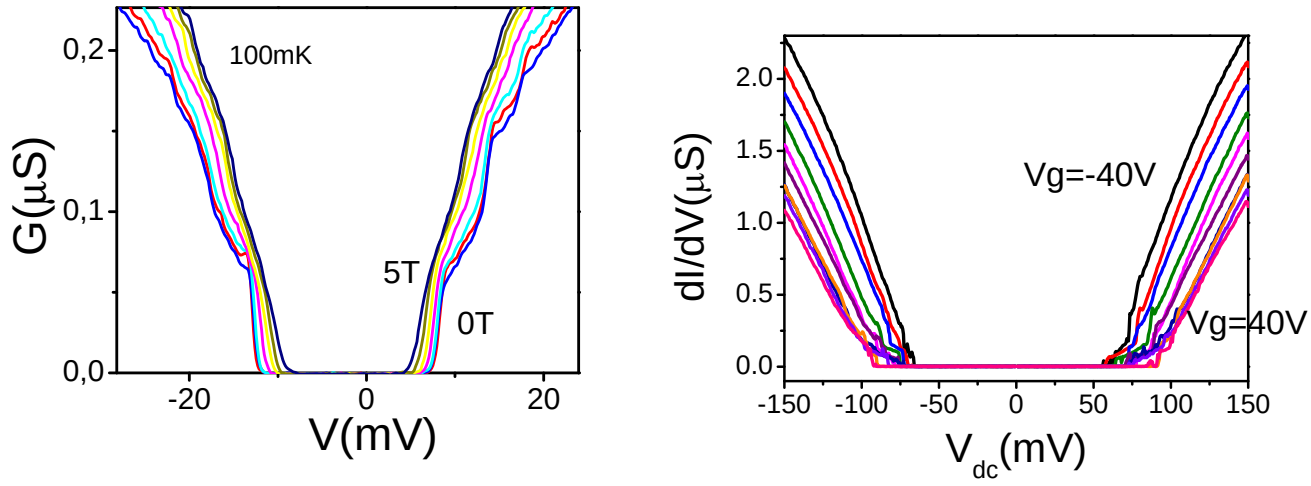

FIGURE 1.17 – Gauche : Conductance différentielle du graphène avec les nanoparticules d'Indium à des champs magnétiques différents. Le champ magnétique critique correspond à un quantum de flux traversant une nanoparticule. Droit : Conductance différentielle à des tensions de grille différentes

présence d'un champ magnétique. On se demande si une tel transition serait possible dans le graphène dans un échantillon moins désordonné que ceux mesurés jusqu'à maintenant. Des recuits sur l'échantillon ou une méthode moins violent pour le dépôt des nanoparticules pourrait peut être donner réponse à cette question.

Chapitre 2

Introduction

This thesis studies some aspects of quantum electronic transport in graphene, the two dimensional crystal made of carbon where conduction electrons behave as massless relativistic particles. Experiments done in this thesis can be classified in two different regimes, a macroscopic regime where there is no quantum interference effects between electrons (the phase coherence length L_ϕ is smaller than the size of the sample L, $L_\phi < L$) and a mesoscopic regime, where electron's wave packets interfere, ($L_\phi > L$).

Experiments we have done in the macroscopic regime correspond to magnetoresistance measurements up to moderate magnetic fields ($H \leq 5T$) where Shubnikov-de Haas oscillations are present. This phenomena is independent of the size of the sample and it is then macroscopic. Magnetoresistance measurements provide the characteristic transport times in graphene, as is explained in chapter 4, which let us elucidate the nature of scatterers in graphene. Comparison of our experimental results for the characteristic transport times with theoretical predictions let us deduce that the main scattering mechanism in our graphene samples is due to strong short range scatterers and not charged impurities as other works suggest. Likely candidates are vacancies, ad-atoms or short range ripples. Our results don't exclude completely the presence of long-range charged impurities, but their contribution to the characteristic transport times in our samples seems to be negligible. This is still a subject of controversy and it is of enormous relevance, since knowing the main scattering process in graphene opens the possibility of improving mobility, a parameter that depends weakly on temperature in graphene and that makes the one atom thick layer a competitive material with respect to doped bulk semiconductors. Semiconductors like $InSb$ exhibit room temperature mobilities up to $\approx 77\,000 cm^2V^{-1}s^{-1}$ when they are undoped [79]. In graphene, mobility might be improved to $\approx 100\,000 cm^2V^{-1}s^{-1}$ even at high electronic densities ($n > 10^{12} cm^{-2}$) by reducing the interaction with impurities.

In the mesoscopic regime, we have studied the superconducting proximity effect. When a normal metal is connected to two superconductors, superconducting features can be induced in the normal metal if it is phase coherent ($L_\phi > L$). Cooper pairs are transfered from one superconductor to the other thanks to a process called Andreev reflection. The particular band structure of graphene brings some specificities to this process, as it will be seen in chapter 6. In our experiment even if we were not able to see these particularities (as the other groups that have tried so far) we have successfully induced a superconducting proximity effect in graphene, by gradually tuning the transparency between graphene and the superconducting electrodes. In the mesoscopic regime, we have also studied universal conductance fluctuations (UCF), the main signature of phase coherence transport in a system. Correlation functions of UCF depend on the diffusion coefficient which has a specific dependence on the electronic density in graphene, as will be seen in chapter 5. We have found a specific experimental correlation function associated to the electronic density dependence of the diffusion coefficient of graphene. We have compared with measurements on a bilayer graphene, finding a different correlation function associated to its different diffusion coefficient. We have observed that for the monolayer the electronic density dependence of the amplitude of conductance fluctuations is different when they are induced by a modulation of electronic density and when they are induced by a modulation of magnetic field. Thus conductance fluctuations in

graphene are non-ergodic. We have also analyzed the second harmonic of conductance fluctuations. This is a very interesting term since it gives information about the e-e interaction in a system. We have found, thanks to the tunability of graphene's conductance, that it decreases with conductance, in accordance with theory. This constituted the first measurement of second order conductance fluctuations in a diffusive system. In the following, I will discuss in detail the physics of the monolayer and the bilayer graphene. These two similar systems, fabricated with the same exfoliation technique, gave us access to two different physics. The first, of relativistic massless particles with a linear dispersion relation, and the second, of massive Dirac particles with a quadratic dispersion relation like most systems.

A bidimensional crystal like graphene was thought impossible 70 years ago. According to Peierls and Landau, there could not be a crystalline long range order in one or two dimensions. Their argument was based on the harmonic approximation in the case of Peierls and on the theory of second order phase transitions in the case of Landau, and it was later extended by Mermin [80] who put Peierls and Landau's argument on a rigorous basis for a large class of interparticle interactions. The impossibility of a long range order resided in thermal fluctuations. Thermal fluctuations at low dimensions lead to a displacement of atoms of the order of the interatomic distance, making 2D crystals unstable, to the point of melting. But since graphene lives in a three dimensional world, thermal fluctuations can be dissipated in the third dimension making the two dimensional crystal stable. This doesn't contradict Peierls and Landau's conclusion since it was based on a bidimensional crystal living in a bidimensional world. The cost of this stability is a deformation in the third direction, which makes graphene not perfectly flat. Observed ondulations in graphene are on average $\approx 1nm$ high and $\approx 10nm$ long, they are smooth and surprisingly they don't create any defects in the crystal.

Graphene is made of carbon, which is built from 6 protons, 6 neutrons and 6 electrons. In the atomic ground state, the 6 electrons are in the configuration $1s^2 2s^2 2p^2$. Two electrons fill the inner shell $1s$ which is close to the nucleus and irrelevant for chemical reactions and 4 electrons occupy the outer shell of $2s$ and $2p$ orbitals. Three of these electrons form strong covalent σ bonds with the neighbor carbon atoms and one electron yields π bonds. There is then 1 π electron per atom responsible for the electronic properties at low energies, and 3 σ electrons that form energy bands far from the Fermi level and that are responsible for the honeycomb lattice. The π electrons have a particular behavior, which comes from the hexagonal structure in which carbon atoms are arranged (figure 2.1). This structure is not a Bravais lattice since atoms in the crystal are not equivalent (they don't see the same environment) they are then classified in atoms of type A and atoms of type B. Atoms of type A have a nearest neighbor in the north and two in the south. Atoms of type B on the other hand have two nearest neighbors in the north and one in the south. Nearest neighbors of A are determined by the vectors $\mathbf{e}_1$, $\mathbf{e}_2$ and $\mathbf{e}_3$ shown in figure 2.1,

$$\mathbf{e}_1 = \frac{a}{2}\left(\sqrt{3}\mathbf{e}_x + \mathbf{e}_y\right) \tag{2.1}$$

$$\mathbf{e}_2 = \frac{a}{2}\left(-\sqrt{3}\mathbf{e}_x + \mathbf{e}_y\right) \tag{2.2}$$

$$\mathbf{e}_3 = -a\mathbf{e}_y. \tag{2.3}$$

The hexagonal (honeycomb) lattice can however be decomposed in a triangular Bravais lattice with a basis of two atoms per unit cell (A and B) as is shown in figure 2.1. Unit lattice vectors $\mathbf{a_1}$ and $\mathbf{a_2}$ can be written like

$$\mathbf{a_1} = \sqrt{3}a\mathbf{e_x} \qquad \mathbf{a_2} = \frac{\sqrt{3}a}{2}\left(\mathbf{e_x} + \sqrt{3}\mathbf{e_y}\right)$$

where $a \approx 0.14nm$ is the distance between nearest neighbors. The reciprocal lattice vectors are given by

$$\mathbf{a_1^*} = \frac{2\pi}{\sqrt{3}a}\left(\mathbf{e_x} - \frac{\mathbf{e_y}}{\sqrt{3}}\right) \qquad \mathbf{a_2^*} = \frac{4\pi}{\sqrt{3}a}\mathbf{e_y}$$

The first Brillouin zone has an hexagonal form (figure 2.2) with two inequivalent points K and K' that cannot be related using reciprocal lattice vectors and that have the associated vectors $\mathbf{K}^+$ and $\mathbf{K}^-$.

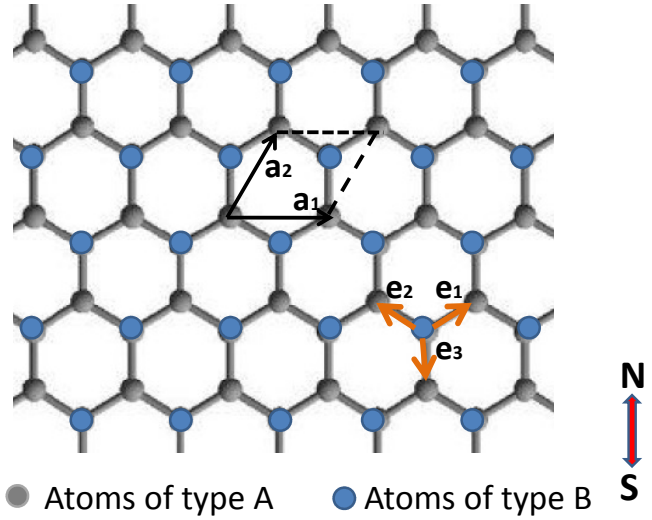

FIGURE 2.1 – Honeycomb lattice structure of graphene. Lattice vectors $\mathbf{a_1}$ and $\mathbf{a_2}$ define a triangular Bravais lattice with two atoms A and B per unit cell. $\mathbf{e_1}$, $\mathbf{e_2}$ and $\mathbf{e_3}$ indicate the nearest neighbors of type B atoms.

Other equivalents points can be obtained from $\mathbf{K}$ and $\mathbf{K'}$ with a translation of the reciprocal vector $G = \gamma_1 \mathbf{e_1^*} + \gamma_2 \mathbf{e_2^*}$ with γ_1 and γ_2 integers.

$$\mathbf{K}^{\pm} = \pm \frac{4\pi}{3\sqrt{3}a} \mathbf{e_x}$$

The most important electronic properties of graphene can be obtained using the tight binding approximation. It was Wallace [75] who calculated for the first time the band structure of graphene and showed the unusual semimetallic behavior of this material. In the following, I discuss the deduction of the dispersion relation using the tight binding hamiltonian as is done in the lecture notes of the course "2D electrons in strong magnetic fields" by Marc Goerbig and Pascal Lederer [76].

It is considered a tight binding hamiltonian for electrons that can hop to the nearest neighbor atoms,

$$H = -t \sum_{i \in A} \sum_{j=1}^{3} \left(a^+_{\mathbf{R_i}} b_{\mathbf{R_i}+\mathbf{e_j}} + b^+_{\mathbf{R_i}+\mathbf{e_j}} a_{\mathbf{R_i}} \right) \tag{2.4}$$

where $a_{\mathbf{R_i}}$ ($a^+_{\mathbf{R_i}}$) annihilates (creates) an electron at the site $\mathbf{R_i}$ of the sublattice A and $b_{\mathbf{R_i}+\mathbf{e_j}}$ ($b^+_{\mathbf{R_i}+\mathbf{e_j}}$) annihilates (creates) an electron of sublattice B at the site $\mathbf{R_i}+\mathbf{e_j}$. $\mathbf{e}_j$ denotes the nearest neighbor atoms (2.1, 2.2 and 2.3) and $t \approx 2.7eV$ is the nearest neighbor hopping energy and it comes from the overlap between wavefunctions of neighbor sites. Next nearest neighbor hopping is not considered since overlap between wavefunctions in that case is $t' \approx 0.1eV$ and affects dispersion relation only at energies of the order of $100meV$. The dispersion relation for graphene at low energies is therefore deduced using the relation 2.4 and the following Fourier transformation

$$a_{\mathbf{R_i}} = \sum_{\mathbf{q}} e^{i\mathbf{q}\cdot\mathbf{R_i}} a_{\mathbf{q}} \qquad b_{\mathbf{R_i}+\mathbf{e_j}} = \sum_{q} e^{-i\mathbf{q}\cdot(\mathbf{R_i}+\mathbf{e_j})} b_{\mathbf{q}}$$

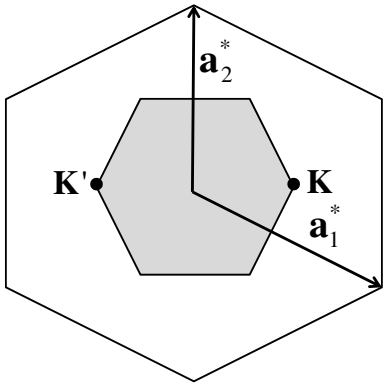

FIGURE 2.2 – First Brillouin zone with the inequivalent points $\mathbf{K}$ and $\mathbf{K}'$.

which permits to write the hamiltonian 2.4 like

$$H = \sum_q \left(a^+_{\mathbf{q}}, b^+_{\mathbf{q}}\right) H_{\mathbf{q}} \begin{pmatrix} a_{\mathbf{q}} \\ b_{\mathbf{q}} \end{pmatrix}$$

where

$$H_{\mathbf{q}} = \begin{pmatrix} 0 & h(\mathbf{q}) \\ h(\mathbf{q}) & 0 \end{pmatrix} \qquad with \qquad h(\mathbf{q}) \equiv -t \sum_j e^{i\mathbf{q}\cdot\mathbf{e_j}}. \tag{2.5}$$

The matrix $H_{\mathbf{q}}$ can be written in terms of the Pauli matrices,

$$\sigma_x = \begin{pmatrix} 0 & 1 \\ 1 & 0 \end{pmatrix}, \qquad \sigma_y = \begin{pmatrix} 0 & -i \\ i & 0 \end{pmatrix}, \qquad \sigma_z = \begin{pmatrix} 1 & 0 \\ 0 & -1 \end{pmatrix}.$$

$$H_{\mathbf{q}} = -t \sum_j \left(\cos(\mathbf{q}\cdot\mathbf{e}_j)\sigma_x + \sin(\mathbf{q}\cdot\mathbf{e}_j)\sigma_y\right),$$

and the diagonalization of this matrix yields the dispersion relation of graphene at low energies

$$\epsilon_{\mathbf{q}} = \pm \sqrt{\left(\sum_j \cos(\mathbf{q}\cdot\mathbf{e}_j)\right)^2 + \left(\sum_j \sin(\mathbf{q}\cdot\mathbf{e}_j)\right)^2} \tag{2.6}$$

the positive and negative sign correspond to the electron and hole bands, which are represented in figure 2.3. Electron and hole bands touch at points $\mathbf{K}$ and $\mathbf{K}'$ called Dirac points. There is then no gap between the two bands. Also, since there are as many electrons π electrons as the carbon atoms, the valence band is full while the conduction band is empty, so that the Fermi level is just at the contact point between the two bands. When considering low energy excitations ($E < t \approx 2.7eV$) the Hamiltonian 2.5 can be developed around points K and K', giving a linear dispersion relation.

If we develop wave vectors $\mathbf{q}$ around $\mathbf{K}^{\pm}$,

$$\mathbf{q} = \mathbf{K}^{\pm} + \kappa \qquad with \qquad |\kappa| << 1/a,$$

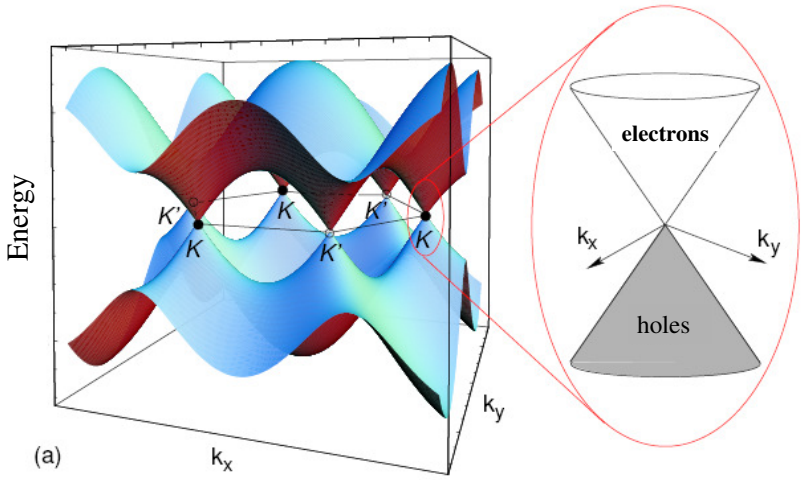

FIGURE 2.3 – Dispersion relation of graphene considering only the nearest neighbor hopping. Electron and hole band touch at Dirac points K and K'. The zoom shows the low energy dispersion relation. (Taken from [76]).

the exponential in the Hamiltonian $H_{\mathbf{q}}$ (2.5) can be written

$$\begin{aligned} h(\mathbf{q}) &= -t\sum_j e^{i\mathbf{q}\cdot\mathbf{e}_j} \simeq -t\sum_j e^{i\mathbf{K}^{\pm}\cdot\mathbf{e}_j}(1+\kappa\cdot\mathbf{e}_j) \\ &= -it\sum_j e^{i\mathbf{K}^{\pm}\cdot\mathbf{e}_j}\kappa\cdot\mathbf{e}_j \end{aligned}$$

since $\sum_j exp(i\mathbf{K}^{\pm}\cdot\mathbf{e}_j)=0$. This comes from the fact that energy is zero at $\mathbf{K}^{\pm}$, $H|\psi_{\pm}(\mathbf{K}^{\pm})\rangle=0$ and so $h(\mathbf{K}^{\pm})=0$ in relation 2.5. Doing the sum over the nearest neighbors whose vectors $\mathbf{e}_j$ are 2.1, 2.2 and 2.3 we have

$$h(\mathbf{q}) \simeq \pm\frac{3}{2}ta(\kappa_x - i\kappa_y). \tag{2.7}$$

which determines a new effective hamiltonian,

$$H^{eff}_{\alpha=\pm}(\kappa) = \frac{3}{2}ta\begin{pmatrix} 0 & \alpha(\kappa_x - i\kappa_y) \\ \alpha(\kappa_x + i\kappa_y) & 0 \end{pmatrix} = \frac{3}{2}ta\alpha\left(\kappa_x\sigma_x + \kappa_y\sigma_y\right) \tag{2.8}$$

There are two effective Hamiltonians $\alpha=+$ and $\alpha=-$ corresponding to the points K and K', they can be written in the following way :

$$H^{eff}_{\alpha=\pm} = \alpha\hbar v_F\kappa\cdot\sigma,$$

which is the Hamiltonian of a massless relativistic particle, revealing the relativistic character of electrons in graphene.

Diagonalization of the Hamiltonian 2.8 gives the dispersion relation around K and K'

$$\epsilon_\alpha(\kappa) = \pm\frac{3}{2}ta|\kappa| = \pm\hbar v_F|\kappa| \tag{2.9}$$

where v_F is the Fermi velocity, the group velocity of electrons near Fermi energy

$$v_F = \frac{3ta}{2\hbar} \approx 1 \times 10^6 m/s. \tag{2.10}$$

The dispersion relation is linear, as is represented in the zoom in figure 2.3. Its validity is restricted to low energies, where the chemical potential is smaller than t. The chemical potential μ can be written in terms of the Fermi wave vector like

$$k_F = \frac{\mu}{\hbar v_F}$$

and using 2.10 we can write $\mu/t = 3ak_F/2$. The condition $\mu << t$ is then equivalent to

$$ak_F << 1 \qquad or \qquad \lambda_F >> a$$

which is precisely what justifies the development of wavevectors around K and K'.

To estimate k_F in our samples we can use the following relation (for voltages far from the Dirac point) [1]

$$k_F = 4.9 \times 10^7 \sqrt{V_g - V_D}\ m^{-1}$$

where V_g is the gate voltage applied to the sample that allows to change the Fermi energy E_F, and V_D is the gate voltage corresponding to the Dirac point. The maximum gate voltage applied to our samples is in general $V_g - V_D \approx 60V$ which gives a minimum bound for λ_F of $\approx 17nm$. The maximum bound to λ_F is given by the minimum electronic density reachable in our samples, which is in general $\approx 0.2 \times 10^{12}/cm^2$. It is limited by the puddles of electrons and holes that impede to target a zero electronic density. k_F is determined from the electronic density using

$$k_{Fmin} = \sqrt{\pi n_{min}}.$$

We have then

$$17nm \lesssim \lambda_F \lesssim 79nm$$

The minimum λ_F being limited by the maximum gate voltage that can be applied to the sample without damaging it ($\approx 60V$), implies that we are always in the regime $\lambda_F > a$ with a the carbon to carbon distance $\approx 0.14nm$, which makes the low energy model a valid model.

The band structure of graphene give it its particularities to this material. The main features can be summarized as :

1. Valence and conduction band touch at zero energy points K and K' that are crystallographically inequivalent. The inequivalence of these two points is not related to the presence of two types of atoms A and B in the unit cell but to the Bravais lattice itself. Graphene is then a zero gap semiconductor with two valleys. It can also be seen as a metal in which valence and conduction bands form a single big band but having a zero density of states near the Fermi level.
2. Near the Fermi level, the dispersion relation of electrons is linear like the one of massless Dirac fermions, $\epsilon = \pm\sqrt{p^2c^{*2} + m^{*2}c^{*2}} = \pm pc^*$ with a zero effective mass $m^* = 0$ and a velocity $c^* = \sqrt{3}ta/2\hbar$ which is related to the lattice constant $a \approx 0.25nm$ and the hopping energy $t \approx 3eV$. The group velocity of electrons in graphene c^* is 300 times smaller than the velocity of light.
3. Near the Fermi level, there is a symmetry between the conduction and the valence band. It is referred to as electron hole symmetry.

Graphene brings us to the bilayer graphene, which is also a very interesting material. In this material semiconducting properties can be controlled by electric field effect. Bilayer graphene can have a gap that can be modulated by applying a bias voltage between the two graphene layers (contrary to the monolayer), but most of all, bilayer graphene gives access to a different physics with respect to the monolayer, with a

1. This relation comes from the capacitor model, which will be described in the next chapter

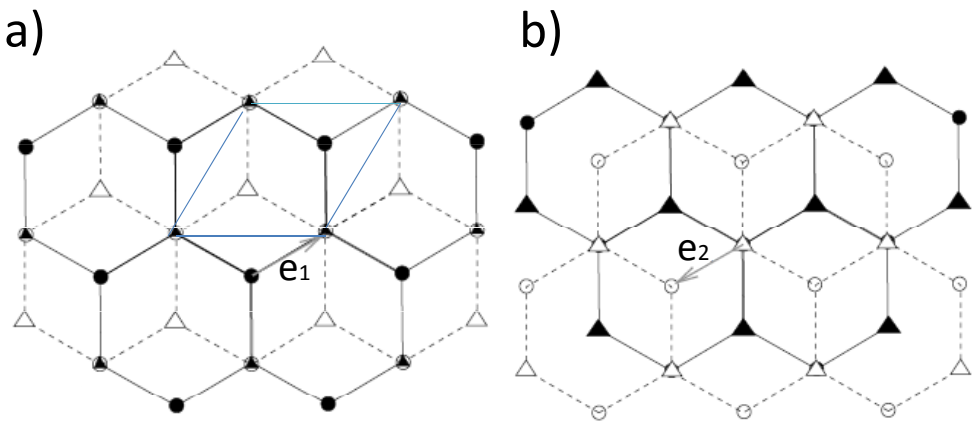

FIGURE 2.4 – The two possibilities for stacking two graphene layers. Black corresponds to the lower layer, white to the upper layer. Circles are sites of type A, triangles sites of type B. In a) the upper layer is displaced by $\mathbf{e_1}$ with respect to the lower layer and in b) the the upper layer is translated by $\mathbf{e_2}$. A unit cell is represented in a). Bilayer graphene has 4 atoms per unit cell. (Taken from [76]).

dispersion relation that is quadratic rather than linear, a different diffusion factor, a different density of states and a different quantization of energy levels in the presence of a magnetic field.

Bilayer graphene consists of two stacked graphene layers separated by $d \approx 2.4a = 0.34nm$. The layers are displaced with respect to each other by $\mathbf{e_1}$ or $\mathbf{e_2}$ (relations 2.1 and 2.2), as is shown in figure 2.4 Bilayer's band structure can be deduced using a tight binding hamiltonian as was done for graphene [77],

$$\begin{aligned} H &= -\gamma_0 \sum_{<i,j>m} \left(a^+_{m,i} b_{m,j} + h.c. \right) \\ &- \gamma_1 \sum_j \left(a^+_{1,j} a_{2,j} + h.c. \right) \\ &- \gamma_3 \sum_j \left(a^+_{1,j} b_{2,j} + a^+_{2,j} b_{1,j} + h.c. \right) \\ &- \gamma_4 \sum_j \left(b^+_{1,j} b_{2,j} + h.c. \right) \end{aligned}$$

where $a_{m,i}$ annihilates an electron on sublattice A in plane $m = 1, 2$ at site $\mathbf{R}_i$ and $b_{m,j}$ annihilates an electron on sublattice B at site $\mathbf{R}_j$ with j nearest neighbor of i. γ_0 is the in-plane hopping energy $t \approx 2.8eV$, $\gamma_1 = t_\perp \approx 0.35eV$ is the hopping energy between atom A_1 and A_2 (see figure 2.5), $\gamma_3 \approx 0.3eV$ is the hopping energy between atom A_1 and atom B_2 (or atom A_2 and atom B_1) and $\gamma_4 \approx 0.2eV$ is the hopping energy between B_1 and B_2. In Fourier space at low energies, wavevector $\mathbf{q}$ can be expanded

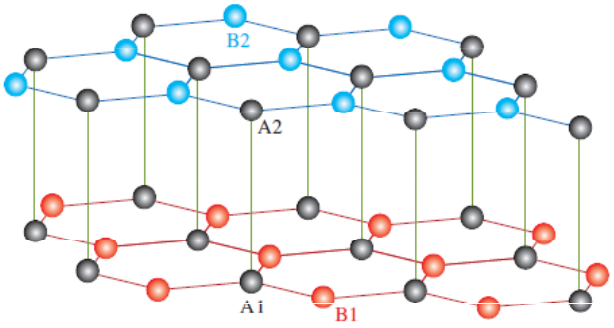

FIGURE 2.5 – Lattice structure of the bilayer. Dark circles represent atoms A and lighter circles atoms B. Taken from [77].

around $\pm\mathbf{K}$ like in the monolayer, giving the following effective Hamiltonian

$$H^{eff} = \begin{pmatrix} -V & \hbar v_F k & 0 & 3\gamma_3 a k^* \\ \hbar v_F k^* & -V & \gamma_1 & 0 \\ 0 & \gamma_1 & V & \hbar v_F k \\ 3\gamma_3 a_k & 0 & \hbar v_F k^* & V \end{pmatrix} \tag{2.11}$$

where $k = k_x + ik_y$ is a complex number and V is half the potential between the two layers. If no potential is applied between the two layers $V = 0$ and $\gamma_3, v_F k << \gamma_1$ high energy states can be eliminated perturbatively and the effective Hamiltonian is reduced to :

$$H^{eff} = \begin{pmatrix} 0 & \frac{\hbar^2 v_F^2 k^2}{\gamma_1} + 3\gamma_3 a k^* \\ \frac{\hbar^2 v_F^2 k^{*2}}{\gamma_1} + 3\gamma_3 a k & 0 \end{pmatrix} \tag{2.12}$$

If $\gamma_3 = 0$ the effective Hamiltonian 2.12 has the eignevalues

$$\epsilon_{k,\pm} \approx \pm \frac{\hbar^2 v_F^2 k^2}{t_\perp} = \pm \frac{\hbar^2 k^2}{2m^*},$$

with $m^* \approx 0.035 m_e$. This dispersion relation correspond to two parabolic bands touching at $\epsilon = 0$ as is shown in figure 2.6. Two additional bands start at $\pm t_\perp$. When $\gamma_3 \neq 0$ the spectrum changes at low energies. Instead of two bands touching at $k = 0$, there are four Dirac like linear bands lying at $k = 0$ and at three equivalent points with a finite momentum. If a gate voltage is applied between the two layers a gap appears that depends on the applied voltage.

The main differences and similarities between the band structure of the bilayer and the monolayer graphene can be summarized as :

1. In bilayer graphene, the valence and conduction band touch each other at zero energy like in the single layer.
2. In the approximation $\gamma_3 = 0$ (no hopping between atoms A_1 and B_2 in figure 2.5), dispersion relation of the bilayer is quadratic and not linear like in the case of the monolayer.

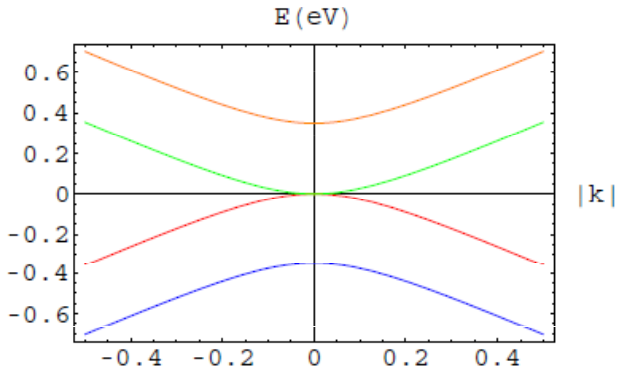

FIGURE 2.6 – Band structure of the bilayer graphene when $V = 0$. There are two bands that start at $\epsilon = 0$ and two additional bands that start at $\pm t_\perp$

3. Valence and conduction bands being symmetric like in graphene for the bilayer, they touch at a single $k = 0$ point contrary to graphene (in the $\gamma_3 = 0$ approximation.)
4. Bilayer graphene opens the possibility of a tunable gap semiconductor.

Lets now discuss the density of states and the diffusion coefficient of these two systems. The density of states $\rho(E_F)$ counts the number of states per unit area $\mathscr{A}$ in the vicinity of Fermi energy. It can be obtained from the number of states N below E_F,

$$\rho(E_F) = \frac{1}{\mathscr{A}} \frac{\partial N}{\partial E}$$

with

$$N_c = g \sum_{\substack{\mathbf{k} \\ k \leq k_F}} \approx g\mathscr{A} \int_{k \leq k_F} \frac{d^2k}{(2\pi)^2} = \frac{g\mathscr{A}}{4\pi^2} 2\pi \int_0^{k_F} dk k = \frac{g\mathscr{A}}{4\pi} k_F^2$$

which is valid for any bidimensional system (g is the degeneracy due to internal degrees of freedom). In the case of graphene and the bilayer we have respectively

$$E_{ML} = \hbar v_F k_F \qquad E_{BL} = \frac{\hbar^2 k_F^2}{2m^*}$$

then $k_F^2 = E_{ML}^2/\hbar^2 v_F^2$ for the monolayer and $k_F^2 = E_{BL} 2m^*/\hbar^2$ for the bilayer, which gives

$$\rho(E_F)_{ML} = \frac{2E_F}{\pi \hbar^2 v_F^2} \qquad and \qquad \rho(E_F)_{BL} = \frac{2m^*}{\pi \hbar^2} \tag{2.13}$$

where I have taken $g = 4$ for the monolayer and the bilayer (degeneracy of spin and valley). The density of states is linear in energy for the monolayer and is a constant for the bilayer, like in most 2D systems.

The diffusion coefficient tells how electrons diffuse in a system. It can be written in terms of the mean free path, $D = v_F l_e/d$ with d the dimension of the system, or in terms of the density of states,

$$D = \frac{\sigma}{e^2 \rho(E_F)}$$

Experimentally conductivity σ is found proportional to k_F^2 for both the monolayer and the bilayer [2]. Then

$$\sigma_{ML} \propto \sqrt{E_F} \quad , \quad \sigma_{BL} \propto E_F$$

and

$$D_{ML} \propto \frac{1}{\sqrt{E_F}} \quad , \quad D_{BL} \propto E_F.$$

The diffusion coefficient has then a different dependence on Fermi energy for the monolayer and the bilayer due to the different density of states of these two systems.

An other remarkable difference between the monolayer and the bilayer lies on the Fermi velocity. Usually, the Fermi velocity changes with energy, as is the case in the bilayer

$$v_{BL} = \frac{\hbar k}{m^*} = \sqrt{\frac{2E}{m^*}}.$$

In the monolayer on the other hand, electrons have always the same velocity no matter their energy or momentum,

$$v_{ML} \approx 1 \times 10^6 m/s.$$

Finally, lets discuss the properties of graphene and bilayer graphene in the presence of a magnetic field. I will follow the approach used during the lectures on graphene given at Orsay by Jean Nöel Fuchs and Marc Goerbig [57].

We can deduce the expressions of the cyclotron mass and the cyclotron radius using Hamilton equations. The Hamiltonian of a system in the presence of a magnetic field, depends on $\mathbf{\Pi}$ the quantity of motion, that in a crystal is $\hbar\mathbf{k}$ with $\mathbf{k}$ the Bloch wavevector. $\mathbf{\Pi}$ is Gauge invariant but is not the conjugated momenta. Conjugated momenta $\mathbf{p}$ is given by

$$\mathbf{p} = \mathbf{\Pi} + q\mathbf{A}$$

which is on the other hand, non Gauge invariant.

Hamiltonian has the form

$$H(\mathbf{p}, \mathbf{r}) = E(\mathbf{\Pi}) = E(\mathbf{p} + e\mathbf{A}) \tag{2.14}$$

where $E(\mathbf{\Pi})$ is respectively for the bilayer and the monolayer,

$$E_{BL} = \frac{\mathbf{\Pi}^2}{2m^*}, \qquad E_{ML} = v_F|\mathbf{\Pi}|. \tag{2.15}$$

$E(\mathbf{\Pi}) = E(|\mathbf{\Pi}|)$ given the symmetry of the band structure of graphene. Hamilton equations are, given that H has the form 2.14

$$\begin{aligned} \dot{\mathbf{r}} = \mathbf{v} &= \frac{\partial H}{\partial \mathbf{p}} = \frac{\partial E}{\partial \mathbf{\Pi}} \\ \dot{\mathbf{p}} &= -\frac{\partial H}{\partial \mathbf{r}} = -\frac{\partial E}{\partial \mathbf{\Pi}} \times \frac{\partial (e\mathbf{A})}{\partial \mathbf{r}} = -e\mathbf{v} \times \mathbf{B} \end{aligned} \tag{2.16}$$

where $\mathbf{v}$ is electrons' group velocity. We also have

$$\dot{\mathbf{\Pi}} = \dot{\mathbf{p}}$$

then

$$\dot{\mathbf{\Pi}} = -e\mathbf{v} \times \mathbf{B} \tag{2.17}$$

and (2.18)

$$\dot{\mathbf{r}} = \mathbf{v} = \frac{\partial E}{\partial \mathbf{\Pi}}$$

2. More precisely conductivity has the form $k^2 \approx \ln^2(k)$ as will be seen in chapter 4

the solution for uniform circular motion is

$$\Pi_c = eBr_c, \tag{2.19}$$

which defines a cyclotron radius and a cyclotron frequency of the form

$$r_c = \frac{\Pi}{eB} \quad , \quad \omega_c = \frac{v}{r_c} = \frac{eB}{\Pi}\frac{\partial E}{\partial \Pi}.$$

Cyclotron mass can be also deduced from $\mathbf{\Pi}$ using the relation

$$m_c \equiv \frac{eB}{\omega_c} = \frac{\Pi}{v}$$

We have then that in the case of the bilayer

$$E_{BL} = \frac{\mathbf{\Pi}^2}{2m^*} \qquad v = \frac{\Pi}{m^*} \qquad \omega_c = \frac{eB}{m^*} \qquad r_c = \frac{\sqrt{2m^*}}{eB}\sqrt{E} \qquad and \qquad m_c = m^*.$$

And for the monolayer,

$$E_{ML} = v_F|\mathbf{\Pi}| \qquad v = v_F \qquad \omega_c = \frac{eB}{E/v_F^2} \qquad r_c = \frac{1}{eBv_F}E \qquad and \qquad m_c = \frac{E}{v_F^2}.$$

We see again that Fermi velocity is independent of energy in the case of the monolayer. We also see that cyclotron frequency depends on energy in the case of the monolayer and it is a constant in the case of the bilayer. Cyclotron radius has a different dependence in both systems, linear in energy for the monolayer and a square root dependence for the bilayer. Finally, we see that cyclotron mass depends on energy for the monolayer and it is a constant in the case of the bilayer.

In the presence of a magnetic field, the quantization of energy levels goes as $\sqrt{n}$ for the monolayer contrary to the bilayer that shows a linear dependence on n.

$$\begin{aligned} E_{ML} &= v_F\sqrt{2\hbar eBn} \\ E_{BL} &= \hbar\omega_c n \end{aligned}$$

with $\omega_c = eB/m^*$.

Having reviewed the principal aspects of electronic transport in graphene and its differences and similarities with the bilayer graphene, we can proceed to the description of the experiments done in graphene at the group of Mesoscopic physics at Orsay during my PhD. I start in chapter 4 describing the experiments that led to the determination of the characteristic transport scattering times in graphene and bilayer graphene, elucidating the nature of impurities in our samples [86]. Chapter 5 is reserved to universal conductance fluctuations in graphene (and bilayer graphene) [87] and finally chapter 6 shows experiments in which a superconducting proximity effect was induced in graphene [88].

	k_F		Energy	
	Monolayer	Bilayer	Monolayer	Bilayer
V_g	$4.9*10^7(V_g - V_D)^{1/2}$ $V^{-1/2}m^{-1}$	$4.9*10^7(V_g - V_D)^{1/2}$ $V^{-1/2}m^{-1}$	$\hbar\, V_F*4.9*10^7$ $(V_g-V_D)^{1/2}$	$\hbar^2\, 23.5*10^{14}$ $(V_g-V_D)/2m^*$
k_F	k_F	k_F	$\hbar\, V_F k_F$	$\hbar^2 k^2/2m^*$
E_F	$E_F/\hbar V_F$	$(2m^*E_F/\hbar)$	E_F	E_F

	Electronic density		Fermi velocity		Effective mass		Density of states	
	Monolayer	Bilayer	Monolayer	Bilayer	Monolayer	Bilayer	Monolayer	Bilayer
V_g	$7.5*10^{10}(V_g-V_D)$ $cm^{-2}V^{-1}$	$7.5*10^{10}(V_g-V_D)$ $cm^{-2}V^{-1}$	$1*10^6$m/s	$(\hbar/m^*)4.9*10^7$ $(V_g - V_D)^{1/2}$	0	0.035m_e	$2*4.9*10^7$ $(V_g - V_D)^{1/2}$ $/(V_F\,\hbar\,\pi)$	$2m^*/\pi\hbar^2$
k_F	k_F^2/π	c^2/π	$1*10^6$m/s	$\hbar k/m^*$	0	0.035m_e	$2*k_F/V_F\hbar\pi)$	$2m^*/\pi\,\hbar^2$
E_F	$E^2/(\hbar^2 V_F^2\pi)$	$2Em^*/\hbar^2\pi$	$1*10^6$m/s	$(2E/m^*)$	0	0.035m_e	$2E_F/v_F^2\hbar^2\pi$	$2E_F/v_F^2\hbar^2\pi$

FIGURE 2.7 – Main quantities in graphene as a function of V_g, k_F and E_F. ($\epsilon_r = 3.8$, $\epsilon_0 = 8.85 * 10^{-12}$)

Chapitre 3

Sample fabrication

Our samples were fabricated using the exfoliation method. This technique was used successfully for the first time on graphite by Novoselov *et al.*[81] in 2004 who obtained the first single-layer graphene presenting an electric field effect. The method consist in a micromechanical cleavage of natural graphene flakes on a oxidized Si wafer with a SiO_2 layer that permits the optical visibility of graphene. Indeed, interference between the reflection paths that come from the air-to-SiO_2 and the SiO_2-to-Si interfaces are affected by thickness variations of a fraction of wavelength, leading to colorshifts that can be easily appreciated by eye.

We used natural graphite purchased from the company NGS Naturegraphit (www.graphite.de) and highly doped Si wafers with a 285nm SiO_2 layer. In a first stage alignment marks in Ta were deposited using e-beam lithography and lift-off techniques. The presence of alignement marks in the wafer is imperative to be able to track graphene layers once they are identified. Prior to the deposition of graphene, the wafers are cleaned using oxygen plasma or Ozone. This increases the chances of having a graphene sticked to the surface. The oxygen plasma at $\approx 1mbar$ removes organic layers like greases, oils or waxes. They are attacked chemically by oxygen, that forms molecules of CO or CO_2. The plasma heats the sample slightly, which together with the vacuum can make some impurities evaporate. Also, high energy particles in the plasma may cause the breaking of impurities into smaller molecules that can be extracted easily. The UV radiation generated from the plasma can destroy impurities as well. Ozone (O_3) also reacts with organics. It is created by ultraviolet radiation that converts O_2 into ozone. Ozone removes organics, photoresist, metals and particles.

We used both the O_2 plasma and the ozone method without noticing a better performance of one or the other. The O_2 plasma methode takes $\approx$ 15 min while the ozone method $\approx$ 1 hour.

The steps followed in the exfoliation technique are resumed in figure 3.1. After the exfoliation, we proceed to scan the sample using an optical microscope with a zoom $\times$500. The thickness of SiO_2 ($285nm$) gives a contrast for graphene in the blue tones. The number of layers is confirmed afterwards using a Raman spectrum. Figure 3.2 shows the optical image of two samples, where a monolayer and a bilayer were identified. The difference in the color of the substrate is due to a numerical filter. In both images the monolayer seems more transparent than the bilayer.

Raman scattering depends on the electronic and vibrational properties of a material, its spectrum in graphite has 3 prominent peaks : G, D, and D'. The **G** peak ($\approx 1580cm^{-1}$, $210meV$) arises from in-plane vibration of atoms (E_{g2} phonon mode) in which the atoms of the two sublattices in graphene (atoms A and B) vibrate in opposite directions. The **D** peak is associated to defects and it appears in graphene at $\approx 1350cm^{-1}$ ($\approx 180meV$). If there are a lot of defects in the material, D will have a pronounced intensity. The **D'** peak ($\approx 2700cm^{-1}$, $\approx 365meV$) also known as the **2D** peak is sensitive to energy dispersion, it is then the indicator for single layer, bilayer graphene and multilayer graphene. In graphene the 2D peak is a single and sharp peak, while in graphite it is the superposition of multiple peaks, it is then broader and shifted with respect to the one of the monolayer. Figure 3.3 [82] shows the Raman spectra of a single layer and a bilayer graphene where the peaks G, D' and G' can be distinguished, the absence of the D peak

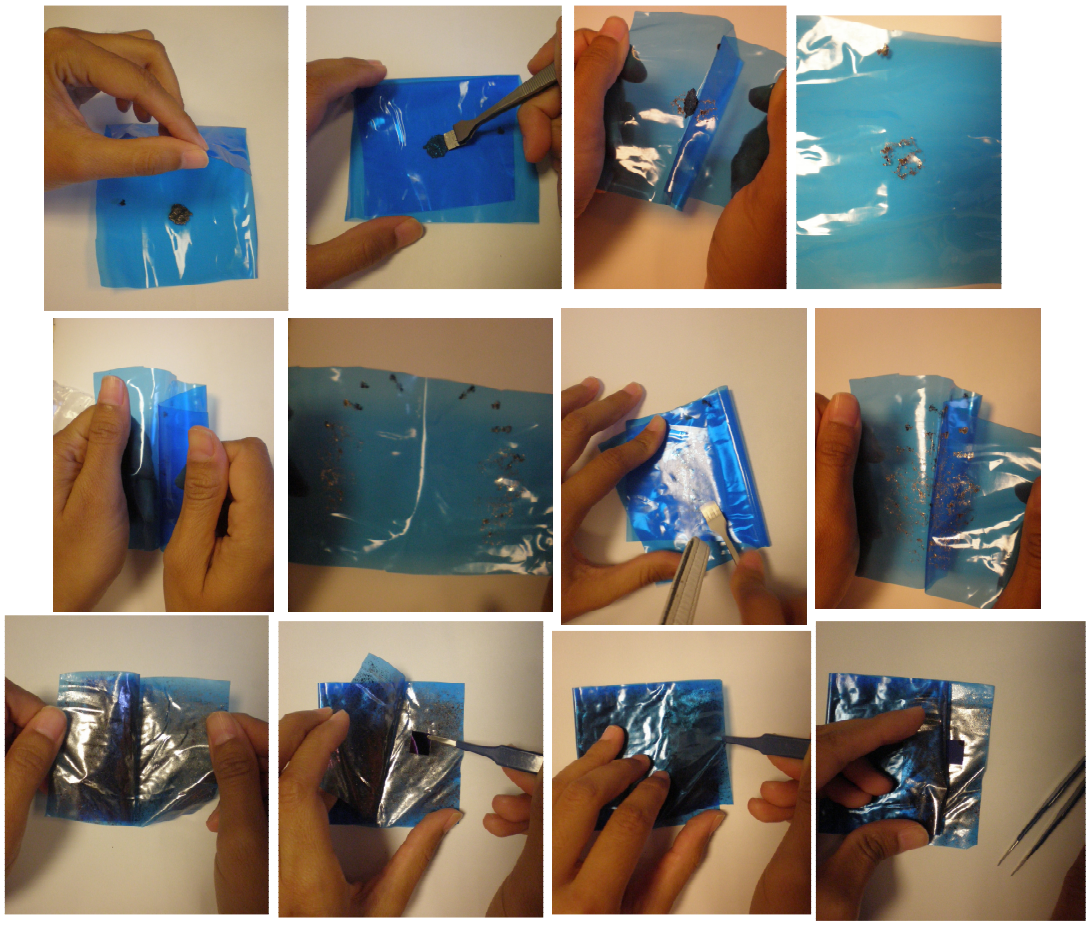

FIGURE 3.1 – Steps to fabricate a graphene sample using the mechanical exfoliation technique

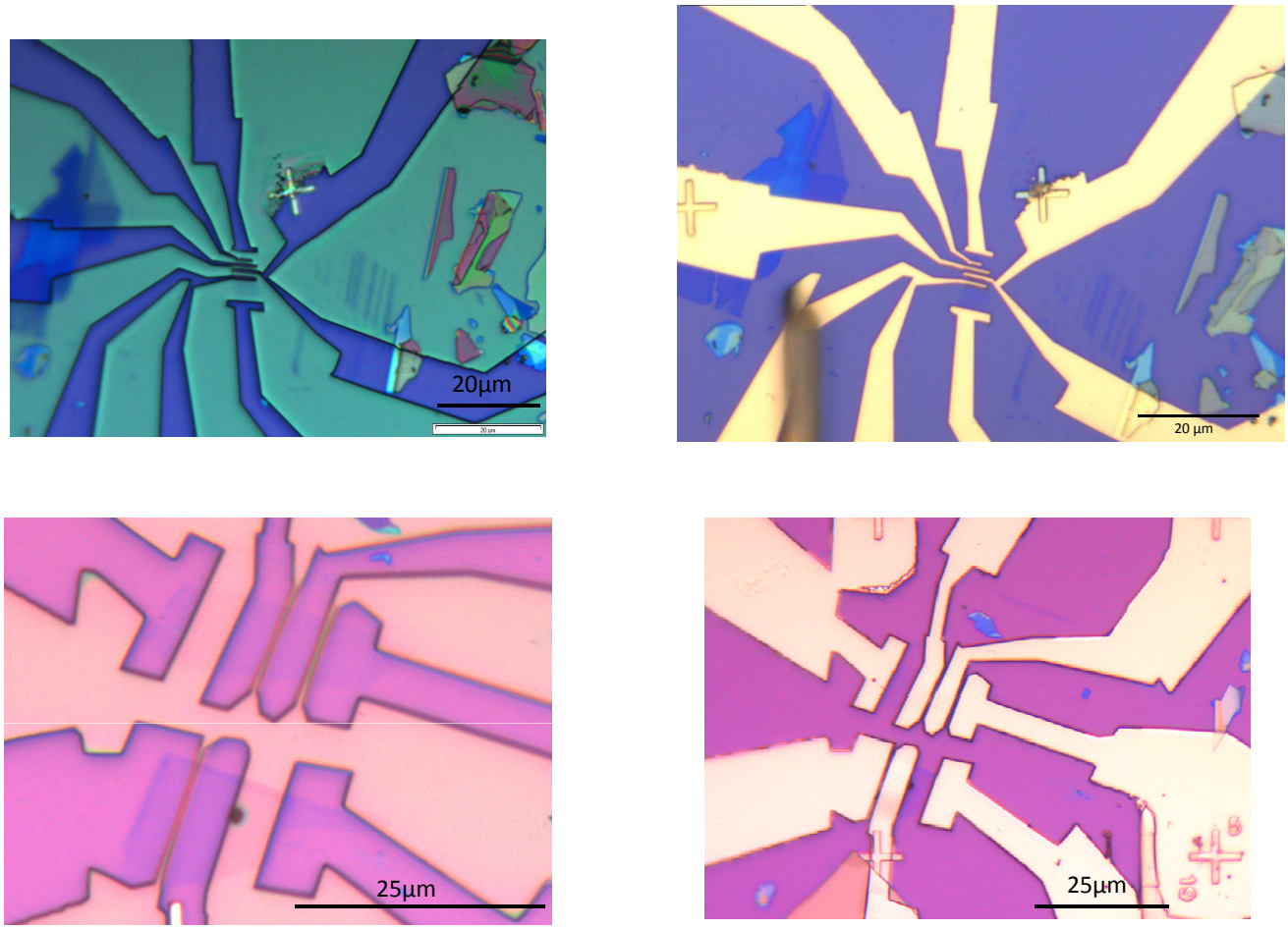

FIGURE 3.2 – Optical image of two samples after the e-beam lithography and after the metal deposition. Top : Ti/Au ($5nm/50nm$) by Joule evaporation. Bottom : Ti/Ta (3nm/100nm) with Tantalum by sputtering.

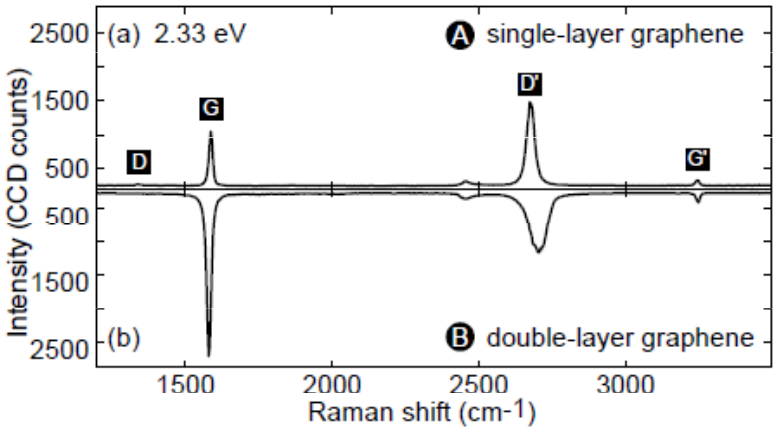

FIGURE 3.3 – Raman spectra for a monolayer (a) and a bilayer (b) showing the positions of peaks D, G,and D'. Taken from [82]

shows the structural quality of the samples. The difference in the 2D peak which discerns the monolayer from the bilayer can be observed. Raman spectroscopy can distinguish a single from a bilayer from few layers (less than 5). More than five layers are almost indistinguishable with respect to bulk graphite. Figure 3.4 shows the 2D peak of the Raman spectrum of two of our samples. The Raman measurements were made at the Université de Paris 7 (Paris Diderot) with the collaboration of Maximilien Cazayous and Yann Gallais, they have also been done at SPEC, CEA Saclay.

The difference between the Raman shift of the monolayer and the bilayer is $\approx 12cm^{-1}$. Once the graphene to be contacted is tracked, we proceed to the e-beam lithography stage in order to deposit afterwards the metallic contacts. We use the polymeric e-beam resist PMMA. Different tests were done to find the appropriate thickness of resist and electron dose in order to have a good lift on graphene samples. The best results were obtained using a single $400nm$ layer of PMMA A6 (which needs a spinning of $4000rpm$) with a baking of $120^{\circ}C$ during 20 min. The doses that worked the best using a working distance of $\approx 8.3mm$ were 260 and 280 $\mu C/cm^2$ for the small details and $300\mu C/cm^2$ for the larger parts.

Before the deposition we anneal the sample with the PMMA mask in vacuum ($P \approx 10^{-6}mtorr$) in order to evaporate impurities from the the exposed regions and minimize the contact resistance. We have done annealings at $150^{\circ}C$ during $45min.$, but mostly at $60^{\circ}C$ up to $3h45min$. Figure 3.2 shows optical images of two samples after the e-beam lithography and after the metal deposition. The methods used for metal deposition are Joule evaporation and sputtering. In the evaporation method, a high current (depending on the metal to be evaporated, $\approx 200A$) crosses a resistive heater to melt the metal and evaporate it. The vapor arrives in a single direction to the sample depositing an uniform layer with a thickness that is controlled with a quartz crystal oscillator. As metal is deposited, the mass of the crystal goes up and the frequency of oscillation goes down, allowing an association of the change in frequency with the deposited metal thickness. The process is done in high vacuum ($\approx 10^{-6}mbar$) in order to avoid scattering of the vapor with gas-phase atoms in the chamber. Using this technique we have deposited Titanium, Gold and Aluminium.

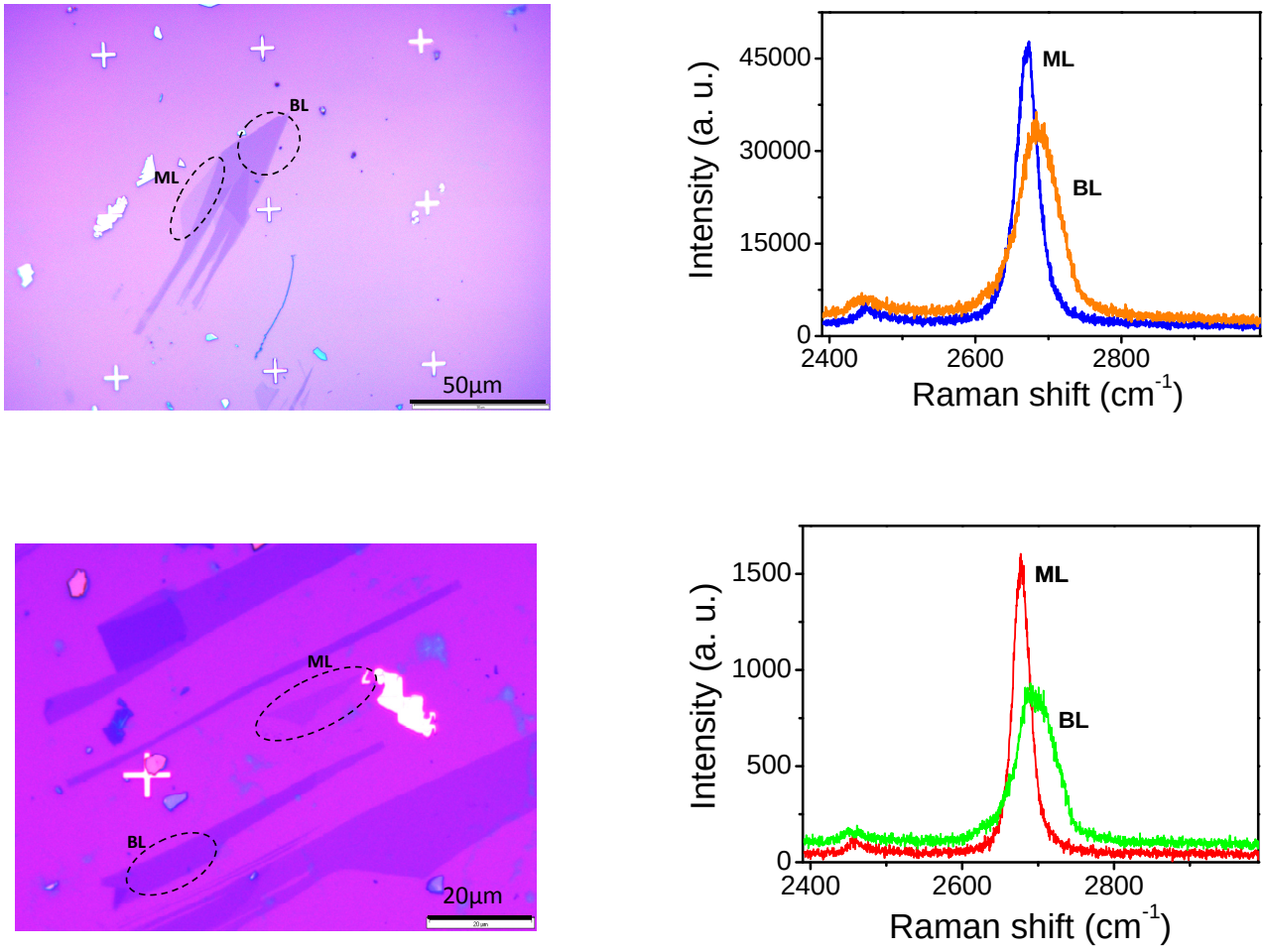

FIGURE 3.4 – Optical image of two of our samples with their respective Raman spectrum. We can distinguish a monolayer which has a narrower 2D peak with respect to the bilayer. They are also shifted of about $12cm^{-1}$.

In the sputtering method, the sample is in a chamber with Argon gas. A voltage difference is imposed between the target metal and the sample which forms a plasma. The argon ions knock the target metal pulling out the metal atoms that are ejected in all directions hitting the sample. In this way a uniform layer is deposited. Materials we have deposited by sputtering are Tantalum, Platinum, Palladium and Niobium. This method contrary to the Joule deposition of atoms is isotropic, which causes the creation of "walls" in the contacts that can cause short circuits. Figure 3.2 shows the lithography and the metal deposition stages for two samples in which we deposited Ti/Au and Ti/Ta. Titanium is evaporated while Tantalum is sputtered. It can be noticed that the Joule deposition technique gives cleaner contacts than the sputtering. Sputtering on the other hand makes a better metal adhesion and improves the contact resistance.

We have tried different materials. Table 3.5 shows a recompilation of the different metals used. We calculated the square resistance for each sample from two probe resistance measurements averaged over different junctions. We have found that the best electrical contact to graphene is achieved with **Pd**, **Ti/Au** and **Ti/Ag**. We have observed that temperature annealing in vacuum between 60˚C and 150˚C before the metal deposition (Ti/Ta, Ti/Au) lowered the two probe resistance.

We have seen that an annealing after metal deposition improves also electrical contact for some materials. The temperature annealing performed in our samples is summarized in table 3.6. Annealing improved two probe resistance in **Pd** and **Ti/Nb** samples. In Pd resistance was divided by 2 and in Ti/Nb (a single junction) resistance decreased by a factor of ~ 50. Annealing was done between $300^{\circ}C$ and $750^{\circ}C$. The effect of annealing on suspended samples is not clear. After annealing some junctions changed from being open to being relatively low resistive. Annealing might have caused the electrodes to fall on the substrate.

Concerning the superconducting materials, the material that let us induce a superconducting proximity effect in graphene was **Pt/Ta**. The disadvantage with this material is that it gets resistive rapidly. Using **Ti/Ta** and **NbN** we observed annomalies in the dI/dV characteristics at high bias. This put in doubt the good quality of the superconductor deposited. Using **Ti/Al** and **Pd/Nb** we were not lucky and we always had a sample with no gate voltage effect or with a leak to the gate. Using **Ti/Nb** the junctions became very resistive in a short time.

We have tried graphene suspension by etching the SiO_2 chemically [1]. We suspended graphene samples with electrodes on Ti/Ta and Ti/Au. The first step is putting a PMMA mask on graphene with windows that permit the entrance of the etching substance (HF) underneath graphene. The sample is immersed then in HF during approximately 70s. The etching rate is approximately $2nm/s$. It is then immersed in water during some seconds to stop etching and at the end in acetone. This permits to dry the sample in a critical point dryer to avoid surface tension. SEM images of suspended samples with Ti/Au and Ti/Ta electrodes are shown in figure 3.7.

dI/dV characteristics of the three-layer suspended graphene sample (corresponding to the sample shown in figure 3.7 left), show quasiperiodical features that were attributed to the optical out of plane phonon mode in graphite (phonon mode ZO' with $E = 15meV$) [2]. This mode corresponds to two neighboring nonequivalent planes vibrating in phase opposition along the c axis. Measurements done on this sample will not be discussed in this document but can be found in figure 4 of [89]. The experiments done on the second sample (figure 3.7 right) were not conclusive.

With the motivation of being able to observe the superconducting proximity effect in the quantum Hall regime, we have fabricated graphene samples with electrodes made of superconducting tungsten, which has a critical magnetic field larger than 5T at 1K. Tungsten electrodes are grown using a Ga focused ion beam (FIB) that decomposes tungsten hexacarbonil, a metallo-organic vapor. Figure 3.8 shows a sample done in collaboration with Miguel Monteverde. It is a few layer graphene in which Pd electrodes were deposited previous to the tungsten electrodes. A cut was done using the FIB separating two areas of the sample, a monolayer and a bilayer. Afterwards, a nice alignment was done and the tungsten was deposited.

1. Suspention of samples was done at SPEC, CEA Saclay with the collaboration of Miguel Monteverde.
2. This ZO' phonon mode is splitted in a supplementary mode with $E = 7.5meV$ in three layer graphene

Material	Name of the sample	No layers	Annealing before deposition	Thickness	Square resistance(kOhms)
Pt/Ta	Graph35-11	ML		3nm/62nm	23.6
	Graph8	BL		3nm/62nm	345.0
	Graph5	BL		2nm/62nm/4nm	5.1
	Graph9_G3511	ML		2nm/62nm/3nm	6.2
				Pt/Ta	**49.5**
Ti/Ta	Graph24	ML		5nm/70nm	42.5
	Graph13-24	ML	60°C 45'	2nm/100nm	10.2
	Graph5-17_5-19	ML, BL	60°C 45'	3nm/100nm	9.8
				Ti/Ta	**12.4**
Ti/Al	Graph8-F3	MML		3nm/100nm	23.6
	Graph4_G3511	ML		4nm/70nm	28.1
				Ti/Al	**25.8**
Ti/Au	Graph 36	ML		5nm/40nm	8.4
	Graph38-20	BL	60°C 3h30'	5nm/50nm	3.0
	Graph 19-12 25-	ML,BL	60°C 1h	5nm/45nm	7.0
				Ti/Au	**5.3**
Pd	M13-M22	ML	150°C 45'	40nm	3.2
	F3	BL	150°C 45'	40nm	4.4
	F15	BL	150°C 45'	40nm	0.48
				Pd	**3.1**
Pd Ag	Graph55-57	BL,ML	60°C 3h45'	70nm	5.4
				Pd Ag	**5.4**
Nb N	Graph 62-60	ML	100°C 30'	40nm	29.2
	Graph 57-29	MML			146.1
				Nb N	**122.7**
Pd/Nb	Graph 5-65	ML,BL	70°C	3.5nm/80nm	12.0
	Graph 64-4	MML		3.5nm/80nm	0.86
				Pd/Nb	**8.28**
Ti/Nb	Graph17-6	BL	60°C 45'	3.4nm/60nm	108.76
				Ti/Nb	**108.76**

FIGURE 3.5 – Recompilation of the different materials deposited to graphene. Materials were tried mostly on monolayers and bilayers. ML means monolayer, BL bilayer and MML multiple layer. Most of the graphene samples were tested with a Raman spectrum, except those where the number of layers is highlighted. The lowest square resistance was measured for Ti/Au, Pd and Pd Ag (highlighted materials)

Material	Sample	No Layers	Thickness	Junction	1_2	2_3	3_4	4_6	6_8	1_3	1_4	5_6	1_5	7_8	8_9	1_2	5_6	4_5	6_7
Ti/Al	Graph4_G3511	ML	4nm/70nm	Before annealing (kOhms)	3.7	3.9	10												
				Annealing 300°C	4.8	5.1	8												
Ti/Au	Graph 36	ML	5nm/40nm	**Junction**	**1_3**														
				Before annealing (kOhms)	3.4														
				Annealing 300°C 1h	3.4														
	Graph36 suspended	ML	5nm/40nm	**Junction**	**1_2**	**1_4**	**5_6**												
				Before annealing (kOhms)	2400	2400	1000												
				Annealing 560°C 1h15'	1000	1000	430												
				Annealing 600°C 1h30'	130	136	106												
				Annealing 700°C 1h30'	19	9	7												
				Annealing 700°C 1h	open	6	7												
Pd	M13	ML	40nm	**Junction**	**1_2**	**1_3**	**1_4**	**1_5**											
				Before annealing (kOhms)	4.1	2.2	10	12											
				Annealing 300°C 1h30'	14.6	11.5	23.3	26											
				10' after annealing	4	2	9.5	4											
				30' after annealing	2	1.3	5.3	6.2											
	F15	BL	40nm	**Junction**	**2_3**														
				Before annealing (kOhms)	3.6														
				Annealing after FIB 700°C 1h	1.3														
Ti/Ta	Graph13-24	ML	2nm/100nm	**Junction**	**1_2**	**2_3**	**3_4**	**4_6**	**6_8**										
				Before annealing (kOhms)	48	1.06	1.48	0.96	0.99										
				Annealing 700°C 1h	37	1.5	1.7	0.99	1										
	Graph5-17_5-19 suspended	ML BL	3nm/100nm	**Junction**	**7_8**	**8_9**	**2_3**	**1_2**	**5_6**	**4_5**									
				Before annealing (kOhms)	open	open	open	open	open	open									
				Annealing 300°C 1h15	28	open	open	open	open	open									
				Annealing 400°C 2h15'	open	open	open	open	open	open									
				Annealing 550°C 1h	1.4	open	200	85	200	300									
				After SEM FEG observation	open	open	?	270	250	380									
				After annealing 550°C 2h	7	5	360	350	200	100									
				Two days later	12	7.6													
				After experiment	13.4	7.9													
Ti/Nb	Graph17-06	BL	3.4nm/60nm	**Junction**	**1_2**	**6_7**													
				Before annealing (kOhms)	240	33													
				Annealing 300°C 50'	260	49													
				Annealing 600°C 55'	4.6	open													
				4 days later	4.7														
				During a gate voltage sweep	50														
				Annealing 750°C 2h	7.5														
				1 month later	open														

FIGURE 3.6 – Recompilation of temperature annealing done in samples after metal deposition.

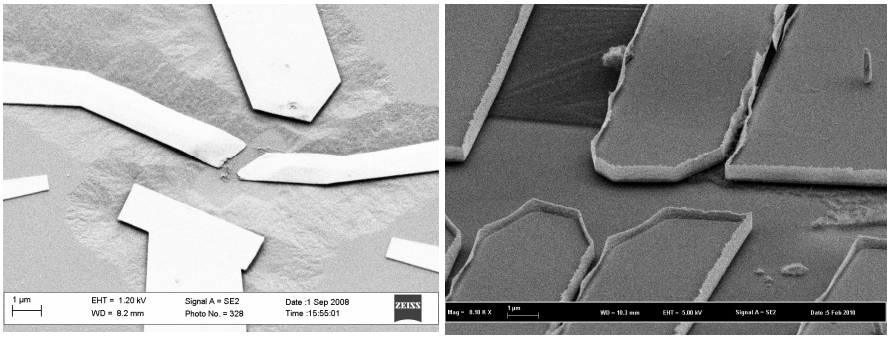

FIGURE 3.7 – Suspended graphene samples with Ti/Au electrodes (left, three layers of graphene) and Ti/Ta electrodes (right). SEM images were made after measurements. In the Ti/Au sample electrodes collpased. We think that the Ti/Ta sample was a truly suspended sample since ripples are distinguishable.

Unfortunately all the junctions were measured in opened circuit. The FIB has been on the other hand, successfully used to do cuts and remove short circuits, as is shown in figure 3.9. In this sample, resistance between electrodes 1 and 2 that were connected to graphene, was measured of 710Ω. This was attributed to graphite crystals shortcutting the electrodes. After a cut made with the FIB, measured resistance was of $4.1k\Omega$ which is reasonable for a graphene junction.

Since FIB seemed to be too aggressive when deposited on graphene, other trials were done in which tungsten was deposited on palladium electrodes previously deposited on graphene. The palladium electrodes should become superconducting through superconducting proximity effect. Figure 3.10 and 3.11 show two samples in which this was done, samples F3 and F15. In sample F3 (figure 3.10), junction 1-6 had a resistance of 350Ω, and after the tungsten deposition it became opened. Junction 2-3 had a resistance of $4.4k\Omega$ but with no gate effect. A temperature bake in vacuum at $700^{\circ}C$ was done which reduced the resistance of the junction 2-3 to $1.3k\Omega$ but with still no gate effect. To verify the resistance of the deposited tungsten, a tungsten electrode was deposited between two Pd electrodes. The measured resistance was of $1.3k\Omega$ which is reasonable. In sample F15, depositing tungsten also made the junctions more resistive. Before the FIB, junction 1-8 was $1k\Omega$. After the FIB, it became of $200k\Omega$. An other try like this was made on sample F42, which was a bilayer with palladium electrodes. After the tungsten deposition on one electrode, the junctions formed by that electrode passed from being around 700Ω to be in opened circuit.

We expect that by changing the deposition conditions, we will be able in the future to deposit this high critical magnetic field tungsten on a monolayer or bilayer graphene.

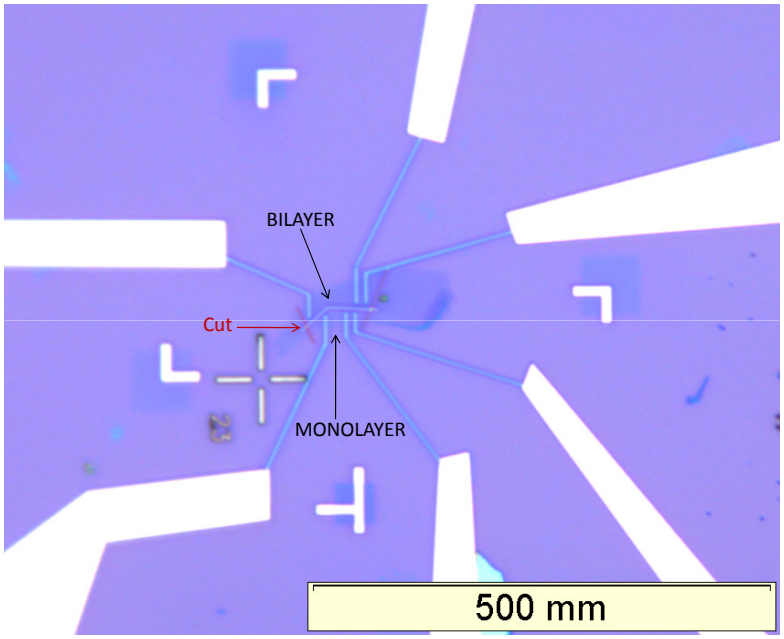

FIGURE 3.8 – Sample F6. A monolayer and bilayer separated by a cut done with the FIB. Tungsten electrodes were deposited using the FIB. Pd electrodes were previously deposited

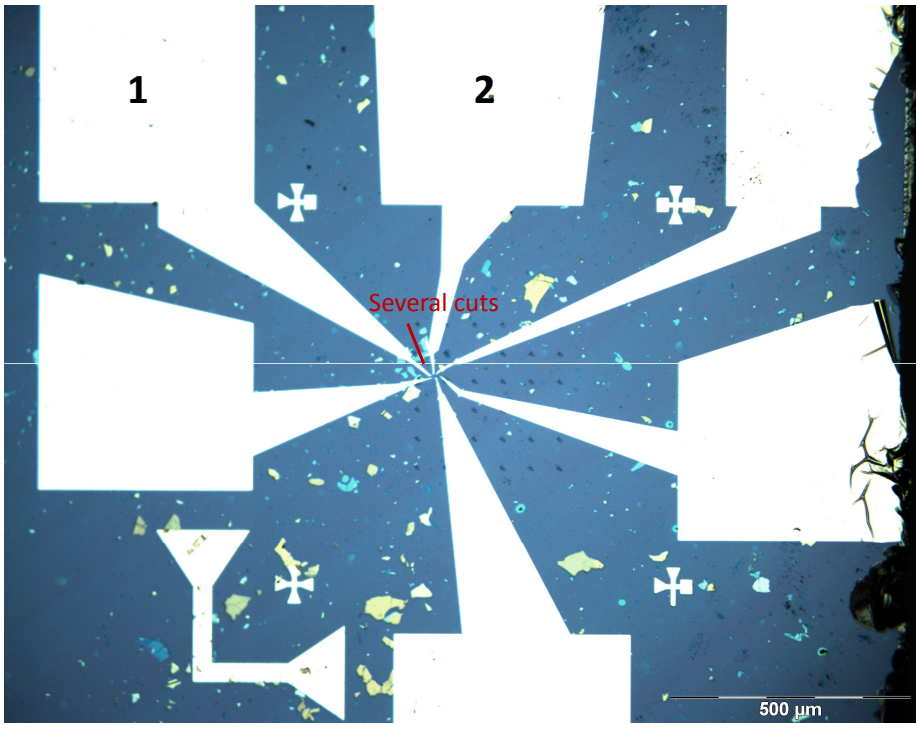

FIGURE 3.9 – Sample M13. Monolayer with palladium electrodes. Several cuts between electrodes 1 and 2 were successfully done with the FIB to eliminate the short circuit.

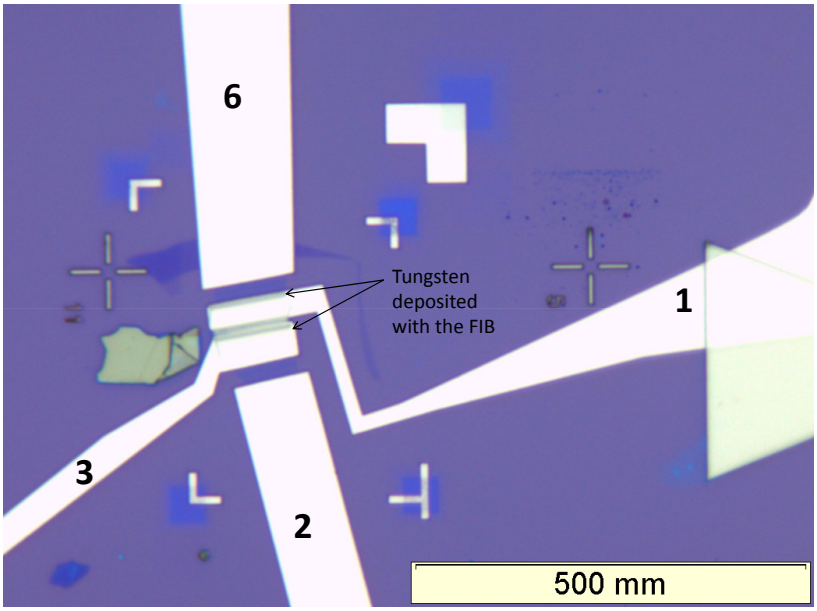

FIGURE 3.10 – Sample F3. Bilayer with palladium electrodes. Tungsten was deposited over palladium. Junction 6-1 is opened after the tungsten depostion.

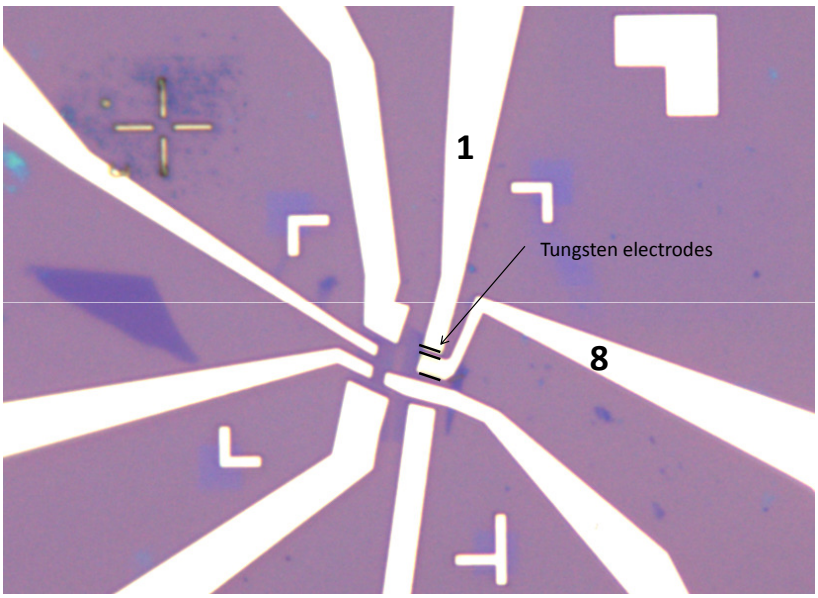

FIGURE 3.11 – Sample F15. Junction 1-8 passed from $1k\Omega$ to $200k\Omega$ after the tungsten deposition.

Chapitre 4

Measurement of characteristic scattering times in graphene and bilayer graphene that reveal the nature of scatters in these systems

4.1 Introduction

The nature of defects that limit the carrier mobility constitute an important issue in graphene. Theoretical works have approached to this question trying to explain the carrier density dependence of conductance, which is strongly related to the nature of impurities in a system. The results at the moment don't show a complete accordance with experimental results, making the subject of the main scattering mechanism in graphene still controversial. In this chapter I expose our approach to the problem which lays on magnetoresistance measurements on the monolayer and bilayer graphene that let us extract the characteristic transport times (the elastic time τ_e and the transport time τ_{tr}). The ratio of these times give information about whether impurities' potential is short or long range.

It is important to distinguish the transport time τ_{tr} that governs current relaxation and enters in Drude conductivity from the elastic scattering time τ_e which is the lifetime of a planewave state. The former is the time that an electron takes to be backscattered, i.e. to reverse its momentum while the latter is the time between two elastic collisions. A schema illustrating both times is shown in figure 4.1 These

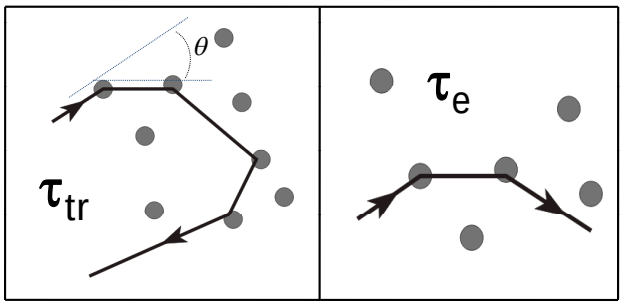

FIGURE 4.1 – Transport time appearing in Drude formula (left). Elastic scattering time which determines the lifetime of a planewave state (right).

times can be defined as follows,

$$\tau_{tr}^{-1} \propto \int_0^{2\pi} P(\theta)(1-\cos\theta)d\theta \qquad \tau_e^{-1} = \int_0^{2\pi} P(\theta)d\theta$$

where θ is the scattering angle and $P(\theta)$ depends on the scattering mechanisms. The factor $(1-\cos\theta)$ in τ_{tr} gives more weight to collisions where the direction of momentum is inverted. A large ratio τ_{tr}/τ_e means that scattering is predominantly in the forward direction. This is the case of the 2D electron gases (2DEG) confined to GaAs/GaAlAs heterostructures, where the dominant scattering mechanism comes from the long range potential associated with donors which are set back from the 2DEG and which produce small angle scattering. In the 2DEG $\tau_{tr}/\tau_e \geq 10$.

A large ratio τ_{tr}/τ_e means that the range of the potential due to scatterers R is bigger than the Fermi wavelength ($\lambda_F < R$). In this case, like in the 2DEG, scatterers are long range. A ratio $\tau_{tr}/\tau_e \approx 1$ on the other hand, gives signature of scatterers for which $\lambda_F > R$.

4.2 Scattering process in graphene

In this section I will discuss what is expected for graphene's conductivity in the presence of short or long range impurities using Edward's model [57]. I will then make a summary of some of the theoretical and experimental works that have addressed this question and that have not for the moment, arrived to an unanimous conclusion.

Edward's model [2] describes a non interacting electron gas with a potential $V(\mathbf{r})$ that comes from N_i identical impurities localized at $\mathbf{r_j}$ and distributed uniformly $n_i = N_i/A = const.$ Impurities are distributed randomly and are characterized by the potential $v(\mathbf{r})$ which is considered as an isotropic central potential.

$$V(\mathbf{r}) = \sum_{j=1}^{N_i} v(\mathbf{r}-\mathbf{r_j})$$

The electron collision time in the presence of such a potential can be estimated [57] using Fermi golden rule to the lowest order of perturbation. We use a representation of plane waves that correspond to the eigenstates of the system's free hamiltonian $|\mathbf{k}>$. The electron collision time τ_k is interpreted as the lifetime of states $|\mathbf{k}>$.

$$\frac{1}{\tau_k} = \frac{2\pi}{\hbar}\sum_{\mathbf{k'}} \left|\langle \mathbf{k'}|V|\mathbf{k}\rangle\right|^2 \delta(\epsilon_{\mathbf{k'}} - \epsilon_{\mathbf{k}}) \tag{4.1}$$

where

$$\begin{aligned}\langle \mathbf{k'}\,|V|\,\mathbf{k}\rangle &= \frac{1}{A}\int d^2r V(\mathbf{r}) e^{i(\mathbf{k}-\mathbf{k'})\cdot\mathbf{r}} = \tilde{V}(\mathbf{k}-\mathbf{k'}) \\ &= \frac{1}{A}\sum_{j=1}^{N} \tilde{v}(\mathbf{k}-\mathbf{k'}) e^{i(\mathbf{k}-\mathbf{k'})\cdot\mathbf{r_j}}\end{aligned}$$

and $\tilde{v}(\mathbf{k})$ is the Fourier transform of $v(\mathbf{r}-\mathbf{r_j})$, the potential associated to each impurity j [1]. We have,

$$\begin{aligned}\left|\langle \mathbf{k'}\,|V|\,\mathbf{k}\rangle\right|^2 &= \sum_{j,j'} e^{i(\mathbf{k}-\mathbf{k'})\cdot(\mathbf{r_j}-\mathbf{r'_j})} \left|\tilde{v}(\mathbf{k}-\mathbf{k'})\right|^2 \\ &= \sum_{j=j'}\ldots + \sum_{j\neq j'}\ldots \\ &= \frac{N_i}{A}\left|\tilde{v}(\mathbf{k}-\mathbf{k'})\right|^2 + \sum_{j\neq j'} e^{i(\mathbf{k}-\mathbf{k'})(\mathbf{r}_j-\mathbf{r'}_j)}\left|\tilde{v}(\mathbf{k}-\mathbf{k'})\right|^2.\end{aligned} \tag{4.2}$$

1. $\tilde{v}(\mathbf{k}-\mathbf{k'})$ has the dimensions of *potential* $\times$ *area*, where the area is associated to the range of potential.

The second term disappears after averaging over the random position of impurities, and replacing in 4.1,

$$\frac{1}{\tau_{\mathbf{k}}} = \frac{2\pi}{\hbar}\frac{N_i}{A}\sum_{\mathbf{k}'}\left|\tilde{v}(\mathbf{k}-\mathbf{k}')\right|^2\delta(\epsilon_{\mathbf{k}}-\epsilon_{\mathbf{k}'}) \tag{4.3}$$

4.2.1 Local short range impurities

If we consider a local short range impurity therefore $\tilde{v} = const$ for $|\mathbf{k}-\mathbf{k}'| \leq 2k_F$, we have (if $\tilde{v} << E_F$),

$$\begin{aligned}\frac{1}{\tau_{\mathbf{k}}} &= \frac{2\pi}{\hbar}\frac{N_i}{A}\tilde{v}^2\sum_{\mathbf{k}'}\delta(\epsilon_{\mathbf{k}}-\epsilon_{\mathbf{k}'}) \\ &= \frac{2\pi}{\hbar}n_i\tilde{v}^2\rho(\epsilon_{\mathbf{k}})\end{aligned} \tag{4.4}$$

where we have replaced the density of states $\rho(\epsilon_{\mathbf{k}})$

$$\rho(\epsilon_k) = \frac{1}{A}\sum_{k'}\delta(\epsilon_k-\epsilon_{k'}) \tag{4.5}$$

At Fermi energy, scattering time is

$$\frac{1}{\tau} = \frac{2\pi}{\hbar}n_i\tilde{v}^2\rho(\epsilon_F) \tag{4.6}$$

We can calculate, using 4.6 the ratio between the transport time τ_{tr} and the elastic time τ_e. As said at the beginning of this chapter, the elastic time is the time between two elastic collisions while the transport time is the time in which the memory of the incident direction is lost. They are written for short range scattering as follows :

$$\begin{aligned}\frac{1}{\tau_e} &= \frac{2\pi}{\hbar}n_i\tilde{v}^2\rho(\epsilon_F)\int_{-\pi}^{\pi}d\theta\left(\frac{1+\cos j\theta}{2}\right) \\ \frac{1}{\tau_{tr}} &= \frac{2\pi}{\hbar}n_i\tilde{v}^2\rho(\epsilon_F)\int_{-\pi}^{\pi}d\theta(1-\cos\theta)\left(\frac{1+\cos j\theta}{2}\right)\end{aligned} \tag{4.7}$$

where θ is the angle between the incident and the scattered trajectory, as illustrated in figure 4.1. The transport time has an angular factor $(1-\cos\theta)$ that counts only trajectories with changing direction after collision. For graphene there is an additional factor. It is $(1+\cos j\theta)/2$ with $j=1$ for the monolayer and $j=2$ for the bilayer. This factor counts for the absence of backscattering in the monolayer. We find :

$$\frac{\tau_{tr}}{\tau_e} = \frac{\int_{-\pi}^{\pi}d\theta\left(\frac{1+\cos j\theta}{2}\right)}{\int_{-\pi}^{\pi}d\theta(1-\cos\theta)\left(\frac{1+\cos j\theta}{2}\right)}$$

That for the monolayer is

$$\frac{\tau_{tr}}{\tau_e}_{ML} = \frac{\int_{-\pi}^{\pi}d\theta\left(\frac{1+\cos\theta}{2}\right)}{\int_{-\pi}^{\pi}d\theta\left(\frac{\sin^2\theta}{2}\right)} = 2, \tag{4.8}$$

and for the bilayer

$$\frac{\tau_{tr}}{\tau_e}_{BL} = \frac{\int_{-\pi}^{\pi}d\theta\left(\frac{1+\cos 2\theta}{2}\right)}{\int_{-\pi}^{\pi}d\theta\left(\frac{(1+\cos 2\theta)(1-\cos\theta)}{2}\right)} = 1. \tag{4.9}$$

Using Drude's relation for conductivity we have

$$\sigma = e^2\frac{v_F^2}{2}\tau\rho(E_F) = \frac{e^2}{2h}\frac{(\hbar v_F)^2}{n_i\tilde{v}^2} \tag{4.10}$$

which is a constant independent of the gate voltage V_g and it is not what is observed experimentally.

4.2.2 Charged impurities

If we consider that the potential due to an impurity is

$$v(\mathbf{r}) = \frac{Ze^2}{\epsilon r}$$

(with ϵ the dielectric constant of the medium). In the Thomas-Fermi approximation we have

$$\tilde{v}_{TF}(q) = \frac{2\pi e^2}{\epsilon(q + q_{TF})} \tag{4.11}$$

where $\mathbf{q} = |\mathbf{k} - \mathbf{k}'|$ and $1/q_{TF}$ is the characteristic screening length

$$q_{TF} \equiv \frac{2\pi e^2}{\epsilon}\rho(\epsilon_F),$$

that in graphene is

$$q_{TF} = 4\frac{e^2}{\epsilon\hbar v_F}k_F.$$

and in the bilayer

$$q_{TF} = \frac{4me^2}{\hbar^2\epsilon}$$

Replacing 4.11 in 4.3 we have,

$$\frac{1}{\tau_{\mathbf{k}}} = \frac{2\pi}{\hbar}\frac{N_i}{A}\sum_{\mathbf{k}'}\frac{(2\pi e^2)^2\delta(\epsilon_{\mathbf{k}} - \epsilon_{\mathbf{k}'})}{\epsilon^2(|\mathbf{k} - \mathbf{k}'| + q_{TF})^2}$$

Summing over $\mathbf{k}'$ is summing over all the possible states of the scattered electron. This implies integrating over the cone shown in figure 4.2,

$$\frac{1}{\tau_{\mathbf{k}}} = \frac{2\pi}{\hbar}\frac{N_i}{A}\frac{A}{(2\pi)^2}\int\frac{(2\pi e^2)^2\delta(\epsilon_k - \epsilon_{k'})}{\epsilon^2(|\mathbf{k} - \mathbf{k}'| + q_{TF})^2}d^2k' \tag{4.12}$$

in graphene we have $E = \hbar vk$ therefore $\delta(\hbar v_F(k - k')) = \frac{1}{\hbar v_F}\delta(k - k')$

$$\begin{aligned}
\frac{1}{\tau_{\mathbf{k}}} &= \frac{2\pi}{\hbar}\frac{N_i}{A}\frac{A}{(2\pi)^2}\frac{(2\pi e^2)^2}{\epsilon^2}\frac{1}{\hbar v_F}\int\frac{\delta(k - k')}{(|\mathbf{k} - \mathbf{k}'| + q_{TF})^2}d^2k' \\
&= \frac{2\pi N_i e^4}{\hbar^2\epsilon^2 v_F}\int\frac{\delta(k - k')}{(|\mathbf{k} - \mathbf{k}'| + q_{TF})^2}k'dk'd\theta \\
&= \frac{2\pi N_i e^4}{\hbar^2\epsilon^2 v_F}\int\frac{k_F}{(2k_F\sin(\theta/2) + q_{TF})^2}d\theta \\
&= \frac{1}{\epsilon^2 k_F^2}\frac{\pi N_i e^4}{2\hbar^2 v_F}\int\frac{1}{(\sin(\theta/2) + q_{TF}/2k_F)^2}d\theta
\end{aligned} \tag{4.13}$$

since $k = k' = k_F$.

Coming back to Drude's expression for conductivity,

$$\sigma = e^2\frac{v_F^2}{2}\tau\rho(E_F)$$

we deduce that conductivity (and therefore mobility) in the presence of charged, long range impurities, depends on ϵ^2, the medium's dielectric constant, on the range of the potential which is present in q_{TF}, the

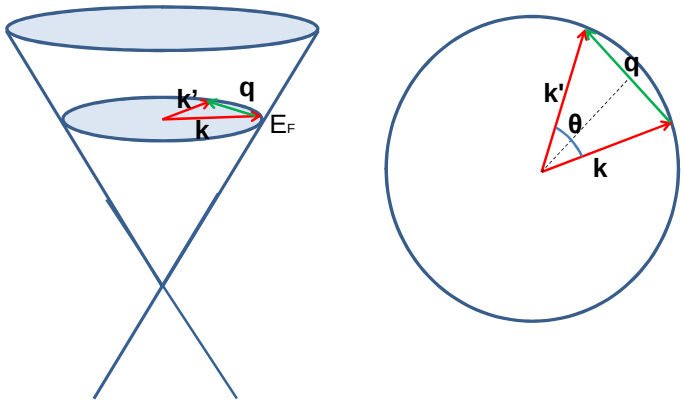

FIGURE 4.2 – Scheme representing the integral 4.12 on the Fermi surface. $\mathbf{k}$ and $\mathbf{k}'$ are the wave vectors of the electron before and after being scattered. They are both on the Fermi surface ($k = k' = k_F$). θ is the angle between $\mathbf{k}$ and $\mathbf{k}'$, and $\mathbf{q} = \mathbf{k} - \mathbf{k}'$

inverse of the screening range and on k_F^2 the electronic density, which is in accordance with experimental results.

Calculating τ_{tr}/τ_e is more complicated in this case, since the potential depends on θ,

$$\frac{\tau_{tr}}{\tau_e} = \frac{\int d\theta \frac{(2\pi e^2)^2 k_F}{(2k_F \sin(\theta/2)+q_{TF})^2}\left(\frac{1+\cos j\theta}{2}\right)}{\int \frac{(2\pi e^2)^2 k_F d\theta}{(2k_F \sin(\theta/2)+q_{TF})^2}(1-\cos\theta)\left(\frac{1+\cos j\theta}{2}\right)}.$$

In the case of short range impurities the potential is isotropic, it is expected then that $\tau_{tr} \sim \tau_e$ as was found in the previews section. In this case of charged screened impurities, the potential depends on θ, which makes $\tau_{tr} \neq \tau_e$. We expect in particular $\tau_{tr}/\tau_e \sim (k_F/q_{TF})$ where $q_T F << k_F$.

Long range impurities have been considered theoretically in several works ([60], [62]-[64]) without having a satisfactory accordance with experiments. Even when charged impurities seem to describe better experimental results with respect to short range impurities, recent experiments in which the change of σ is measured upon immersion of graphene samples in different dielectric media, show different results [65] ,[66]. In the following, a short recompilation of some works in this direction is made.

Namura and MacDonald [60] have studied numerically both short range and Coulomb distributed scatterers. They have evaluated numerically a finite size Kubo formula, considering the eigenstates a the Dirac equation. They have considered a constant potential in k-space in the case of short range impurities and a potential like the one in 4.11 for screened long range impurities. The results using both kind of potentials are shown in figure 4.3. For short range scatters, the electronic density dependence of the conductivity is non linear and approaches to a constant for $|E_F| >> \hbar/\tau$. Its minimum value $\sigma(E = 0)$ is close to the value predicted by self-consistent Born approximation calculations $(1/\pi)e^2/h$ [61]. In the case of screened Coulomb scatters, they have found that the conductivity σ increases linearly with electronic density $|n|$. The minimum value of conductivity $\approx e^2/h$ is a few times larger than the one in the short range model.

Das Sarma *et al.* [62]-[64] claim that most of the observed transport properties in graphene such as the minimum value of the conductivity or its linear dependence with electronic density at high densities can be explained quantitatively by scattering from charged impurities. The difference with Namura *et al.* calculations is that Das Sarma *et al.* treat electron interactions in a RPA scheme [2]. Developing an analytic

2. Using RPA and Thomas Fermi approximation in the limit of strong interactions $r_s >> 1$ is questionable, since in this regime the screening length is smaller than the Fermi wavelength ($R_{screening} < \lambda_F$)

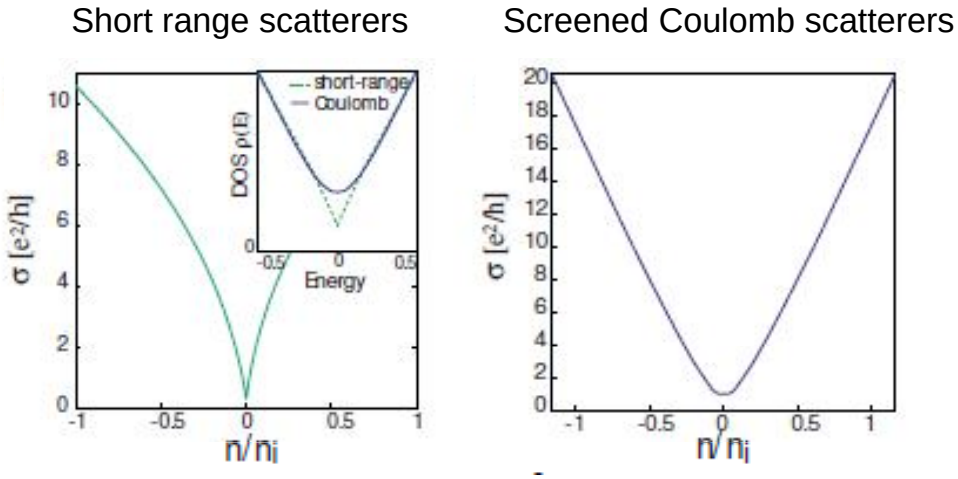

FIGURE 4.3 – Electronic density dependence of Dirac-fermion conductivities for short range scatters (left) and screened Coulomb scatters (right) as calculated numerically by Nomura and Mac Donald [60]. In the case of short range scatterers conductivity approaches to a constant for $|E_F >> \hbar/\tau|$. The inset shows the density of states in both cases.

solution for the Boltzmann transport theory using a RPA treatment of the charged impurity scattering they have found [64],

$$\sigma = \frac{e^2}{h}\frac{n}{n_{imp}}\frac{2}{G(2r_s)} \tag{4.14}$$

with

$$r_s = e^2/(\hbar v_F \epsilon)$$

and

$$\frac{G(x)}{x^2} = \frac{\pi}{4} + 3x - \frac{3\pi x^2}{2} + \frac{x(3x^2-2)\arccos(1/x)}{\sqrt{x^2-1}}.$$

r_s is the fine structure constant in graphene, which is the ratio between the graphene Coulomb potential energy and the kinetic energy. This constant quantifies the intensity of electron-electron interactions. For graphene on a SiO_2 substrate, $r_s = e^2/(\hbar v_F \epsilon) \approx 0.8$, which means a strong e-e interaction. $G(2r_s) \approx 1/10$ and

$$\sigma \approx 20\Big(\frac{e^2}{h}\Big)\Big(\frac{n}{n_{imp}}\Big),$$

which increases linearly with n, as observed experimentally. We note here that for graphene on SiO_2, conductivity depends only on the charged impurity scattering concentration n_{imp}. As a consequence, the only way to improve the mobility on a sample with fixed r_s is improving the quality of the sample. However, we can see in the more general expression 4.14 that the conductivity depends on the substrate dielectric constant ϵ. Changing the SiO_2 substrate for an other with a higher dielectric constant should increase the mobility of the sample.

They have also found that the minimum conductivity σ_0 has the form

$$\sigma_0 \approx 20\Big(\frac{e^2}{h}\Big)\Big(\frac{n^*}{n_{imp}}\Big)$$

where n^* is the residual carrier density that manifest itself experimentally by a residual conductivity plateau. It is deduced self-consistently using Boltzmann theory and the RPA method. The ratio n^*/n_{imp}

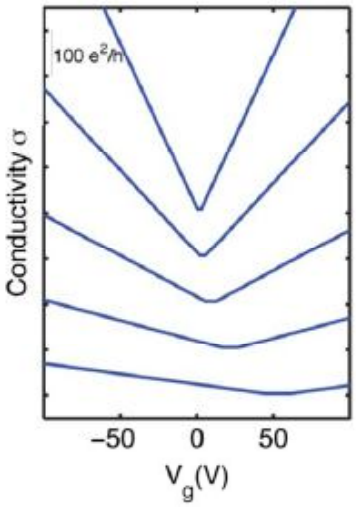

FIGURE 4.4 – Predicted conductivity for different values n_{imp}. In units of $10^{10}cm^{-2}$ they are from top to bottom : 20 (very clean), 40, 80, 160, 320 (very dirty). Curves are offset vertically by $100e^2/h$ for clarity. Taken from [64].

is a monotonically decreasing function of n_{imp} with a dependence that gets weaker for larger impurity density. For dirty samples with $n_{imp} \approx 3.5 \times 10^{12}cm^{-2}$, σ_0 is close to the value usually observed experimentally $4e^2/h$ and is not very sensitive to changes in disorder, whereas for cleaner samples with $n_{imp} \approx 2 \times 10^{11}cm^{-2}$, $\sigma_0 \approx 8e^2/h$ and it is sensitive to the value of n_{imp}. Predicted values for σ_0 for different impurity densities are in accordance with representative experimental results from Columbia, Manchester and Maryland [64]. From these results Das Sarma *et. al.* concluded that the graphene minimum conductivity is not universal and that future cleaner samples will have higher values of σ_0. The plateau at minimum conductivity comes from the effect of charged impurities near the Dirac point which provide a inhomogeneous electron-hole puddle landscape where the conductivity is approximately a constant over a finite range of gate voltage. Charged impurities explain also in Das Sarma's work the linear dependence of conductance on electronic density at high densities. Figure 4.4 shows the predicted conductivity as a function of gate voltage for different impurity concentrations. It is seen that for dirtier samples the linear dependence gets weaker and at the Dirac point a conductivity plateau appears. The gate voltage corresponding to the Dirac point also gets shifted.

Experiments have been done to test if the dominant source of scattering in graphene is charged impurities. In these experiments, transport is studied in different dielectric environments. If transport in graphene is limited by charged impurities, changing the interaction constant α by changing the dielectric constant of the substrate ϵ_{subs} or the environment $\epsilon_{air/vac}$ should have a clear effect on mobility.

$$\alpha = \frac{2e^2}{(\epsilon_{subs} + \epsilon_{air/vac})\hbar v_F}$$

C. Jang *et. al.* [65] have made experiments in which a water layer is added on graphene in ultrahigh vacuum. Usually graphene transport experiments are done on SiO_2 substrate with $\epsilon_{subs} \approx 3.9$ and $\epsilon_{air/vac} \approx 1$, which makes graphene a weakly interacting electron system with $\alpha \approx 0.8$. Adding ice changes $\epsilon_{air/vac}$ to ≈ 3.2, which decreases α from ≈ 0.81 to ≈ 0.56.

Experimentally, it was observed that when adding ice, the maximum slope of $\sigma(V_g)$ became steeper and that the curve $\sigma(V_g)$ became more nonlinear. As the number of ice layers increased, the mobility increased and saturated after approximately three layers of ice to $\approx 12000cm^2/Vs$. These results were analyzed within Boltzmann transport theory including screening using the RPA method like in Das

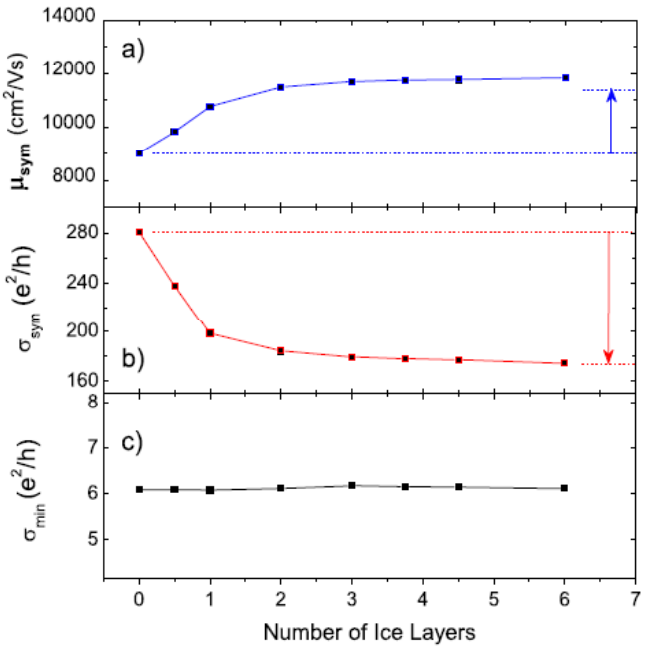

FIGURE 4.5 – Mobility (a), conductivity (b) and the minimum of conductivity (c) of the symmetric conductivity characteristics of graphene as a function of the number of ice layers. Dashed lines indicate the values for pristine graphene and arrows show the theoretical expectations for ice-covered graphene. Taken from [65].

Sarma's work, where conductivity depends strongly on the coupling constant α (see relation 4.14 where $\alpha = r_s$). They found a very good quantitative agreement with theoretical values for the conductivity, the minimum value for conductivity and the mobility. Figure 4.5 show these quantities as a function of the number of ice layers and the theoretical expectations for ice covered graphene. The enhanced mobility of graphene after adding ice was attributed to the decreased interaction between charge carriers and impurities and the decreased screening by charge carriers.

On the other hand, experiments carried by Ponomarenko *et al.* [66] found no significant changes in carrier mobility when studying graphene placed on different substrates and in high ϵ media. They tried different substrates motivated by the fact that the removal of the substrate leads to much higher mobilities, which suggests that impurities may come from the silicon oxide. Figure 4.6 *a* shows the electric field effect for graphene on mica, SiO_2 and PMMA. Samples have mobilities of ≈ 0.25, 0.45 and 0.8 m^2/Vs respectively at $n \approx 2\times10^{12} cm^{-2}$, values that are within the sample-to-sample variations typically observed for graphene on SiO_2. They conclude that limited mobility is not directly related to the substrate but does not discard charged impurities. Since the sample fabrication procedure was the same for all samples, one can imagine that the concentration of charged impurities trapped underneath graphene is always the same. To address this possibility, Ponomarenko *et al.* studied the effect of dielectric screening on mobility. They argued that if transport in graphene is limited mostly by charged impurities, the strength of scattering should strongly depend on dielectric environment and mobility should increase by at least one order of magnitude (reaching above $100000 cm^2/Vs$) when covering graphene with glycerol, ethanol or water. Figure 4.6 *b* shows the field effect on graphene first measured in He atmosphere ($\epsilon \approx 1$) and then covered with a small droplet of glycerol ($\epsilon \approx 42$). It can be seen that glycerol significantly increased the device characteristics making the peak in resistance narrower, more symmetric and shifting it towards zero, which is consistent with the dielectric screening of charged impurities. Nevertheless, mobility increased by only a

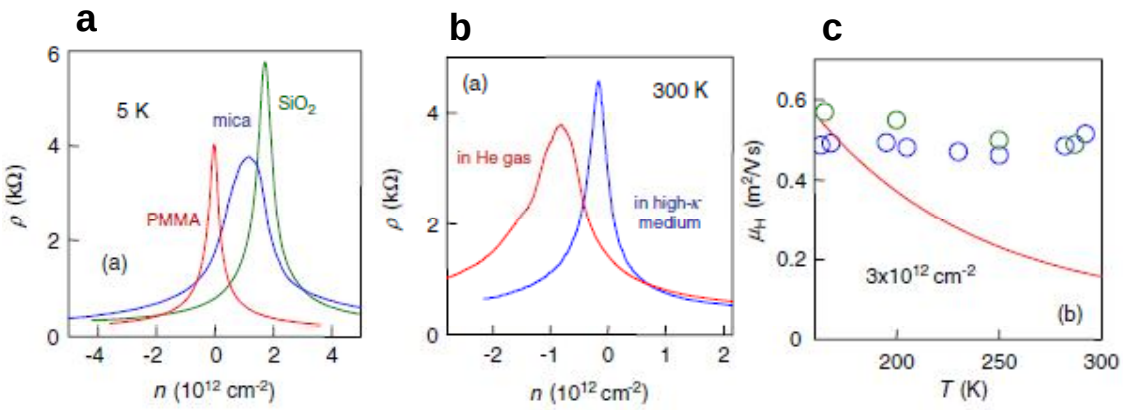

FIGURE 4.6 – Electric field effect for graphene on top of SiO_2, mica and PMMA (a), graphene on top of SiO_2 but in a helium atmosphere and after covering it with a thin layer of glycerol at room T (b). Mobility as a function of temperature for two devices immersed in ethanol (dielectric constant of ethanol increases from ≈ 25 to ≈ 55 with decreasing temperature). The solid curve is the theoretical temperature dependence in the presence of Coulomb scatterers. Taken from [66]

factor of 1.6 and in higher quality devices, the increase in mobility did not exceed 30%. When depositing ethanol ($\epsilon \approx 25$) mobility of graphene increased between a few and 50% depending on graphene's initial quality (for high quality samples increases were smaller). This small increase of graphene's mobility compared to the expected factor of 10, discredits the role of charged impurities as the limiting scatterers.

Ethanol offers the possibility of changing ϵ in-situ by varying temperature. Figure 4.6*c* shows the mobility found by Ponomarenko *et al.* for two samples immersed in ethanol as a function of temperature. As temperature decreases, ϵ increases reaching ≈ 55 near the freezing point. The increase of ϵ didn't lead to a significant change in mobility, which disagrees with the theoretical prediction if a Coulomb scattering mechanism is present (see relation 4.14).

According to these results, charged impurities don't constitute the primary source of scattering in graphene, even if Coulomb scatterers certainly influence μ, they don't limit it in typical devices with $\mu \approx 10\,000\, cm^2/Vs$.

In C. Jang *et al.* experiment, a few atomic layers of ice were assumed to change the dielectric constant of the substrate. According to Ponomarenko *et al.* depositing a few atomic layers is not enough, a few nanometers of dielectric are necessary on top graphene in order to have a consistent comparison with Das Sarma's work.

4.3 Transport and elastic scattering times as probes of the nature of impurity scattering in graphene

In order to gain insight into the scattering mechanism in graphene, we have extracted the characteristic transport times τ_e and τ_{tr} from magnetoresistance measurements. The extraction of these times from the data has been done by Miguel Monteverde. Their ratio gives information about the nature of scatterers that limit transport. We have found that both times and their dependences on carrier density are very different in the monolayer and bilayer graphene but their ratio is almost the same and independent of carrier density. We have found, based on comparison with theoretical calculations that the main scattering mechanism in our samples is due to strong short range resonant scatterers.

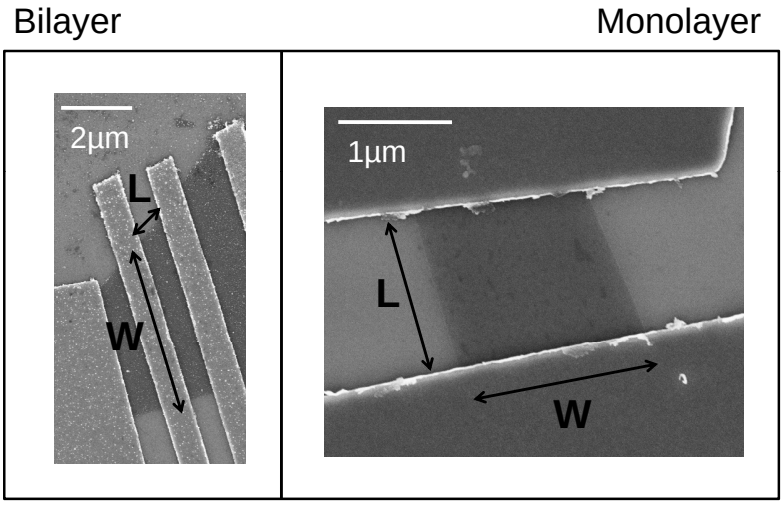

FIGURE 4.7 – SEM photos of the monolayer (right) and the bilayer (left). (Samples A and B).

Samples were fabricated by exfoliation of natural graphite and deposited on a doped silicon substrate with a $285nm$ thick silicon oxide. Carrier density was tuned from electrons to holes through the charge neutrality point with a voltage applied on the backgate. Figure 4.7 shows a SEM pictures of the monolayer and bilayer graphene studied (samples A and B). Electrodes of samples A and B were fabricated by electron beam lithography and sputter deposition of $40nm$ thick palladium . Additional samples (samples C, D and E) were fabricated using Joule evaporation of a bilayer 5nm Ti/70nm Au [3]. I will mostly discuss samples A and B, a monolayer and bilayer graphene of respective dimensions $W = 1.6\mu m$, $L = 1.3\mu m$ and $W = 4.8\mu m$, $L = 0.7\mu m$, where L is the distance between the electrodes covering nearly the entire sample width W. The contact resistances were measured to be 20Ω for the bilayer from a four-probe measurement and calculated of 200Ω from magnetoresistance measurements for the monolayer. The calculation was made from two probe magnetoresistance measurements made on the monolayer, $R + R_C = R_0 + \alpha B^2$ where R_C is the contact resistance and doesn't depend on the magnetic field.

Figure 4.8 shows the conductance dependence on gate voltage for different magnetic fields. At zero magnetic field there is a sublinear dependence of conductance on gate voltage on both sides of the neutrality point. The mobility varies between 3000 and 5000 cm^2/Vs for the monolayer and 3000 and 6000 cm^2/Vs for the bilayer. These values were deduced from Drude formula together with two-probe magnetoresistance measurements at low temperatures. As will be seen in the following, magnetoresistance measurements give a more accurate method to determine transport parameters compared to using exclusively the capacitance model. Above $2T$, steps in the conductance of the monolayer occur near quantized values $4\big(n+1/2\big)e^2/h$ as expected for quantum Hall effect in graphene. The oscillations in the bilayer with a maximum of conductance are due to the aspect ratio of the sample L/W. It is known [67] that for any square sample ($L = W$) with ideal contacts on opposite sides and longitudinal and Hall conductivities σ_{xx} and σ_{xy}, the macroscopic conductance depends on the microscopic transport coefficients in the following way,

$$G_{L=W} = \sqrt{\sigma_{xx}^2 + \sigma_{xy}^2}. \tag{4.15}$$

When the sample is not a perfect square, the conductance problem can be reduced for any geometry, to the one of a rectangle using a conformal mapping approach [67]. Two terminal conductance is determined in that case by a single parameter, the aspect ratio L/W of the sample (L the distance between the

3. Samples D and E were fabricated and measured by Keyan Bennaceur at SPEC, CEA Saclay. The data from these samples is an additional proof of the validity of our work.

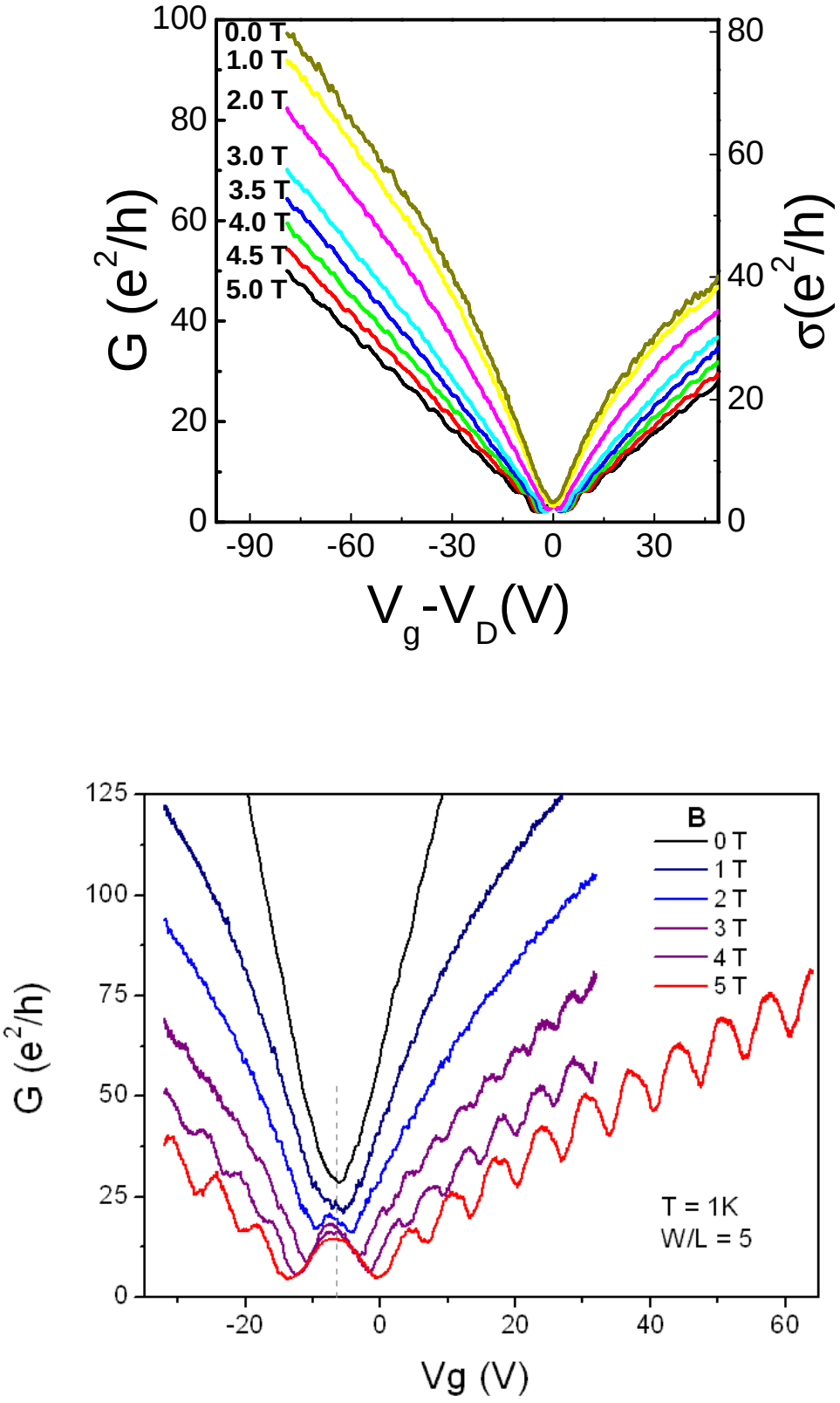

FIGURE 4.8 – Gate voltage dependence of the two terminal conductance at different magnetic fields for the monolayer (top) and the bilayer (bottom). Contact resistance have been subtracted.

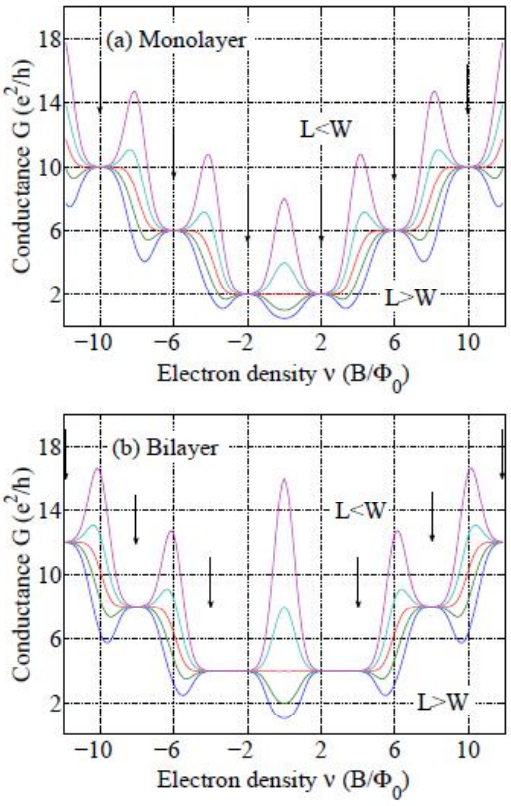

FIGURE 4.9 – Two terminal conductance for a rectangular monolayer (top) and a rectangular bilayer (bottom) with different aspect ratios ($L/W = 0.25, 0.5, 1, 2, 4$). Arrows mark the incompressible densities which are determined by equation 4.16 for the monolayer and by equation 4.17 for the bilayer. Taken from [67]

contacts and W the width of the sample). Abanin and Levitov [67] have studied theoretically the problem of the two probe conductance in graphene and bilayer graphene using the analytic results for a conducting rectangle and a semicircle model for transport coefficients σ_{xx} and σ_{xy} to which I will come later. They have found that in a square geometry there should be a conductance plateau at the neutrality point, and that for rectangular geometry the conductance should exhibit maxima at the incompressible densities corresponding to quantum Hall effect for wide samples and minima for narrow samples, explaining the oscillations we observe in our wide bilayer. They have found also that the positions and relative sizes of these features are different for the monolayer and the bilayer, as is shown in figure 4.9. The incompressible quantum hall densities for the monolayer and bilayer are

$$\nu_{n-ML} = 4\big(n + 1/2\big)|B|/\Phi_0, \qquad n = 0, \pm1, \pm2 \ldots, \tag{4.16}$$

$$\nu_{n-BL} = 4n|B|/\Phi_0, \qquad n = \pm1, \pm2 \ldots \tag{4.17}$$

Our measurements shown in figure 4.8 are then comparable with theoretical predictions shown in figure 4.9. Measured conductance in the monolayer resembles the one predicted for a square monolayer. In the case of the bilayer, the measured conductance with the maximum of conductance at the neutrality point, resembles the one predicted for a wide bilayer ($L < W$). Measurements by Williams *et al.* also confirm these theoretical predictions [68].

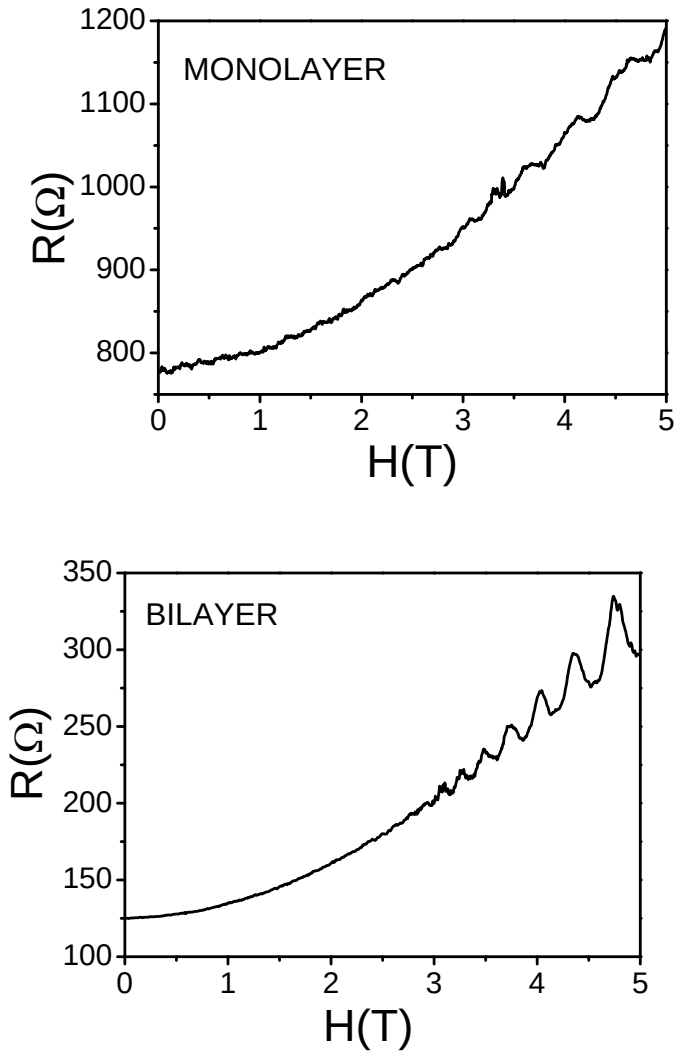

FIGURE 4.10 – Magnetoresistance measurements for the monolayer (top) and bilayer graphene (bottom) far from the charge neutrality point. Contact resistance was subtracted in both cases.

4.3.1 Determination of the transport characteristic times

I will describe now how from magnetoresistance measurements shown in figure 4.10 we extracted τ_{tr} and τ_e, which are essential to find the nature of main scatterers in graphene. To extract τ_{tr} one possibility is using Drude formula (equation 4.10) that in case of graphene has the form

$$\sigma = 2k_F v_F \tau_{tr} \frac{e^2}{h}, \tag{4.18}$$

and the capacitor model to get k_F without passing by any magnetoresistance measurement,

$$k_F^2 = \pi n = \frac{\pi C(V_g - V_{DP})}{e} \tag{4.19}$$

(C is the capacitance per unit area formed by the Si oxide and V_{DP} the voltage corresponding to the charge neutrality point). This approach needs only a measurement of resistance as a function of gate voltage but

it is inaccurate. It is known that near the Dirac point puddles of electrons and holes are present in all samples [69], which makes that the value of electronic density extracted from the capacitance model corresponds actually to an average of the electronic density of electrons and holes puddles. Because of this reason, we use the two terminal magnetoresistance measurements combined with Drude formula. At low magnetic fields (see figure 4.10), quadratic magnetoconductivity yields τ_{tr} and at high magnetic fields, when the cyclotron frequency is larger than $1/\tau_e$, the magnetoconductivity exhibits Shubnikov-de Haas oscillations related to the formation of Landau levels. The broadening of these levels at low temperatures yields τ_e.

The two terminal magnetoresistance results from the mixing of the diagonal ρ_{xx} and off diagonal ρ_{xy} components of the resistivity tensor. The degree of mixing depends on the aspect ratio of the sample. For a square geometry like the one of the monolayer

$$R(B) = \left(\rho_{xx}^2 + \rho_{xy}^2\right)^{1/2}, \tag{4.20}$$

(which is equivalent to relation 4.15). For a short wide sample like the bilayer,

$$R(B) = \frac{L}{W}\frac{\left(\rho_{xx}^2 + \rho_{xy}^2\right)}{\rho_{xx}}. \tag{4.21}$$

Abanin and Levitov developed a method to consider any intermediate geometry. It consist on calculating the net current I and the voltage drop between the two contacts V of a rectangular sample with an arbitrary aspect ratio L/W as a function of the longitudinal and transversal electric fields in the sample E_x and E_y. The electric field components E_x and E_y can be obtained from the real and imaginary parts of an analytic function $f(z)$,

$$E_y + iE_x = -e^{f(z)}$$

where

$$f(z) = i\theta - \sum_{n>0(odd)} \frac{4\theta}{n\pi}\frac{\sinh(n\pi iz/W)}{\cosh(n\pi L/2W)}$$

and $\theta = \tan^{-1}\left(\sigma_{yx}/\sigma_{xx}\right)$ is the Hall angle. Integrals giving I and V have to be done carefully to avoid singularities of $f(z)$. At the end the two probe resistance at low magnetic fields ($\omega_C\tau << 1$) can be written in a form with a single parameter depending on the aspect ratio of the sample α_g :

$$R(B) - R(0) = \rho_0\frac{L}{W}\left(\omega_C\tau_{tr}\right)^2\alpha_g \tag{4.22}$$

$$\rho_0^{-1} = \sigma = \left(\frac{2e^2}{h}\right)k_F v_F \tau_{tr}$$

and

$$\omega_C = \frac{eB}{m^*} \tag{4.23}$$

m^* the cyclotron mass, depends on the Fermi wavevector in the monolayer and in the bilayer can be approximated (in the range of V_g explored where $|E_F| \leq 80meV$ [71]) by an effective mass that is independent of the carrier density

$$m_{ML}^* = \frac{\hbar k_F}{v_F} \qquad m_{BL}^* \approx m_{eff} = 0.035m_e. \tag{4.24}$$

The values found numerically for α_g for the geometries of the monolayer and the bilayer are

$$\alpha_{g-ML} = 0.53 \pm 0.01 \qquad \alpha_{g-BL} = 0.84 \pm 0.02 \tag{4.25}$$

Being able of reconstructing the two probe resistance from the longitudinal and transversal resistance is important to deduce τ_{tr} and τ_e as will be seen in the following.

Magnetoresistance at low magnetic fields : determination of τ_{tr}

At low magnetic fields ($\omega_C\tau_{tr} << 1$ with ω_C the cyclotron frequency) we can extract the transport time τ_{tr} from the resistivity tensor,

$$\begin{pmatrix} \rho_{xx} & \rho_{xy} \\ -\rho_{xy} & \rho_{xx} \end{pmatrix} = \rho_{(B=0)} \begin{pmatrix} 1 & \omega_C\tau_{tr} \\ -\omega_C\tau_{tr} & 1 \end{pmatrix} \tag{4.26}$$

The two probe resistivity can be reconstructed from the resistivity tensor using relations 4.20 and 4.21 or using the Abanin and Levitov approach. Given the geometry of the monolayer sample (see figure 4.7) we can approximate the two probe resistivity by relation 4.20,

$$\rho_{ML} \approx \sqrt{\rho_{xx}^2 + \rho_{xy}^2} = \rho_0\big(1 + \frac{1}{2}\big(\omega_C\tau_{tr}\big)^2\big). \tag{4.27}$$

In the case of the bilayer, given its wide geometry we can make the approximation

$$\rho_{BL} \approx \frac{1}{\sigma_{xx}} = \frac{\rho_{xx}^2 + \rho_{xy}^2}{\rho_{xx}} = \rho_0\big(1 + \big(\omega_C\tau_{tr}\big)^2\big). \tag{4.28}$$

With ρ_0 the resistivity at zero magnetic field. These two relations are actually almost identical to the expression 4.22 deduced from Abanin and Levitov's equations with α_g given by 4.25. In order to get τ_{tr} we have to get first k_F which is implicit in the cyclotron frequency ω_C through the effective mass m^* for the monolayer (equation 4.23). This can be done through a zero field measurement using Drude formula which contains τ_{tr} as well (equation 4.18). We actually choose to extract k_F from the period of Shubnikov De-Haas oscillations which appear at intermediate magnetic fields as is seen in the next subsection. Extracting k_F in this way makes the calculation independent of the contact resistance, which is very convenient (see figure 4.16).

Having k_F, τ_{tr} can be determined using 4.27 and 4.28. Representing the quadratic low field magnetoresistance (which was found to be independent of temperature between 1 and 4K), τ_{tr} can be obtained from the slope of the curves as shown in figure 4.11. It is seen that the slope increases in the vicinity of Dirac point reflecting the divergence of the effective mass of the monolayer near that point.

Figure 4.12 shows the transport times obtained for the different k_F for the monolayer and the bilayer. It can be seen the different k_F dependence in the monolayer and the bilayer. In the case of the monolayer, transport time increases with increasing k_F while for the bilayer it decreases with increasing k_F. This comes from the different dependence on k_F of the diffusion coefficient for the monolayer and the bilayer that as was seen in the introduction, it is associated to the different physics these two systems follow. Transport time is unknown near the charge neutrality point, and the reason is that, as was mentioned before, in any graphene sample there are puddles of electrons and holes near the Dirac point that impede to have access to the zero electronic density point. To illustrate this, figure 4.13 shows how sweeping gate voltage, the value of k_F jumps when approaching to Dirac point, which shows that it is not accesible in our samples. It is also shown the electronic density dependence on gate voltage. Near the Dirac point electronic density saturates into a non-zero value. Figure 4.12 shows also the k_F dependence of τ_{tr} obtained using the capacitance model (4.19). It is seen that this model gives false results near Dirac point. Far from Dirac point it gives results that approach what is found with the magnetoresistance measurements.

Magnetoresistance at intermediate magnetic fields : determination of τ_e

Shubnikov de-Haas oscillations that appear at intermediate magnetic fields ($\approx 3T$), where $\omega_C\tau_{tr} \approx 1$ or ($\omega_C\tau_e \approx 1$) permit to extract the elastic collision time τ_e. The resistivity tensor at intermediate magnetic fields has the form

$$\begin{pmatrix} \rho_x \\ \rho_y \end{pmatrix} = \rho_{(B=0)} \begin{pmatrix} 1 + 2\delta\nu/\nu & \omega_C\tau_{tr} - \frac{\delta\nu/\nu}{\omega_C\tau_{tr}} \\ -\omega_C\tau_{tr} + \frac{\delta\nu/\nu}{\omega_C\tau_{tr}} & 1 + 2\delta\nu/\nu \end{pmatrix} \tag{4.29}$$

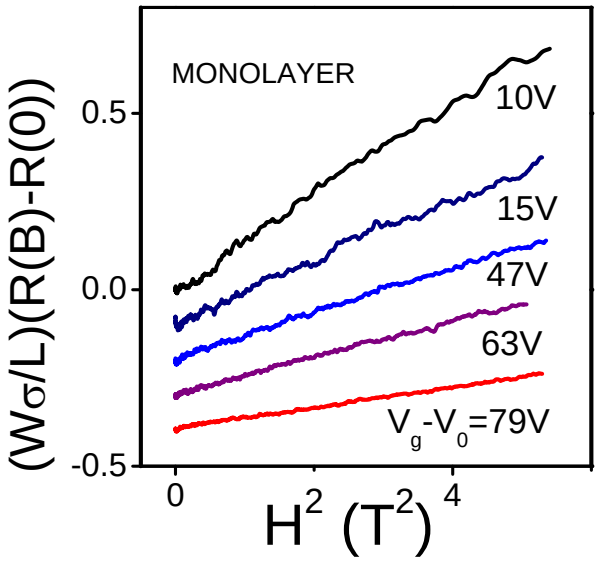

FIGURE 4.11 – B^2 dependence of the magnetoresistance in the monolayer at different gate voltages. τ_{tr} is extracted from the slope of these curves according to 4.27. (Curves have been shifted for clarity)

where ν is the filling factor. $\delta\nu/\nu$ is an oscillatory term which can be approximated by its first harmonic due to the formation of Landau levels,

$$\frac{\delta\nu}{\nu} = 2D_T \exp\left(-\frac{\pi}{\omega_C\tau_e}\right)\cos\left(\frac{j\pi E_F}{\hbar\omega_C} - \phi\right). \tag{4.30}$$

where ω_C is given by 4.23 and

$$E_{F(ML)} = \hbar v_F k_F \qquad E_{F(BL)} = \frac{\hbar^2 k_F^2}{2m}. \tag{4.31}$$

The phase ϕ is either π or 2π and the parameter j is 1 or 2 depending on the nature of the sample (monolayer or bilayer). The prefactor D_T describes the thermal damping of the oscillations

$$D_T = \frac{\gamma}{\sinh\gamma}$$

with

$$\gamma = \frac{2\pi^2 K_B T}{\hbar\omega_C}.$$

$\delta\nu/\nu$ determines Shubnikov-de Haas oscillations of the longitudinal resistivity ρ_{xx}. Considering a square geometry for the monolayer and that the bilayer is a very wide sample (like in 4.27 and 4.28) we have,

$$\begin{aligned} \rho_{ML} &= \rho\left(1+\omega_C^2\tau_{tr}^2\right)^{1/2}\left(1+\frac{\delta\nu/\nu}{1+\omega_C^2\tau_{tr}^2}\right) \\ \rho_{BL} &= \rho_0\left(1+\omega_C^2\tau_{tr}^2(1-2\delta\nu/\nu)\right) \end{aligned} \tag{4.32}$$

where $\rho_0 = 1/\sigma$ is the zero field resistivity. Having the two terminal resistivity $\rho_{ML}(B)$ and $\rho_{BL}(B)$, τ_e can be extracted from the exponential term in $\delta\nu/\nu$ (equation 4.30). $\delta\nu/\nu$ can be determined from the following relations. Defining $\beta = \omega_c\tau_{tr}$ we have,

$$\frac{\rho_{ML}}{\rho_0} = \left(1+\beta^2\right)^{1/2}\left(1+\frac{\delta\nu/\nu}{1+\beta^2}\right)$$

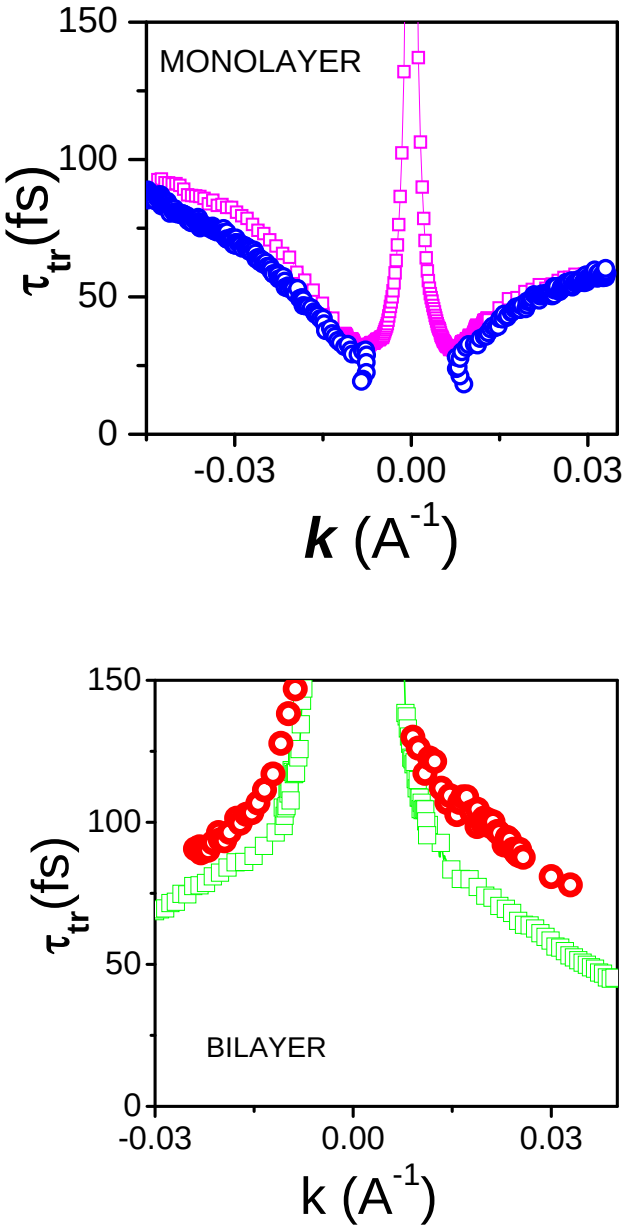

FIGURE 4.12 – k_F dependence of the transport time for the monolayer (top) and the bilayer (bottom). Circles show the results using magnetoresistance measurements. Squares correspond to results using the capacitance model. The points near Dirac point for the monolayer deduced using the capacitance model are not trustable since we do know we cannot have access to these k values due to the puddles of electrons and holes near Dirac point.

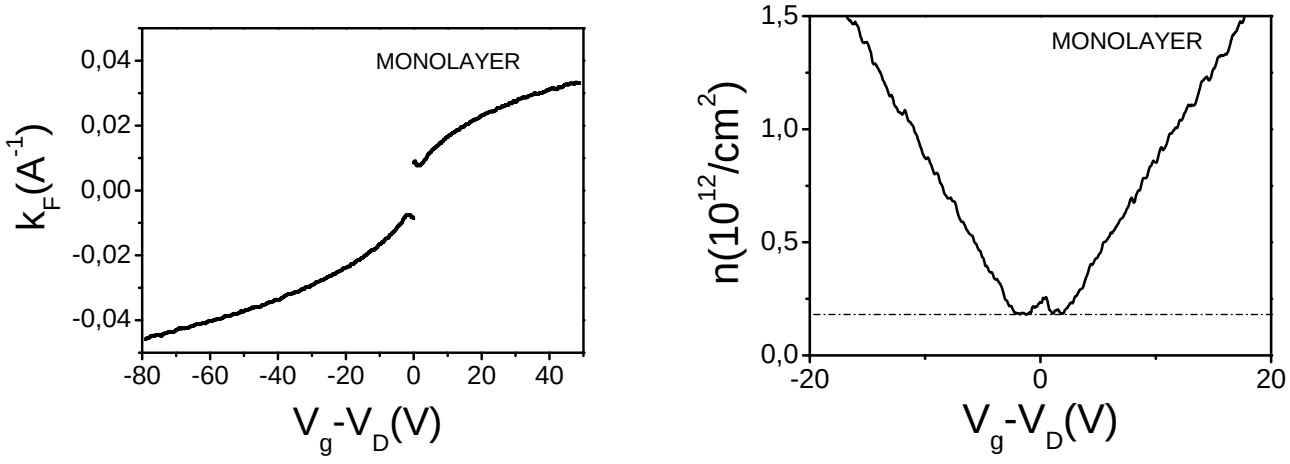

FIGURE 4.13 – Left : Values of k_F found for different V_g using magnetoresistance measurements. Values of k_F near Dirac point are not accessible. Right : V_g dependence of electronic density calculated from the values of k_F ($n = k_F^2/\pi$)

and defining ξ as the value of ρ_{ML}/ρ_0 when $\delta\nu/\nu = 0$, $\xi = \left(1+\beta^2\right)^{1/2}$, ρ_{ML}/ρ_0 becomes

$$\frac{\rho_{ML}}{\rho_0} = \xi + \frac{\delta\nu/\nu}{\xi}$$

which shows how $\delta\nu/\nu$ can be determined from ρ_{ML} ,

$$\frac{\delta\nu}{\nu} = \left(\frac{\rho_{ML}}{\rho_0} - \xi\right)\xi.$$

In the same way, we can write for the bilayer

$$\rho_{BL} = \rho_0\left(1+\beta^2\left(1-2\frac{\delta\nu}{\nu}\right)\right)$$

and

$$\frac{\rho_{BL}}{\rho_0} - 1 = \beta^2\left(1-2\frac{\delta\nu}{\nu}\right).$$

Defining ζ as the value of $\rho_{BL}/\rho_0 - 1$ when $\delta\nu/\nu = 0$

$$\zeta = \frac{\rho_{BL}}{\rho_0} - 1 = \beta^2,$$

we have

$$\frac{\delta\nu}{\nu} = \frac{1}{2} - \frac{1}{2\zeta}\left(\frac{\rho_{BL}}{\rho_0} - 1\right) \tag{4.33}$$

Figure 4.14 shows the intermediate field magnetoresistance of the bilayer fitted by equation 4.32 and the extraction of τ_e from the exponential decay of oscillations (equation 4.30). $\delta\nu/\nu$ was deduced using relation 4.33 Figure 4.15a shows magnetoresistance for the bilayer at $V_g = 70V$ at different temperatures. This time a quadratic envelop has been subtracted. It is seen at first sight how oscillations decay as magnetic

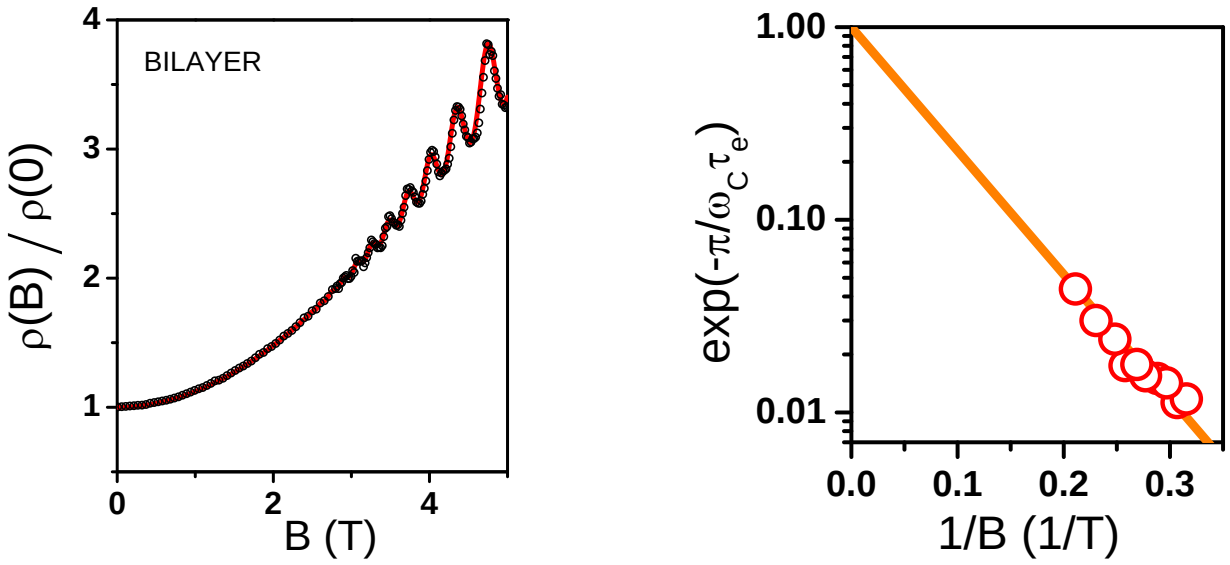

FIGURE 4.14 – Left : Resistivity of the bilayer as a function of the magnetic field at $V_g = 64V$ fitted with 4.32 and 4.30. Right : Maximums of the Shubnikov-de Haas oscillations (circles) fitted with an exponential function (continuous line). Figure is in log-scale. τ_e is deduced from the slope of the line. This procedure is repeated on magnetoresistance measurements taken at different gate voltages.

field decreases, and how they get damped with increasing temperature. Figure 4.15b shows the fit of the amplitude of oscillations according to factor D_T appearing in relation 4.30,

$$D_T = \frac{\gamma}{\sinh \gamma} \tag{4.34}$$

with

$$\gamma = \frac{2\pi^2 k_B T}{\hbar \omega_C}.$$

This fit yielded and effective mass of $m_{eff} = (0.035 \pm 0.002)m_e$ in the whole range of gate voltage investigated.

From Shubnikov-de Haas oscillations we also deduced k_F, which appears in the argument of the cosines in equation 4.30. The oscillatory part of resistivity has the form

$$\rho_{ML/BL} \propto \cos\left(\frac{j\pi E_F m^*}{\hbar e} B^{-1} + \phi\right) \tag{4.35}$$

The phase ϕ is either π or 2π and j is either 1 or 2 depending on the nature of the sample (monolayer or bilayer). E_F depends on k_F for the monolayer and the bilayer (see relations 4.31) and m^* depends on k_F in the case of the monolayer (see relations 4.24). k_F extracted using this method yielded the same values deduced using the first method. Figure 4.16 shows magnetoresistance data for the monolayer and the bilayer represented as a function of $1/B$. A quadratic envelope has been subtracted to the field oscillations.

Figure 4.17 shows the k_F dependences of τ_{tr} and the ratio τ_{tr}/τ_e for the monolayer and bilayer samples (A and B) and also for the other three monolayer samples (C, D and E). C is a two terminal sample and D and E are multiterminal samples with a Hall bar geometry.

In all cases, despite large variations of τ_{tr}, τ_{tr}/τ_e is nearly independent of k_F. It is equal to 1.7 ± 0.3 for the monolayers A, C, and E and to 1.8 ± 0.2 for the bilayer in the whole range explored ($1.5 \times 10^{11} < n < 5 \times 10^{12}$).

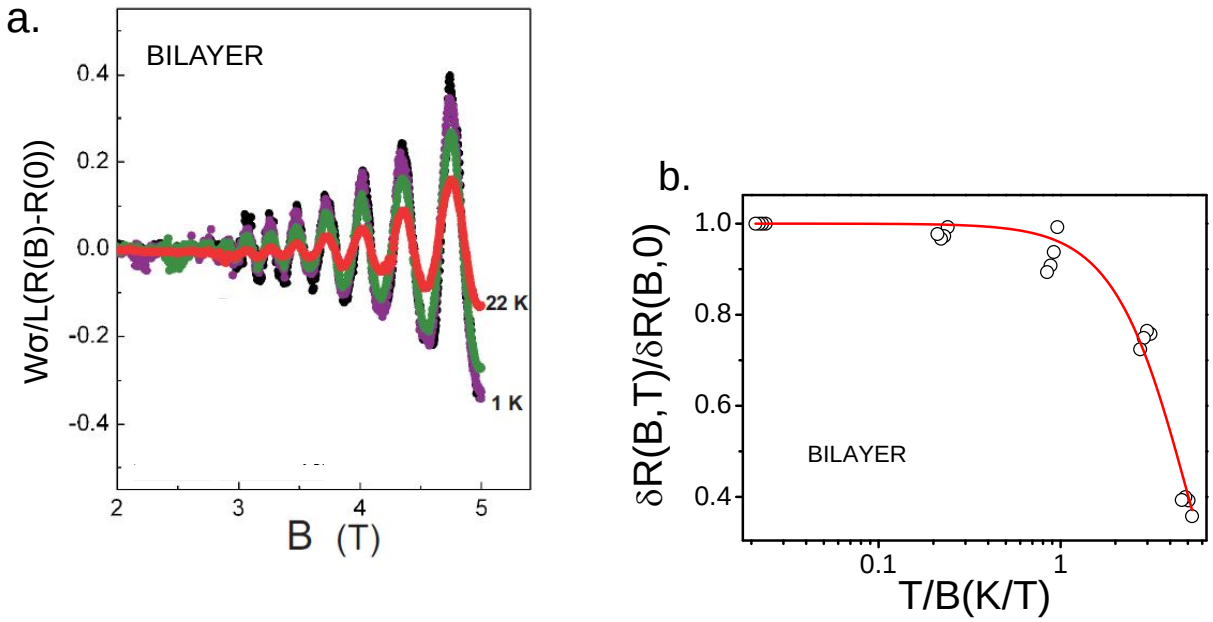

FIGURE 4.15 – Left : Longitudinal component of resistivity for the bilayer at different temperatures. A quadratic envelop was subtracted. Right : Fit of D_T (equation 4.34). The fitting parameter is m_{eff} that was found to be $(0.035 \pm 0.002)m_e$ for all the curves measured at different gate voltages.

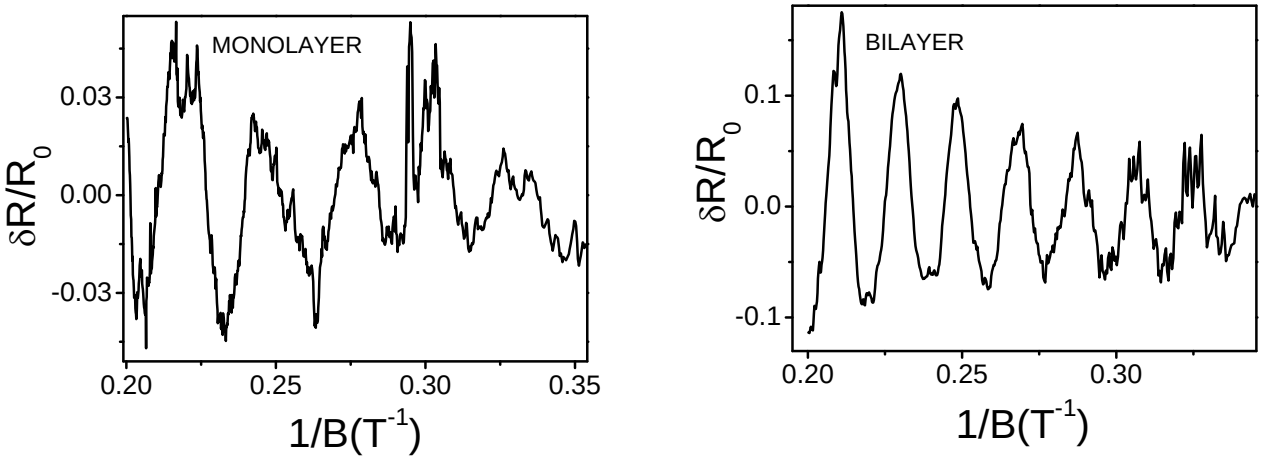

FIGURE 4.16 – Shubnikov-de Haas oscillations as a function of the inverse of magnetic field for the monolayer (left) and bilayer (right). An envelope has been subtracted. (R_0 is the resistance at zero magnetic field). k_F can be deduced from the period of oscillations (relation 4.35).

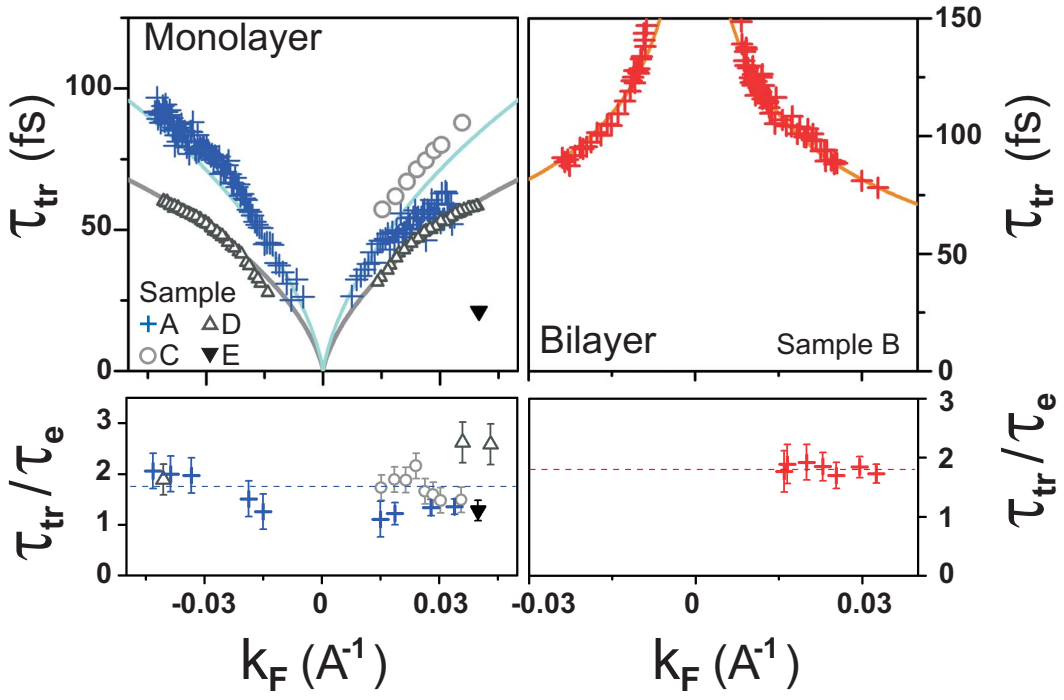

FIGURE 4.17 – k_F dependence for τ_{tr} and the ratio τ_{tr}/τ_e. Left pannel shows data from the monolayers A, C, D and E. The right panel shows data from the bilayer B. Continuous lines correspond to the fit of a resonant impurity model which I will discribe in the next section. This model explain very well our results. The ratio τ_{tr}/τ_e is near 1.8 for all the samples studied, as is indicated by the pointed line.

Having τ_{tr}/τ_e of the order but smaller than 2 indicates that the typical size of the scatterers R does not exceed Fermi wavelength ($\lambda_F > R$), which correspond to short range scattering[4]. (This can be confirmed coming back to relation 4.8). We note however, that sample D has a value $\tau_{tr}/\tau_e > 2$ ($\cong 2.4$). The reason might be that the area of this sample ($12\mu m^2$) is much larger than the are of the other samples A, B, C and E ($\cong 1\mu m^2$). A large sample contains more spatial inhomogeneities than the other smaller samples which could explain the reduced value for τ_e.

Mobility of the different samples measured was between 3000 and 5000 $cm^2V^{-1}s^{-1}$ for samples A and B. Mobility of sample C was 4500 $cm^2V^{-1}s^{-1}$. Sample D had a mobility of 2500 $cm^2V^{-1}s^{-1}$ and sample E 800 $cm^2V^{-1}s^{-1}$. It is very interesting how samples with so different mobilities exhibit such a similar ratio τ_{tr}/τ_e.

We also found $\tau_{tr}/\tau_e \approx 2$ for the bilayer. In the case of weak short range impurities this ratio is expected to be ~ 1 (see 4.9). For strong short range impurities, it has not been calculated up to now.

Samples D and E were fabricated and measured by Keyan Bennaceur at CEA, Saclay. Measurements of these samples are shown in figure 4.18. The Hall bar configuration of these samples permitted to analize the longitudinal and Hall resistivities separately. Transport time was deduced from the ratio of Hall resistance at low fields and zero field resistivity (relation 4.36), k_F was deduced from the periodicity of Shubnikov de-Haas oscillations as was detailed before, and τ_e was deduced from a semi-logarithmic plot of the amplitude of the oscillations vs. the inverse of magnetic field, as was done for the other samples. Expressions for the longitudinal and Hall resistivities can be deduced from the resistivity tensor (equation

4. $\lambda_{min} \sim 12.6nm$ which means $R \lesssim 12.6nm$

4.29),

$$\frac{\delta\rho_{xx}(B)}{\rho_0} = 4D_T \exp\left(-\frac{\pi}{\omega_C\tau_e}\right)\cos\left(\frac{j\pi E_F}{\hbar\omega_C} - \phi\right) \tag{4.36}$$

$$\frac{\rho_{xy}(B)}{\rho_0} = \omega_C\tau_{tr} - \frac{\delta\rho_{xx}(B)}{\rho_0}\frac{1}{2\omega_C\tau_{tr}} \tag{4.37}$$

Checking the values of τ_e using the semicircular model proposed by Abanin and Levitov

It is possible to fit the gate voltage dependence of conductance in our samples $G(V_g)$ shown in figure 4.8 using the values of τ_e determined above. Curves taken at $5T$ are in the quantum Hall regime, this let us use a semicircle model [67] that takes into account the contributions of the n^{th} Landau level to the longitudinal an Hall conductivities $\delta_n\sigma_{xx}(\nu)$ and $\delta_n\sigma_{xy}(\nu)$:

$$\delta_n\sigma_{xx}^2 + (\delta_n\sigma_{xy} - \sigma_{xy,n}^0)(\delta_n\sigma_{xy} - \sigma_{xy,n+1}^0) = 0 \tag{4.38}$$

$n = \ldots -2, -1, 0, 1, 2\ldots$ for the monolayer and $n = \ldots -2, -1, 1, 2\ldots$ for the bilayer and $\sigma_{xy,n}^0$ is the quantized Hall conductivity at the n^{th} plateau,

$$\sigma_{xy,n,ML}^0 = 4\left(n + \frac{1}{2}\right)\frac{e^2}{h} \qquad \sigma_{xy,n,BL}^0 = 4n\frac{e^2}{h}$$

The longitudinal conductivity $\delta_n\sigma_{xx}(\nu)$ exhibits a peak centered at the Landau level which is modeled by a Gaussian,

$$\delta_n\sigma_{xx} \approx e^{(-\ln 2(\nu-(\nu_n+\nu_{n+1})/2)/\Gamma_\nu)^2}$$

where Γ_n is the width of the Landau level function of the filling factor ν, it is related to the width of Landau levels function of energy which depends on τ_e,

$$\Gamma_E = \hbar\sqrt{\frac{2\omega_C}{\pi\tau_e}}$$

Γ_ν and Γ_E are related through the relation

$$\Gamma_\nu = \Gamma_E\frac{2}{\hbar v_F}\sqrt{\frac{\nu_n\Phi_0}{\pi B}}.$$

The total conductivity tensor is given by the sum of the contributions of all Landau levels,

$$\sigma_{xx} = \sum_n \delta_n\sigma_{xx}(\nu) \qquad \sigma_{xy} = \sum_n \delta_n\sigma_{xy}(\nu) \tag{4.39}$$

A good agreement is found between experimental data and the two-terminal conductivity $G(V_g)$ for the monolayer calculated from the conductivity tensor. For the bilayer the semicircular model is modified into an "elliptical" model described in [68] to take into account the rectangular geometry of the sample. Figure 4.19 shows the fit of the gate voltage dependence of conductivity for the monolayer and the bilayer at 5T using the semicircular model (equation 4.38) to get σ_{xx} and σ_{xy} together with the method proposed by Abanin and Levitov (described at the beginning of this section) to get the two probe conductivity. σ_{xx} and σ_{xy} were found using the values for τ_e found previously. The dashed vertical lines indicate the positions of ν_n which as expected are different for the monolayer ($\nu_n = \pm 4(n + 1/2)$) and the bilayer ($\nu_n = \pm 4n$). It is seen that the conductance quantization is well obeyed for the monolayer but it is only approximative for the bilayer. This can be explained by the aspect ratio of the bilayer sample.

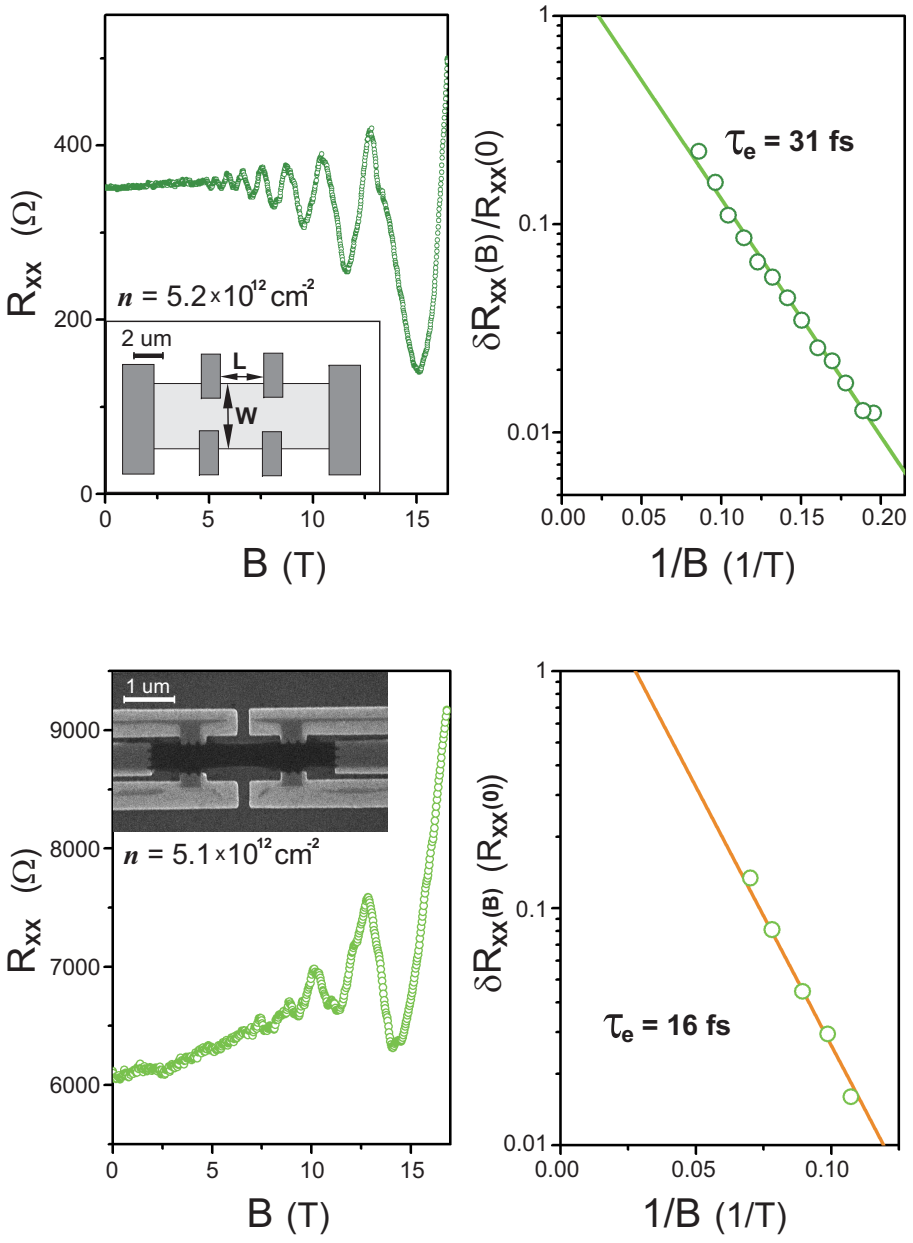

FIGURE 4.18 – Left panel : Longitudinal resistance R_{xx} as function of magnetic field for sample D (top) and E (bottom), measured $n = 5.2 \times 10^{16} m^{-2}$ for sample D and $n = 5.1 \times 10^{16} m^{-2}$ for sample E. Measurements were done at $4K$. Right panel : Semi-logarithmic plot of the SdH oscillations. The slope yields $\tau_e = 31fs$ for sample D, which gives a ratio $\tau_{tr}/\tau_e = 1.9 \pm 0.3$. In the cas of sample E $\tau_e = 16fs$ with $\tau_{tr}/\tau_e = 1.3 \pm 0.2$. Geometry and contact scheme are presented as an inset. Dimensions of sample D were $L = 2.9\mu m$ and $W = 4.2\mu m$ and geometry of sample E $L = 2.3\mu m$ and $W = 0.7\mu m$. Sample D exhibited a mobility $\mu = 2500 cm^2/Vs$ while sample E had a mobility $\mu = 800 cm^2/Vs$

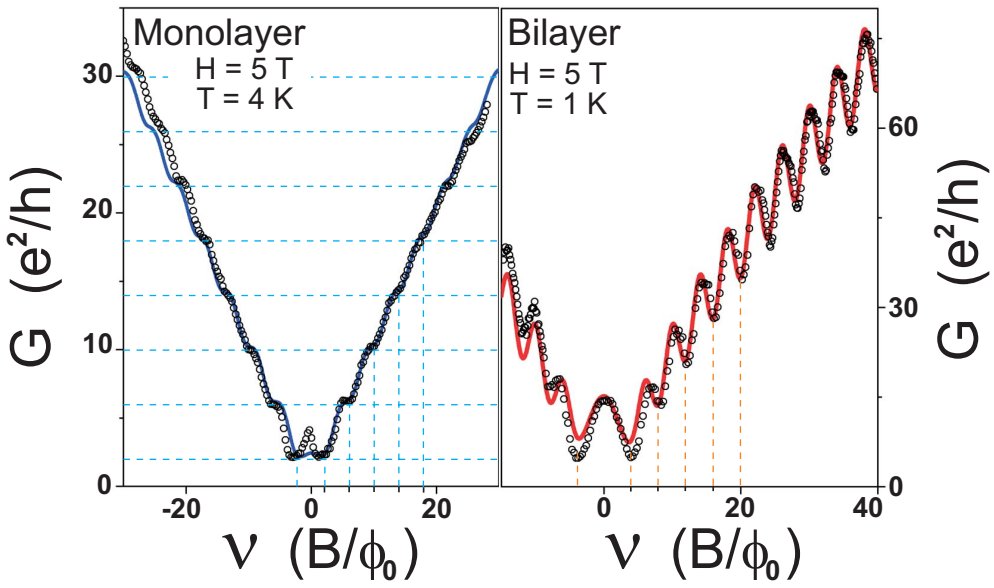

FIGURE 4.19 – Comparison of $G(\nu)$ at $5T$ for samples A and B with the expression of conductance derived using Abanin and Levitov's method and the semicircular model 4.38 with the $\tau_e(k)$ determined above.

4.4 Comparison of our results to theoretical predictions

We have found that conductivity has a sublinear dependence on n (or V_g) as is observed in figure 4.8 contrary to what is predicted by Das Sarma *et al.* and Nomura *et al.* for charged long range impurities, where conductivity is supposed to be linear with n. Conductivity is neither a constant with n for large electronic densities with a minimum at low electronic densities as predicted by Nomura *et al.* for short range impurities.

Concerning the characteristic transport times, it has been predicted [63] using Thomas Fermi approximation that in the presence of charged impurities, characteristic transport times should go as $\tau_{kF} \propto k_F$ for the monolayer and it should be independent of k_F for the bilayer. This is not what we have observed. In the case of the monolayer we have seen a sublinear dependence on k_F and for the bilayer τ_{kF} decreases with k_F. We have observed a ratio $\tau_{tr}/\tau_e \sim 2$ for both the monolayer and the bilayer. This is in accordance to what is expected for short range scattering for the monolayer but it differs to the predicted value for the bilayer (see relations 4.8 and 4.9).

An alternative explanation is resonant scattering resulting from vacancies or any other kind of impurities of short range R such that $a \leq R << 1/k_F$ (a is the carbon-carbon distance). As will be seen in the following, if scatterers are short range resonant impurities, transport time has the form

$$\tau_{ML} \approx \frac{k \ln^2(kR)}{n_{imp} v_F \pi^2} \propto k \ln^2(kR) \qquad \tau_{BL} \approx \frac{k \ln^2(kR)}{n_{imp} v_F \pi^2} \propto \ln^2(kR)$$

which explains well our results as is seen in figure 4.17.

4.4.1 Low energy scattering of a 2D Dirac particle on a strong impurity of short range

If we recall the 2D scattering theory of a particle incident on a strong impurity of short range, we can, considering that the incident particle is a massless Dirac particle (in the case of the monolayer) and a massive Dirac particle (in the case of the bilayer) deduce the scattering cross section A_{tr}, that gives access to the transport time τ_{tr} as well as the conductivity leaded by these Dirac particles [5].

We consider a potential such that

$$U(r) = \begin{cases} V_0 > 0 & r < R \\ 0 & r > R \end{cases} \tag{4.40}$$

where V_0 is the potential strength and R is the potential range. We consider an incident low energy massless Dirac particle with wavevector k such that $kR << 1$ (which is equivalent to say that potential $U(r)$ is short range), we have that the scattering amplitude has the form

$$\begin{aligned} f(\theta) &= \frac{e^{i2\delta(k)} - 1}{i\sqrt{2\pi k}} \left(1 + e^{-i\theta}\right) \\ &= \frac{-\sqrt{\pi/2k}}{\frac{J_0(\tilde{k}R)}{kRJ_1(\tilde{k}R)} + \ln\left(\frac{2}{\gamma_E kR}\right) + i\frac{\pi}{2}} (1 + e^{-i\theta}) \end{aligned} \tag{4.41}$$

where $\delta(k)$ is the s wave scattering phase shift, $\gamma_E = e^{\gamma} = 1.781\ldots$ and J_n are Bessel functions. The wavevector $\tilde{k}$ is defined as

$$\tilde{k} \equiv \frac{|\epsilon - V_0|}{\hbar v_F}$$

where $\epsilon = \hbar v_F k$ is the electron energy and $v_F \approx 10^6 m/s$ in a graphene monolayer.

If the potential is weak $V_0 << \epsilon$ and $\tilde{k} \approx k$. If the potential is strong $V_0 >> \epsilon$ and $\tilde{k} \approx V_0/\hbar v_F$. We consider the case of a strong potential where

$$\tilde{k}R \approx \frac{V_0 R}{\hbar v_F}$$

does not depend on k.

The differential cross section $dA/d\theta$ is given by

$$\frac{dA}{d\theta} = |f(\theta)|^2 = \frac{8\sin^2\delta(k)}{\pi k}\frac{1+\cos\theta}{2}$$

and the transport cross section and total cross section are

$$A_{tr} = \int d\theta(1-\cos\theta)|f(\theta)|^2 = \frac{4\sin^2\delta}{k} = \frac{1}{2}A \tag{4.42}$$

$$A = \int d\theta|f(\theta)|^2 = \frac{8\sin^2\delta(k)}{k} \tag{4.43}$$

There is a factor 2 between the two cross sections because in graphene there is an additional factor in the integral $(1+\cos\theta)/2$ that suppresses back scattering. We have therefore for the monolayer $\tau_{tr} = 2\tau_e$. The transport time τ_{tr} can be determined via A_{tr} using the relation,

$$\frac{1}{\tau_{tr}} = n_{imp} v_F A_{tr} = 4 n_{imp} v_F \frac{\sin^2\delta(k)}{k} \tag{4.44}$$

5. This model was adapted by Jean Ni¿½el Fuchs. (Taken from Jean Ni¿½el's notes, see complementary material [86]).

where n_{imp} is the impurity density and v_F the Fermi velocity. In the same way, the elastic scattering time τ_e can be found from

$$\frac{1}{\tau_e} = n_{imp} v_F A. \tag{4.45}$$

The conductivity is related to τ_{tr} by the usual relation

$$\sigma = 2\frac{e^2}{h} v_F k_F \tau_{tr}(k_F) \tag{4.46}$$

In order to predict a k_F dependence of τ_{tr} and σ, we have to consider different limits determined by the three terms in the denominator of $f(\theta)$ (equation 4.41). In particular, when $J_0(\tilde{k}R) \approx 0$ the logarithmic term wins. This can happen because $\tilde{k}R \approx V_0 R/\hbar v_F$ can be larger than one even if $kR << 1$. This is called the resonant case even if it is not necessary to fine-tune k_F to fit this condition. In this situation, the phase shift of the scattered wavefunction has the form

$$\delta(k) \approx -\frac{\pi}{2\ln(kR)} \to 0$$

which leads to a transport cross section

$$A_{tr} \approx \frac{4\delta^2}{k} \approx \frac{\pi^2}{k\ln^2(kR)}$$

and a transport time

$$\tau_{tr-ML} \approx \frac{k\ln^2(kR)}{n_{imp} v_F \pi^2} \propto k\ln^2(kR). \tag{4.47}$$

This gives a conductivity

$$\sigma \approx \frac{2}{\pi} n_c \frac{e^2}{h} \frac{\ln^2\left(R\sqrt{\pi n_C}\right)}{n_{imp}} \tag{4.48}$$

where $k_F^2 = \pi n_C \propto V_g$.

In the case of the **bilayer**, the differences in the calculation are : the effective mass is no longer $m = 0$, the chirality factor appearing in the transport cross section is not $(1+\cos\theta)/2$ but $(1+\cos 2\theta)/2 = \cos^2\theta$ and the first term in the denominator of 4.41 is equal to zero. This gives contrary to the case of the monolayer $A_{tr} = A$ and therefore $\tau_{tr} = \tau_e$ [6]. Given that

$$v_{F,BL} = \frac{\hbar k_F}{m^*}$$

with $m^* = 0.035 m_e$, τ_{tr} has a different dependence on k_F for the bilayer :

$$\tau_{tr-BL} \approx \frac{k\ln^2(kR)}{n_{imp} v_F \pi^2} \propto \ln^2(kR). \tag{4.49}$$

Conductivity on the other hand has the same dependence on k_F as the monolayer.

We conclude that considering a short range resonant impurity, leads to a conductance that increases with V_g with logarithmic corrections for both the monolayer and the bilayer. In both cases, our extracted $\tau_{tr}(k_F)$ is fitted very well by the square logarithmic dependence of equations 4.47 and 4.49 as is seen in figure 4.17.

It is possible to estimate with this model the range of the impurity potential, $0.5\mathring{A} \leq R \leq 2.5\mathring{A}$ and the concentration of impurities $n_i = (8 \pm 2) \times 10^{11} cm^{-2}$, which corresponds to approximately 4 impurities every 10000 hexagonal units. The concentration of impurities turns out to be identical for samples A and B and it is of the order of the minimum value of the carrier density $n_{min} = 1.5 \times 10^{11} cm^{-2}$, extracted from

6. This is only valid in the regime $R << \lambda_F$

the experiment . It is also interesting to note that the minimum conductivity expected for this resonant impurity model,

$$\sigma_{min} = \left(\frac{2e^2}{\pi h}\right) \times \left(\frac{n_{min}}{n_i}\right) \ln^2\left(R\sqrt{\pi n_{min}}\right)$$

is $3.7e^2/h$ for the monolayer and $4.5e^2/h$ for the bilayer. These values are very similar to the observed experimental values, $\sigma_{min,ML} = 3.3e^2/h$ and $\sigma_{min,BL} = 4.1e^2/h$.

This analysis also corroborates our results on the ratio τ_{tr}/τ_e for the monolayer indicating that the scatterers present in our samples have a range smaller than the Fermi wavelength but possibly of the order of or slightly larger than the lattice spacing $a < R << \lambda_F$. We have essentially short range intravalley scattering (since $R > a$)

The resonant character as mentioned before, is not essential for the validity of equations 4.47 and 4.48 for massive carriers but it is essential for massless carriers in the monolayer. It has been demonstrated in the case of scattering centers created by vacancies in graphene over a wide range of Fermi energies [72].

4.5 Conclusions

In conclusion, our results indicate that the main scattering mechanism in our graphene samples is due to strong neutral defects, with a range shorter than the Fermi wavelength and possibly of the order of a, inducing resonant scattering. Likely candidates are vacancies, as observed recently in transmission electron microscopy [73], voids, adatoms, or short-range ripples as suggested in [74]. This does not exclude the presence of long-range charged impurities responsible for electronhole puddles but their contribution to the scattering rates $1/\tau_{tr}$ and $1/\tau_e$ appears to be negligible in all the samples we have investigated.

Chapitre 5

Measurement of the universal conductance fluctuations in graphene and bilayer graphene

5.1 Introduction

Reproducible conductance fluctuations are one of the most relevant signatures of phase coherent transport. In a disordered coherent sample coupled to two perfect conductors, the conductance comes from the interference of all wave packets traversing the sample. Interference phenomena between wavepackets can be modified through an external parameter like magnetic field, gate voltage or the configuration of impurities in the sample. This give rise to reproducible fluctuations of conductance with a universal amplitude that is independent of the size of the sample at $T = 0$.

In graphene, as will be seen in this chapter, conductance fluctuations present particular features. The amplitude of fluctuations depends on the doping and correlation functions have a special dependence on electronic density n, depending on whether the system is made of a monolayer or a bilayer. This is due to the different variations with n of the diffusion coefficient, illustrating the contrast between massive and massless carriers. In addition, second order conductance fluctuations (mesoscopic rectification) as will be discussed for graphene, can give information about the e-e interaction in a system.

5.2 Introduction to the physics of phase coherent transport

Conductance in the diffusive regime can be related to the probability distribution $P(\vec{r_1}, \vec{r_2})$ for an electron initially at $\vec{r_1}$ to reach $\vec{r_2}$. It can be written as

$$P(r_1, r_2) = \sum_p A_p A_p^* + \sum_{p \neq p'} A_p A_{p'}^*, \tag{5.1}$$

where A_p is the complex amplitude of the contribution of a path p going from r_1 to r_2. $A_p = |A_p| e^{iS_p/\hbar}$, where S_p is the action along a trajectory p,

$$S_p = \int_p \left(\hbar \vec{k}(\vec{r}) - e\vec{A}(\vec{r}) \right) d\vec{r} - Edt,$$

and E is the energy of the trajectory. The quantities $\vec{k}(\vec{r})$ and $\vec{A}(\vec{r})$ are the wave vector and vector potential along the trajectory.

In a coherent system there are interference terms in 5.1 that are associated to pairs of interfering trajectories p and p',

$$|A_p||A_{p'}| e^{i(S_p - S_{p'})/\hbar} = |A_p||A'_p| e^{i\Delta\phi_{p-p'}}$$

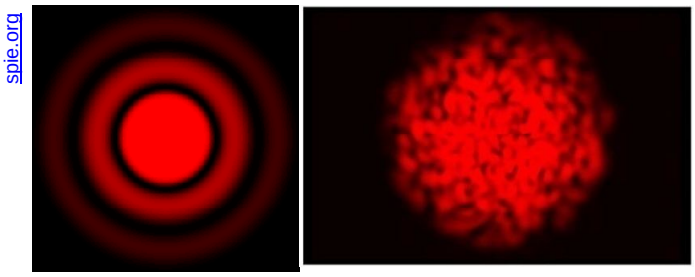

FIGURE 5.1 – In optics an interference pattern can be produced not only by a coherent light beam passing through a circular slit (a), but also when a coherent beam passes through a disordered optical medium (b)

where $\Delta\phi_{p-p'}$ is the phase difference between two trajectories. This phase shift depends on the Fermi energy or the magnetic flux Φ through the sample in the following way

$$\begin{aligned} \Delta\phi_{p-p'}(E) &= \frac{1}{\hbar}E_F(t_p - t_{p'}) = \frac{1}{2}k_F(L_p - L_{p'}) \qquad (5.2)\\ &\approx \frac{E\tau_D}{\hbar} \\ \Delta\phi_{p-p'}(B) &= \frac{1}{\hbar}\int_p e\vec{A}(\vec{r})d\vec{r} - \frac{1}{\hbar}\int_{p'} e\vec{A}(\vec{r})d\vec{r} \qquad (5.3)\\ &= 2\pi\Delta\Phi_{p-p'}/\phi_0 \end{aligned}$$

where $t_p - t'_p$ is the travelling time difference between the paths p and p' and it is in average the typical diffusion from r_1 to r_2, τ_D . $\Delta\Phi_{p-p'}$ is the magnetic flux enclosed between the two trajectories p and p' and $\Phi_0 = h/e$ is the flux quantum [1].

Thus changing Fermi energy on the sample or imposing a magnetic flux through the sample has an influence on the phase difference between two electronic trajectories. As a result conductance is modulated, giving rise to **reproducible conductance fluctuations**. Conductance fluctuations can also be generated by changing the microscopic configuration of disorder in the sample.

Reproducible conductance fluctuations have their origin in the interference of electronic wavepackets. They are analogous to the interference pattern produced by a coherent light source. When a coherent light source passes through a circular slit a well defined interference pattern appears, like the one showed in figure 5.1. When there is a random static medium, interferences are still produced giving rise to an speckled interference pattern. In the case of electrons, conductance plays the role of the intensity of light and the configuration of impurities in a metal plays the role of a disordered optical medium [2].

When changing the Fermi energy or the magnetic flux through the sample, a complete phase randomization of the electronic wavepackets traversing the sample is achieved when $\Delta\phi_{p-p'}$ is of the order of 2π, which gives (using equations 5.2 and 5.3)

$$E_F = \frac{h}{\tau_D} = E_C \qquad (5.4)$$

$$B_{p-p'} = \frac{\Phi_0}{S} = B_C \qquad (5.5)$$

where τ_D and S is the typical time and area over which interference occur. h/τ_D is called the Thouless energy.

If many paths contribute to the interference, and the change in Fermi energy or magnetic field is $E_F > E_C$ or $B_{p-p'} > B_C$, the amount of fluctuations is the same as the one produced by a complete

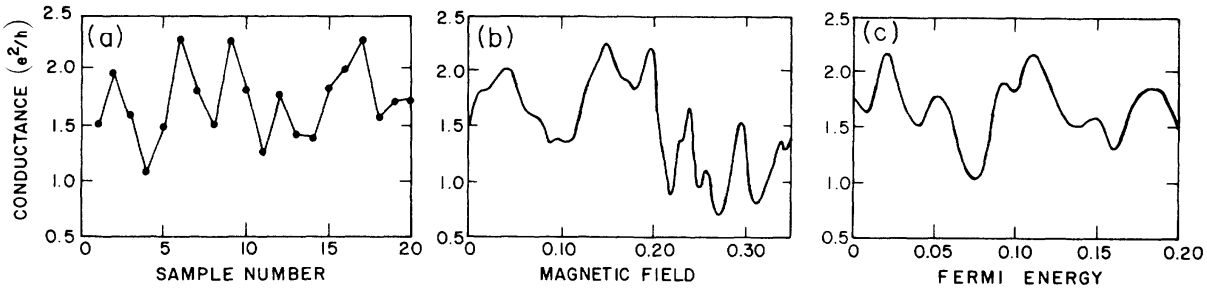

FIGURE 5.2 – Data from numerical simulations on a 100 × 10 site Anderson model taken from reference [19]. Sample to sample fluctuations, fluctuations in g(B) and g(E) are compared. Fluctuations are similar in all three cases supporting the ergodic hypothesis in diffusive conductors.

rearrangement of disorder inside the sample, which means that fluctuations are ergodic. The hypothesis that in metals equivalent fluctuations are caused by changing impurity configuration, magnetic field or energy is called the ergodic hypothesis and it is supported by analytical and numerical calculations. Figure 5.2 shows data from numerical simulations [19] comparing sample to sample fluctuations, fluctuations in magnetic field and fluctuations in energy. The size of fluctuations is roughly the same in all three cases, giving a qualitative support to the ergodic hypothesis.

If interference effects are associated to a given configuration of disorder, one would expect that they disappear upon averaging over disorder (or over different sweeps of gate voltage or magnetic field). Actually, after averaging over disorder, traces of phase coherent transport persist. Even in optics, when the speckle pattern is averaged over different realizations of disorder there is still a signature of phase coherence reflected on an angular dependence of the light intensity.

If the probability 5.1 is averaged over disorder, the phase of the first term is equal to zero independently of the disorder and thus survives after averaging. This first sum corresponds to the Drude conductivity and it is called diffuson. It is associated to pairing trajectories like those shown in figure 5.3 a).

$$P(r_1, r_2)_{Cl} = \sum_p |A_p|^2. \tag{5.6}$$

Most of the terms in the second sum of 5.1 average to zero, some others survive like the one represented in figure 5.3 b) where pairing trajectories that have followed identical series of collisions cross forming a loop. The two trajectories corresponding to the two different possible circulations around the loop (clockwise or counterclockwise) interfere constructively. The distribution of these crossed trajectories in opposite directions is associated to the probability of returning to the origin (O in the figure), which constitutes a correction to the classical Drude conductivity 5.6. The probability of returning to O is enhanced (return probability) which reduces the probability of reaching r_2. This results in a negative correction to the conductance which is called the **weak localization** correction. The existence of a weak localization correction to conductance shows that even after averaging over disorder, there remain traces of phase coherence. However, these reversed trajectories acquire a phase if a flux is applied in the loop. Conductance recovers then its classical value giving rise to positive magnetoconductance on a field scale corresponding to a flux quantum in a coherent region of the sample.

Lets return to universal conductance fluctuations and discuss their universal amplitude [2]. A classical metallic conductor of size $L >> L_\phi$ [1] can be considered as a statistical ensemble of N independent

1. L_ϕ is the phase coherent length, the characteristic length over which electronic wavepackets are coherent and can present interference phenomena.

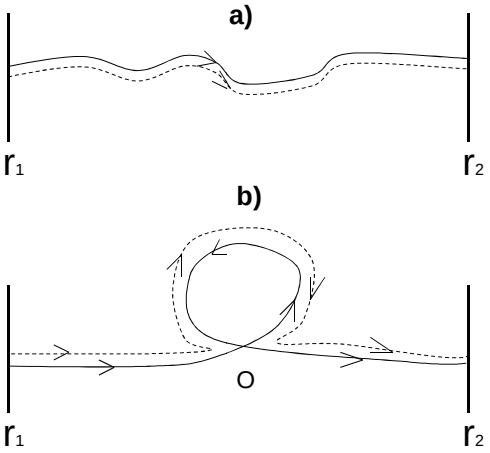

FIGURE 5.3 – Example of electronic trajectories contributing to 5.1

subsystems $N = \left(L/L_\phi\right)^d$ where phase coherence is preserved in each subsystem (d is the dimension of the system). In such a disordered conductor, any measured quantity is equivalent to an average over the different realizations of disorder. One would expect that a cubic system of side L should present relative fluctuations of conductance $\sqrt{\langle \delta G^2 \rangle}/\langle G \rangle$ of the order of $1/\sqrt{N}$,

$$\frac{\sqrt{\langle \delta G^2 \rangle}}{\langle G \rangle} \propto \left(\frac{L_\phi}{L}\right)^{d/2}.$$

Since the average conductance is given by Ohm's law, $\langle G \rangle = \sigma_0 L^{d-2}$, we expect a variance of conductance fluctuations of

$$\left\langle \delta G^2 \right\rangle \propto L^{d-4}.$$

Thus, fluctuations in a classical metallic conductor disappear in the macroscopic limit $L \to \infty$ (for $d \leq 3$).

In contrast, systems with a size $L < L_\Phi$ (systems in the mesoscopic regime) present conductance fluctuations with an amplitude that is universal and independent of disorder and sample size,

$$\left\langle G^2 \right\rangle - \langle G \rangle^2 \approx e^2/h.$$

The reason is that again, below L_Φ interference effects are important.

If we neglect any process of phase coherence loss ($L_\phi \gtrsim L$) we can write the multichannel Landauer formula for the adimensional conductance $g = G/(e^2/h)$ in terms of t, the transmission matrix for a plane-wave going through a multichannel scatterer as shown in figure 5.4.(For $b_r = 0$ $a_r = t a_l$).

$$g = 2Tr\left\{tt^+\right\}$$

The trace $Tr\left\{tt^+\right\}$ cannot be expressed within multiplicative eigenvalues since t is non-multiplicative (for two consecutive segments 1 and 2, $t_{12} \neq t_1 t_2$). Contrarily, the transfer matrix T defined as

$$\begin{pmatrix} a_r \\ b_r \end{pmatrix} = T \begin{pmatrix} a_l \\ b_l \end{pmatrix}, \tag{5.7}$$

is multiplicative and its eigenvalues can be written as powers of the eigenvalues of some matrix. The trace $Tr\left\{tt^+\right\}$ can be related to the trace of the matrix TT^+, so the adimensional conductance g is essentially determined by multiplicative eigenvalues. Because of disorder in our mesoscopic system we choose T to

FIGURE 5.4 – Scheme of a multichannel scatterer. The amplitude of the N incoming channels from the left (right) are given by the components of the vector a_l (b_r). The amplitude of outgoing channels is given by b_l (a_r).

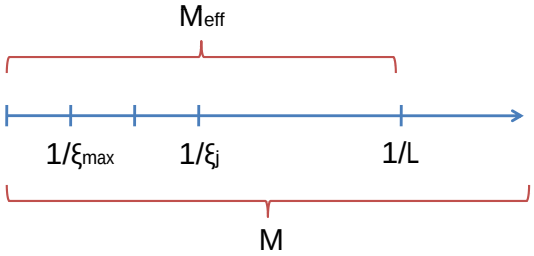

FIGURE 5.5 – Scheme of the eigenvalues of the random matrix tt^+

be a random matrix. It can be shown [17] that $Tr\{tt^+\} = \sum_{j=1}^{M} x_j^L$ where x_j are real, positive and smaller than unity eigenvalues of some random matrix and L the size of the sample, for large L only the eigenvalues close to the unity will remain. Eigenvalues x_j smaller but closer to unity can be written as e^{-L/ξ_j} where $1/\xi_{j+1} - 1/\xi_j$ is the spacing between eigenvalues and L is the size of the sample with $\xi_j >> L$. We can write,

$$g = 2\sum_{j}^{N} e^{-L/\xi_j}.$$

From the theory of random matrices we know that eigenvalues have tendency to repel each other, which means that the probability of having two eigenvalues close to each other goes to zero, or that the probability of having degenerate eigenvalues is zero. As is represented in figure 5.5, the first eigenvalue is determined by $1/\xi_{max}$ and the last one by $1/L$. ξ_{max}, the localization length is known to be of the order of Ml_e where M is the total number of channels. Considering that eigenvalues are more or less equally spaced, the number of eigenvalues N_{eigen} is given by

$$N_{eigen} = \frac{1/L}{1/\xi_{max}} = \frac{Ml_e}{L}$$

Since the eigenvalues e^{-L/ξ_j} are of the order of unity, the conductance is actually determined by N_{eigen} eigenvalues which correspond to the number of effective channels M_{eff}.

$$g = 2N_{eigen} = 2M_{eff} = 2\frac{Ml_e}{L}$$

If $L = l_e$, $M_{eff} = M$ and $g = 2M$ which correspond to a ballistic system. If $L = \xi$, M_{eff} goes to unity, which is the case of a strongly localized, single channel system.

The amplitude of conductance fluctuations is given by the square root of the variance of g, which is thus the variance of the number of effective channels. This is of the order of unity, as can be proved using

the results of random matrices theory. The transfer matrix T is a random matrix like TT^+, appearing in the calculation of $Tr\{tt^+\}$. One of the results of the random matrix theory is that for any quantity g expressed in terms of a sum over some smooth function f of the eigenvalues x_j,

$$g = \sum_{j=0}^{N} f(x_j)$$

the variance of g over the appropriate ensemble of random matrices is given by

$$\langle g^2 \rangle - \langle g \rangle^2 = 2 \int_{-\infty}^{\infty} |t| \phi(t) \phi(-t) dt$$

where $\phi(t)$ is the Fourier transformation of $f(t)$, $\phi(t) = \int_{-\infty}^{\infty} f(x) exp(-2\pi i x t) dx$. Using this result, the variance of the dimensionless conductance $var(g)$ was found to be of the order of unity and independent of L, N and l_e, which constitute the universality of conductance fluctuations [17].

The exact prefactor of the variance of conductance fluctuations depends on the symmetry of the random matrix. An orthogonal symmetry corresponds to a situation with no magnetic field and a spin degeneracy. In this case $var(g) \approx 4$. In the presence of a magnetic field $var(g) \approx 2$, time reversed symmetry is broken and symmetry is unitary. If magnetic field breaks spin degeneracy as well, $var(g) \approx 1$. If there is a strong spin orbit coupling, $var(g) \approx 1$ and the symmetry is symplectic.

Contrary to metals, in the case of disordered insulators where only a small number of paths contribute to transmission, conductance fluctuations are no longer universal, the ergodic hypothesis is no longer verified and conductance fluctuations are log-normal distributed instead of being Gaussian (i.e. $\ln G$ has a Gaussian distribution, see figure 5.19). Figures 5.6 A and B show conductance fluctuations in a GaAs :Si wire in the strongly localized regime where fluctuations are non-ergodic [18]. In this regime, the fluctuations as a function of gate voltage have a different variance with respect to fluctuations as a function of magnetic field, $var(lnR)_H \approx 0.22 < var(lnR)_{Vg} \approx 1.10$. Figure 5.6 shows also conductance fluctuations near the Anderson transition (C and D), where ergodic hypothesis becomes valid, $var(lnR)_H \approx 0.19 \approx var(lnR)_{V_g} \approx 0.27$. Observing panels A and C (or B and D in log scale) we can contrast non-ergodic conductance fluctuations with ergodic ones. It can be seen in figure A that fluctuations as a function of voltage are very different from the fluctuations as a function of magnetic field.

Reproducible conductance fluctuations have been observed in semiconductors, silicon mosfets, Si doped GaAs and GaAs-GaAlAs heterostructures. In doped GaAs where it is possible to change the configuration of impurities through annealing, uncorrelated conductance fluctuations as a function of the magnetic field for different arrangements of the impurities have been observed [3]. In silicon mosfets where the Fermi energy can be tuned with a gate voltage, uncorrelated magnetoconductance traces have also been observed for gate voltages that correspond to a shift in chemical potential of the order of E_C [4]. In this system, gate voltage dependent and magnetic field dependent conductance fluctuations have been observed to have an identical variance, in accordance with the ergodic character of conductance fluctuations.

Graphene is an interesting system to study universal conductance fluctuations thanks to the extraordinary advantage of being able to tune the Fermi energy and the diffusion coefficient over a large carrier density range, passing from electron to hole carriers. From the theoretical point of view, numerical simulations have shown that the amplitude of conductance fluctuations in graphene depend on the disorder in the sample [5]. They find a large enhancement of the sample to sample fluctuations above the UCF value. In contrast, the variance of the energy dependent fluctuations doesn't show this enhancement and agree with the UCF prediction. The origin of this result has been understood as a percolation transition, to which I will return later. These results show that the ergodic hypothesis does not hold in graphene.

It has also been shown that the amplitude of fluctuations depends strongly on the type of disorder, depending on if it produces intervalley or intravalley scattering [6]. A model based on percolating current patterns has been introduced in [7] to explain the scaling dependencies of the conductance on doping and disorder.

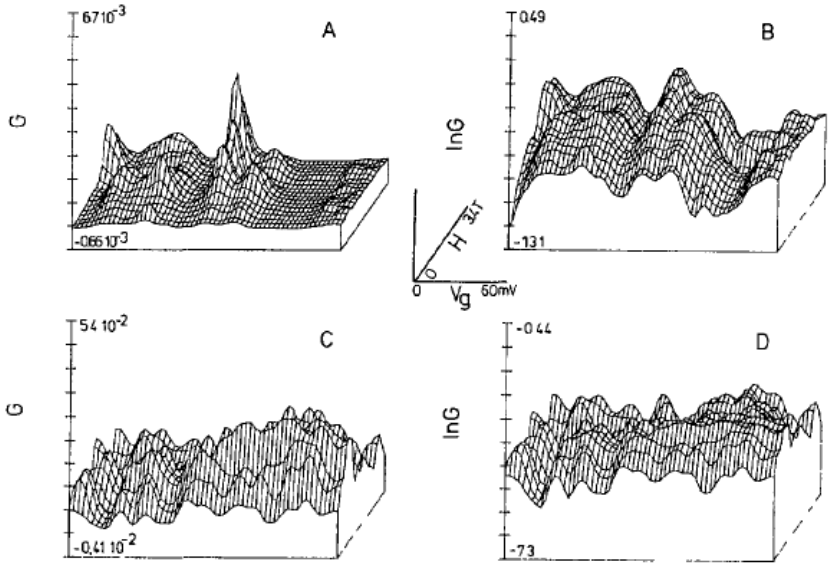

FIGURE 5.6 – Conductance as a function of gate voltage V_g and field H in a 3D plot for a GaAs :Si wire. Low conductances give non-ergodic conductance fluctuations (panel A linear scale and B log scale). Moderate conductances give ergodic conductance fluctuations (panels C and D). Taken from [18].

On the experimental side, several groups have reported reproducible conductance fluctuations (CF) in graphene [20]-[25]. They have observed CF in transport measurements [20]-[24] and also by scanning probe microscopy [25]. In transport measurements the fluctuations have been used as electron thermometer [23] and also to resolve spin transport in graphene [24]. K. Kechedzhi *et. al.* in [23] have proposed a method to measure the temperature of electrons in a mesoscopic conductor through the correlation function of UCF. From energy dependent fluctuations measured at different temperatures the correlation energy can be extracted, which is proportional to k_BT with T the electron's temperature (if the Thouless energy $E_{Th} < K_BT$). Lundeberg *et. al.* have reported in [24] that the application of a magnetic field produces a Zeeman splitting of conductance fluctuations that is reflected in an offset in gate voltage of spin-up and spin-down conductances. This allows one to distinguish each spin contribution in CF.

On the scanning probe microscopy side, Berezovsky *et. al.* have reported reproducible CF versus scatterer position. When a charged tip is near the surface of graphene, an image charge is created that acts as a movable scatterer. An image of the sample conductance vs. tip position provides a spatial "fingerprint" that is unique to the arrangement of scatterers at a given Fermi energy.

The experiments showed in the following represent the first complete analysis of CF in graphene. We study their correlation and amplitude as a function of Fermi energy and magnetic field for a monolayer and a bilayer graphene. These two systems with similar resistivities and mean free paths present different diffusion coefficients due to their different dispersion relations. Taking advantage of the possibility of tuning the Fermi energy in graphene, we measure conductance fluctuations at different Fermi energies, finding specificities for the monolayer and bilayer. We have also studied second order conductance fluctuations, which provide a probe of Coulomb interaction and screening, an important issue in graphene. In the following, I will discuss the correlation functions and the amplitude of fluctuations for magnetic field dependent and energy dependent CF. I will also discuss in detail experiments on second order CF, which constitute a first measurement in a diffusive mesoscopic system.

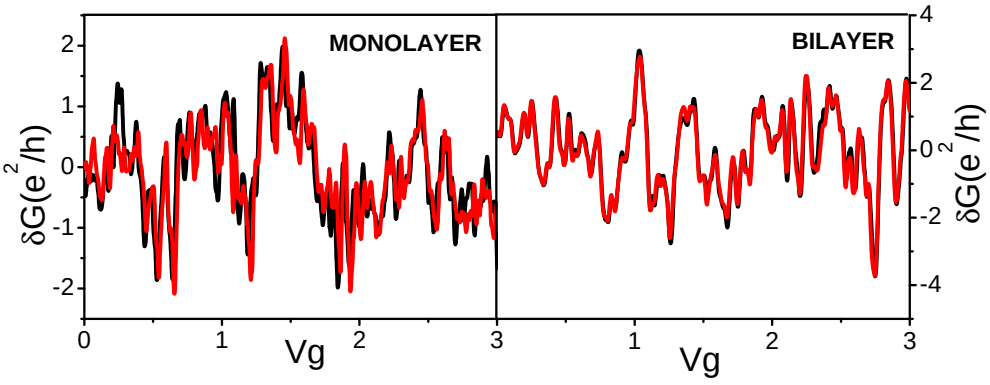

FIGURE 5.7 – Reproducible conductance fluctuations as a function of the gate voltage for the monolayer and bilayer graphene taken at $67mK$. An excitation current of 100nA was used.

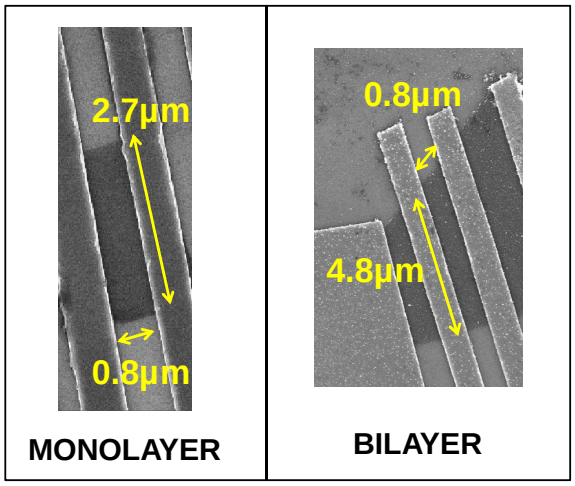

FIGURE 5.8 – SEM images of the monolayer and bilayer graphene measured.

5.3 Correlation functions of conductance fluctuations and their dependence on diffusion coefficient

Figure 5.7 shows reproducible conductance fluctuations measured for the monolayer and bilayer graphene as a function of gate voltage, far from the Dirac point (charge neutrality point CNP) at $T = 60mK$. At first sight they look alike, but it is only through the correlation function that a difference is revealed based on the different physics of transport in these two systems. Figure 5.8 shows SEM images of the two samples measured [2]. In the theory of mesoscopic diffusive samples, the characteristic energy scale entering in the correlation function for energy dependent conductance fluctuations is the Thouless energy if ($T < E_{Th}$). As mentioned before, complete phase randomization is achieved in the sample when there is a shift of the Fermi energy larger than E_c (or E_{Th} the Thouless energy). This characteristic energy is related to the time scale in which electrons diffuse across the sample and become sensitive to its boundaries (τ_D).

2. Contact resitances for these samples were : 200Ω for the monolayer and 20Ω for the bilayer as is specified in the preceding chapter.

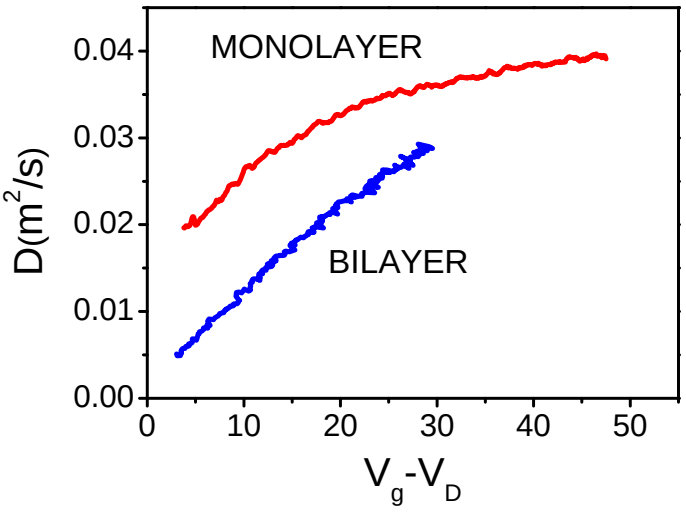

FIGURE 5.9 – V_g dependence of the diffusion coefficient calculated from $D = v_F^2 \tau_{tr}/2$. V_g dependence of τ_{tr} was extracted from magnetoresistance measurements shown in chapter 4.

It is defined in terms of the diffusion coefficient, $E_c = \hbar D/L_{min}^2$ where L_{min}^2 is the area where quantum interferences occur and $L_{min} = min(L, L_T, L_\phi)$ with L the length of the sample, $L_T = \sqrt{\hbar D/k_B T}$ the temperature characteristic length and L_ϕ the phase coherent length. The diffusion coefficient is defined as $D = v_F l_{tr}/d = v_F^2 \tau_{tr}/d$ (v_F is the group velocity of the electrons' wave function at the Fermi level, d is the dimension of the system and τ_{tr} is the time that takes an electron before being backscattered).

For magnetic field dependent fluctuations, complete phase randomization is achieved when $B > B_c = \phi_0/S$ where S is the surface of the sample perpendicular to the magnetic field. S is given by $L_{min} W_{min}$ with $W_{min} = min(W, L_T, L_\phi)$.

As was mentioned in the introduction, near CNP monolayer graphene has a linear dispersion relation $E = \hbar v_F k_F$ with a constant Fermi velocity, while bilayer graphene has a quadratic dependence on k_F, $E = \hbar^2 k_F^2/2m^*$ ($m^* = 0.03 m_e$) with a Fermi velocity that depends on the Fermi level, $v_F = \hbar k_F/m^*$. The diffusion coefficient has also a very different gate voltage dependence in the monolayer and bilayer graphene as is shown in figure 5.9. This can be seen through the density of states. Diffusion coefficient can be written as $D = \sigma/\left(e^2 \rho(E_F)\right)$, where the density of states ρ is linear in k_F [3] for the monolayer and it is a constant for the bilayer ($\rho_{ML} = \frac{4}{h v_F} k_F$ and $\rho_{BL} = \frac{2m}{\hbar^2 \pi}$). If we consider that conductivity σ goes like k_F^2 (within a correction of $Ln^2(k_F)$ [4]), we have different dependencies for the diffusion coefficient in the monolayer and bilayer, $D_{ML} \propto k_F \propto \sqrt{V_g}$ and $D_{BL} \propto k_F^2 \propto V_g$, as can be checked in figure 5.9.

In order to compare with the theory for diffusive mesoscopic systems, correlation functions were calculated. Experimental data consisted of conductance measurements taken as a function of the gate voltage or magnetic field. In the case of the gate voltage dependent fluctuations, sweeps of 3V were taken varying the average electronic density at each sweep using the gate voltage. As can be seen in figure 4.13 a variation of $3V$ corresponds to a variation of maximum 5% in electronic density n far from Dirac point ; near the Dirac point, the electronic density is constant. A variation of $3V$ correspond to a variation in energy of $dE = 15 V_g^{-1/2} dV_g meV$, which is maximum $\sim 45 meV$. This is big enough compared to the average Thouless energy, which is $0.17 meV$. In conclusion, a sweep in gate voltage of 3V gives us a good enough statistics and an electronic density almost constant. For the magnetic field dependent fluctuations,

3. Far from the charge neutrality point
4. The origin of this correction is detailed in the first chapter

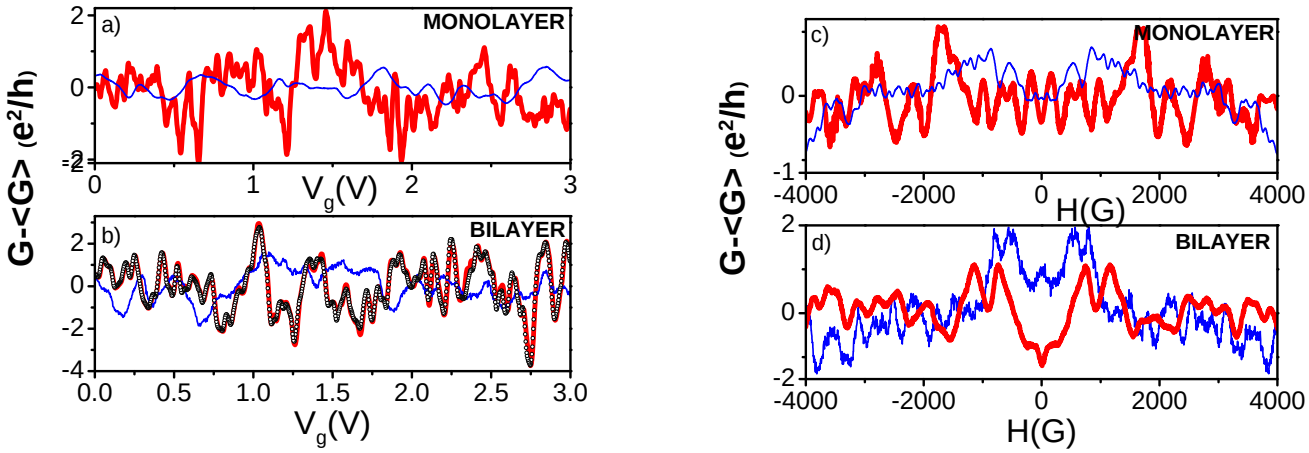

FIGURE 5.10 – Red thick curves were measured around $V_g = V_0$ the Dirac point. Thin blue lines correspond to measurements far from Dirac point, $V_g - V_0 = 40.5V$ in the monolayer and $V_g - V_0 = 15V$ in the bilayer. The Dirac point is at $V_g = 15.5V$ for the monolayer and at $Vg = -6V$ for the bilayer. Panel b) shows the reproducibility of conductance fluctuations.

sweeps were made from $-0.4T$ to $0.4T$ also at different average electronic densities. The conductance is symmetric in magnetic field as expected for a two probe measurement, due to time-reversal invariance. Figure 5.10 shows some sets of data analyzed. A line was subtracted to remove the average conductance.

The correlation field and gate voltage was determined in the following way. We calculated the discrete Fourier power spectrum of the fluctuations as a function of k, the conjugate variable of B or Vg for each set of field or gate voltage data corresponding to a given average carrier density. The Fourier power spectrum is the average square of the modulus of the Fourier transform. It gives us the correlation function of fluctuations in Fourier space (thanks to the property of Fourier transform for a convolution of two functions $\mathcal{F}(f \star f) = |\mathcal{F}(f)|^2$).

Each data set yielded exponential-like functions which are shown in figure 5.11. They correspond in the direct space to a Lorentzian correlation function,

$$\mathcal{F}^{-1}\left\{e^{-x_c|k|}\right\} = 2x_c/\left(x_c^2 + 4\pi V g^2\right).$$

Correlation energies and fields x_c were deduced from the exponential decay $exp(-kx_c)$ at low k of the Fourier power spectrum. From the semilog representation in figure 5.11 we have $x_c = (ln10 * slope)/2\pi$. The relation between the correlation energy E_c and the correlation gate voltage V_c for the monolayer is given by the expression

$$E_{cML} = \hbar v_F \sqrt{\frac{\pi C}{4eV_g}} V_c,$$

since $E = \hbar v_F \sqrt{\pi C V_g / e}$ (C is the capacitance per unit area). In the case of the bilayer, the correlation energy is given by

$$E_{cBL} = \frac{\hbar^2 \pi C}{2em^*} V_c$$

where m^* is the effective mass in the bilayer $m^* = 0.03m_e$.

We now compare the variations of E_c and B_c to the predictions E_c^{theory} and B_ϕ. As it was already

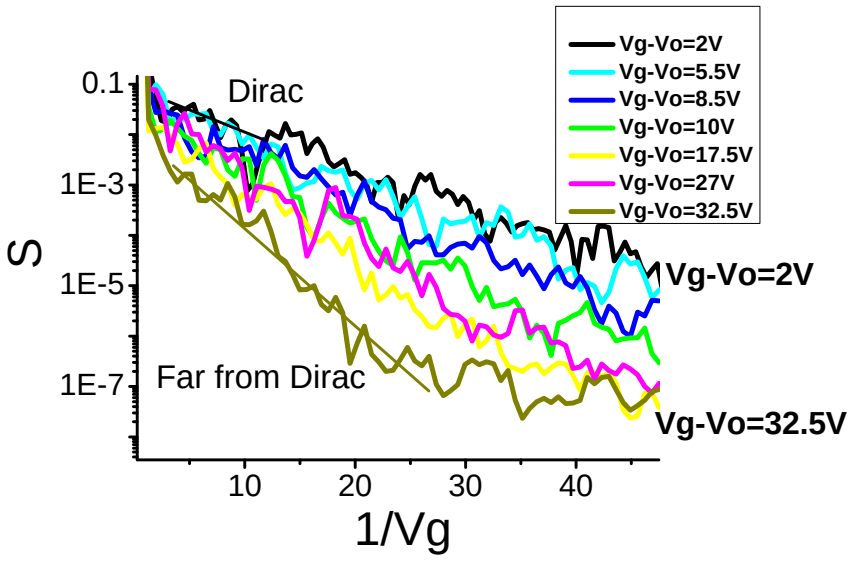

FIGURE 5.11 – Fourier power spectrum of conductance fluctuations at different gate voltages in a semilog scale. The correlation voltage or magnetic field is extracted from the exponential fit at small ΔV_g^{-1}

mentioned these quantities depend on the diffusion coefficient,

$$E_c^{theory} = \frac{\hbar D}{L_{min}^2} \qquad B_\phi = \frac{\Phi_0}{L_{min} W_{min}} \qquad where \qquad L_{min} = min(L, L_T, L_\phi) \qquad W_{min} = min(W, L_T, L_\phi)$$

L_{min} and W_{min} correspond to the typical longitudinal and transverse lengths of interfering trajectories. $L_T = \sqrt{\hbar D/k_B T}$ is the thermal coherence length and L_Φ the phase coherent length. In the density range investigated L_T varies between $1.2\mu m$-$1.7\mu m$ for the monolayer and between $0.7\mu m$-$1.4\mu m$ for the bilayer. This calculation as well as the one for E_{Th} and B_Φ was done using the diffusion coefficient $D = v_F^2 \tau_{tr}/2$ (Figure 5.9), where $v_F = \hbar k/0.035 m_e$ for the bilayer and $v_F = 10^6 m/s$ for the monolayer. τ_{tr} (and v_F in the case of the bilayer) was extracted using the magnetoresistance measurements shown in chapter 4. They provide accurate values for τ_{tr} near the charge neutrality point. Having calculated L_T, we could compare this length with the dimensions of the samples shown in figure 5.8 and we determined which of these lengths was the smaller length L_{min} (and W_{min}). We conclude that $W_{min} = L_T$ and $L_{min} = L$ and therefore $E_c^{theory} = E_{Th}$.

To verify that the correlation energy and magnetic field have the expected dependence on the gate voltage, we have plotted along with the experimentally deduced E_c and B_c, the E_{Th} and $\Phi_0/(LL_T)$ deduced from the diffusion coefficient extracted from magnetoresistance measurements shown in chapter 4. As is shown in figure 5.12 the correlation energy extracted from the experimental data follows $E_c = 5E_{Th}$. The correlation field follows $B_c = 6\Phi_0/(LL_T)$ for the monolayer and $B_c = 4\Phi_0/(LL_T)$ for the bilayer as shown in figure 5.13.

These dependencies can be understood through the diffusion coefficient, represented in Figure 5.9. Using the Drude formula, $\sigma = \left(e^2 v_F^2/2\right)\tau\rho(E_F)$ the diffusion coefficient can be written in terms of the density of states at the Fermi level $\rho(E_F)$, which has a different dependence for the monolayer and bilayer graphene.

$$D = \sigma/\left(e^2\rho(E_F)\right).$$

In theory, for a perfect sample, the density of states is independent of V_g for the bilayer and it goes like

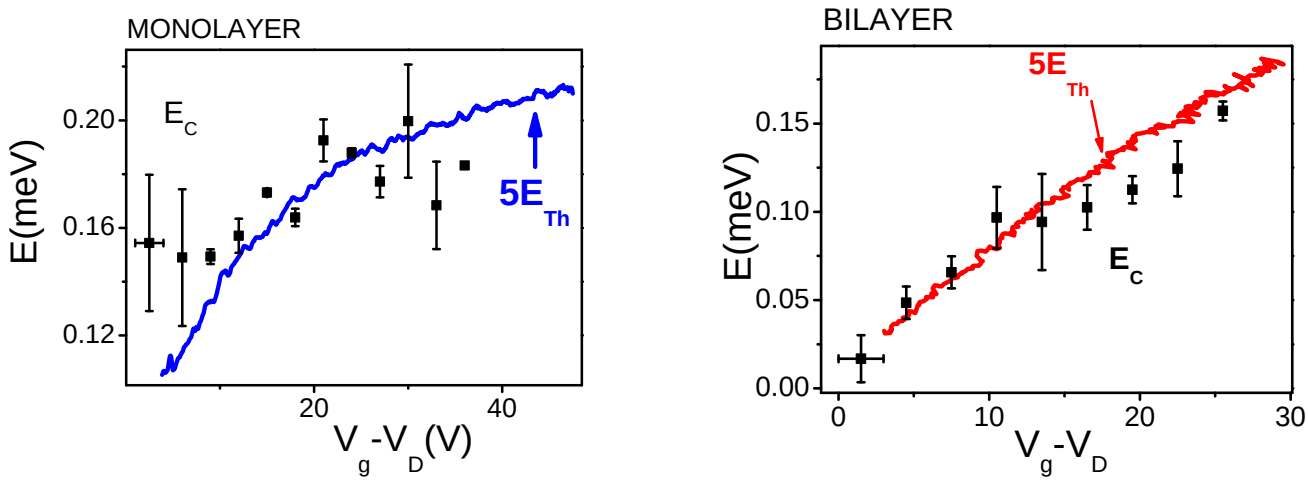

FIGURE 5.12 – Correlation energy for the conductance fluctuations in the monolayer and bilayer. Dots represent the correlation energies extracted from the data. Error bars represent the uncertainty in fit parameters and horizontal bars the 3V range used to calculate correlation energies. Continuous lines represent $5E_{Th}$, which was calculated using experimental data for τ_{tr} shown in chapter 4.

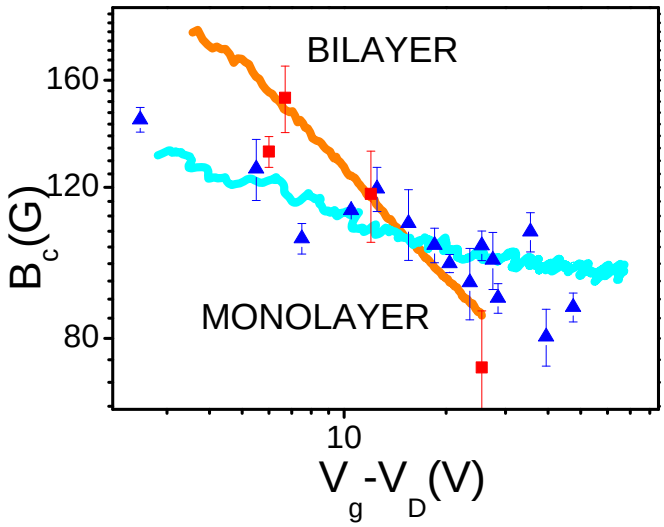

FIGURE 5.13 – Correlation magnetic field for the monolayer (triangles) and the bilayer (squares). Continuous lines are $B_\Phi = 6\Phi_0/(L_T L)$ for the monolayer and $B_\Phi = 4\Phi_0/(L_T L)$ for the bilayer

$\sqrt{V_g}$ for the monolayer,

$$\rho_{ML}(E_F) = \frac{2}{\hbar v_F \pi} k_F = \frac{2}{\hbar\sqrt{\pi} v_F}\sqrt{n} \qquad \rho_{BL}(E_F) = \frac{2m}{\hbar^2\pi}$$

(where $n = \frac{\epsilon_r \epsilon_0}{ed} V_g$). We have found that the conductivity varies with gate voltage like

$$\sigma \approx \frac{2}{\pi}\frac{e^2}{h}\frac{nln^2\left(R\sqrt{\pi n}\right)}{n_{imp}}$$

where n_{imp} is the density of impurities in graphene. If we approximate the variation of σ as linear, we can check in figure 5.12 that

$$E_{cML} \propto \sqrt{V_g} \qquad and \qquad E_{cBL} \propto V_g.$$

Similarly, the correlation magnetic field $B_c \propto \Phi_0/(LL_T)$ is expected to vary like

$$B_{cML} \propto \frac{1}{\sqrt{D_{ML}}} \propto \frac{1}{V_g^{1/4}} \qquad and \qquad B_{cBL} \propto \frac{1}{\sqrt{D_{BL}}} \propto \frac{1}{V_g^{1/2}}$$

as can be checked in figure 5.13.

5.4 Amplitude and non-ergodicity of conductance fluctuations in graphene

Figure 5.14 shows the variance δG_1 of energy dependent and magnetic field dependent conductance fluctuations in the monolayer and bilayer graphene. The amplitude of the V_g-dependent conductance fluctuations is larger near the Dirac point. In contrast, the B-dependent fluctuations do not depend significantly on the density n for the monolayer. Thus, conductance fluctuations in graphene are non ergodic [5]. This might be a consequence of the spatial inhomogeneities of n close to Dirac point. In a good conductor (large g), changing the Fermi energy is equivalent to changing the disorder configuration, and induces Gaussian conductance fluctuations of order e^2/h. In graphene on the other hand, it has been shown [8] that near Dirac point the system breaks into conducting puddles of electrons and holes, and transport takes place along an intricate percolating network of these n- and p-type regions. Indeed, strong fluctuations of the local charge density and conductivity near Dirac point can be modeled by a network of n-type and p-type regions with finite transparency [7].

Rycerz *et. al.* [5] have found numerically that the variance of conductance fluctuations due to variations in trajectories in the sample are enhanced when changing disorder. They do not find such an enhancement for fluctuations due to wavefunction phase shifts. Figure 5.15 shows the calculated variance of conductance as a function of disorder strength for sample to sample fluctuations and energy dependent fluctuations. A large enhancement appears of the sample to sample fluctuations above the UCF value. In contrast, the variance of the energy dependent fluctuations doesn't show this enhancement and agrees with the UCF prediction. The origin of this result has been understood as a percolation transition. The presence or absence of a percolating trajectory produces large sample to sample fluctuations in the conductance that can increase with increasing k_F or ξ (the impurity range) as has been observed in simulations.

As remarked by Rycerz *et. al.* sample to sample fluctuations contain contributions from variations in phase shifts but mostly from variations in trajectories, which gives rise to an enhancement of conductance fluctuations. On the other hand, in energy dependent fluctuations variation in phase shifts gives the dominant contribution, which results in conductance fluctuations that don't get altered with changing disorder. In our experiment, when we change the gate voltage near Dirac point, we change not only

5. We believe that both B-dependent conductance fluctuations and V_g dependent conductance fluctuations have their origin in interference between electronic trajectories

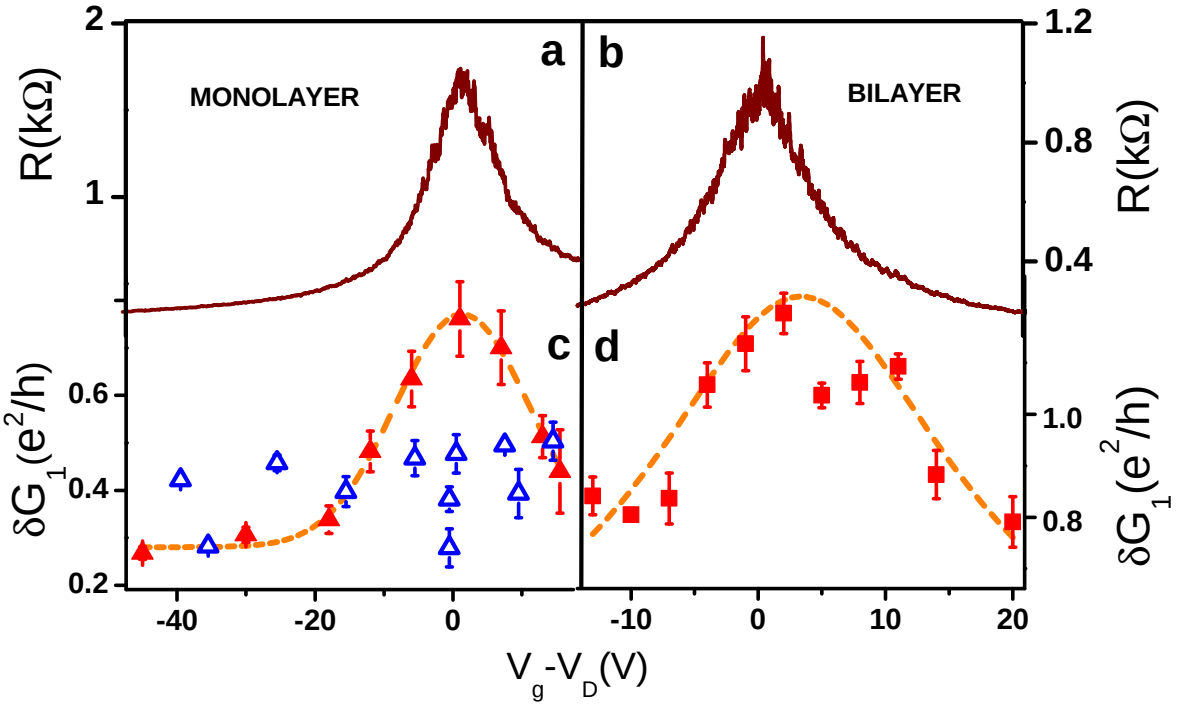

FIGURE 5.14 – Amplitude of the conductance fluctuations compared to the gate voltage dependent resistance. The Vg-dependent fluctuations (filled symbols) are larger near the Dirac point for both the monolayer and bilayer graphene(panels c) and d)). Error bars are the standard deviation of the difference of two different sweeps, dashed lines are guide for the eyes. The Vg-dependent fluctuation amplitude changes with Vg in a qualitatively similar way as the resistance. The B-dependent conductance fluctuations (open triangles) does not change much with Vg.

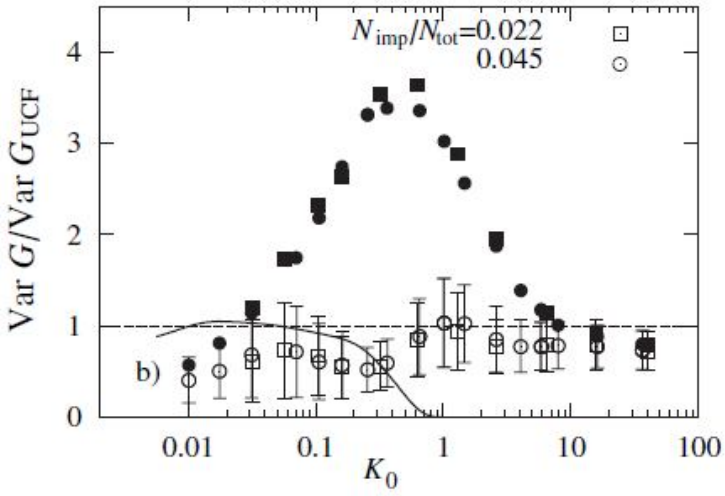

FIGURE 5.15 – Variance of conductance as a function of disorder strenght. Filled symbols give $VarG$ of the sample to sample fluctuations. Open symbols correspond to to the variance of energy dependent fluctuations. Taken from [5]

the Fermi energy (E_F) but also the configuration of puddles of electrons and holes in the sample and thus the percolating trajectories responsible for interferences. We explain our results shown in figure 5.14 considering that energy dependent CF [6] near Dirac point come from percolating trajectories and that magnetic field dependent CF come from variation in phase shifts.

We find that the amplitude of magnetic field dependent CF is $(0.4 \pm 0.1)e^2/h$. Theory predicts [9] $\delta G = 0.7\sqrt{W/L}e^2/h$ when the distance between electrodes is smaller than L_T. This yields $1.2e^2/h$ for the monolayer which is three times the measured value.

Figure 5.16 shows measurements of energy dependent CF at different temperatures. It can be seen that the amplitude of conductance fluctuations is smaller with increasing temperature. We also analyze the dependence of the correlation energy with temperature. At low temperatures the correlation energy is close to the Thouless energy (as expected, the correlation energy at low temperatures is fixed by the Thouless energy). When temperature increases, the correlation energy follows as expected, K_BT. This differs from the results of Kechedzhi *et al.* who found that in the regime $k_BT >> E_{Th}$ the correlation energy follows αk_BT with $2.7 < \alpha < 2.9$ for nanoribbons. The discrepancy with this result might be due to the geometry of our sample, which consists of a wide junction instead of the nanoribbon investigated by Kechedzhi *et al.* (see figure 5.8).

Figure 5.17 and 5.18 show the histograms of conductance for gate voltage dependent and magnetic field dependent conductance fluctuations. Histograms were made from different sets of data (two to four sets of data each time) like those showed in figure 5.10. In the case of Vg dependent conductance fluctuations histograms were calculated from data over a range of 6V near the Dirac point (2000 data points) and a range of 12 V far from Dirac point (4000 data points). We had good statistics given that the correlation energy ranges from $0.10meV$ to $0.21meV$ (near and far Dirac point respectively) and a change of $1V$ in gate voltage corresponds to a change of $\sim 15meV$ in energy, which is ten times bigger. For conductance fluctuations in the monolayer as a function of magnetic field the calculation was made from data taken at three different voltages near and far from Dirac point (12000 data points). In the case of the bilayer

6. Only those generated by a phase shift by the gate voltage

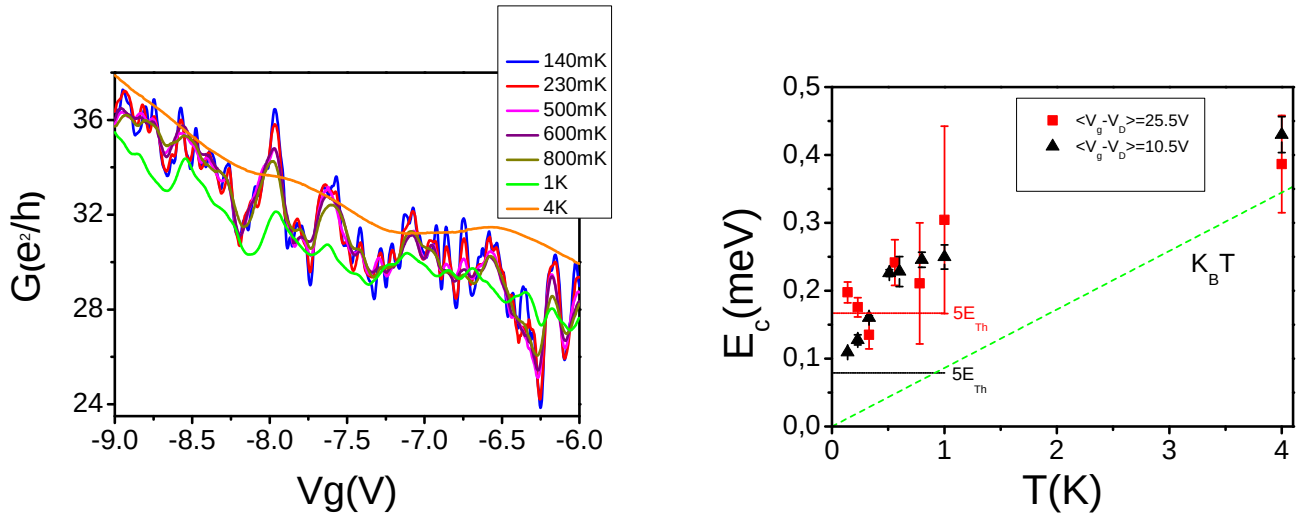

FIGURE 5.16 – Conductance fluctuations measured for different temperatures in the bilayer near the Dirac point. Fluctuations' amplitude is smoothed with increasing temperature as expected (left). Right : Temperature dependence of the correlation energy. Correlation energy is represented for data taken far from the Dirac point (red squares, $24V \leq V_g - V_D \leq 27V$) and at an intermediate gate voltage (black triangles $9V \leq V_g - V_D \leq 12V$). Continuous horizontal lines represent Thouless energy in each region. $k_B T$ is represented as a pointed line for reference. (Correlation energy was calculated from experimental data using the capacitance model, contrary to the experimental correlation energy shown in figure 5.12 which was calculated using magnetoresistance measurements. Magnetoresistance data was not available to calculate the correlation energy at different temperatures.)

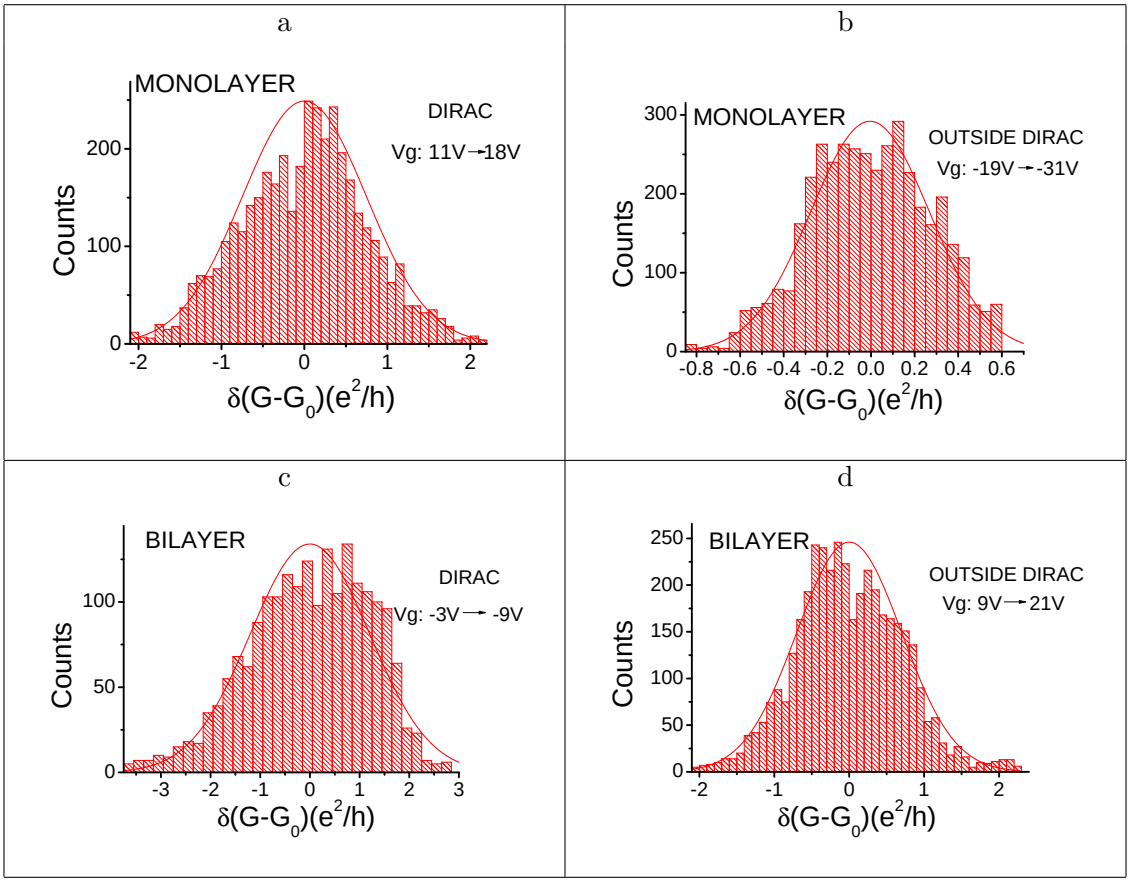

FIGURE 5.17 – Histograms of the gate voltage dependent conductance fluctuations for the monolayer with a Dirac point at 15.5V (panels (a) and (b)) and bilayer graphene with a Dirac point at -6V (panels (c) and (d)). In all the cases they follow a Gaussian distribution (continuous line)

calculations were made with data at a single gate voltage value (4000 data points). In all the cases they follow a gaussian distribution, contrary to the log-normal distribution characteristic of a system going through an insulating transition. Figure 5.19 shows the difference between a Gaussian and a log-normal distribution. In a log normal distribution,

$$P(f(x))\frac{df(x)}{dx}dx = P(\ln x)\frac{d\ln x}{dx}dx$$

with $f(x) = \ln(x)$ and P a Gaussian distribution. This gives the expression shown in the top of figure 5.19. An example of the distribution of fluctuations in an insulating system is shown in figure 5.20. It corresponds to a 1D GaAs device.

5.5 Weak localization

As was said at the beginning of this chapter, in a quantum coherent system, electron waves that propagate in opposite directions, form a loop and interfere at the point of intercept, have a zero phase difference that is independent of disorder. Upon averaging over disorder these pairing trajectories give rise to a negative correction of the conductance called the weak localization correction. However, these time reversed trajectories acquire a phase in the presence of a magnetic field, which results in a positive magnetoconductance. The bilayer presents such positive magnetoconductance as a signature of weak localization. In the monolayer on the other hand, because the Berry phase is π instead of 2π like in the

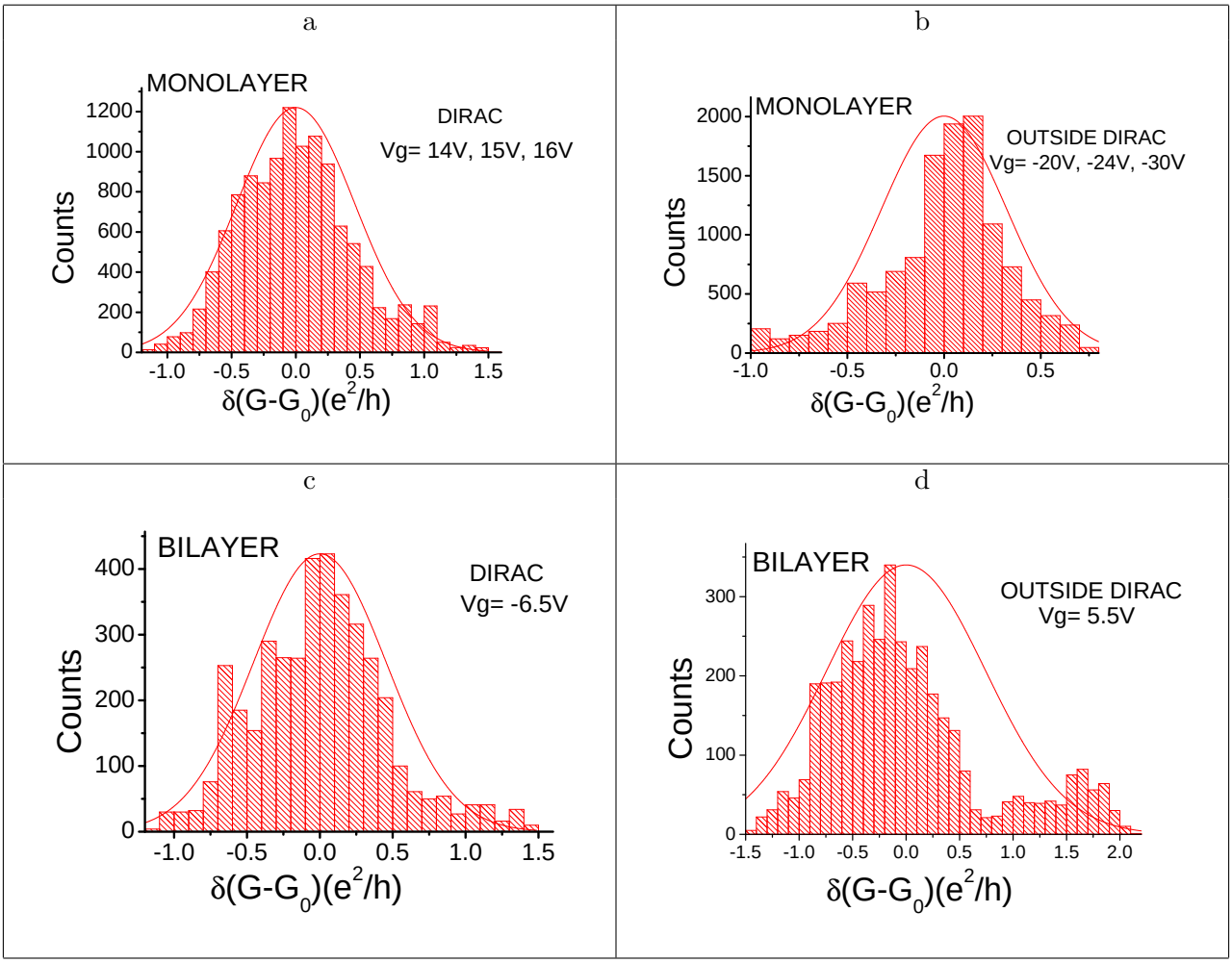

FIGURE 5.18 – Histograms of magnetic field dependent conductance fluctuations for the monolayer with its Dirac point at 15.5V (panels (a) and (b)) and bilayer graphene with its Dirac point at -6V (panels (c) and (d)). For the bilayer graphene the statistics are poorer.

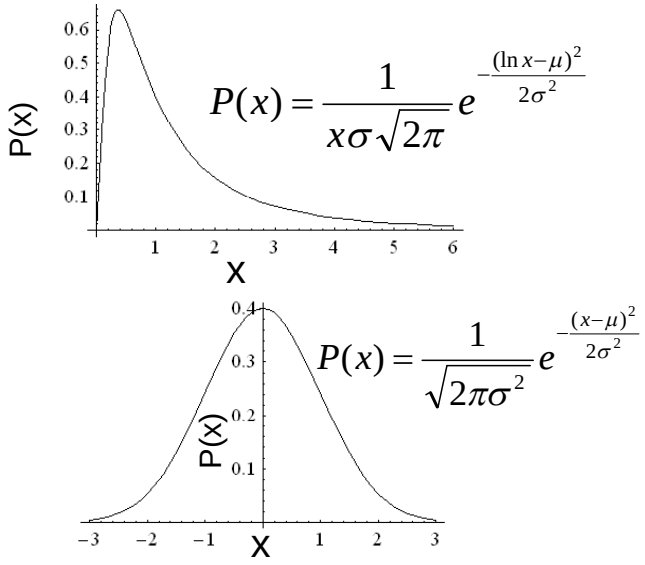

FIGURE 5.19 – Log-normal distribution (top) and gaussian distribution (bottom) with $\sigma = 1$ and $\mu = 0$.

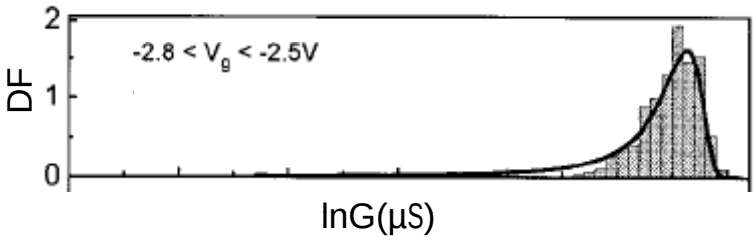

FIGURE 5.20 – Distribution function (DF) for conductance fluctuations in a 1D GaAs device. (Taken from [26])

bilayer, backscattering is suppressed and there is a positive correction of the conductivity called **weak antilocalization** correction, leading in the presence of a magnetic field to a negative magnetoconductance.

In graphene (and the bilayer) weak localization has the remarkable feature that it is sensitive not only to inelastic processes (phase breaking associated to τ_ϕ) but also to elastic scattering mechanisms like intervalley scattering (τ_i), associated to sharp defects like the edges of the sample, that are able to scatter electrons between the two valleys and intravalley scattering (τ_*). The following formula shows how magnetoconductance $\Delta\sigma(B) = \sigma(B) - \sigma(B=0)$ in the monolayer and the bilayer is controlled by the inelastic and elastic rates τ_ϕ^{-1}, τ_i and τ_*,

$$\frac{\pi\hbar}{e^2}\Delta\sigma(B) = \mathcal{F}\left(\frac{\tau_B^{-1}}{\tau_\phi^{-1}}\right) - \mathcal{F}\left(\frac{\tau_B^{-1}}{\tau_\phi^{-1}+2\tau_i^{-1}}\right) \mp 2\mathcal{F}\left(\frac{\tau_B^{-1}}{\tau_\phi^{-1}+\tau_i^{-1}+\tau_*^{-1}}\right). \tag{5.8}$$

(The third term is negative for the monolayer and positive for the bilayer). In the case of the monolayer negative magnetoconductance and thus antilocalization is determined by the negative third term. If there is no intervalley nor intravalley scattering ($\tau_i, \tau_* \to \infty$) the first two terms of 5.8 cancel each other and $\Delta\sigma(B)$ is controlled by the third term, resulting in antilocalization. If on the contrary, there is strong intravalley and intervalley scattering (small τ_i and τ_*) both negative terms are suppressed and the first term dominates which gives rise to a positive magnetoconductance and thus electron localization. What favors antilocalization in graphene are then small ratios τ_ϕ/τ_* and τ_ϕ/τ_i. This can be achieved by increasing the temperature which decreases τ_ϕ or lowering the carrier density which increases τ_i. Antilocalization is destroyed if there is intravalley scattering ($\tau_i >> \tau_\phi >> \tau_*$). However, if intervalley scattering is possible ($\tau_i \sim \tau_\phi >> \tau_*$) then weak localization occurs. Figure 5.21 shows magnetoresistance curves of a monolayer taken at different gate voltages and at different temperatures. It is seen that near Dirac point where there is few intervalley scattering (small τ_i^{-1}) antilocalization is strong and gets more pronounced with increasing temperature as expected.

In the case of the bilayer, weak localization always occurs due to the positive sign of the third term of 5.8. If there is no intervalley nor intravalley scattering, the first two terms of 5.8 cancel each other and magnetoconductance is reduced to the third term which results in the conventional form of weak localization (positive magnetoconductance). Figure 5.21 shows the average magnetoconductance of a bilayer near Dirac point at different temperatures. It is seen that weak antilocalization is never present in contrast to graphene.

We have studied weak localization in our samples. Figure 5.22 shows reproducible conductance fluctuations ($\sigma(V_g, B) - \sigma(V_g, B=0)$) near Dirac point and far from Dirac point and the average of conductance fluctuations in these two regions. We see that weak localization is present and it seems to be more pronounced far from Dirac point. However, the few curves we disposed of (only five) impeded us to do a valuable conclusion. In this five curve avearge we didn't see any trace of antilocalization in graphene. Figure 5.23 shows reproducible conductance fluctuations as a function of the magnetic field for the bilayer. We have averaged 5 curves at different electronic densities. We can see a positive magnetoconductance signature of weak localization that gets smoothed with increasing temperature. Figure 5.23 shows data from a second junction on the same sample. Average over different curves shows also the presence of weak localization.

5.6 Second order nonlinear conductance fluctuations

In a mesoscopic sample the disorder potential breaks spatial inversion symmetry which gives rise to the existence of a non-zero second order conductance (mesoscopic rectification). There is then a non-linear term that appears in the I-V relation, $I = G_1 V + G_2 V^2$. This non-linear term was predicted theoretically [10] and measured experimentally [11] in the 80's and more recently it has been proved theoretically that it gives information about e-e interactions in the sample both in chaotic [12] and diffusive systems [13]. Second order conductance is characteristic of systems lacking spatial inversion symmetry and they stem

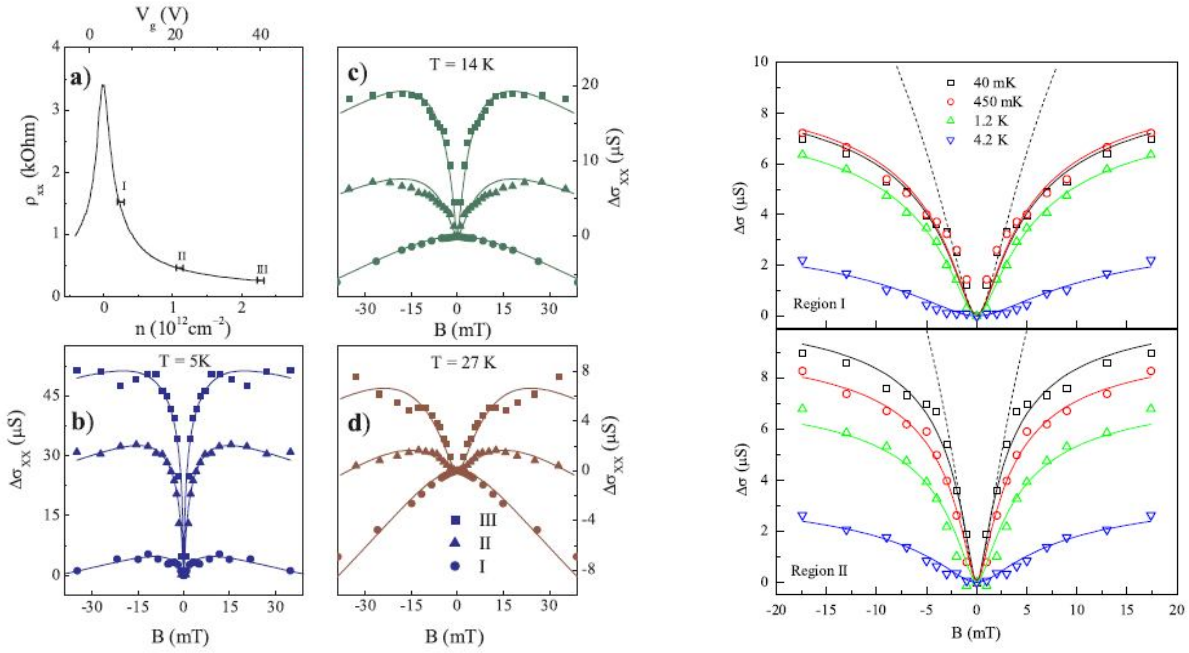

FIGURE 5.21 – Left : a) Resistivity as a function of the carrier density for a MONOLAYER. b), c) and d) show the evolution of the average magnetoconductance at different electronic density regions (indicated by bars in a)) and different temperatures. Solid curves correspond to fits of equation 5.8. Taken from [83]. Right : Average magnetoconductance for the BILAYER near Dirac point at different temperatures. Dashed curves are fits using only the first term of equation 5.8 and solid lines are fits using the first two terms. Taken from [84]

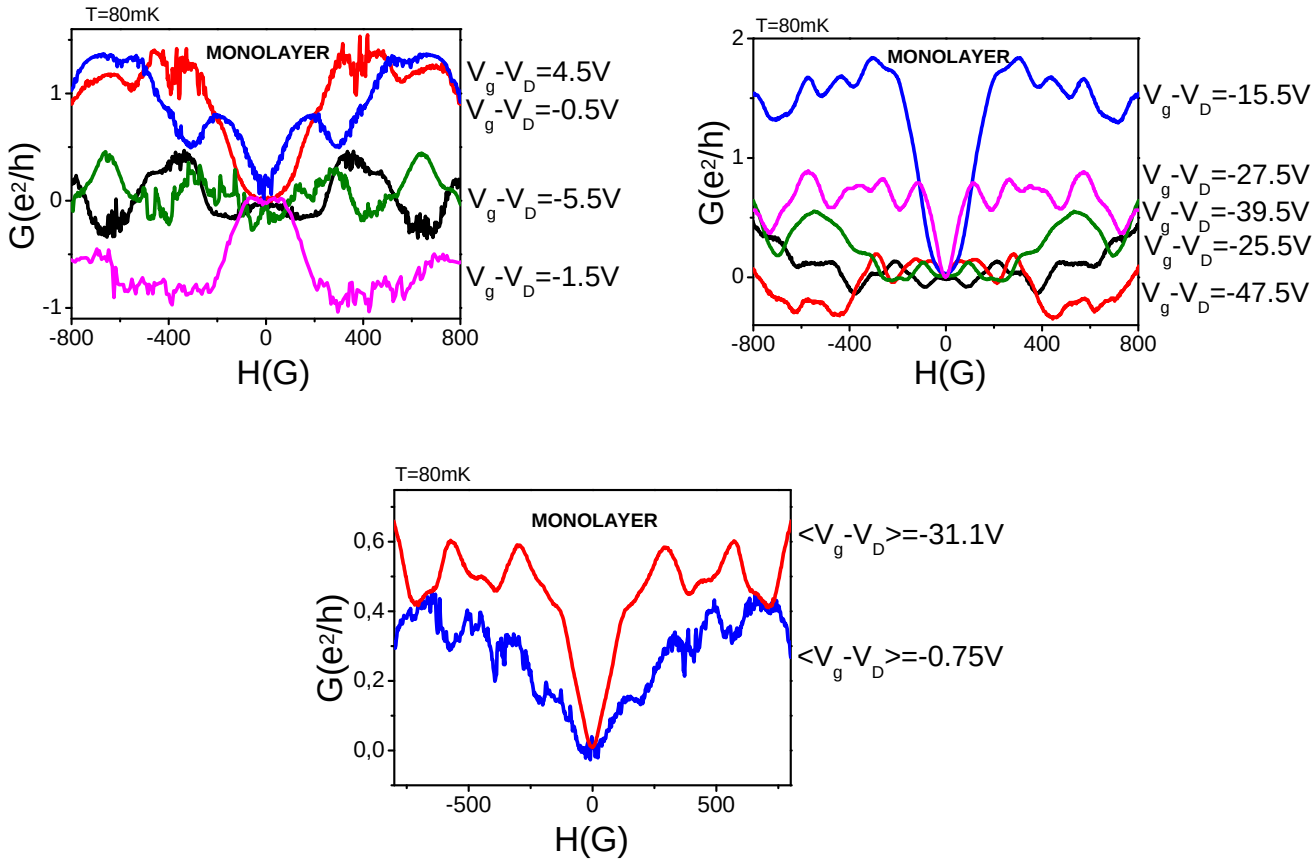

FIGURE 5.22 – Top : Magnetoconductance curves $(G(B) - G(B = 0))$ for the monolayer near Dirac point and far from Dirac point. Bottom : Averaged curves.

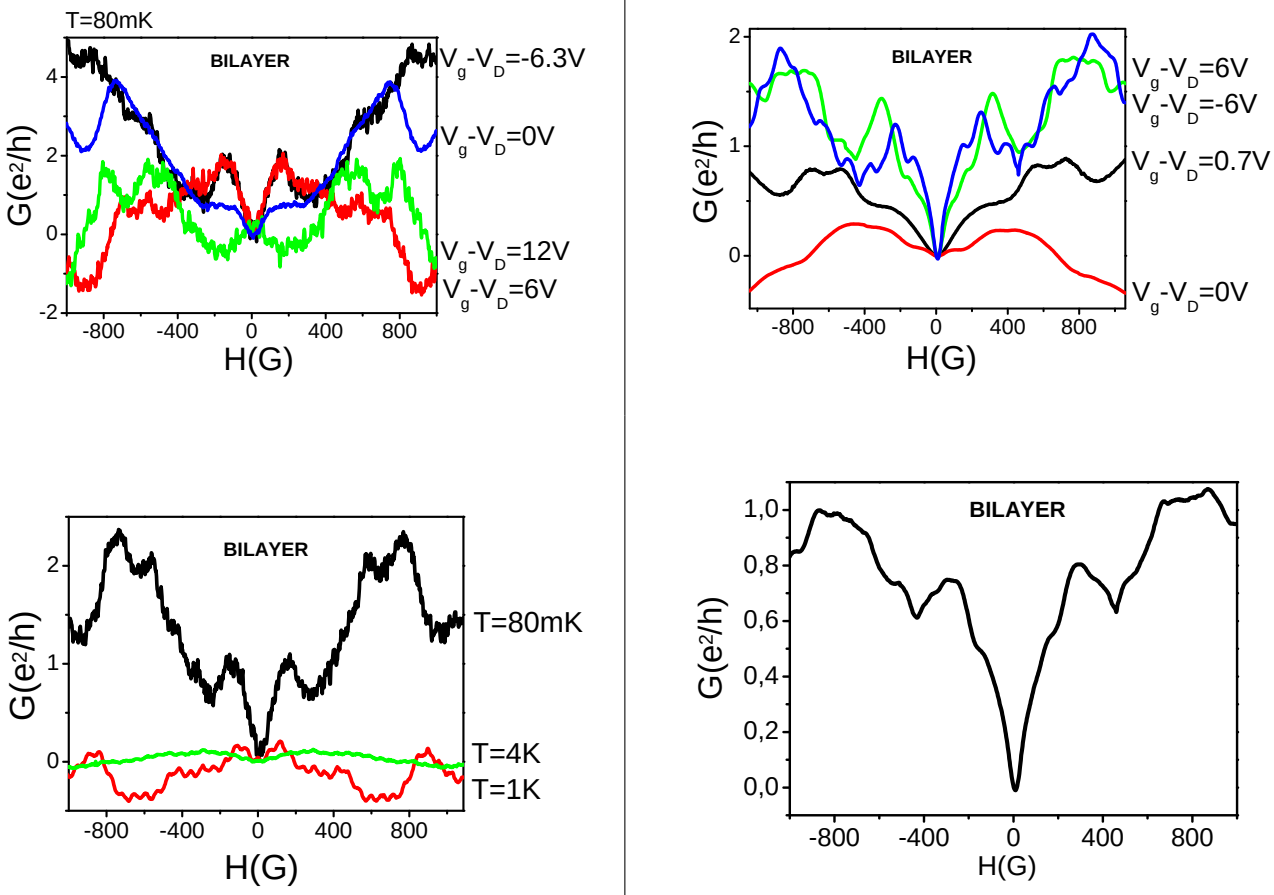

FIGURE 5.23 – Left : Magnetoconductance curves ($G(B) - G(B = 0)$) for the bilayer at different gate voltages (near and far Dirac point). Average of these curves is shown below with the average of sets of three curves taken at 1K and 4K. Right : Magnetoconductance curves for a second junction in the same sample. Below is shown the average of these curves.

from current-induced changes in the carrier density, which in turn, via Coulomb interaction, modify the electrostatic potential landscape, thereby inducing a current-dependent conductance.

A mesoscopic graphene sample presents no spatial inversion symetry (because of the random position of impurities) that allows the observation of the second order conductance, which can be used as a probe of screening and interactions, a subject of great interest in graphene.

5.6.1 Physical origin of the non linear conductance

When a bias voltage is applied to the sample, charges are accumulated around impurities and sample edges. The change of local electronic density is proportional to the injected current through a certain function $h(\vec{r})$, $dn(\vec{r}) = h(\vec{r})I$ and modifies locally, via Coulomb interactions, the electrostatic potential throughout the sample by $dU_{dis}(\gamma_{int}, V)$ where γ_{int} quantifies e-e interactions. Electrons passing in the neighborhood of the impurity feel the variation of the electrical potential and are dephased by [27]

$$d\phi \sim \frac{1}{\hbar}\int dU_{des}\big(\vec{r}(t)\big)dt$$

This expresses the fact that the electronic phase accumulated along the trajectory is very sensitive to any change in the disorder. This dephasing will have a signature in conductance fluctuations through a non linear contribution that is bias dependent,

$$G = G\big[U_{eq}\big] + dG\big[dU_{dis}(\gamma_{int}, V)\big]$$

where U_{eq} is the potential in zero bias. Linear conductance is then given by

$$G_1 = G\big[U_{eq}(\vec{r})\big]$$

and second order conductance,

$$G_2 = \left(\frac{\partial dG\big[dU_{dis}, V, \gamma_{int}\big]}{\partial V}\right)_{V=0}$$

If a magnetic field B is applied, dipoles formed around impurities rotate in a different direction depending on the sign of magnetic field. More generally, the electronic density in the sample $dn(B)$ has an odd component in magnetic field which changes locally the potential $dU_{dis}(\gamma_{int}, V)$. As a consequence, in the presence of interactions, G_2 acquires both an odd and an even component in magnetic field, contrary to the linear conductance G_1 which is symmetric in magnetic field and follows the Onsager relations. The amplitude of these components have been calculated theoretically for a diffusive samples with weak interactions [13] and for a chaotic cavity [12]. For diffusive systems the amplitude of the symmetric and antisymmetric components of G_2 can be written [16] :

$$\delta G_2^S \cong \delta G_1 \frac{e}{E_{Th}} \qquad \delta G_2^{AS}(\Phi) \cong \gamma_{int}\frac{\delta G_1}{g} f\Big(\frac{\Phi}{\Phi_c}\Big)\delta G_2^S \tag{5.9}$$

where $g = \langle G_1 \rangle$ is the average conductance and $\delta G_1 \simeq 1$ the typical amplitude of G_1 fluctuations, both in units of e^2/h. f is a function such that $f(x) = x$ for $x \ll 1$ and $f(x) = 1$ for $x > 1$. $\Phi_C = B_C S$ with B_C the typical scale of conductance fluctuations (this corresponds to a quantum flux through the area defined by the coherent trajectory of electrons in the sample. See equation 5.5). (For a cavity with narrow apertures, $\Phi_C = B_C S/\sqrt{n_t}$ with n_t the number of incoherent electronic trajectories in the cavity [7]). In an open system on the other hand $\Phi_C = B_C S$.

7. $n_t = \tau_{dw}/\tau_{Th}$ with τ_{dw} the time that the electron is in the cavity ($\tau_{dw} = h/(N\Delta)$) and τ_{Th} the coherent time ($\tau_{Th} = h/E_{Th}$)

γ_{int} quantifies e-e interaction and is defined differently by Spivak and Zyuzin and by Sanchez and Büttiker. Spivak and Zyuzin, who considered a weak interaction regime define γ_{int} as :

$$\gamma_{int} = \frac{2\nu dU_{dis}(\vec{r})}{dn(\vec{r})} \ll 1$$

(where ν is the density of states per unit surface) while Sanchez and Büttiker, in a self consistent treatment of Coulomb interaction, define γ_{int} by :

$$\gamma_{int} = \frac{C_\mu}{C} = \frac{1}{1 + C\Delta/2e^2} \tag{5.10}$$

where C_μ is an electrochemical capacitance and C is a geometrical capacitance. C_μ is related to the electronic compressibility $1/C_\mu = 1/C + \Delta/2e^2$ and is defined rigorously in reference [12]. Δ is the average separation between energy levels. According to Sanchez and Büttiker γ_{int} characterizes screening. $\gamma = 0$ correspond to no screening and $\gamma = 1$ to good screening and thus an important e-e interaction. The theory of Sanchez and Büttiker find the good agreement with experiments in quantum dots [14].

The ratio r between the symmetric variance δG_2^S and the antisymmetric variance δG_2^{AS} is predicted to be independent of conductance in ballistic systems. ($\delta G_2^S = \big(e^2/h\big)\big(e/(gE_{Th})\big)$ [15]) but in diffusive systems it should vary like

$$\frac{\delta G_2^{AS}}{\delta G_2^S} = \frac{\gamma_{int}}{g}$$

since $\delta G_2^S = \big(e^2/h\big)\big(e/E_{Th}\big)$. Conductance g is in units of e^2/h. The factor $1/g$ suggests that the field asymmetry should be detectable in systems with low conductance and it should not be observable in metallic mesoscopic samples. We have observed in graphene that r significantly decreases with carrier density, in contrast to ballistic GaAs/GaAlAs rings [16] where r was nearly independent of the conductance g.

5.6.2 Measurement of the non-linear conductance

The non-linear conductance G_2 was measured from the first and the second harmonics response $V_1\cos(\omega t)$ and $V_2\cos(2\omega t)$ to a current excitation $I_0\cos(\omega t)$ [8].

$$G_1 = I_0/V_1 \qquad and \qquad G_2 = 2V_2I_0/V_1^3, \tag{5.11}$$

where $V_2 = R_2I_0^2/2$. The relation for G_2 is deduced from Ohm's law to second order $V = R_1I + R_2I^2$,

$$\begin{aligned} V &= R_1I + R_2I^2 && (5.12)\\ &= R_1\big(I_0\cos\omega t\big) + R_2\big(I_0\cos\omega t\big)^2 \\ &= R_1\big(I_0\cos\omega t\big) + R_2I_0^2\Big(\frac{1+\cos 2\omega t}{2}\Big) && (5.13)\\ &= V_1\cos\omega t + V_2\cos 2\omega t + \frac{R_2I_0^2}{2} \end{aligned}$$

where

$$V_1 = R_1I_0 \qquad and \qquad V_2 = \frac{R_2I_0^2}{2}. \tag{5.14}$$

From 5.12 we can write, neglecting second order terms,

$$\begin{aligned} \frac{V}{R_1} &= I + \frac{R_2}{R_1}I^2 \\ \frac{V}{R_1} &= I + \frac{R_2}{R_1}\Big(\frac{V}{R_1}\Big)^2 \\ I &= \frac{1}{R_1}V - \frac{R_2}{R_1^3}V^2 \end{aligned}$$

8. Measurements were done in a two-terminal geometry

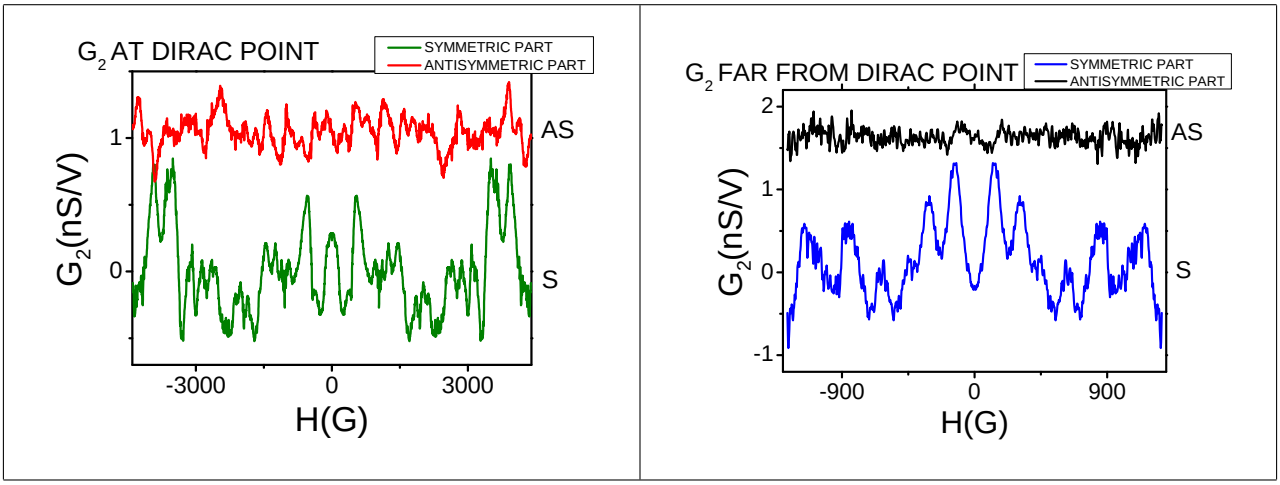

FIGURE 5.24 – G_2^{AS} and G_2^S near and far Dirac point for the monolayer. Curves were vertically offset for clarity.

by definition $I = G_1 V + G_2 V^2$. Thus we can deduce using 5.14,

$$G_1 = \frac{1}{R_1} \qquad and \qquad G_2 = -\frac{2V_2 I}{V_1^3}$$

When measuring the first harmonic we were careful to keep I_0 low enough so that the relation between V_1 and I_0 was constant. For the second harmonics a quadratic dependence of V_2 with I_0 was checked.

Figure 5.24 shows the antisymmetric part G_2^{AS} and the symmetric part G_2^S of conductance fluctuations as a function of magnetic field at two different carrier densities (near and far the Dirac point) for the monolayer. The antisymmetric part and the symmetric part were extracted from data using the relations $G_2^{AS} = \big(G_2(H) - G_2(-H)\big)/2$ and $G_2^S = \big(G_2(H) + G_2(-H)\big)/2$. It can be noticed at first sight that the amplitude of the antisymmetric part near the Dirac point is more important than the one far from the Dirac point.

Figure 5.25 shows the ratio of the odd to even amplitude of the second order conductance fluctuations $r = \delta G_2^{AS}/\delta G_2^S$. The ratio r should go like $\frac{\delta G_2^{AS}}{\delta G_2^S} = \frac{\gamma_{int}}{g}$ as predicted by the theory for diffusive systems (equation 5.9). γ_{int} can be calculated for graphene using expression 5.10.

$$\gamma_{int} = \frac{1}{1 + C\Delta/2e^2} \lesssim 1 \tag{5.15}$$

where C is the capacitance formed between graphene and the backgate and Δ is the spacing between energy levels dE/dN. In graphene $E = \hbar v_F k_F$ and N the total number of conduction electrons in the sample.

$$N = 2 \cdot 2 \cdot \frac{\pi k_F^2}{\left(\frac{2\pi}{L_x}\right)\left(\frac{2\pi}{L_y}\right)}$$

then $k_F = \sqrt{\pi N/(L_x L_y)}$ (factor 4 counts for spin and valley degeneracy) and

$$\Delta = \frac{dE}{dN} = \hbar v_F \sqrt{\frac{\pi}{L_x L_y}} \frac{1}{2\sqrt{N}}. \tag{5.16}$$

The number of electrons in graphene is given by the capacitance model,

$$\begin{aligned} Q &= CV \\ N &= \frac{CV_g}{e} \end{aligned} \tag{5.17}$$

so replacing 5.16 and 5.17 in equation 5.15 we have

$$\begin{aligned}\frac{2e^2}{C\Delta} &= \frac{2e^2}{C}\frac{2}{\hbar v_F}\sqrt{\frac{L_x L_y C V_g}{\pi e}} \\ &= \frac{4e^2}{\hbar v_F}\sqrt{\frac{L_x L_y V_g d}{\epsilon_0 \epsilon_R L_x L_y \pi e}} \\ &= \frac{4e^2}{\hbar v_F}\sqrt{\frac{V_g d}{\epsilon_0 \epsilon_R \pi e}} \end{aligned} \tag{5.18}$$

thus,

$$\begin{aligned}\gamma_{int\ ML} &= \frac{1}{1+\frac{\hbar v_F}{4e^2}\sqrt{\frac{\epsilon_0\epsilon_R\pi e}{V_g d}}} \\ &= \frac{131\sqrt{V_g}}{1+131\sqrt{Vg}},\end{aligned}$$

(where γ is dimensionless and V_g is in Volts). The interaction constant in the monolayer $\gamma_{int\ ML}$ has a very small dependence on the gate voltage, $\gamma_{int} \approx 1$ over the entire electronic density range investigated, within less than 4/1000. Screening is strong, even close to the CNP where $\gamma = 0.996$. We attribute this to the puddles of electrons and holes near the CNP which makes the Dirac point unaccessible in our samples. We conclude that in graphene the ratio of the odd to even amplitude of the second order conductance should go as $r \propto 1/g$.

In the case of the bilayer, the spacing between levels is

$$\Delta_{BL} = \frac{\hbar^2 \pi}{2 m L_x L_y}$$

and

$$\gamma_{int\ BL} = \frac{1}{1+\frac{\hbar^2 \pi \epsilon_0 \epsilon_r}{4 m e^2 d}},$$

which is equal to 0.999, corresponding to a strong screening. γ_{int} is for the bilayer independent of gate voltage in contrast with the monolayer.

Figure 5.25 shows the gate voltage dependence of r (the odd to even amplitude of the second order conductance). It follows $1/g$ with a multiplicative factor 7. This factor compared to 1 expected for $L = W$, may be due to the large aspect ratio of the sample ($L = 0.8\mu m$ and $W = 2.7\mu m$). The reason is that δG_1 enters in the calculation of r,

$$\frac{\delta G_2^{AS}}{\delta G_2^{S}} \propto \delta G_1 \frac{\gamma_{int}}{g}$$

and the value of δG_1 is ≈ 1 for a square sample but depends on the aspect ratio, $\delta G_1 \approx 0.7\sqrt{\frac{W}{L}}$ (with W/L in our case 3.4). However we find a value for δG_1 which is 1/5 of the predicted value. Each point in figure 5.25 was calculated taking into account the reproducibility of two different scans, quantified in $Noise_{Asym}$ and $Noise_{Sym}$. Noise is calculated from the variance of the difference of two different scans,

$$Noise_{Asym/Sym} = \frac{1}{2}\frac{1}{N-1}\sum_{i=1}^{N}\left(x_{up} - x_{dn}\right)^2$$

the factor 1/2 comes from the fact that noise in two different scans is not correlated, as is shown in the following. Each scan can be written like $x_{up} = x + \delta x_{up}$ and $x_{dn} = x + \delta x_{dn}$ then $x_{up} - x_{dn} = \delta x_{up} - \delta x_{dn}$

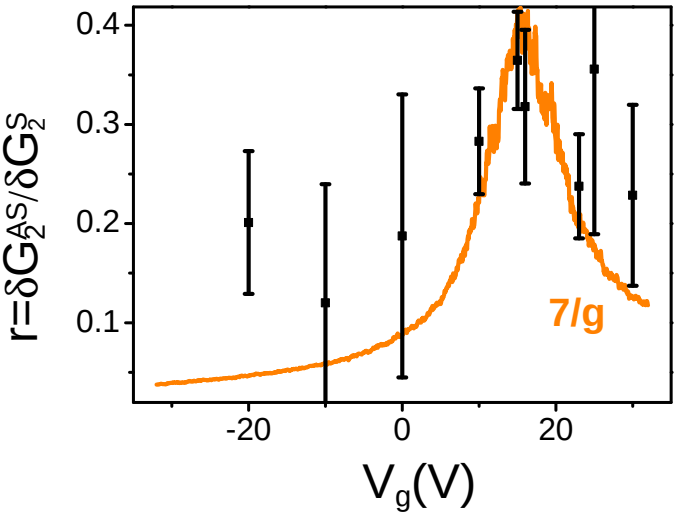

FIGURE 5.25 – The ratio $r = \delta G_2^{AS}/\delta G_2^S$ extracted from data is compared to $7/g$ (continuous line). Data correspond to a monolayer.

and

$$\begin{aligned} \left\langle |x_{up} - x_{dn}|^2 \right\rangle &= \left\langle |\delta x_{up}|^2 \right\rangle + \left\langle |\delta x_{dn}|^2 \right\rangle - 2 \left\langle \delta x_{up} \delta x_{dn} \right\rangle \\ &= 2 \left\langle |\delta x_{noise}|^2 \right\rangle \end{aligned} \tag{5.19}$$

then

$$\left\langle |\delta x_{noise}|^2 \right\rangle = \frac{1}{2} \left\langle |x_{up} - x_{dn}|^2 \right\rangle = Noise_{Asym(Sym)}.$$

The asymmetry is calculated using

$$r = Asymmetry = \sqrt{\frac{Var_{Asym} - Noise_{Asym}}{Var_{Sym} - Noise_{Sym}}},$$

where the variance of the symmetric and antisymmetric part of the second order conductance, Var_{Asym} and Var_{Sym} is the average of two different scans up and dn,

$$Var_{Asym(Sym)} = \frac{Var_{up} + Var_{dn}}{2}$$

where

$$Var_{up,dn} = \frac{1}{N-1} \sum_i^N \left(x_i - \langle x \rangle \right)^2.$$

We estimate the error bars in figure 5.25 calculating $\delta r/r$. Considering

$$r = \sqrt{\frac{Var_{Asym}}{Var_{Sym}}},$$

we have

$$\begin{aligned}\frac{\delta r}{r} &= \frac{1}{2}\frac{\delta r^2}{r^2} \\ &= \frac{1}{2}\frac{Var_{Sym}}{Var_{Asym}}\Big[\frac{Noise_{Asym}Var_{Sym}+Var_{Asym}Noise_{Sym}}{Var_{Sym}^2}\Big] \\ &= \frac{1}{2}\Big[\frac{Noise_{Asym}}{Var_{Asym}}+\frac{Noise_{Sym}}{Var_{Sym}}\Big]\end{aligned}$$

but the noise of the symmetric part is 10 to 30 times smaller than the variance of the symmetric part, we consider then only the first term which gives us an expression to quantify error bars for the asymmetry r

$$\frac{\delta r}{r} = \frac{1}{2}\frac{Noise_{Asym}}{Var_{Asym}}.$$

5.7 Conclusion

In conclusion we have shown that mesoscopic graphene samples exhibit conductance fluctuations which Fermi energy- and B-dependent correlation functions can be described by theoretical predictions for diffusive systems over a wide range of carrier concentration, for both monolayer and bilayer. The different behaviors of the correlation energy and fields are intimately related to the fundamentally different dispersion relations of both systems. A significant increase of the amplitude of the Fermi energy-dependent fluctuations is observed close to the neutrality point, whereas the B-dependent fluctuation amplitude is nearly constant over the entire carrier density range. This nonergodicity of fluctuations may be attributed to the particular disorder due to electron and hole puddles in graphene near the charge neutrality point. Finally, we have measured the second-order nonlinear conductance. We have exploited the tunability of graphene's conductance to find that its field asymmetry decreases with g, in agreement with theoretical predictions for diffusive systems. This indicates strongly screened electron-electron interactions in graphene

Chapitre 6

Superconducting proximity effect in graphene

6.1 Introduction

The superconducting proximity effect in a normal metal gives signature, just as universal conductance fluctuations, of coherent transport in a sample. In a superconductor-normal metal-superconductor junction (SNS) for example, the normal part must be coherent, for both electrons composing each Cooper pair in the superconductors to be able to be transmitted simultaneously and in a coherent way . Choosing graphene as a normal metal lets graphene acquire superconducting properties by proximity effect, opening somehow a bridge between relativity and superconductivity in a real material.

The particularity of choosing graphene as the normal metal, comes from its band structure. Graphene, with an electron band and a hole band that touch each other at a point, opens the possibility (through a process called Andreev reflection) of having each electron forming an Andreev pair belonging to a different band. This phenomenon is predicted to have an experimental signature although as will be seen in the following, experimental conditions to be in this regime are hard to attain.

In this chapter I will expose an experiment done in a superconductor/graphene/superconductor junction in which superconductivity was induced in-situ in graphene by changing gradually the transparency between the superconducting electrodes and graphene. In a second part I will talk about experiments where superconductivity is induced in graphene by superconducting islands on top of graphene. In this regime it is possible to observe a metal-insulator transition mediated by superconductivity.

6.2 Introduction to the physics of the Josephson effect and the superconducting proximity effect

When there is a potential barrier between two metals, electrons can tunnel if the potential is not large enough to localize electrons at one side or the other of the barrier. An insulator between two metals for example, forms a potential barrier. In this case, the tunneling probability becomes important when the thickness of the insulator is of the order of some atomic layers or less, giving rise to a tunneling current I that is proportional to the voltage difference across the barrier V. The junction behaves then as an ohmic resistance, $I = GV$ (figure 6.1). If instead of two normal metals, there are two superconductors separated by an insulating barrier (SIS junction), at zero temperature there is no transport of quasiparticles until $V = 2\Delta/e$ where Δ is the superconducting gap. In this situation, the quasiparticle density of states of both superconductors contributes to the tunnel current which exhibits a discontinuity (figure 6.2). Figure 6.3 shows data from such a SIS junction. It is made from two tunnel junctions in series, it has the form $Ta/Pt/I/Graphene/I/Pt/Ta$ where I is an insulating barrier. Data shows the differential conductance versus applied dc voltage. A tunnel gap of $250\mu eV$ appears which closes with magnetic field, as is expected

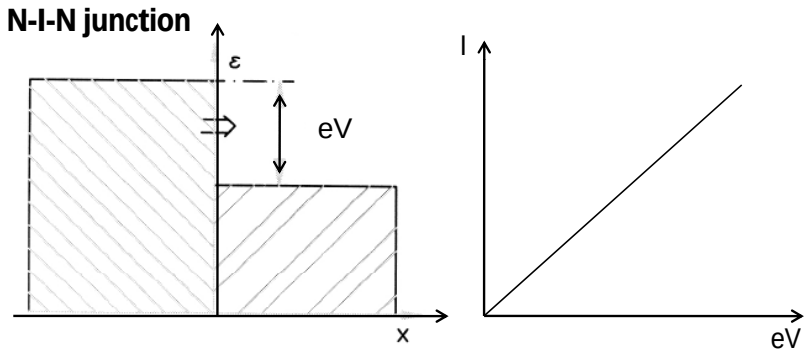

FIGURE 6.1 – Normal-insulating-normal junction with its I-V characteristics. Taken from [28].

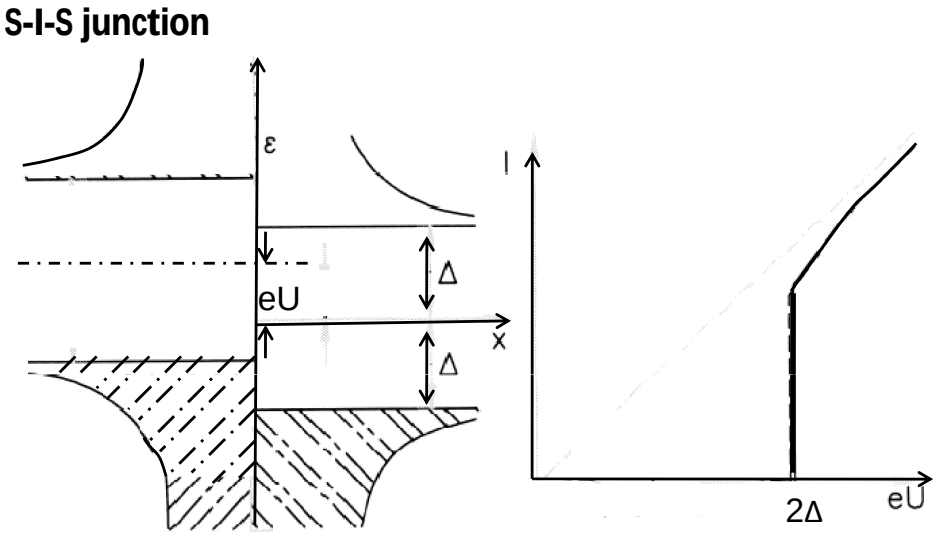

FIGURE 6.2 – Superconductor-insulator-superconductor junction with its I-V characteristics. Taken from [28].

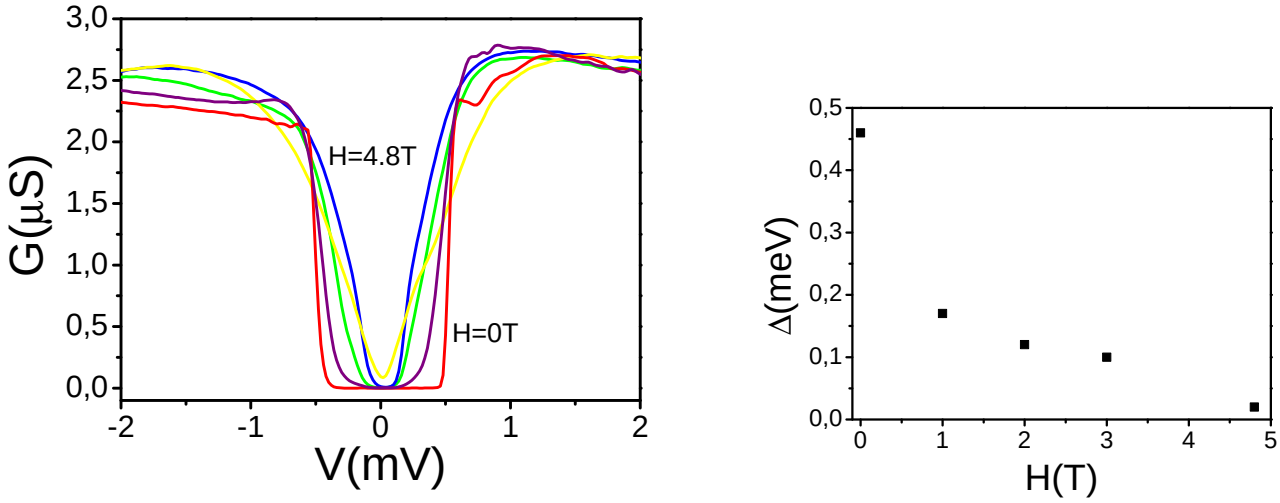

FIGURE 6.3 – Left :Differential conductance characteristics for a tunnel junction made of graphene and Pt/Ta/Pt electrodes. Curves correspond to 0T, 2T, 3T and 4.8T. Right : Evolution of the superconducting gap with magnetic field.

for a superconducting gap. [1]. It closes at $4.8T$, which is lower that the maximum magnetic field that is supposed to preserve the superconducting state according to the Clogston criteron ($H < 2\Delta/\mu_B = 8.7T$ with $\mu_B = e\hbar/2m_e$).

If in the place of an insulating barrier forming a tunnel junction, we have a normal metal with a good contact with the superconductors (an SNS junction), there are two experimental signatures that indicate the transport of Cooper pairs through the normal metal or a ***superconducting proximity effect***. One is multiple Andreev reflections and the other is the Josephson effect.

In a bias voltage configuration, when the junction is polarized with a voltage bigger than two times the superconducting gap, $V > 2\Delta$, electrons cross the junction as quasiparticles, like in the tunnel junction. If instead $V < 2\Delta$ electrons arriving to the N-S interface cannot enter as quasiparticles because there are no quasiparticle states in the gap. Instead, they are reflected back into the normal metal as holes, thus transferring a charge 2e across the interface to the superconductor. This is called Andreev reflection and occurs if the metal is coherent enough. More precisely, electrons enter as evanescent states in the gap which decay into the condensate over a distance ξ, the superconducting characteristic length [29].

Electrons coming from the normal metal with an energy $eV < 2\Delta$ when approaching the superconductor will be Andreev reflected several times (multiple Andreev reflections MAR), gaining at each reflection a potential energy eV. The energy needed to do n reflections is $eV = 2\Delta/n$ (with n the number of Andreev reflections) as is shown in figure 6.4. The experimental signature of Andreev reflections shown in figure 6.5. Data corresponds to an SNS juction where the normal part is made of graphene. Each time a voltage of $2\Delta/n$ is imposed to the junction, transport is favored in the junction as explained in figure 6.4, and there is a maximum in conductance.

The second manifestation called Josephson effect, appears when there is a good interface between the superconductor and the phase coherent normal part (a better interface than in the case shown in figure 6.5). In this case a current biased configuration is adopted and no applied voltage is needed in order to have transport through the junction. In 1962 Josephson predicted that a supercurrent I should flow at

1. In this section there are no specificities associated to graphene.

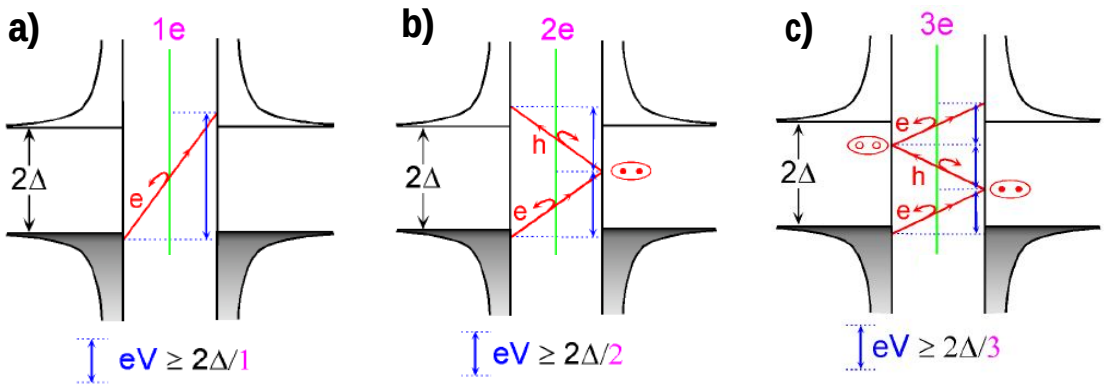

FIGURE 6.4 – To illustrate multiple Andreev reflections, density of states of the two superconducting electrodes are represented. If a voltage $V \geq 2\Delta/1$ is imposed, there is single charge transfer as shown in a). The transmitted electron gains an energy of eV provided by the voltage source. b) shows the case when a voltage $eV \geq 2\Delta/2$ is imposed .An electron coming from the normal metal cannot find an empty state in the right electrode and is reflected into a hole, which gains an energy eV. In this case two electron charges are transfered from left to right. For voltages $eV \leq 2\Delta$, there are multiple reflections before the electron (or hole) finds an empty state in the right (or left) electrode. c) shows a three charges transfer. Two charges are transfered after a first Andreev reflection and a third one at the second Andreev reflection. In this case, the condition for the electron to find an empty state in the right electrode is no longer $eV \geq 2\Delta$ or $eV \geq \Delta$ but only $eV \geq 2\Delta/3$. (Taken from [32])

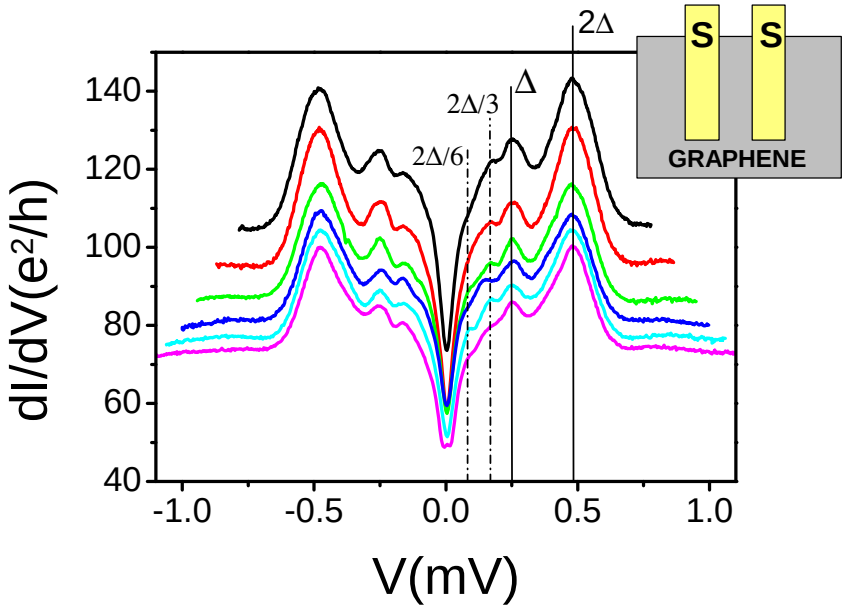

FIGURE 6.5 – dV/dI characteristics of a SNS junction showing multiple Andreev reflections. In these data, the normal part is graphene. The superconducting electrodes are made of Pt/Ta/Pt (3nm/70nm/3nm). Different curves correspond to different back gate voltages.

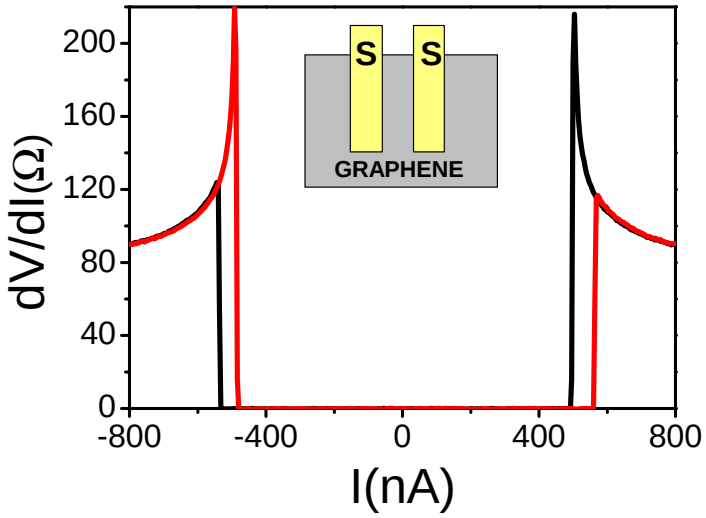

FIGURE 6.6 – dV/dI characteristics of an SNS junction. A dissipationless current crosses the sample at zero applied voltage (V=0). In these data, the normal part is made of graphene

zero voltage (V=0) between two superconductors separated by a thin insulating barrier, with the form

$$I = I_C \sin(\theta_1 - \theta_2) \tag{6.1}$$

where $\theta_1 - \theta_2$ is the phase difference of the superconductors. In this process, each pair of electrons forming Cooper pairs in the superconductor tunnels simultaneously in a coherent way between the two superconductors and not like quasiparticles. The Josephson effect has been observed not only in tunnel junctions but also in weak links, where current flows along a conducting, either normal or superconducting material. These are for example superconducting point contacts, proximity effect bridges, SNS junctions. In the SNS case, the pair correlation that characterizes the two superconductors can penetrate well into the neighboring conductor material only if it is phase coherent ($L_\phi > L$), this is an important aspect of superconducting proximity effect.

Under these conditions, a collective state is formed between the two superconductors through the normal junction which means that it is possible to form a Cooper pair with two electrons belonging to two different superconductors. This leads to a finite superconducting current even if there is no voltage applied to the junction. Josephson current is carried by Andreev coherent states that are formed in the normal part. These states come from the quantization of the difference of two wavevectors, the one of the incident electron in the S-N interface and the one of the reflected hole. The spectrum of Andreev coherent states determines the supercurrent through the sample. The experimental signature of such a supercurrent is shown in figure 6.6. dV/dI characteristic reveal a current that goes through the junction with zero resistance.

The Josephson relation for the superconducting current (equation 6.1) can be found from the expression for the energy in the tunnel junction. It is proportional to $\Delta_1 \times \Delta_2$ or $\psi_1 \times \psi_2$ ($\psi_{1/2}$ being the "wave functions" including all the Cooper pairs in superconductor 1 or 2). It can be written in the following way given that $\psi_{1/2} = |\psi_{1/2}|e^{\theta_{1/2}}$ with $\theta_{1/2}$ the phase of the superconductors [28],

$$\begin{aligned} E &= C \int dxdy \Big[|\psi_1(\mathbf{r})\psi_2(\mathbf{r})| - \frac{1}{2}\Big(\psi_1(\mathbf{r})\psi_2^*(\mathbf{r}) + \psi_1^*(\mathbf{r})\psi_2(\mathbf{r})\Big)\Big] \\ &= 2C \int dxdy |\psi_1(\mathbf{r})\psi_2(\mathbf{r})| \big[1 - \cos(\theta_1 - \theta_2)\big] \end{aligned} \tag{6.2}$$

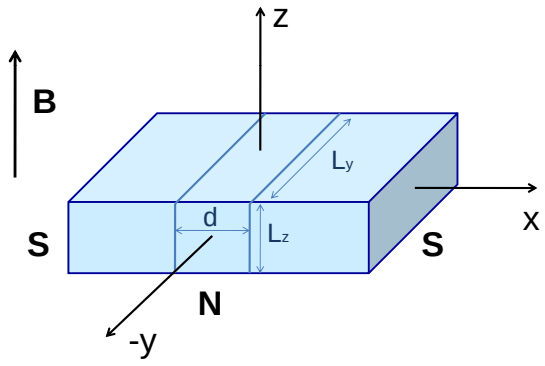

FIGURE 6.7 – Geometry of an SNS junction in the presence of a magnetic field.

where C is a constant and x-y is the plane of the junction (see figure 6.7). If a magnetic field described by the potential vector $\mathbf{A} = -By\hat{x}$ is applied , thanks to Gauge invariance, energy can be written :

$$E = C \int dxdy|\psi_1(\mathbf{r})\psi_2(\mathbf{r})|\Big[1 - \cos\Big(\theta_1 - \theta_2 + \frac{2\pi\Phi(y)}{\Phi_0}\Big)\Big]$$

since the phase difference induced by the magnetic field is the magnetic flux $\Phi(y)$ through the area $y \times d$. ($\Phi(y) = \int A_x dx = Byd$).

The sensibility of the energy to a magnetic flux induces a current density, thus we can write

$$j = -\frac{\delta E}{\delta \Phi} = \frac{2\pi}{\Phi_0} C|\psi_1\psi_2| \sin\Big(\theta_1 - \theta_2 + \frac{2\pi\Phi(y)}{\Phi_0}\Big),$$

which in the absence of magnetic field gives the Josephson relation

$$j = j_c \sin(\theta_1 - \theta_2).$$

When a magnetic field is applied, the Josephson current tries to screen the magnetic field. If $\mathbf{B}||\mathbf{z}$ considering that the junction is in the x-y plane as shown in figure 6.7, the measured current can be written as

$$\begin{aligned} I &= L_z \int_0^{L_y} j(y)dy \\ &= L_z \int_0^{L_y} j_c \sin\Big(\theta_1 - \theta_2 + \frac{2\pi Byd}{\Phi_0}\Big)dy \\ &= j_c \frac{\phi_0 L_z}{Bl}\Big[\cos(\theta_1 - \theta_2) - \cos\Big(\theta_1 - \theta_2 + \frac{2\pi BL_y d}{\Phi_0}\Big)\Big] \\ &= I_c \frac{\Phi_0}{\pi\Phi} \sin\Big(\frac{\pi\Phi}{\Phi_0}\Big) \sin\Big(\theta_1 - \theta_2 + \frac{\pi\Phi}{\Phi_0}\Big) \end{aligned} \tag{6.3}$$

and the maximum current the junction can hold is

$$I_{max} = I_c \left|\frac{\sin(\pi\Phi/\Phi_0)}{\pi\Phi/\Phi_0}\right|. \tag{6.4}$$

This expression is represented in figure 6.8. The current is zero each time the magnetic flux in the sample is a multiple of the flux quantum. This form is known as the Fraunhoffer diffraction pattern by analogy with the light intensity through a narrow rectangular slit.

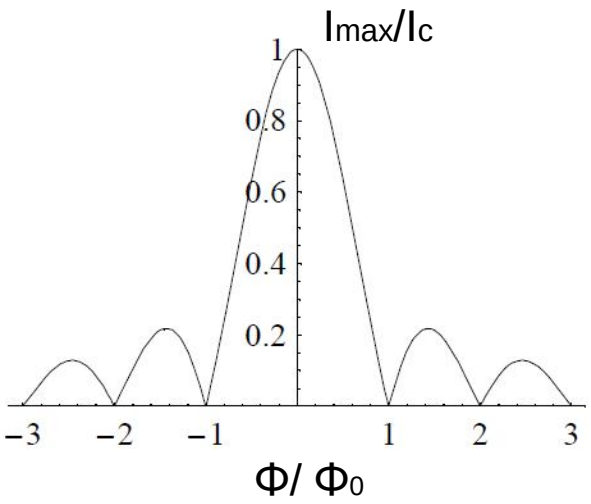

FIGURE 6.8 – Dependence of the maximum Josephson current in the junction as a function of the magnetic flux through the junction.

6.3 Predictions for the superconducting proximity effect in graphene

I will discuss in the following the superconducting proximity effect in graphene. The specificity of the superconducting proximity effect in graphene comes from Andreev reflections. Electron-hole conversion is different in graphene thanks to its band structure. The two members of the Cooper pairs $\mathbf{k}$ and $-\mathbf{k}$ belong to two different valleys. Moreover, the fact that the electron and hole band touch each other in graphene an bilayer graphene opens the possibility of having incident electrons and reflected holes that participate in Andreev reflections belonging to different bands.

Andreev showed [52] that the electron hole conversion at a NS interface is associated to a retroreflection, in which the reflected hole retraces the path of the incident electron. In graphene on the other hand, it has been suggested [30] that Andreev reflection can be specular, which means that for the reflected hole, only the component of velocity perpendicular to the interface changes sign. A scheme of both types of reflections is shown in figure 6.9. Figure 6.10 shows the process of Andreev reflections in graphene. An electron excitation which is a filled state at energy ϵ above the Fermi energy E_F is converted into a hole excitation that corresponds to an empty state at ϵ below E_F. For ϵ below the superconducting gap, the reflected hole is the empty state left by the electron that is paired with the incident electron to form the Cooper pair [31]. Andreev reflection is an elastic process, so the excitation energy ϵ of electron and hole is the same. In graphene, electron and hole come from opposite corners of the Brillouin zone $\pm\mathbf{K}$ in order to form a Cooper pair with zero momentum (they have time reversed trajectories). Figure 6.10 represents the case where electron and hole belong to the same band ($\epsilon < E_F$), corresponding to a traditional Andreev retroreflection. When $\epsilon > E_F$ the hole is an empty state in the valence band rather than an empty state in the conduction band, giving rise to an interband Andreev reflection, which gives a specular reflection. This kind of reflection does not occur in usual metals where the Fermi energy is very large, and is hard to reach the valence band.

The linear dispersion relation of graphene can be written in terms of the excitation energy $\epsilon = |E - E_F|$ of electrons and holes participating in Andreev reflection

$$\epsilon = |E_F \pm \hbar v \left(\delta k_x^2 + \delta k_y^2\right)^{1/2}| \tag{6.5}$$

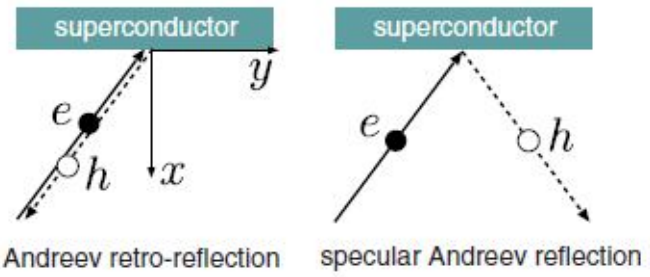

FIGURE 6.9 – Andreev retroreflection at the interface between a superconductor and a normal metal (left panel) and specular Andreev reflection in graphene (right panel). Solid and dashed lines correspond to an electron or a hole respectively. Arrows indicate the direction of velocity. Taken from [31]

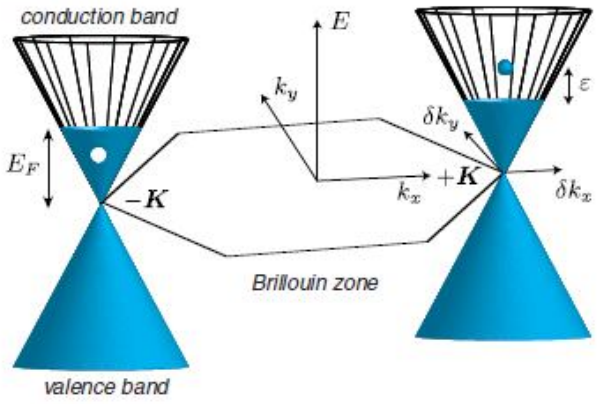

FIGURE 6.10 – Representation of electron and hole excitations in the conical band structure of graphene. An electron in **K** cone is converted into a hole in the **-K** cone by Andreev reflection at the boundary with the superconductor. The electron and hole have equal energies $\epsilon = |E - E_F|$. (Taken from [31])

where the ± sign corresponds to excitations in the conduction or valence band. From this expression we can deduce the sign of velocity of the reflected hole. Lets consider an interface graphene-superconductor at $x = 0$ and electrons approaching from $x > 0$ like in figure 6.9. δk_y and ϵ are conserved upon reflection, thus equation 6.5 gives four different δk_x. The reflected state will be a superposition of these solutions. The velocity v_x of the reflected state has to be positive, then only the δk_x that has a positive derivative $\hbar^{-1} d\epsilon/d\delta k_x$ (the expectation value of the velocity v_x) will be part of the reflected state. Only two δk_x give a positive slope, one corresponding to an electron excitation and the other to a hole excitation. The reflected hole can be an empty state in the conduction band ($\epsilon < E_F$) or an empty state in the valence band ($\epsilon > E_F$). A conduction band hole moves opposite to its wave vector, so v_y changes sign and also v_x (retroreflection). In contrast, a valence band hole moves in the same direction as its wave vector, so v_y remains unchanged and only v_x changes sign (specular reflection).

In the following, I will explain more in detail the origin of these two types of reflections using figure 6.11. Let's start with Andreev retro-reflections (top). This type of reflections occur in graphene when it is sufficiently doped so that Fermi energy is far from the Dirac point. An electron e_1 in valley $+\mathbf{K}$ is coupled to an electron e_2 in valley $-\mathbf{K}$ to form a Cooper pair (electrons e_1 and e_2 have opposite $\mathbf{k}$). Equivalently, we can say that e_1 is reflected into the hole h_2 associated to e_2. To place h_2 in the figure, I take into account that $\mathbf{k}_{hole} = -\mathbf{k}_{electron}$ and that the hole's band is inverted with respect to the electron's band ($\epsilon_{\mathbf{h}}(\mathbf{k_h}) = -\epsilon_{\mathbf{e}}(\mathbf{k_e})$). It can be checked that k_y is conserved in the reflection, $k_{y_{e_1}} = k_{y_{h_2}}$. Knowing that the components of velocity can be written like $v_x = \hbar^{-1} d\epsilon/dk_x$ and $v_y = \hbar^{-1} d\epsilon/dk_y$ it can be deduced from the figure that an incident electron with $v_x < 0$ and $v_y > 0$ will be reflected into a hole with $v_x > 0$ and $v_y < 0$, which corresponds to a retroreflection.

In the case of specular Andreev reflection, the Fermi energy is near the Dirac point. Near Dirac point, the state of electron e_1 coming from valley $+\mathbf{K}$ has a time reversed state with respect to electron e_2 in valley $-\mathbf{K}$. (It can be checked in both figures that e_1 and e_2 have opposite velocities). An electron e_1 is reflected into the hole h_2 associated to e_2. h_2 is time reversed with respect to e_2, it has an inverted band structure with respect to e_2 and it has an opposite $\mathbf{k}$ with respect to e_2 except that $k_y > 0$, since k_y must be conserved in the reflection. Under these conditions, an incident electron with $v_x < 0$ and $v_y > 0$ is reflected into a hole with $v_x > 0$ and $v_y > 0$ which corresponds to a specular reflection.

Andreev retroreflection creates between the two superconductors localized states known as Andreev levels, while Andreev specular reflection creates propagating modes that contribute to thermal transport along the channel (see figure 6.12).

The experimental signature of specular Andreev reflections should be found in the dIdV characteristics according to the calculations of Beenaker *et. al.*. Figure 6.13 shows the calculated differential conductance as a function of a normalized V . It has a singularity at $eV = \Delta_0$, as in any SN junction, but it has a different form and value for retroreflections and specular Andreev reflections. When the Fermi energy is large with respect to the superconducting gap ($E_F >> \Delta$), or equivalently the Fermi wavelength is small with respect to the coherent length of the superconductor, there are Andreev retroreflections and the anomaly in the dIdV characteristics is a peak. When the Fermi energy is small ($\Delta >> E_F$) specular Andreev reflections dominate and the peak gets reduced in the normalized conductivity from 2 to 4/3. Figure 6.14 shows the crossover between retroreflection and specular reflection. It happens in a non-monotonous way. When the Fermi energy is tuned close to the Dirac point becoming smaller than the superconducting gap, the peak associated with Andreev retroreflections becomes a dip when $E_F \leq \Delta_0$. It can be remarked that the differential conductance vanishes at $eV = E_F$ since when the excitation energy equals the Fermi energy ($\epsilon = E_F$) there is no Andreev reflection for any angle of incidence. Experimentally this crossover should be observed when changing the Fermi energy through gate voltage.

Some experiments have been done on graphene connected to superconducting electrodes, but none of these have found signatures of specular Andreev reflections. Xu Du *et. al.* [33] and Hubert B. Heersche *et. al.* [34] have observed a Josephson effect in a superconductor-graphene-superconductor junction. They have measured a supercurrent that is modulated by a gate voltage and that can flow at zero charge density, near the Dirac point. The supercurrent is, depending on the gate voltage, carried by electrons in

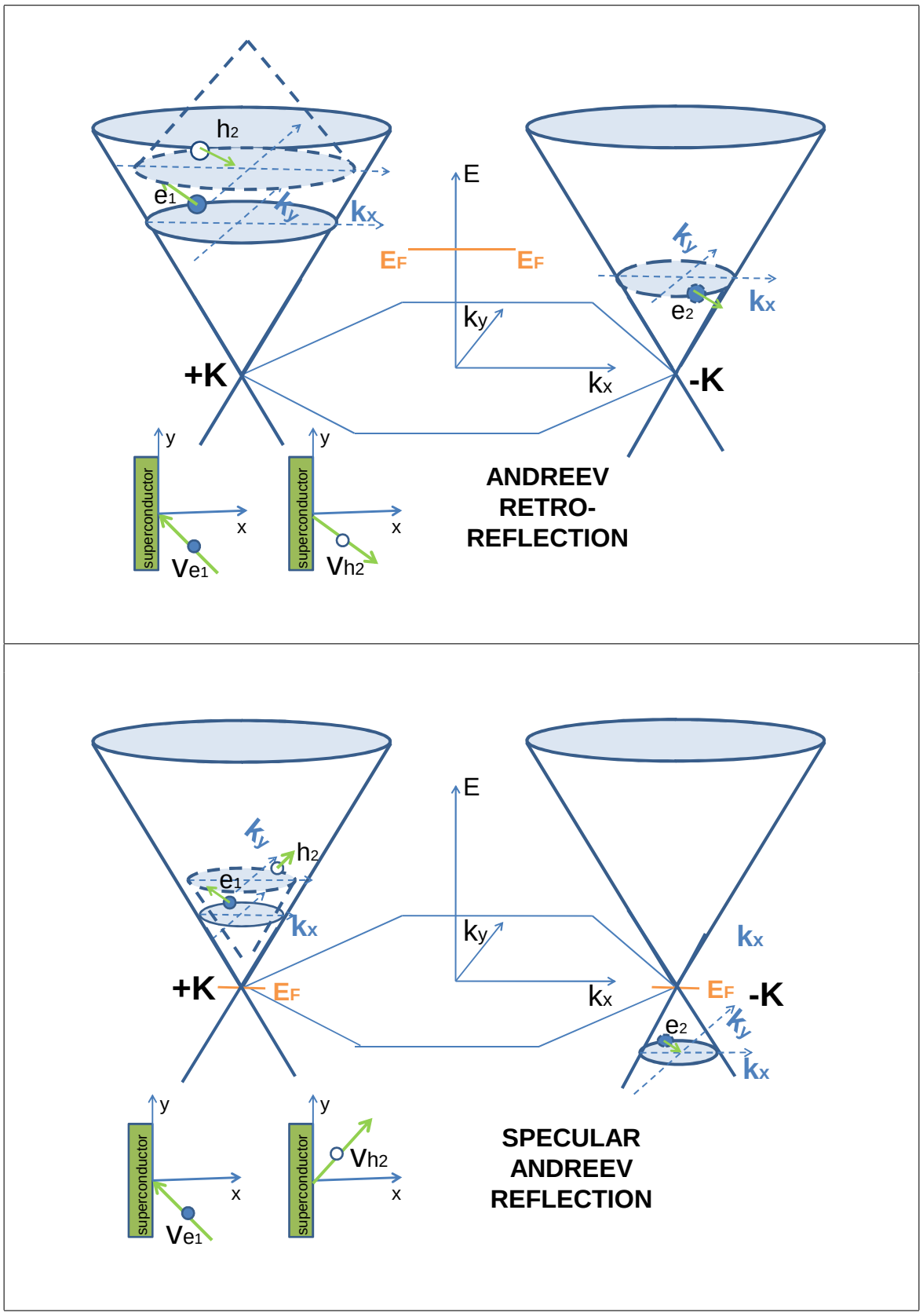

FIGURE 6.11 – Andreev reflections in graphene for $\epsilon < E_F$ (top) and $\epsilon > E_F$ (bottom). Both valleys are represented (+K,-K) since electrons participating in Andreev reflections in graphene come from different valleys. Electrons are represented with filled circles and holes with empty circles. Arrows represent the velocity of propagation. Inspired from [46].

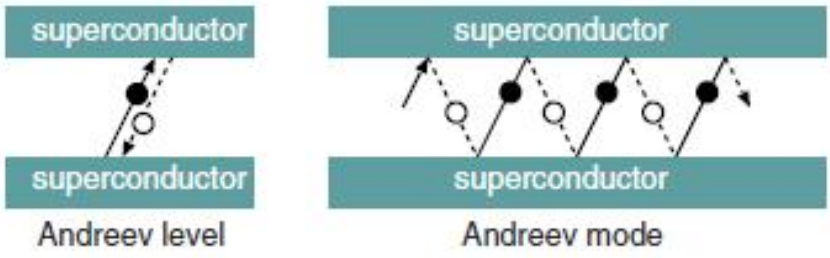

FIGURE 6.12 – Bound states states versus propagating modes in Andreev reflections

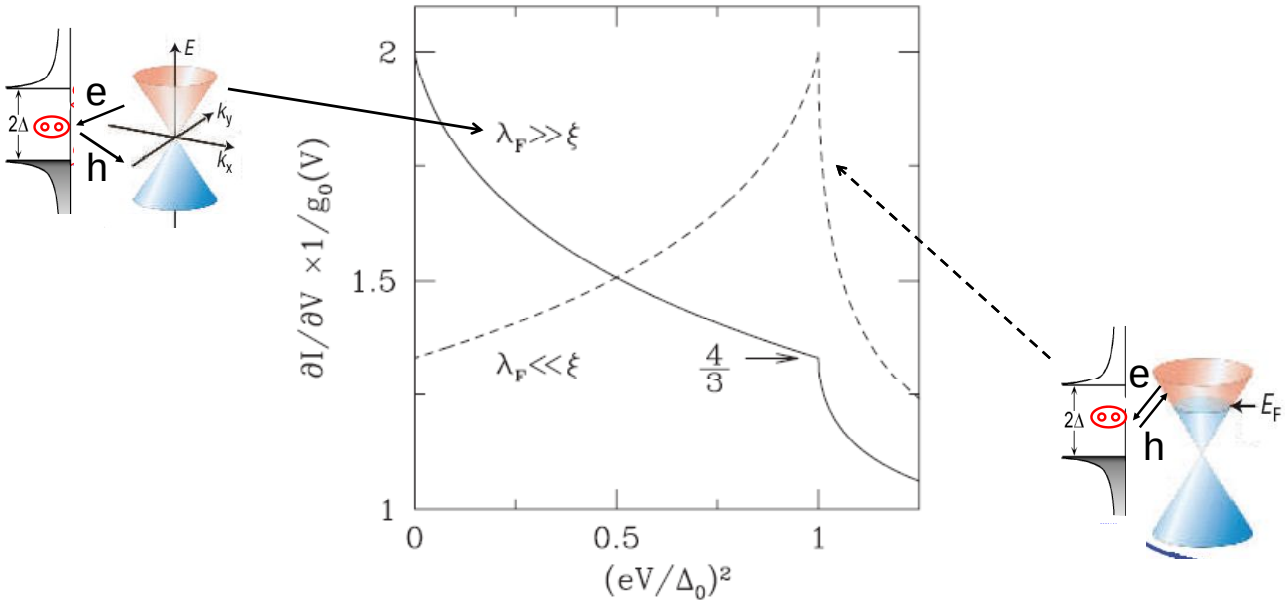

FIGURE 6.13 – Normalized differential conductance at the interface between normal and superconducting graphene. Electron hole conversion is predominantly retroreflection for $\lambda_F << \xi$ (dashed curve) and specular Andreev reflection for $\lambda_F >> \xi$ (solid curve). Taken from [30]

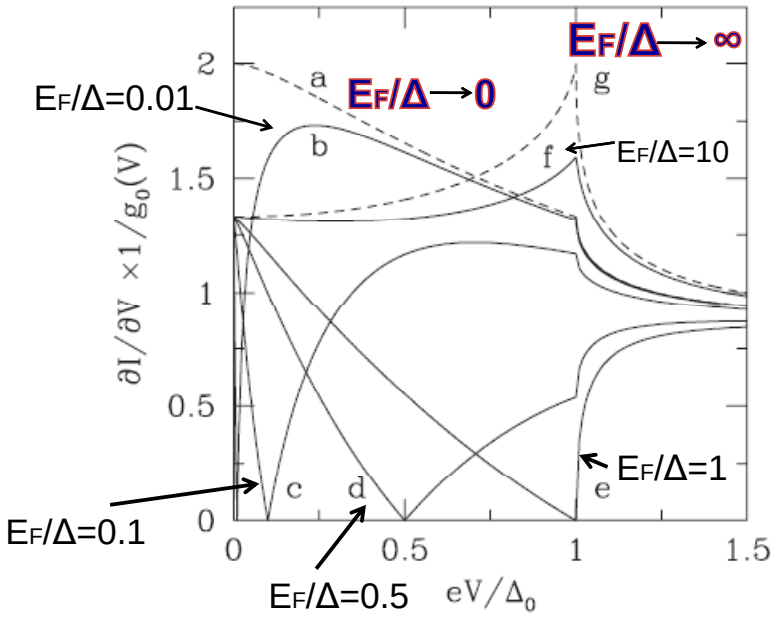

FIGURE 6.14 – Differential conductance for different ratios E_F/Δ_0. The asymptotic cases $E_F/\Delta_0 \to 0, \infty$ are represented by dashed curves [30].

the conduction band or holes in the valence band. At finite bias they have found a subgap structure in the differential resistance due to Andreev reflections. Figure 6.15 shows the gate voltage dependence of supercurrent and dV/dI characteristics observed by Heersche *et. al.*. Shailos *et. al.* [35] have also observed anomalies in the dV/dI characteristics associated with Andreev reflections (peaks in resistance and not dips like in the others works). They have seen a sharp dip at zero resistance bias but no Josephson current was detected probably because of the large distance between the electrodes ($> 2\mu m$).

6.4 Tuning the proximity effect in a superconductor-graphene- superconductor junction

One of the factors that have inhibited the observation of the particular Andreev reflections in graphene is the spatial inhomogeneities of doping. Near Dirac point, some regions of the sample have $E_F > \Delta$ and others $E_F < \Delta$. Dirac point is then larger than the superconducting gap, $\delta E_F >> \Delta$. The observation of specular Andreev reflections requires the combination of superconducting electrodes with larger gaps and also a lower local density in graphene, which means cleaner graphene samples. It has been shown that a way to improve the quality of graphene samples is annealing. One way of doing annealing is increasing the temperature of the sample to 100-900°C in a vacuum chamber. A second way is through current. This technique consist in running a current of the order of several mA through graphene in most of the cases at low temperatures, inside the cryostat. This procedure removes contamination adsorbed on the surface of graphene or causes adsorbed impurities migrate to the edges. The current density applied to the sample through annealing is in general of the order of $10^8 A/cm^2$. Figure 6.16 shows AFM images taken by J. Moser *et. al.* of a freshly exfoliated graphene sample that has been submitted to current annealing. After a first annealing, impurities migrate to the center of the sample. After a second one (bias voltage applied is V=4.6V), the area between source and drain becomes as smooth as the substrate [36]. Moser

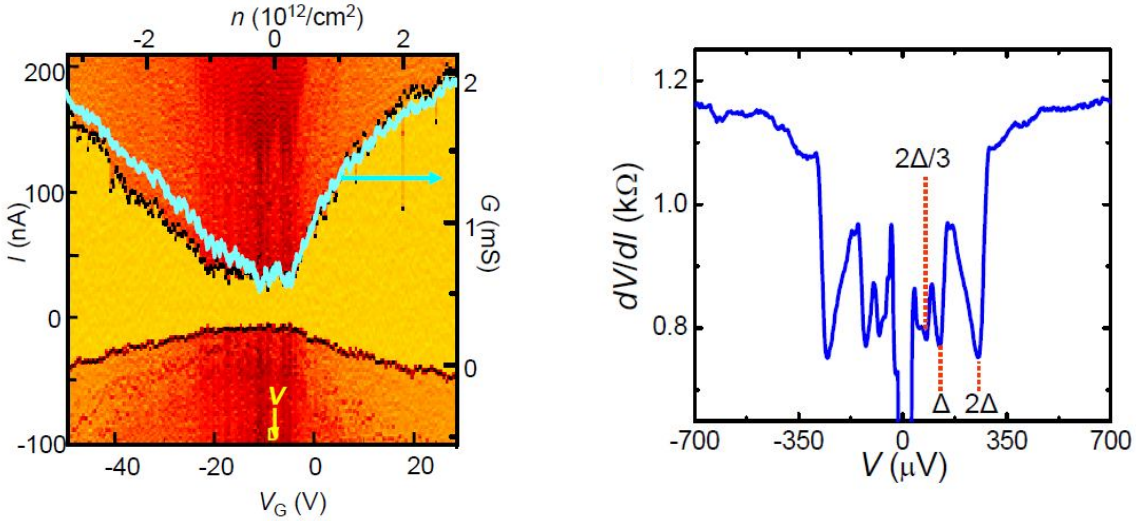

FIGURE 6.15 – Left : color plot of the dV/dI versus current I and gate voltage V_g. Yellow corresponds to zero resistance. Supercurrent at Dirac point is finite. The asymmetry of the supercurrent with respect to the Dirac point was also seen in the normal state conductance, which is represented by the blue line. Right : Differential resistance dV/dI showing dips below the superconducting gap. They appear at $V = 2\Delta/en$ and correspond to multiple Andreev reflections. Taken from [34]

et. al. also found that annealing has an influence on the sample doping, as is shown in d). After annealing the minimum of conductance which was not reachable before with gate voltage, moved close to $V_g = 0$. The sample changed from being hole doped to being weakly doped, opening the possibility of modulating carriers from electrons to holes through gate voltage. Experiments on suspended samples [37] have shown that annealing leads to an enhancement of mobility and a narrowing of the Dirac point, which was not observed for annealing on samples on substrate. The reason is that in suspended samples impurities are not trapped between substrate and graphene and impurities from both sides of the graphene sheet are free to desorb. Annealing on unsuspended graphene however, has shown to improve the cleanliness of the sample and also the quality of electrical transport.

6.4.1 Current annealing as a dial for the superconducting proximity effect

We have found that annealing improves the quality of the graphene/superconductor contact and gradually changes the signatures of the superconducting proximity effect. Subgap anomalies become better defined after each anealing and at the end a supercurrent is induced in graphene.

In this experiment the sample was fabricated as usual, using exfoliated graphene deposited on a doped silicon substrate with a 285-nm-thick oxide. Raman spectroscopy confirmed that the sample was made of a single layer. Electrodes were made of a trilayer of Pt/Ta/Pt (3/70/3 nm) using e-beam lithography and lift-off. Platinum (used as a sticking layer to graphene) and Tantalum were sputter deposited. The critical temperature of the leads is 2.5K and critical field 2T. Figure 6.17 shows an optical and SEM image of the sample. The distance L between electrodes of the measured junction was of 330nm and its width $W = 2.7\mu m$. Two terminal differential resistance measurements were done and carrier density was controlled through a voltage applied to the doped silicon (gate voltage). Figure 6.18 shows the gate voltage dependence of resistance measured at 4K. The Dirac point is at 5V showing that the sample is electron doped. From these data the mean free path and mobility were deduced,

$$l_e = \frac{h\sigma}{2k_F e^2} \qquad \mu = \frac{\sigma\pi}{ek_F^2}$$

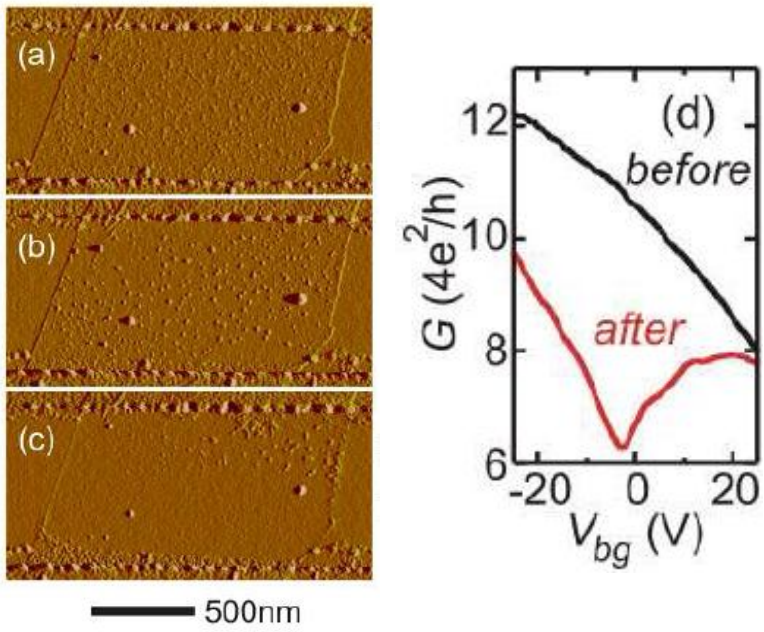

FIGURE 6.16 – AFM image of a graphene sample after exfoliation (a), after a first annealing (b) and after a last annealing (c). Gate voltage dependence of the two point conductance changes with annealing as is shown in (d). Taken from [36]

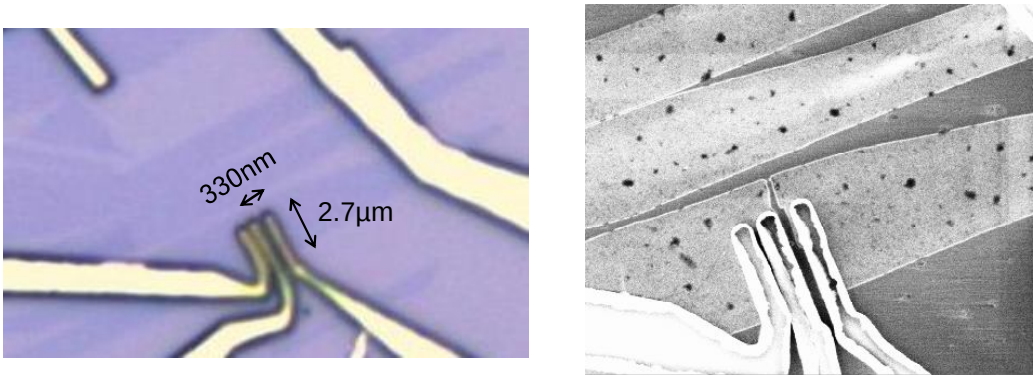

FIGURE 6.17 – Optical image of the sample (left) and SEM image after experiment (right). At the end of the experiment the graphene junction ripped after a last large current annealing

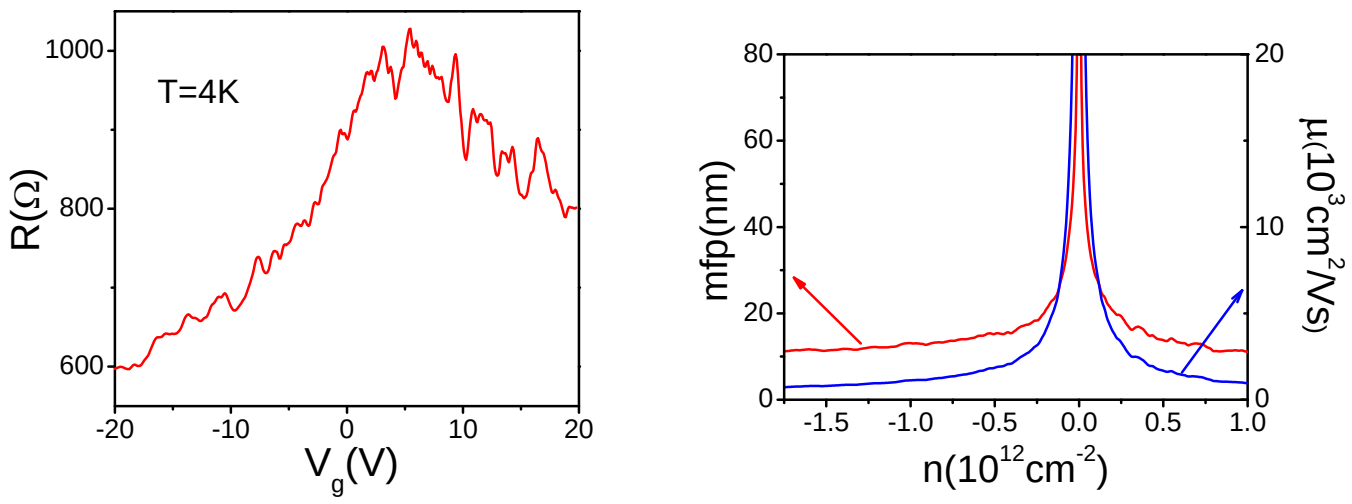

FIGURE 6.18 – Mean free path and mobility of the sample as a function of electron density (right) calculated from the gate voltage dependence of the resistance at 4K (left)

using

$$k_F = \sqrt{\frac{\epsilon_r \epsilon_0 \pi}{ed}} \sqrt{V_g - V_{Dirac}}. \tag{6.6}$$

Figure 6.18 shows the mean free path and mobility for the sample at 4K. Away from the Dirac point at a density of $n = 5 \times 10^{11} cm^{-2}$ we find a mean free path of $l_e = 15nm$ which corresponds to diffusive transport. Diffusive transport is due to scattering with impurities in graphene and defects between graphene and the SiO_2 substrate. As was seen in a preceding chapter, the most likely scatterers in graphene are short range (non charged) impurities such as ad-atoms. Graphene has in general a great spatial inhomogeneity in doping, which gives rise to a gate voltage width of Dirac point. In our sample this is translated into an inhomogeneity of the Fermi energy of about $85meV$, deduced using the conversion of gate voltage into Fermi energy via the plane capacitor model, $E = 30\sqrt{V_g} meV$ (see equation 6.6). Mobility was measured around $2000 cm^2/Vs$ (before annealing) which is lower than found by other groups (a mobility of $20000 cm^2/Vs$ is reported in [33] and [38] for graphene on substrate). The low mobility of our sample can be attributed to contact resistance which lowers the apparent mean free path and mobility deduced from the total resistance.

Figure 6.19 shows the gate voltage dependence of the two probe resistance measured at 60mK before annealing and after three different annealings. After each annealing and before doing any measurement we wait for some minutes while the dilution refrigerator returns low temperatures, since the temperature could go up to 10K during annealing. The first annealing was done at 3mA during approximately 30 seconds, which corresponds to a current density $J = 2 \times 10^8 A/cm^2$ (if we take graphene thickness to be 0.36nm). The second annealing was of 6mA during 10 seconds and the last annealing of 11mA during some seconds.

Before and after the first annealing, the Dirac point was located near 5V. This offset is attributed to doping by charged impurities on graphene or impurities between graphene and the substrate. After a second annealing the Dirac point was shifted by more than 20V and the resistance decreased by a factor of 2 far from the Dirac point and by a factor of 8 with respect to the original Dirac point. After the third annealing the resistance decreased even further and a full proximity effect was induced in the sample with zero resistance at low current bias. This indicates that annealing not only induced a doping in the sample and might have improved the mean free path making the sample cleaner, but the most important,

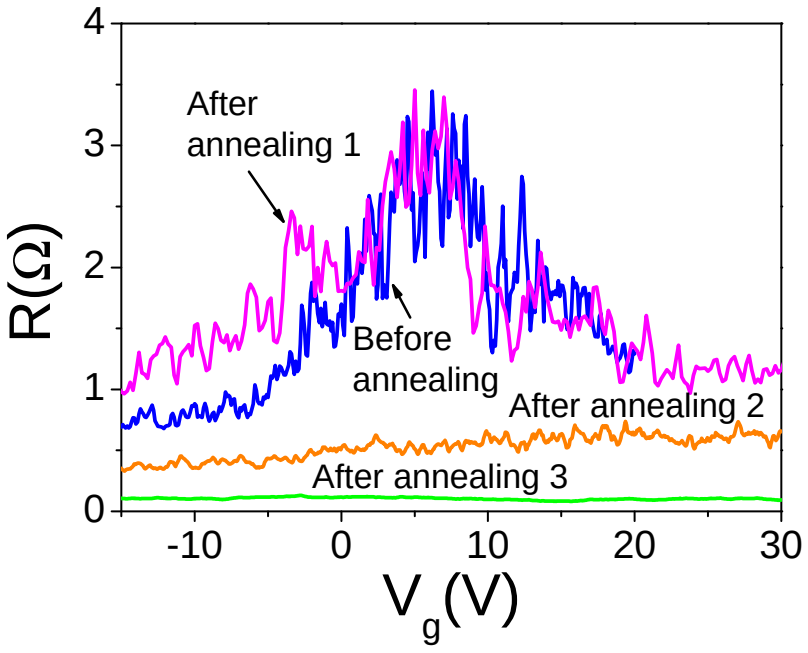

FIGURE 6.19 – Gate voltage dependence of the two wire resistance of the sample before and after different annealing steps. The last annealing induced a full proximity effect in the sample : a supercurrent ran through the graphene. This curve was measured with a 200G magnetic field which destroys proximity effect and thus measures the intrinsic sample resistance in this final stage. Oscillations in resistance correspond to reproducible conductance fluctuations.

it enhanced the electrical contact to graphene. Indeed, increasing doping or mean free path alone would not have caused the appearance of a supercurrent, it would only have increased the value of an already existing critical current.

Let's now discuss the effect of annealing on the proximity effect. Figure 6.20 shows the two probe differential resistance of the sample at 60mK after the different annealing stages. It can be remarked again that the S/graphene/S junction resistance decreases with annealing over the entire bias voltage range. In particular the zero bias peak disappears at the last annealing step when a supercurrent is induced in graphene (there is a zero resistance state at zero bias). A second effect of annealing is increasing the number of anomalies attributed to multiple Andreev reflections (MAR) occurring at the graphene/superconducting electrode interface. Different anomalies associated to MAR are observed after the 3 annealings. They can be identified in figure 6.20 but mostly in figure 6.21.

In figure 6.21 I plot the differential resistance characteristics after the first and the second annealing. The different curves correspond to different gate voltages showing that gate voltage has no influence on Andreev reflections. The effect of annealing is in contrast clear. Comparing both figures it can be noticed that a new anomaly appears after the second annealing and that high order anomalies become better defined. Comparing the central (low bias) peak of the differential conductance after the first and the second annealing step, it can also be seen that the amplitude and width of the peak decreases, which explain the fact that anomalies get better defined.

Resistance dips after the first annealing appear at voltages of 167, 253 and 482 μV which is close to $2e\Delta/n$ with $n = 1, 2, 3$. A fourth dip appears after the second annealing at $96\mu V$ which corresponds to n=5. In the third annealing, anomalies are smoothed due to improved transparency of the interface

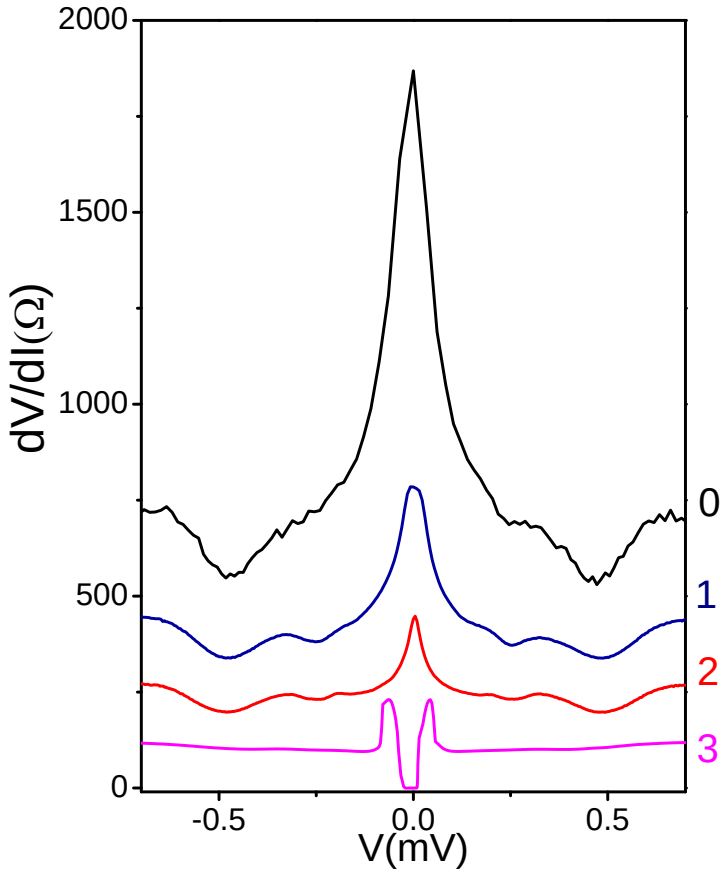

FIGURE 6.20 – Differential resistance vs bias voltage for the different annealing steps. The curves were taken at gate voltages of 0, -20, -16 and 15V respectively. In curve 3 the 40Ω resistance of the wires leading to the sample was subtracted. Curves are not shifted vertically.

but they don't disappear completely as would be expected for a perfectly transparent interface [39]. The superconducting gap of our junction is then $\Delta = 250\mu eV$. This same value was found in a different sample with a tunnel junction formed by a graphene sheet and a similar Pt/Ta/Pt trilayer. dI/dV characteristics for this sample were shown at the beginning of this chapter (figure 6.3).

The superconducting gap of our S/graphene/S junction is smaller than the one predicted by the BCS formula $\Delta_{BCS} = 1.76 \times k_B T_C = 379\mu V$ given the measured critical temperature $T_C = 2.5K$. This can be attributed to the thin Pt layer deposited between graphene and the Ta layer. It is known that the measured T_C of a Pt/Ta bilayer with thick Ta is practically the bulk T_C of Ta whereas the gap can be much smaller than the one of bulk Ta [41]. The reason is that the presence of Ta makes that in a two probe measurement there is a resistance drop at the critical temperature of Ta regardless the presence of Pt. On the other hand, the presence of Pt influences the electron-electron interaction which changes the gap of the density of the states.

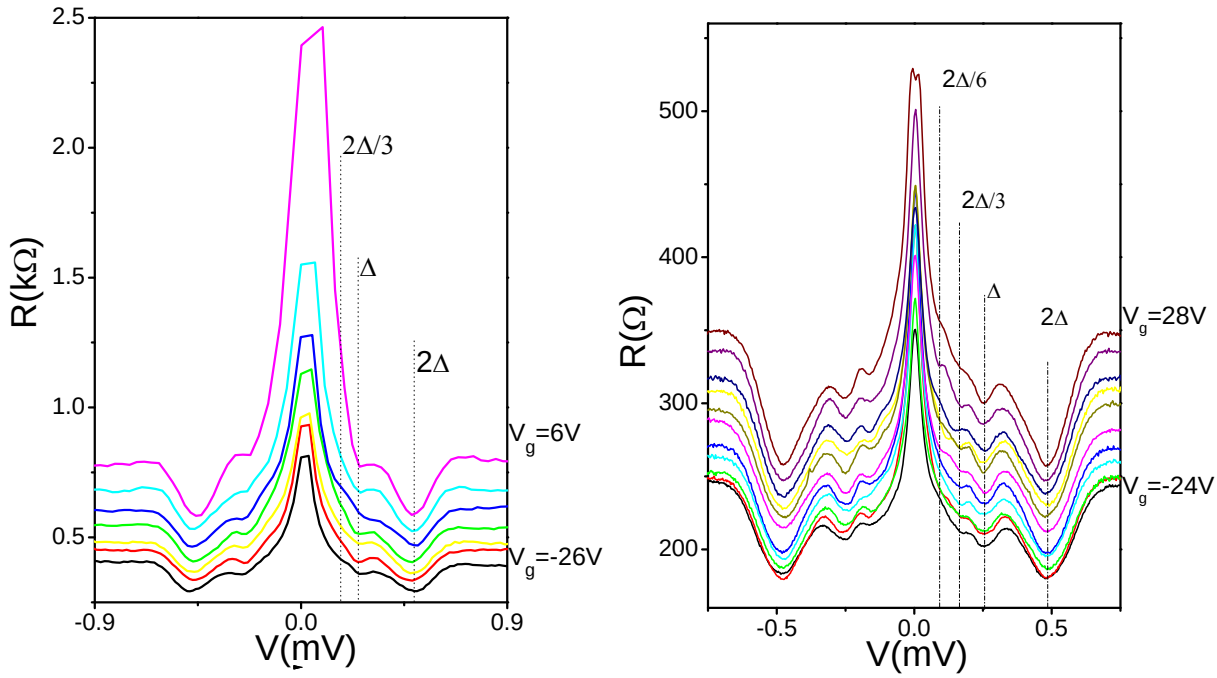

FIGURE 6.21 – MAR seen in the differential resistance as a function of bias voltage after annealing 1 (left) and annealing 2 (right) at 60mK. Gate voltage does not affect the curves qualitatively. Up to four MAR dips have been seen after the second annealing step. Note that curves are not shifted vertically.

6.4.2 The effect of a magnetic field on the dV/dI characteristics

Figure 6.22 shows the magnetic field dependence of the dV/dI characteristics. After the first annealing the effect of magnetic field is only smoothing the MAR anomalies and reducing the central zero bias peak. After the second annealing on the other hand, the magnetic field not only softens MAR peaks but also changes the zero bias peak to a large dip near H=2.5T, the critical field of Pt/Tantalum electrodes. The superconducting transition of graphene is shown in figure 6.23. It can be seen that the electrodes transit at $\approx 2.5T$ It is interesting in figure 6.22 (bottom) that the zero bias resistance dip disappears in the presence of a magnetic field giving rise to a peak and again to a dip back at 2T, below the transition of the contacts at 2.5T. For higher resistive samples (top), the zero bias resistance is not a monotonous function of the field, it goes through a minimum just below the critical field of the electrodes.

6.4.3 The effect of annealing on the transparency of electrodes and the OBTK model

Figure 6.24 shows the differential resistance normalized after the different annealings. It can be seen again in this figure that MAR anomalies get better defined after the second annealing. They get smoothed when a full proximity effect is induced in the sample (curve 3). This figure can be quantitatively compared to numerical simulations made by M. Octavio *et. al.* in which they considered an SNS junction with a variable transparency. The differential resistance is calculated for $T = 0$ as the barrier strength is changed from $Z = 0$ (no barrier) to $Z = 1$ (half of the incident electrons at the interface are scattered with a probability 1 of being Andreev reflected). Calculations are presented in figure 6.24. The presence of a barrier sharpens the peaks at the gap and its subharmonics and changes their overall shape.

When comparing with the dV/dI characteristics of our junction, we remark that the effect on subgap anomalies of decreasing barrier strength is that anomalies are smoothed. The differential resistance at the full proximity effect may correspond to an intermediate case between the most transparent case ($Z = 0$) and a weak barrier. However no calculations exist in our knowledge for a diffusive SNS junction with a finite interface transparency or better yet including the specificities of graphene. It would be interesting to know at which transparency supercurrent is induced in graphene and also if there is a specificity in MAR anomalies due to the particular band structure of graphene.

In the following I discuss generally the Octavio *et. al.* calculations known as the OBTK theory (M. Octavio, M. Tinkham, G. E. Blonder and T. M. Klapwijk) [39]. In OBTK theory, a Boltzmann equation approach is used to calculate the electron populations in the normal part of an SNS junction. With respect to a previous work [40], this theory considers Andreev reflections as well as normal reflections at the interface with the superconductor.

Octavio *et. al.* model S-N interfaces at positions $x = 0$ and $x = L$ as a δ-function potential of strength $V(x) = H\delta(x)$ as is shown in figure 6.25. All scattering events are assumed to occur at the SN interfaces and no scattering events are assumed to occur in the normal region, in other words the normal part is considered as ballistic. Their idea is to sum all electron currents in the normal metal, where electrons and holes are well defined. In order to do this, they calculate the distribution function of electrons traversing the normal part separating them in two subpopulations based on the direction of motion, $f_{\rightarrow}(E, x)$ and $f_{\leftarrow}(E, x)$. They relate these distribution functions at the boundaries with the distribution functions in the superconducting regions. Boundary conditions at the SN interfaces are :

$$f_{\rightarrow}(E, 0) = A(E)\big[1 - f_{\leftarrow}(-E, 0)\big] + B(E) f_{\leftarrow}(E, 0) + T(E) f_0(E)$$

$$f_{\leftarrow}(E, L) = A(E)\big[1 - f_{\rightarrow}(-E, L)\big] + B(E) f_{\rightarrow}(E, L) + T(E) f_0(E)$$

where A(E) is the probability of being Andreev reflected, B(E) the probability of being normal reflected and T(E) the probability of being transmitted. The expressions for the energy dependences of A, B and T can be written in terms of u_0 and v_0, the BCS parameters u, v evaluated outside the Fermi surface. They have the general form

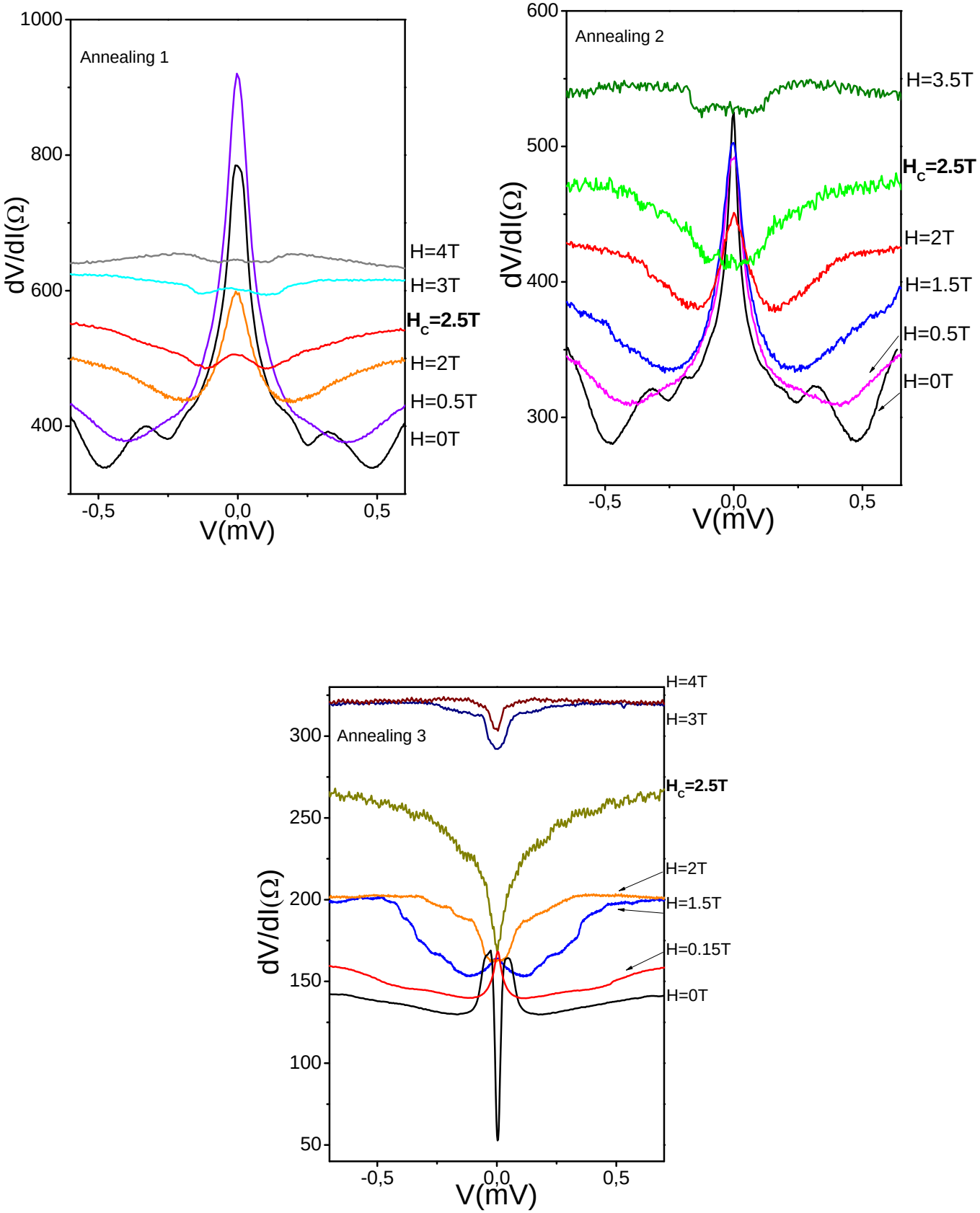

FIGURE 6.22 – dV/dI characteristics at different magnetic fields after the different annealings. Curves are not shifted.

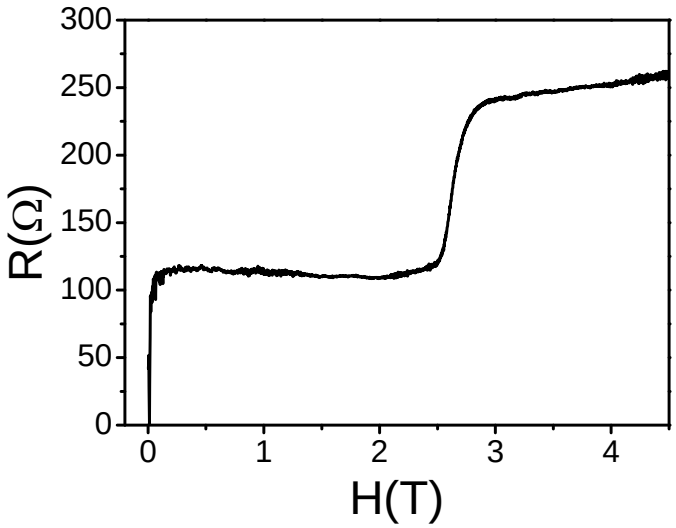

FIGURE 6.23 – Graphene's two probe resistance as a function of magnetic field. The large resistance jump at 2.5T correspond to the long Pt/Ta wires connected to the graphene sample that become normal at this magnetic field. The superconducting state of graphene is broken at low magnetic fields ($\approx 100G$).

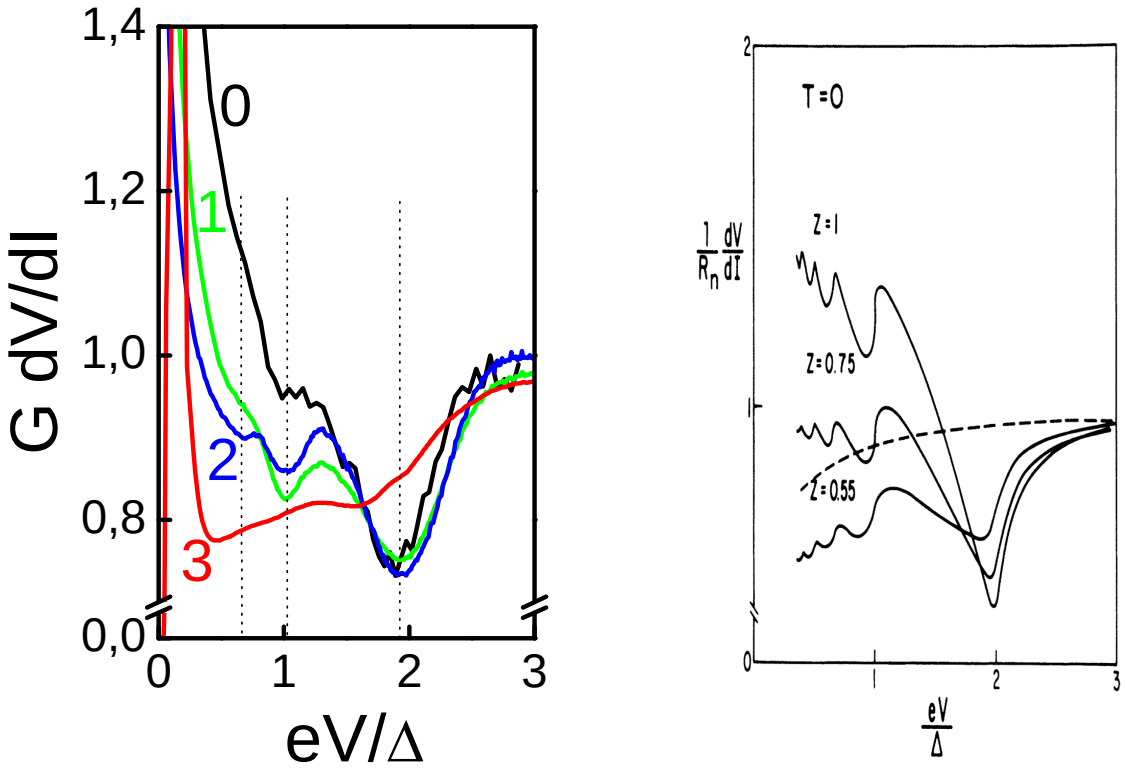

FIGURE 6.24 – Differential resistance normalized with a zoom around the MAR region (left) is compared to the results by [39] where the differential resistance dV/dI vs eV/Δ at $T = 0$ is calculated as a function of the barrier strength. Taken from [39]

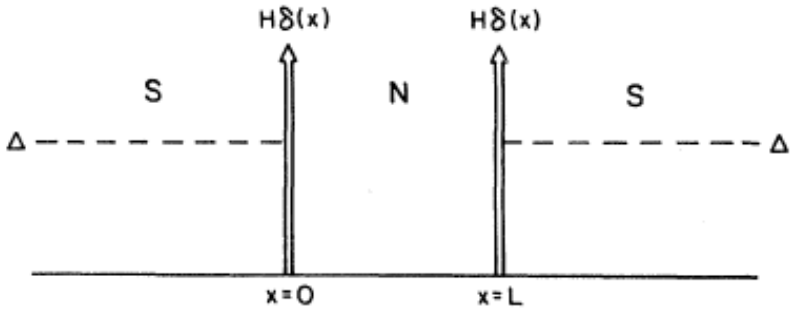

FIGURE 6.25 – SNS junction in OBTK model with δ functions potentials at the SN interfaces at $x = 0$ and $x = L$. $V = 0$

	A	B	T
$E < \Delta$	$\frac{\Delta^2}{E^2+(\Delta^2-E^2)(1+2Z^2)^2}$	1-A	0
$E > \Delta$	$\frac{u_0^2 v_0^2}{\gamma^2}$	$\frac{(u_0^2-v_0^2)^2 Z^2(1+Z^2)}{\gamma^2}$	$\frac{(u_0^2-v_0^2)(1+Z^2-v_0^2)}{\gamma^2}$

where

$$\gamma^2 = \left[u_0^2 + Z^2(u_0^2 - v_0^2)\right]^2 \qquad and \qquad u_0^2 = 1 - v_0^2 = \frac{1 + \left[(E^2 - \Delta^2)/E^2\right]^{1/2}}{2}$$

In the case where there is no barrier, (Z=0)

	A	B	T
$E < \Delta$	1	0	0
$E > \Delta$	$\frac{v_0^2}{u_0^2}$	0	$1 - A$

In this case, the probability of being Andreev reflected at $E < \Delta$ is equal to 1. The probability of being normal reflected is equal to zero. Probability of Andreev reflection and normal reflection for other transmission coefficients Z are shown in figure 6.26. A(E) has a sharp peak at the gap that becomes too narrow to be observable for large values of Z.

Some details of the procedure to solve $f_{\rightarrow}$ and $f_{\leftarrow}$ are given in [39]. Expression for these functions are selfconsistent equations that can be reduced to a finite set of equations and solved by writing them in a matrix form. Figure 6.27 shows the effect on distribution functions when there is a finite scattering probability ($Z \neq 0$) at $T = 0$. In the absence of scattering (Z=0), $f_{\rightarrow}$ and $f_{\leftarrow}$ are essentially displaced Fermi step functions except for some structure at $E > \Delta$ for $f_{\rightarrow}$, and at $E < -(\Delta + eV)$ for $f_{\leftarrow}$ which is related to a finite Andreev reflection above the gap. The effect of including a finite strength barrier is to change the distribution functions from Fermi step functions to thermal-like functions with $T_{eff} \approx eV/k_B$. Distribution functions present also a sharp structure of periodicity eV.

It is then the inclusion of a barrier or a normal scattering probability that sharpens the subgap structure in $f_{\rightarrow}$ and $f_{\leftarrow}$.

In order to calculate current going through the junction it suffices to take the difference between $f_{\rightarrow}$ and $f_{\leftarrow}$ and to integrate over E,

$$I = AJ = 2N(0)ev_F A \int_{-\infty}^{\infty} \left[f_{\rightarrow} - f_{\leftarrow}\right] dE$$

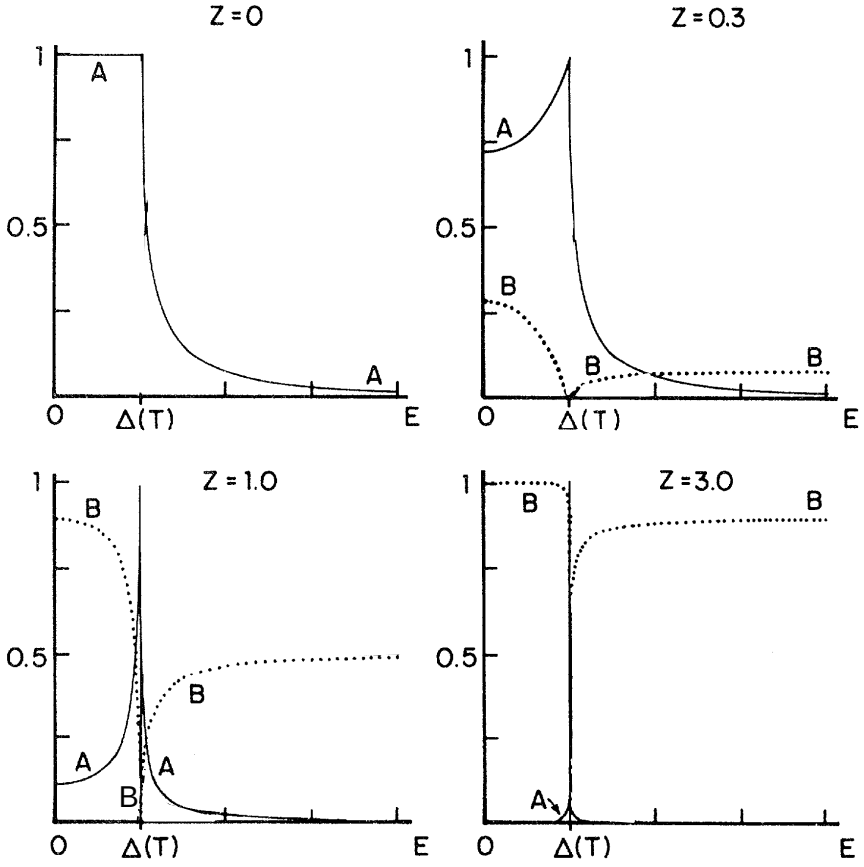

FIGURE 6.26 – Plots of normal reflection coefficient (B) and Andreev reflection coefficient (A) at the N-S interface. Z quantifies the barrier strength at the interface. Taken from [40]

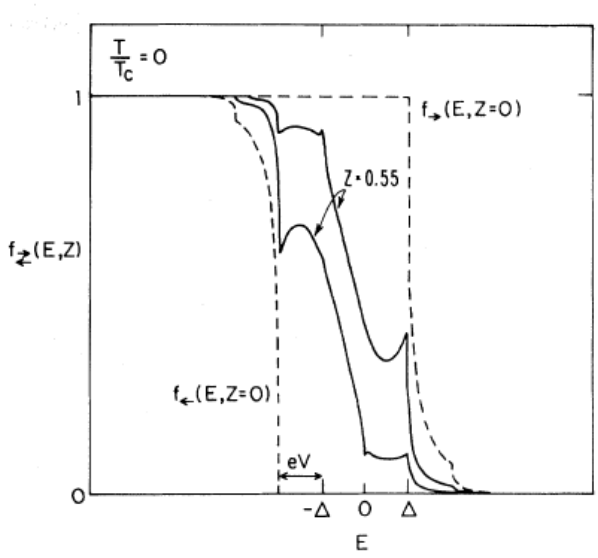

FIGURE 6.27 – Comparison of the distribution functions at $T = 0$ and $eV = \Delta$ for no scattering (Z=0) and finite scattering (Z=0.55)

where A is the effective cross-sectional area. Having an expression for current, dV/dI characteristics can be calculated, as shown in figure 6.24. It can be remarked again in figure 6.24 that the effect of including a normal scattering ($Z \neq 0$) is to sharpen the peaks at the gap and its subharmonics, as was observed in the S/graphene/S junction when the different annealings were made.

6.4.4 Induced supercurrent in graphene

We now turn to the supercurrent induced in graphene after the third annealing step. As is shown in figure 6.28, we saw a small and monotonous gate voltage dependence of the magnitude of the critical current. This is due to the fact that after the last annealing step the Dirac point moved to a non reachable voltage. In the color plot orange corresponds to zero resistance and red to the normal resistance, around 90Ω. Figure 6.29 shows the V(I) curve at 60mK and $V_g = 15.5V$. There is a zero resistance state for currents smaller than $I_C = 600nA$ and a linear dependence for larger currents. The corresponding normal resistance is $R_N = 90\Omega$. The switching current varies from 720nA at $V_g = -64V$ to 480nA at $V_g = 64V$ and the normal resistance varies from $R_N = 80\Omega$ to $R_N = 105\Omega$. The product $R_N I_C$ varies between $58\mu V$ and $50\mu V$, which is roughly $\Delta/5e$.

The ratio of the superconducting coherence length and the size of the sample is used to classify diffusive SNS junctions in short or long junctions. Short junctions are those with a length L much shorter than the superconducting coherence length

$$L << \xi = \sqrt{\frac{\hbar D}{\Delta}},$$

where D is the diffusion coefficient $D = \frac{v_F l_e}{2}$ and l_e the mean free path. In this regime of short junctions, the Thouless energy is bigger than the superconducting gap ($E_{Th} >> \Delta$), the characteristic energy is thus Δ and the product $R_N I_C$ is given by (as found numerically by P. Dubos [42])

$$R_N I_C \approx 2.07\Delta$$

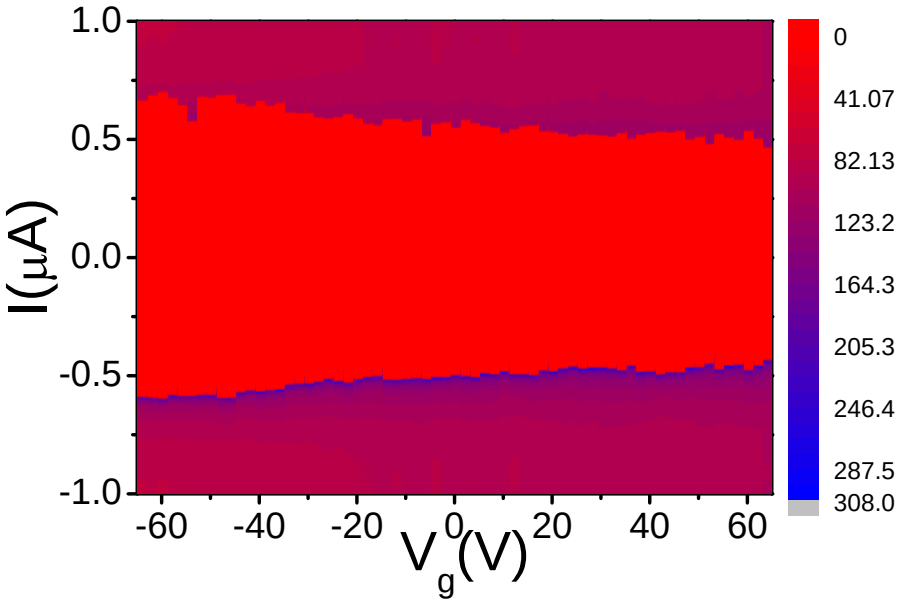

FIGURE 6.28 – Color coded differential resistance as a function of the bias current and the gate voltage. Orange means zero resistance.

Long junctions on the other hand, have a greater length L than the superconducting coherence length

$$L >> \xi = \sqrt{\frac{\hbar D}{\Delta}}.$$

The superconducting gap is bigger than Thouless energy $\Delta >> E_{Th}$ and then the characteristic energy scale is the Thouless energy. In this regime $eR_N I_C$ grows linearly with E_{Th} [42]

$$eR_N I_C = 10.82 E_{Th}$$

The minimum between Δ and $10E_{Th}$ determines the characteristic energy of the junction and also the critical current.

To find out the regime of our junction, we calculated the superconducting coherence length ξ and compared it with the size L of the junction. We used the elastic mean free path l_e after annealing 3, where the Dirac point is not clearly defined but is estimated to be at a gate voltage $V_g = 65V$. The mean free path calculated at a gate voltage of $V_g = 15.5V$ is $l_e = 46nm$, which yields $\xi = 245nm$. This of the order of the distance between contacts, $L = 330nm$. The Thouless energy is then of the same order as the superconducting gap,

$$E_{Th} = \hbar D/L^2 = 133\mu eV \qquad \Delta = 250\mu eV$$

and our S/graphene/S junction is in the intermediate regime between long and short junction. However, the temperature dependence of the switching current points to a rather short junction since it follows a Kulik-Omelyanchuck type dependence. We have compared the temperature dependence of the critical current in the S/graphene/S junction with different theories as is shown in figure 6.30. Ambegaokar and Baratoff have developed a complete theory for a tunnel junction in the dc regime (V=0). In this regime Critical current is :

$$I_C(T) = \frac{\pi}{2R_N e}\Delta(T)\tanh\frac{\Delta(T)}{2k_B T}$$

where $\Delta(T)$ is the equilibrium value of the energy gap and R_N is the resistance of the junction in the normal state. $\Delta(T)$ is almost constant al low temperatures. Here $R_N I_C$ does not depend on any parameter

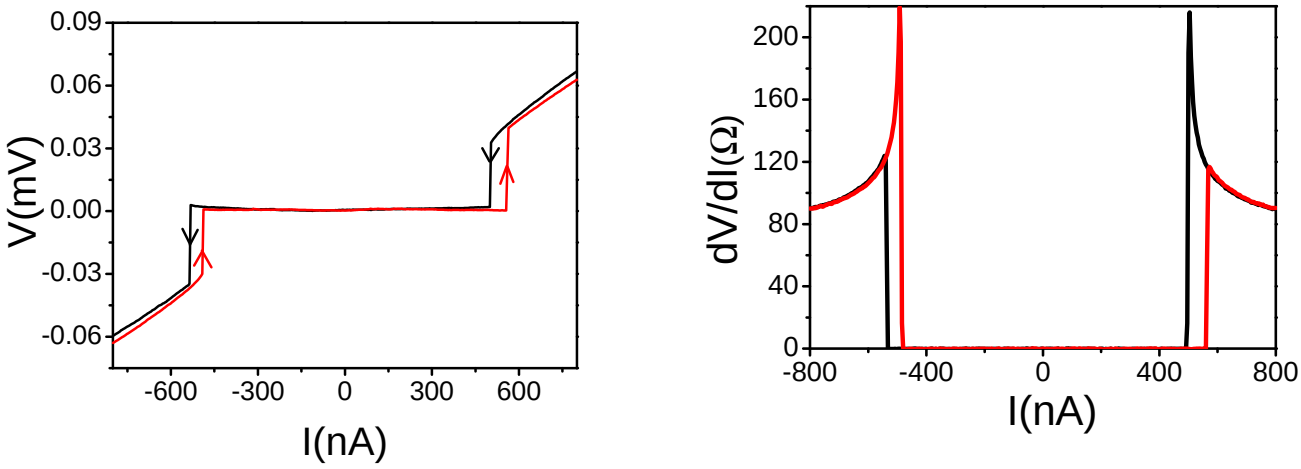

FIGURE 6.29 – I(V) curve (left) and dV/dI(I) characteristics of the S/graphene/S junction after the third annealing, where a full proximity effect is induced in the sample. Data was taken at 60mK.

of the barrier but only on the operating T and critical temperature through $\Delta(T)$. The dependence of critical current on temperature is shown in figure 6.30. For diffusive short weak links ($L << \xi$) which have a length L much larger than the mean free path of electrons l_e, a theory has been developped by Kulik and Omelyanchuck in 1975 which is also shown in figure 6.30. The temperature dependence of our S/graphene/S junction seems to follow the theory of diffusive short links.

The ratio $L/\xi = 1.3$ leads to a theoretical $R_N I_C$ product

$$R_N I_C = \frac{1.3\Delta}{e}$$

which is 6.5 times bigger than what is measured, $R_N I_C = \Delta/5e$. This discrepancy being too large to be explained by only an interface resistance, can be due to dephasing by fluctuators in graphene and the electromagnetic environment, which would cause a switching current smaller than expected.

6.4.5 Magnetic field dependence of the switching current as a proof of full proximity effect induced in graphene

A question that arises is whether the induced supercurrent could be caused by migration of superconducting grains onto the graphene sheet during annealing. These grains could form a superconducting weak link through which the supercurrent would flow. The experimental answer to this question is shown in figure 6.31. This figure shows the switching current modulated by the magnetic field (applied perpendicularly to the graphene sheet) which has the form of a Fraunhofer diffraction pattern like the one of figure 6.8. This dependence is characteristic of a wide rectangular superconductor-normal metal-superconductor junction. The fit using expression 6.4 is not perfect, in particular the effective sample area must be increased by a factor of two to fit the experimental data. The larger effective area may be explained by a finite penetration depth and non-local trajectories in the graphene sheet beyond the superconducting electrodes. The penetration depth for a disordered superconductor in the presence of a perpendicular magnetic field is given by

$$\Lambda_\perp = \frac{\Lambda_0^2 \xi_0}{l_e d}$$

where $\Lambda_0 = \sqrt{m/(ne^2\mu_0)}$ is the London penetration depth in a clean metal, $\xi_0 = \hbar v_F/(\pi\Delta)$ is the clean superconducting coherence length, l_e the mean free path in the superconductor, d the superconductor

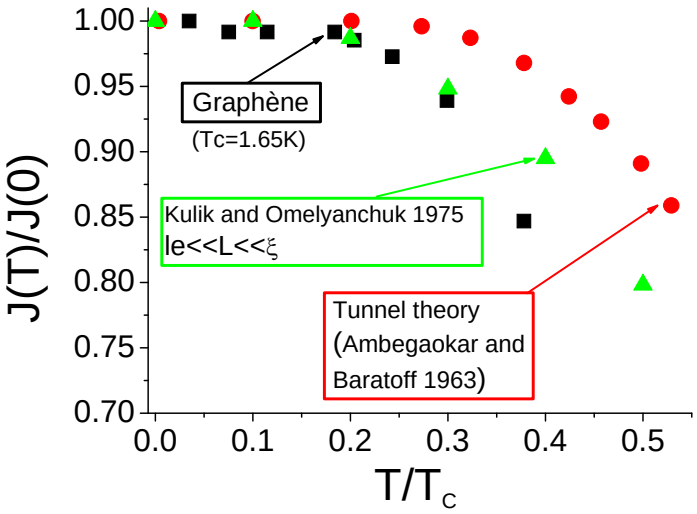

FIGURE 6.30 – Temperature dependence of the switching current of the S/graphene/S junction (square black points) compared to the Ambegaokar-Baratoff theory for tunnel junctions (red circles) and the Kulik-Omelyanchuck theory for diffusive short weaklinks (green triangles). Data follows theory for short weaklinks.

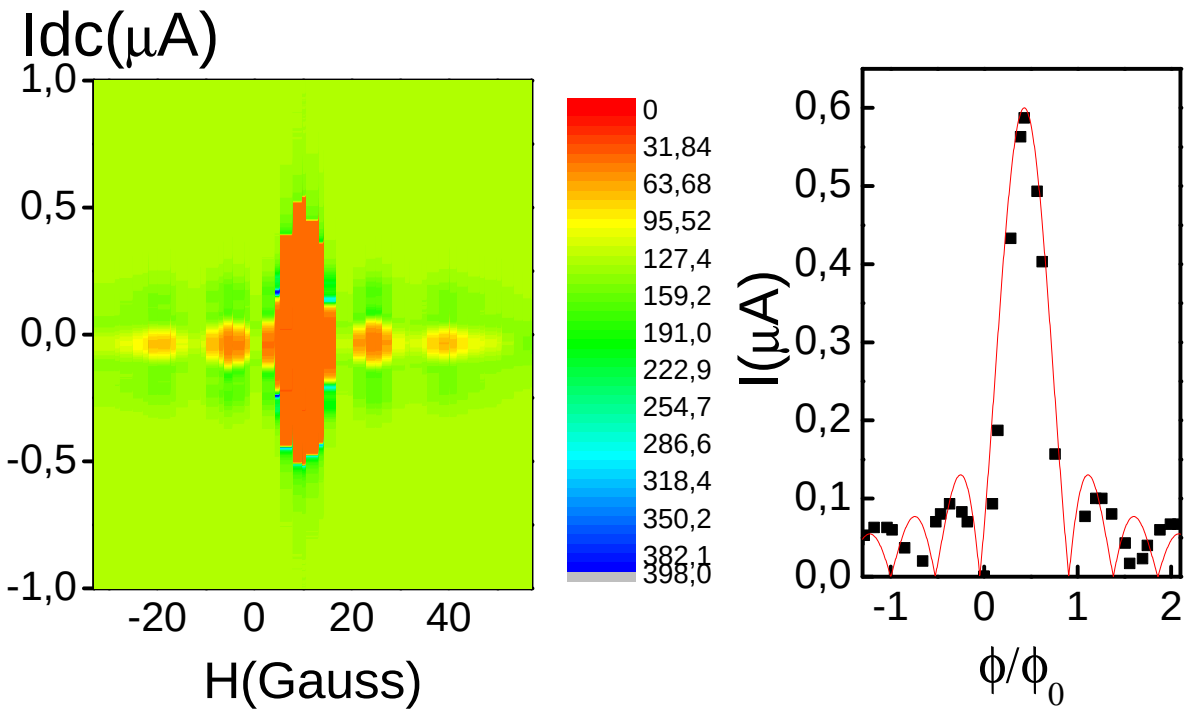

FIGURE 6.31 – Color coded differential resistance representing the modulation of the switching current by the magnetic field (Orange means zero resistance). The form of this figure is known as Fraunhofer diffraction pattern by analogy with optics, its origin is explained at the beginning of this chapter.

thickness and n the electron density. This yields a perpendicular penetration depth for our sample

$$\Lambda_\perp = 120nm,$$

which practically doubles the effective normal surface. In conclusion, the field periodicity of the interference pattern excludes the formation of a superconducting tantalum link crossing our graphene sample. The observed supercurrent comes from a full proximity effect induced in graphene.

6.5 Universal conductance fluctuations UCF in graphene with superconducting electrodes

Before the last annealing step which induced a supercurrent in graphene, reproducible conductance fluctuations were observed. As was seen in a previous chapter, reproducible conductance fluctuations are a signature of phase coherent transport in a system and they have some specificities in graphene. In this sample with superconducting electrodes, we have also observed reproducible conductance fluctuations, with the particularity that the variance decreases in the presence of a magnetic field (the variance increases in the superconducting regime).

It is known that for a normal-superconducting system, the onset of superconductivity increases the amplitude of conductance fluctuations. Beenakker and Brouwer [43] have found using random matrix theory, that the amplitude of fluctuations δG in a NS junction with respect to fluctuations in a NN junction when there is time reversal symmetry τ (no magnetic field) is

$$\delta G_{NS}(B=0) \approx 2\delta G_{NN}(B=0).$$

They have also found that δG_{NS} is insensitive to the time reversal symmetry breaking,

$$\delta G_{NS}(B=0) \approx \delta G_{NS}(B\neq 0)$$

Altland and Zirnbauer have found on the other hand [44] that when time reversal symmetry is broken, δG_{NS} decreases by a factor of $\sqrt{2}$,

$$\delta G_{NS}(B=0) = \sqrt{2}\delta G_{NS}(B\neq 0)$$

and that in the absence of magnetic field δG_{NS} is $2\sqrt{2}$ times bigger than δG_{NN}.

$$\delta G_{NS}(B=0) = 2\sqrt{2}\delta G_{NN}(B=0).$$

Figure 6.32 shows reproducible conductance fluctuations vs V_g measured after annealing step 1. At low temperatures and zero magnetic field we have a coherent NS system that shows conductance fluctuations with an amplitude $\delta G_{NS}^{H=0} = 2.4e^2/h$. We compare this value to the conductance fluctuations in the NN junction measured after applying a magnetic field, applying a DC current or heating the junction. When we apply a magnetic field of $4T$ the superconducting electrodes become normal and we have a coherent NN system at low temperature and high field whose fluctuations have an amplitude $\delta G_{NN}^{High\ H} = 0.8e^2/h$. This is three times smaller than what is measured in the superconducting regime and it is close to the prediction of Altland and Zirnbauer. A close value is also obtained when a DC current is applied to the sample (NN system in zero field) $\delta G_{NN}^{H=0} = 0.7e^2/h$ and at 4.2K (NN system with shorter coherence length) $\delta G_{NN}^{High\ T} = 0.7e^2/h$. Amplitude of fluctuations was deduced by calculating the variance of the whole gate voltage dependence of conductance after an envelope was subtracted. Contact resistance was unknown. A better treatment of conductance fluctuations was done in the preceding chapter where the electrodes of the sample were normal metals. There, the amplitude of fluctuations was calculated by intervals of 3V in gate voltage and we had better statistics.

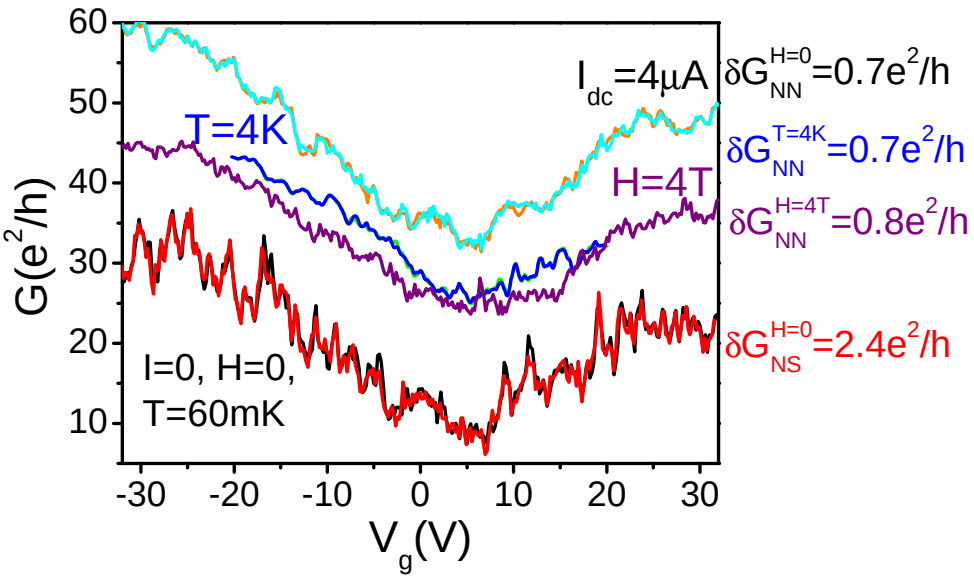

FIGURE 6.32 – Gate voltage dependence of conductance after annealing 1, in different conditions of temperature, bias current and magnetic field. The fluctuations are reproducible. The standard deviation deduced from the high pass filtered curve, is $2.4e^2/h$ for the low temperature zero field curve in which electrodes are superconducting ; $0.8e^2/h$ for the low temperature curve above the critical field of the superconductor(4T), $0.7e^2/h$ for the low-temperature zero field curve with a current bias above the critical current of the electrode. The fluctuations are $0.7e^2/h$ for the curve at 4.2K where the electrodes are normal.

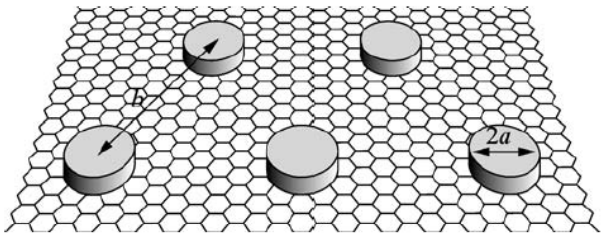

FIGURE 6.33 – Graphene sheet covered with superconducting islands. Taken from [47]

Reproducible conductance fluctuations in graphene with superconducting contacts have also been observed by *Trbovic et. al.* [45]. They used a few graphene layer nanoribbons connected to Ti/Al leads. They observed an enhancement of the conductance variance of the sample in the superconducting state with respect to the normal state by a factor between 1.4 and 1.8. They explained the difference with theory by a finite phase-breaking length $l_\phi < L$ at the temperature at which the sample is superconducting.

6.6 Superconducting proximity effect induced in graphene by superconducting islands

An other way of inducing superconductivity in graphene is through superconducting islands. Graphene can become superconducting by proximity effect by printing small superconducting islands that cover a tiny fraction of the graphene area. Feigel'man *et. al.* [47] have shown that even a small area of graphene covered by superconducting islands with a good electric contact to graphene, can lead to a macroscopically superconducting state of graphene with T_C in the Kelvin range (for a certain average distance between the islands).

6.6.1 Theoretical predictions for proximity effect

Feigel'man *et. al.* considered a system of superconducting islands distributed uniformly in the graphene sheet as shown in figure 6.33. The radius of the islands a is smaller than the distance b between the islands and the mean free path is smaller than or of the order of the radius of the islands $l \leq a$. They assumed graphene Fermi energy bigger than the island superconductive gap ($E_F >> \Delta_0$).

They say that graphene can become superconducting by proximity effect with superconducting islands because of the following reasons :

1. Graphene has a high diffusion constant $D \geq 10^2 cm^2/s$
2. Graphene has a very low electron density (in comparison to metals)

Thus it allows to combine moderate values of dimensionless conductance

$$\frac{\hbar}{e^2 R_\square} \geq 3$$

(where $R_\square$ is the square resistance of graphene) with a high Thouless energy

$$E_{Th} = \frac{\hbar D}{b^2} \tag{6.7}$$

In fact, very large conductances don't favor the proximity effect. They can induce a suppression of superconductivity in the islands due the inverse proximity effect. In graphene, inverse proximity effect can be neglected since

$$G_{Graph}\delta \leq \Delta_0$$

where G_{Graph} is the conductance of graphene including interface conductance and δ is the level spacing of the islands. For small size islands, the level spacing can be large ($\delta \approx 1/L^2$) but this is compensated by moderate conductance (if contact resistance is small).

Graphene is treated in Feilgel'man's work as a normal diffusive 2D metal using Usadel equations. Their calculations show that it goes through a Berezinsky-Kosterlitz-Thouless transition in a temperature range of $T_c = 1 - 3K$ (for graphene with a diffusion coefficient $D = 500cm^2/s$ and distance between superconducting islands $b = 0.5\mu m$). Josephson coupling is short ranged at $T \approx T_C$. At $T > T_C$ phases in the different islands are decorrelated and at $T < T_C$ phases become identical. At $T << T_C$ Josephson coupling becomes long-range. In this regime, solution of Usadel equations leads to the formation of spectral gap E_g similar to the minigap in the SNS junctions. For an ideal interface between the superconductor and graphene, the value of this spectral gap is

$$E_g \approx \frac{2.65E_{Th}}{ln\big(b/4a\big)},$$

where E_{Th} is defined in equation 6.7. Like the minigap in SNS junctions, the spectral gap in graphene depends on the Thouless energy, that in this case, is determined by distance between nanoparticles. The predicted existence of a spectral gap is surprising since only a small fraction of graphene is in contact with the superconducting islands, it is actually strongly related to the structure of the islands assumed. Any irregularity on the position of the islands will give rise to a smearing of the gap. The gap will also get smeared by thermal fluctuations of the island's phases ϕ_i and by a finite thermal coherence length L_T. The gap is suppressed if the contact resistance with graphene is large.

Even in the presence of gap smearing, it is predicted that a strong suppression of the local density of states of graphene at $E < E_g$ should be observed by low temperature scanning tunneling microscopy. The presence of this spectral gap is signature of collective proximity effect. The corresponding spatial scale is

$$\xi_g = \sqrt{\frac{\hbar D}{E_g}} \approx b\sqrt{\ln\left(b/a\right)}$$

which plays the role of the low temperature coherence length in a superconductor in the dirty limit.

A low magnetic field at low temperatures creates vortices with a core size $\xi_g \geq b$ pinned by the underlying array structure and with a local density of states gapless in the core regions. In this situation a critical current is still expected. When a flux quantum crosses an area $2\pi\xi_g^2$ ($H = \phi_0/(2\pi\xi_g^2)$) the vortex cores overlap and the proximity gap is completely destroyed.

6.6.2 Superconducting islands on graphene for the study of superconducting transition with variable carrier concentration

An experimental work [48] has been published in which large superconducting islands are printed in graphene with small distances between them. The goal of this experiment is to address the question of superconducting transition analyzing separately the effects of disorder and carrier density. Kessler *et. al.* [48] deposited a non-percolating network of superconducting islands on graphene in order to have an homogeneous dirty superconductor over a tunable substrate. Here, the superconducting transition can be studied at fixed disorder and variable carrier concentration via a field effect on graphene. Figure 6.34 shows the sample measured.

For sample fabrication, the authors exploited the poor wettability of graphite. They evaporated Sn on pristine graphene at room temperature. Sn with its low melting point formed self-assembled islands with 80 ± 5 nm diameter and 25 ± 10 nm gaps between them. Even when 40% of the graphene surface is covered with Sn, the electronic properties of graphene remained, like mobility $\mu > 1000cm^2/(Vs)$ and bipolar transport. The value of mobility was however reduced by a factor five, the Dirac point was shifted and there appeareared an asymetry in electron-hole transport, as is shown in figure 6.34.

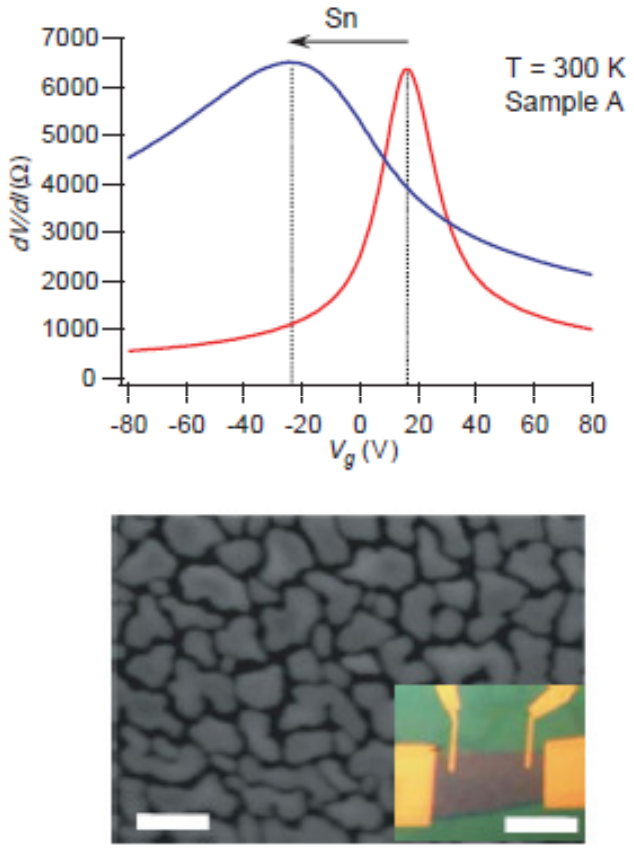

FIGURE 6.34 – Top : Gate voltage dependence of the differential conductance before and after the deposition of Sn in the work of Kessler *et. al.*. Dirac point gets shifted. Bottom : Scanning electron image of the sample (scale bar=100nm). Inset : optical image showing the four probe configuration (scale bar=10μm). Taken from [48]

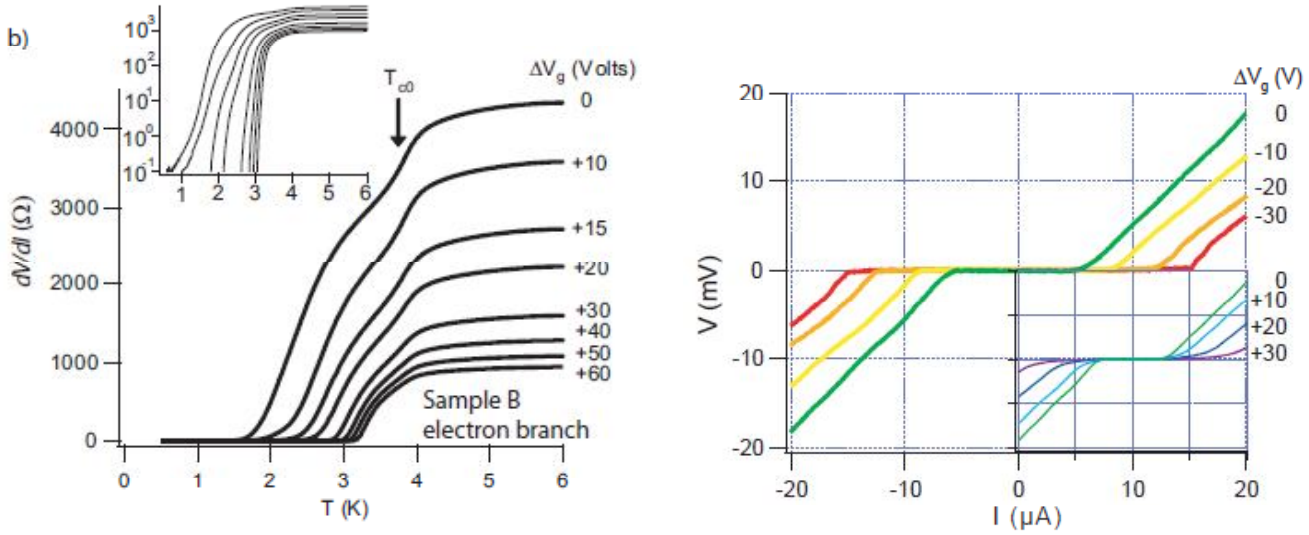

FIGURE 6.35 – Left : Graphene resistance versus temperature at different gate voltages (curves are similar for negative gate voltages). Dirac point is at $V_g = 40V$. The arrow indicates the superconducting transition of Sn islands. Right : Current voltage characteristics at 100mK and zero magnetic field for different gate voltages corresponding to hole transport. The inset represents similar curves for electron transport. Taken from [48]

Superconducting islands not only changed the normal transport properties of graphene, but mainly induced superconducting correlations in graphene. Figure 6.35 shows the temperature dependence of resistance for different gate voltages. A first partial drop occurred at $\approx 3.5K$ that didn't change with gate voltage. This correspond to the superconducting transition of Sn. At lower temperatures full range superconducting correlations appeared and the sample became superconducting. The critical temperature of the sample had a strong dependence on gate voltage, as is shown in figure 6.35. It is qualitatively similar to the one observed in isolated graphene junctions of micron size, the difference being that supercurrent is maintained over distances of tens of microns, showing a full phase coherence in the system.

6.6.3 Superconducting islands on graphene that induce a tunable metal insulator transition

We have also studied samples of graphene with superconducting islands. Contrary to the experiment of Kessler *et al.*, the distance between particles ($\approx 50nm$) was much larger than the size of the particles ($5nm$). Samples were fabricated by Alik Kasumov by sputtering a thin layer of In (less than 1nm during $\approx 2s$) over graphene with the substrate previously heated at 300˚C. (The substrate was kept at this temperature during the deposition). Heating the substrate at 300˚C favors the formation of nanoparticles since melting temperature of nanoparticles is 150˚C. By choosing the temperature of the substrate it is actually possible to control the size of nanoparticles. The higher the temperature, the bigger the particles and the larger the distance between them. Figure 6.36 shows a preliminary sample in which In nanoparticles are deposited over a grid for transmission electron microscopy (TEM) covered with a thin amorphous carbone membrane. The crystallographic planes of the particles can be distinguished in the right panel of figure 6.36. Figure 6.37 shows a microscope image of the graphene sample before and after deposition of In nanoparticles. Bigger nanoparticles are formed on graphene than on the substrate. We measured gate voltage dependence of the two probe resistance before and after the deposition of nanoparticles (Figure

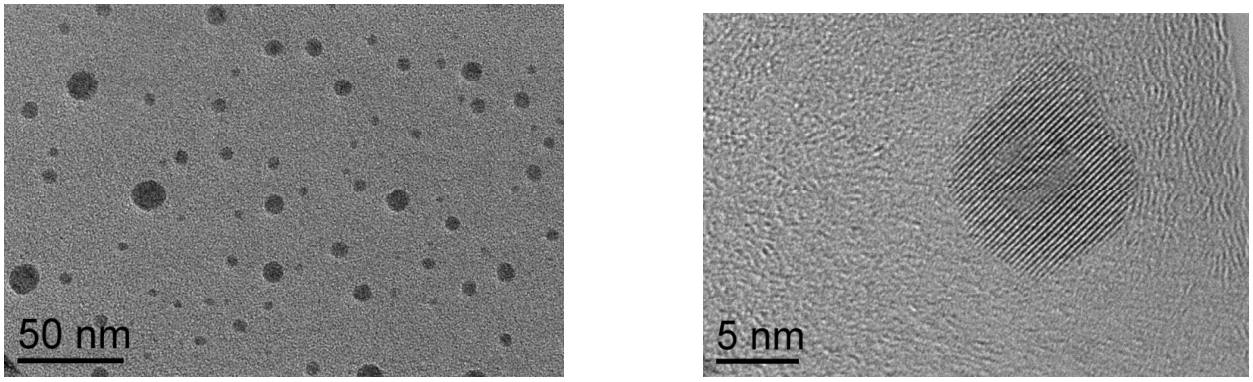

FIGURE 6.36 – Indium nanoparticles over a thin amorphous carbon membrane. Right : zoom on one nanoparticle.

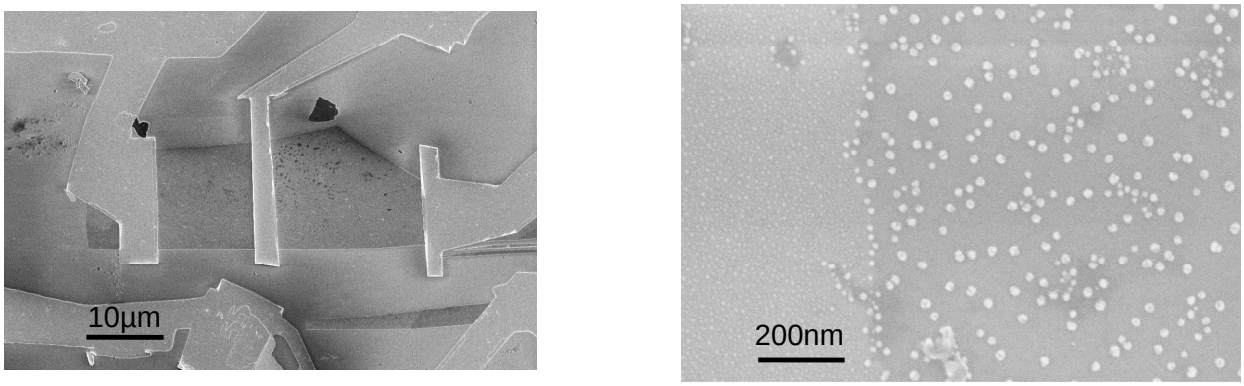

FIGURE 6.37 – Left : SEM image of the sample before the deposition of In nanoparticles. Right : Zoom over a region after deposition of In nanoparticles.

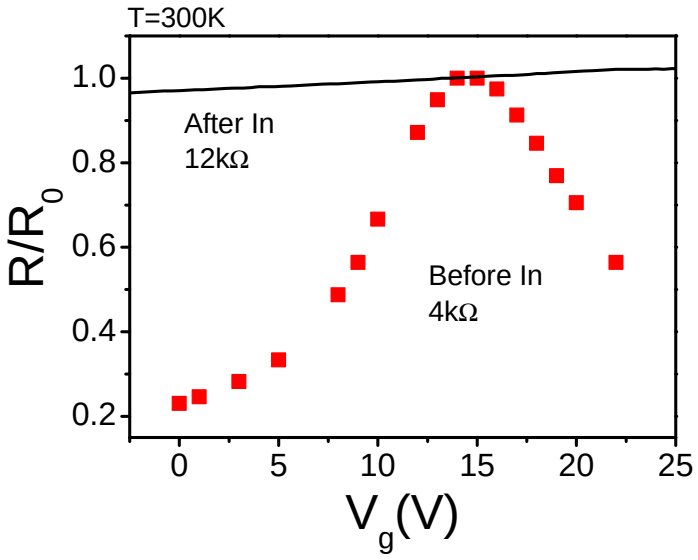

FIGURE 6.38 – Normalized two probe resistance versus gate voltage of the sample before and after deposition of In nanoparticles.

6.38). Resistance of the sample increased dramatically after deposition of the nanoparticles but was lowered back to $12k\Omega$ (three times de resistance before the deposition) after an annealing for 2 hours à $700^{\circ}C$. Dirac point moved to a gate voltage that was not reachable anymore with the back gate.

As in the work of Kessler *et al.* the Dirac point moved after deposition of nanoparticles. On the other hand, when going to low temperatures, contrary to what Kessler *et al.* found, graphene became insulating as is shown in figure 6.39 [2]. This figure can be contrasted with figure 6.35. In our case it is conductance and not resistance that dropped to zero when temperature was lowered. The explanation of the different behavior we find might be related to disorder in our sample. Sputtering a metallic layer over all the graphene surface is certainly more aggressive with graphene than the deposition by evaporation, used by Kessler *et al.*. Disorder induced in graphene during the deposition process might be responsible for the insulating behavior we observed. In Kessler's *et al.* sample the average density of superconducting islands is much larger this might have helped the appearance of a supercurrent crossing the sample, as is seen in figure 6.35.

It is known that disorder modifies the electronic wavefunctions of a system giving rise to an insulating state. Anderson showed that in the presence of a random potential, if disorder is important enough electronic wavefunctions tend to localize. If disorder is weak, the Fermi wavelength is still small with respect to the mean free path ($k_F l_e >> 1$) and the conductivity can still be expressed in terms of the Drude formula,

$$\sigma = \frac{ne^2\tau_e}{m}.$$

There are however quantum corrections to conductivity due to interferences between wavepackets. As was mentioned at the beginning of the previous chapter, conductance can be expressed in terms of a distribution probability of electrons initially at r_1 to reach r_2 (equation 5.1). This distribution probability has constructive interference terms associated to time-reversed paths that enhance the return probability (probability of being at O in figure 5.3) with respect to its classical value. This reduces the probability of reaching the point r_2 and decreases average conductivity. As was mentioned in the preceding chapter,

2. Data shown in figures 6.39 and 6.41 was taken and analyzed by Jordan Andieux during his internship in the group.

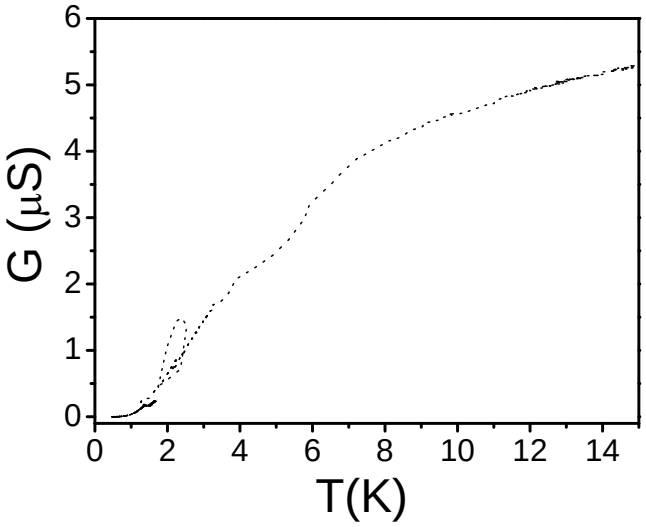

FIGURE 6.39 – Temperature dependence of the graphene conductance. At low temperatures graphene becomes insulating.

this is called the weak localization correction to conductivity.

In this situation of weak disorder, even if wave packets diffuse in a random way, they can still be described as plane waves delocalized all over the system. However, when $k_F l_e$ becomes of the order of 1 and at sufficiently low temperatures, for dimensions $d < 3$, the nature of diffusion greatly enhance the return probability and electron's trajectories have a tendency to localize in closed trajectories, entering into a regime of strong localization. In this regime the system is in an insulating state. The amplitude of wavefunctions decreases exponentially over a distance ξ_{loc} called the localization length.

$$|\psi^2(r)| \approx exp\Big(-\frac{|r-r_0|}{\xi_{loc}}\Big)$$

The localization length for $d = 2$ depends exponentially on disorder. It has the form

$$\xi_{loc}^{d=2} = l_e exp\Big(\frac{\pi}{2} k_F l_e\Big)$$

In the insulating regime, conductance can be thermally activated. When temperature is such that $L_\phi \approx \xi_{loc}$, transport is given by thermally activated jumps between neighbor localized volumes. Conductance is then given by

$$G(T) = G_0 e^{-E_{Act}/K_B T}$$

where E_{Act} is the transport activation energy.

The behavior of conductance versus temperature we have measured (figure 6.39) can be fitted well by such an activation energy law, as is shown in figure 6.40. Activation energy turns out to be $E_{Act} = 0.5meV$ which coincides with the superconducting gap of Indium ($0.54meV$). In the presence of a magnetic field activation energy changes slightly, as can be seen in figure 6.40.

Such a behavior has been observed in thin films of amorphous indium oxide [85] where a superconducting-insulating transition is driven by the application of a perpendicular magnetic field. In the insulating phase, the characteristic temperature of activated conduction is close to the superconducting transition temperature and changes when a magnetic field is applied.

However, in our samples the thermally activated behavior does not seem to be clearly related to the In particles becoming superconducting since it is still observed for temperatures larger than the critical

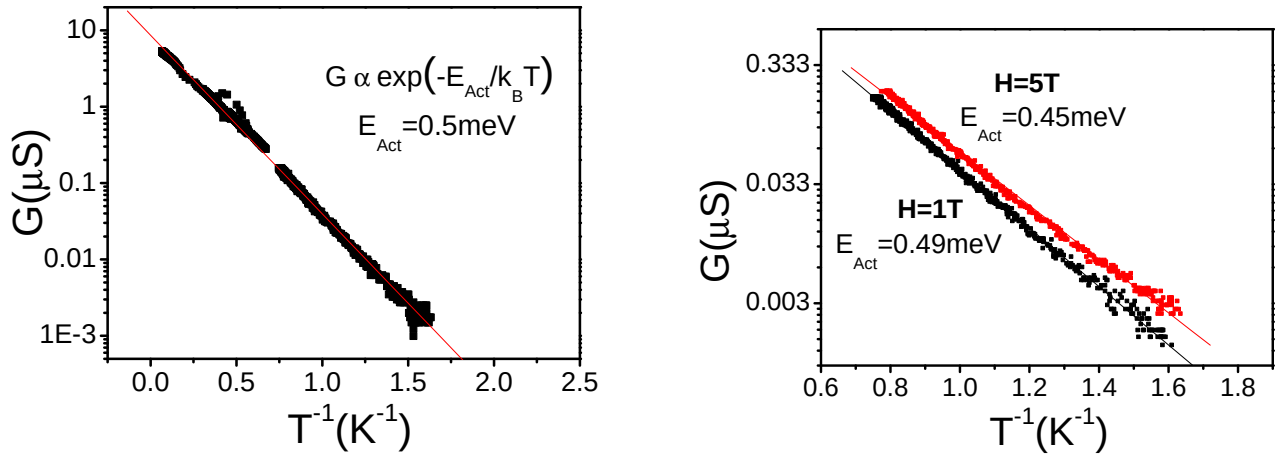

FIGURE 6.40 – Left : Temperature dependence of conductance in log scale. The sample follows a thermal activation behavior with an activation energy of $0.5meV$. Right : The activation energy decreases slightly with increasing magnetic field.

temperature of Indium $T > 3.4K$ ($T^{-1} < 0.3$). The thermally activated behavior puts in doubt the relationship between the insulating phase and superconductivity in our samples.

Activation energy can also be compared to the spectral gap E_g predicted by Feigel'man *et. al*,

$$E_g \approx \frac{2.65}{\ln(b/4a)} \frac{\hbar D}{b^2}.$$

If we consider that graphene has a diffusion coefficient $D \approx 10^{-3} m^2/s$ and that In particles are distant in average of $b = 50nm$, we have $E_g = 0.8meV$. However, the spectral gap E_g only has a sense in a superconducting sample.

We can also identify an insulating gap appearing in the dI/dV characteristics which decreases in the presence of a magnetic field perpendicular to the sample, as is shown in figure 6.41. This gap might be related to the superconducting gap of the nanoparticles but it is much larger. The critical magnetic field of the sample may correspond to a flux quantum going through one particle. Taking into account the dimensions of the nanoparticles, it should be of the order of $25T$ which explains why an applied magnetic field of $5T$ closes partially the gap.

$$B_C = \frac{\phi_0}{Area} = \frac{2.067 \times 10^{-15}}{\pi R^2} = 25T$$

Although, before such a high field, the superconductivity of the nanoparticles will should be destroyed at $B > 2\Delta/\mu_B = 15T$ with $\mu_B = e\hbar/2m_e$, according to Clogston criterium.

Figure 6.42 shows how increasing temperature closes the insulating gap. For this sample unfortunately, gate voltage was not efficient at low temperatures. On a second graphene sample on the other hand, that also presented an insulating behavior, we observed a gate voltage dependence of the insulating gap. Figure 6.43 shows the effect of depositing superconducting particles on the gate voltage dependence of resistance. A temperature annealing of $700^{\circ}C$ was also performed. The two probe resistance increased by a factor of ≈ 60 with respect to its value before the deposition of nanoparticles, much more than in the first sample. The gate voltage dependence of the differential conductance for this second sample can be observed in figure 6.45. For negative gate voltages, the gap becomes smaller, like if gate voltage had a similar effect

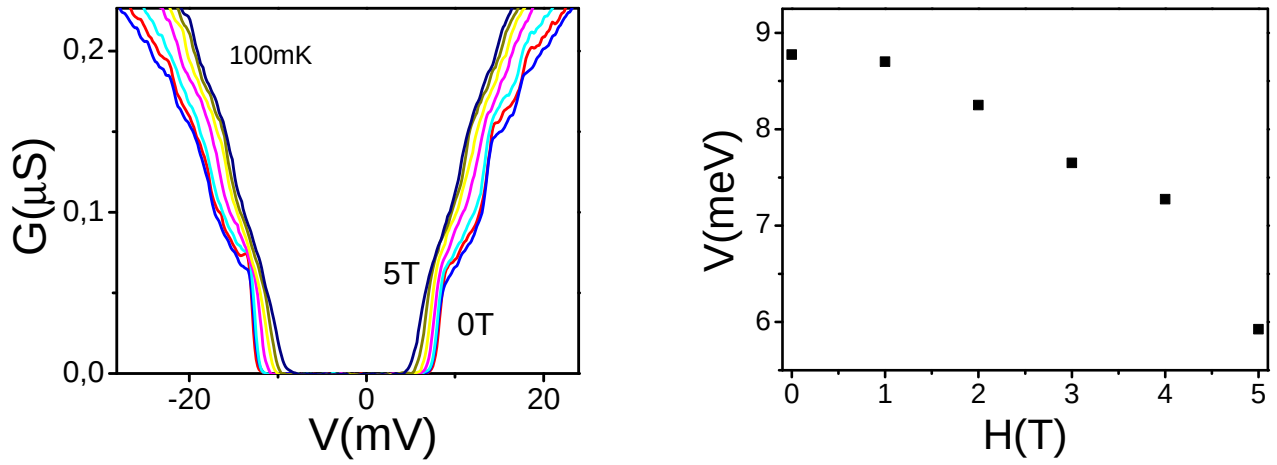

FIGURE 6.41 – Left : Differential conductance of graphene with In nanoparticles at different magnetic fields : $0T$, $1T$, $2T$, $3T$, $4T$ and $5T$. Right : Evolution of the isolating gap with magnetic field.

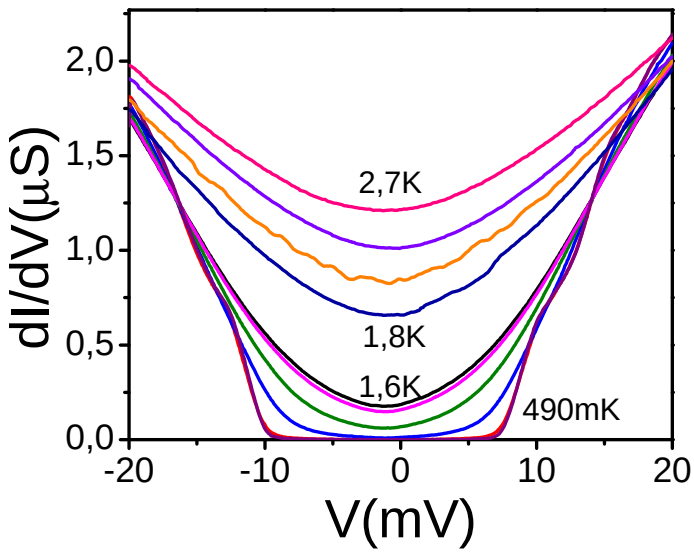

FIGURE 6.42 – Differential conductance of graphene with In nanoparticles at zero magnetic field and different temperatures. Temperatures are : 490mK, 550mK, 840mK, 1.2K, 1.5K, 1.6K, 1.8K, 2.2K, 2.4K and 2.7K

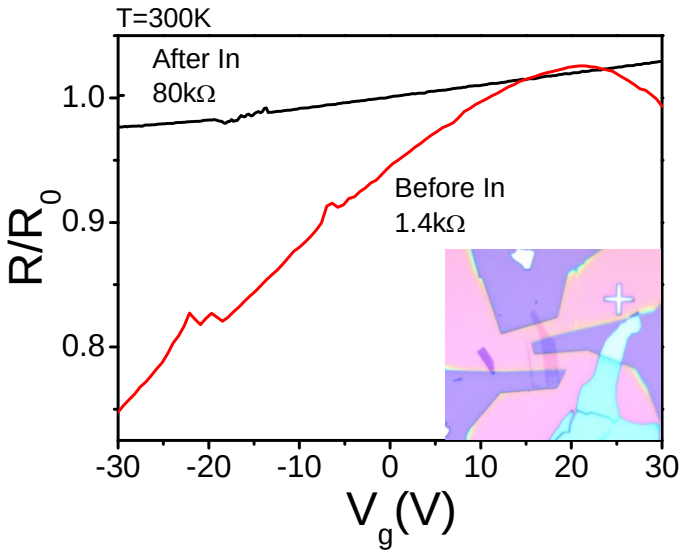

FIGURE 6.43 – Normalized two probe resistance versus gate voltage of the sample before and after deposition of In nanoparticles. Inset : optical image of the graphene sample before In nanoparticles.

than the one of magnetic field or temperature. The dependence of the insulating gap with the gate voltage is represented in figure 6.44. As is shown in figure 6.46, magnetic field as in the first sample, tends to close the superconducting gap. Increasing temperature also smooths the superconducting gap.

These measurements open the question of whether it is possible to induce an insulating-metallic transition in graphene by changing charge carriers. Graphene being bidimensional, it is susceptible to interesting quantum phase transitions. Two dimensions is the lower critical dimension for both localization and superconductivity. Would it be possible in graphene to transit from the behavior we observed in our samples to the one observed by Kessler *et al.* ?. Is it possible to induce in graphene through gate voltage, better than a insulating-metallic transition, an insulating-superconducting transition ?.

Fisher [50] argued that a superconducting thin film, in the presence of a magnetic field should go through a transition into an insulating state at zero temperature. When a magnetic field is applied on a superconducting film, a formation of vortices arises which are bosonic particles. At the critical magnetic field, vortices (that were paired in the superconducting state) delocalize and go through a Bose condensation. This condensation requires that the electrons pairs be localized, just as in in the superconducting state Cooper pair condensation needs localized vortices. Near the transition there is then a competition between condensation of Cooper pairs (superconductivity) and condensation of vortices (localization). Fisher *et al.* [51] demonstrated that at the superconducting-insulating transition, the system behaves like a normal metal with a finite, non zero resistance at T=0. They argued that the value of resistance per square $R_\square$ is universal and depends only on the universality class of the transition.

Superconducting-insulating transition (SIT) has been largely studied in thin superconducting films [53], [54], [55], [56]. Experimentally this transition is induced by decreasing the film thickness (changing disorder), or by a magnetic field. Figure 6.47 show data [49] from TiN films in which the superconducting-insulating transition is mediated by disorder. Increasing disorder in different films makes samples switch abruptly from a superconducting behavior to a insulating one. It is seen that around 1K films have almost the same resistance $R_\square$. It is only at low temperatures that films choose between a superconducting or isolating ground state.

It would be very useful in our samples to be able to determine $k_F l_e$ which tell us know if we are in an insulating regime. This could be extracted using a four probe geometry or from magnetoresistance measurements, as was done at the beginning of this chapter. Unfortunately such measurements have not been done for the moment.

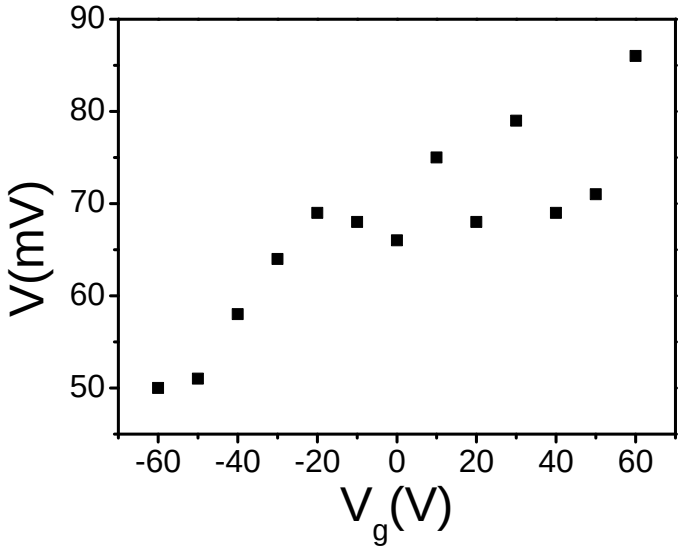

FIGURE 6.44 – Dependence of the insulating gap on gate voltage for the second sample.

6.7 Conclusions

A question that arises for our samples is whether such a thermally activated behavior with a characteristic temperature of $\sim 3.4K$ would be present if particles were not superconducting. If superconductivity does play a role, we think that a superconducting-insulating transition might be observable in graphene in less disordered samples than those measured until now. This could be done by annealing the sample at higher temperatures without damaging the In nanoparticles or changing the deposition of particles to a less energetic technique. In this way it should be possible to observe percolation of superconductivity when $L_t \approx b$

Given the former theoretical and experimental works on 2D superconducting samples, we think that graphene covered with superconducting islands might be a system where superconducting-insulating transition could be tuned not by changing disorder or magnetic field but by adjusting resistance $R_\square$ through the gate voltage. This would make the sample switch from a superconducting state to an insulating one by changing gate voltage.

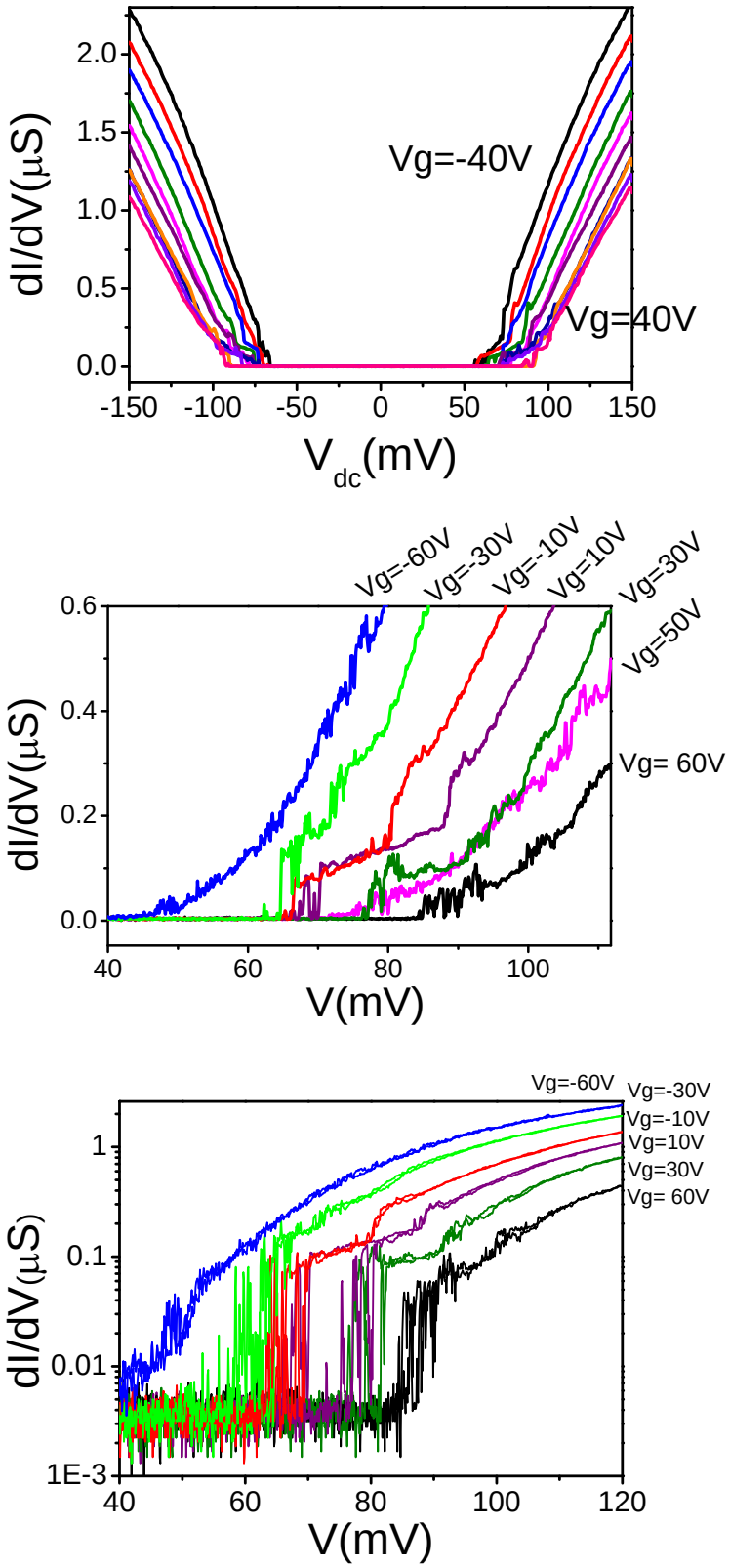

FIGURE 6.45 – Top : dI/dV characteristics of the second sample shows a gap that depends on gate voltage. Middle : Zoom near zero conductance in linear scale and log scale (Bottom).

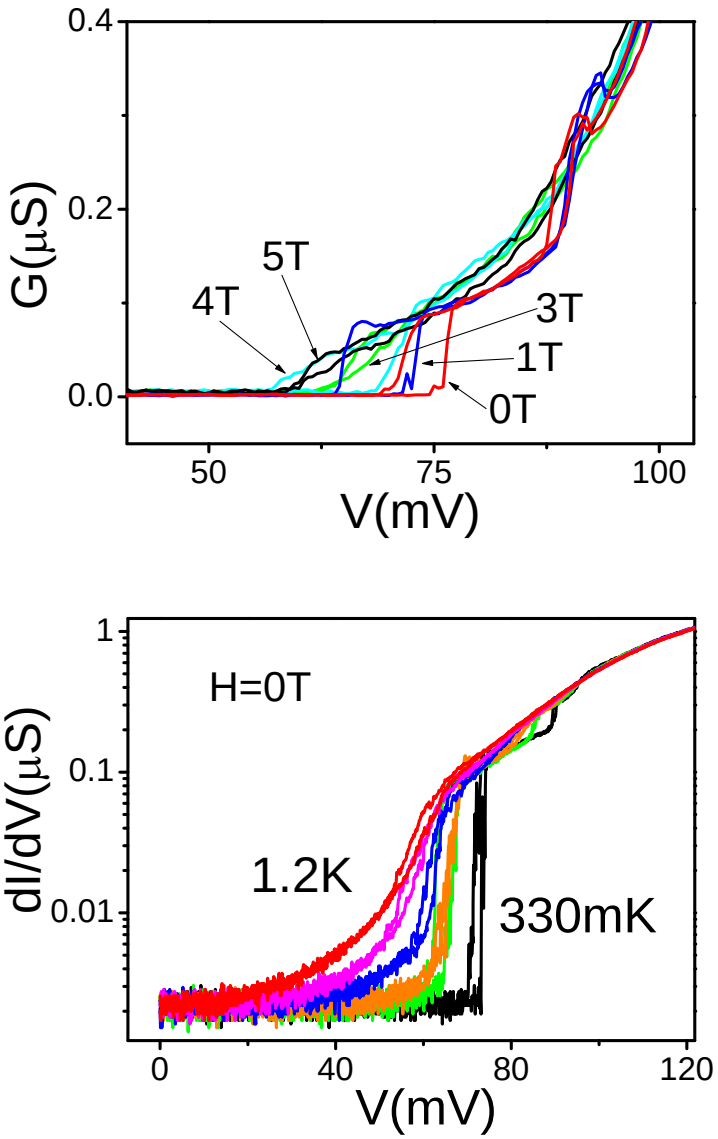

FIGURE 6.46 – Differential conductance for different magnetic fields (top) and different temperatures (330mK, 615mK, 760mK, 930mK, 1.05K, 1.2K) (bottom). Gate voltage was $V_g = 0V$.

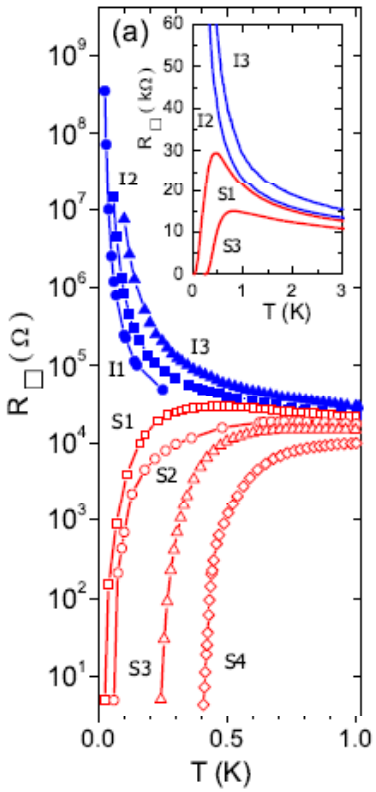

FIGURE 6.47 – Temperature dependence of resistance for samples with different thickness at zero magnetic field. Taken from [49]

Bibliographie

[1] H. Bouchiat Course 2 Mesoscopic Quantum Physics, Les Houches Session LXI, 1995 Elsevier Science.

[2] E. Akkermans, G. Montambaux, Physique mésoscopique des électrons et des photons 2004 EDP Sciences.

[3] D. Mailly and M. Sanquer, Journal de Physique I France 2 (1992) 357.

[4] W. Skocpol et al., Phys. Rev. Lett. **56**(1986) 2865.

[5] A. Rycerz, J. Tworzydlo and C. W. J. Beennakker EPL **79** 57003 (2007).

[6] M. Y. Kharitonov et al, Phys. Rev. B **78**, 033404 (2008).

[7] V. V. Cheianov et al, Phys. Rev. Lett. **99**, 176801 (2007).

[8] J. Martin, N. Akerman, G. Ulbricht, T. Lohmann, J. H. Smet, K. von Klitzing and A. Yacoby, Nature Phys. **4**, 144 (2008).

[9] B. L. Altshuler, JETP Lett **41**, 648 (1985) ; P.A. Lee, A.D. Stone and H. Fukuyama, Phys. Rev. B **35**, 1039 (1987).

[10] B.L. Altshuler and D.E. Khmel'nitskii, JEPT Lett. **42**, 359 (1985) ; A.I. Larkin and D.E. Khmel'nitskii, JETP **64**, 1075 (1986).

[11] P.G.N. de Vegvar et al. Phys. Rev. B **38**, 4326 (1988) ; R.A. Webb et al. Phys. Rev. B **37** 8455 (1988).

[12] D. Sanchez et al. Phys. Rev. Lett. **93**, 106802 (2004).

[13] B. Spivak et al. Phys. Rev. Lett. **93**, 226801 (2004) ; E. Deyo et al. Phys. Rev. B **74** 104205 (2006).

[14] D. M. Zumbühl et al. Phys. Rev. Lett. **96**, 206802 (2006)

[15] Calculation made by Mikhail Polianski.

[16] L. Angers et al. Phys. Rev. B **75**, 115309 (2007).

[17] Y. Imry Europhys. Lett. **1**, 249 (1986).

[18] F. Ladieu, D. Mailly and M. Sanquer J. Phys. I France **3**, 2321 (1993).

[19] P. A. Lee, A. Douglas Stone and H. Fukuyama Phys. Rev. B **35**, 1039 (1987).

[20] C. Berger *et. al.* Science **312**, 1191 (2006).

[21] H. B. Heersche *et. al.* Nature (London) **446**, 56 (2007).

[22] N. E. Staley, C. P. Puls and Y. Liu Phys. Rev. B **77** 155429 (2008).

[23] K. Kechedzhi *et. al.* Phys. Rev. Lett. **102**, 066801 (2009).

[24] M. B. Lundeberg and J. A. Folk Nature Physics **5**, 894 (2009).

[25] J Berezovsky *et al* Nanotechnology **21**, 274013 (2010).

[26] R. J. F. Hughes Phys. Rev. B **54**, 2091 (1996).

[27] Lionel Angers, PhD Thesis (2007).

[28] Laurent-Patrick Lévy "Magnétisme et supraconductivité", CNRS Éditions.

[29] M. Tinkham "Introduction to superconductivity" Dover publications 1996.

[30] C. W. J. Beenaker Phys. Rev. Lett. **97**, 067007 (2006).

[31] C. W. J. Beenaker Rev. Mod. Phys. **80**, 1337 (2008).

[32] Thèse Ronald Cron Groupe Quantronique SPEC Saclay (2001).

[33] X. Du, I. Skachko, and E. Y. Andrei, Phys. Rev. B **77**, 184507 (2008).

[34] H. B. Heersche, P. Jarillo-Herrero, J. B. Oostinga, L. M. K. Vandersypen, and A. F. Morpurgo, Nature (London) **56**, 446 (2007).

[35] A. Shailos, W. Nativel, A. Kasumov, C. Collet, M. Ferrier, S. Guéron, R. Deblock, and H. Bouchiat, EPL **79**, 57008 (2007).

[36] J. Moser, A. Barreiro, and A. Bachtold, Appl. Phys. Lett. **91**, 163513 (2007).

[37] K. I. Bolotin, K. J. Sikes, Z. Jiang, G. Fundenberg, J. Hone, P. Kim, and H. L. Stormer, Solid State Commun. **146**, 351 (2008).

[38] Z. Jiang, Y. Zhang, H. L. Stormer and P. Kim, Phys. Rev. Lett. **99**, 106802 (2007).

[39] M. Octavio, M. Tinkham, G. E. Blonder and T. M. Klapwijk, Phys. Rev. B **27**, 6739 (1983), K. Flensberg, J. Bindslev Hansen and M. Octavio Phys. Rev. B **38**, 8707 (1988).

[40] G. E. Blonder, M. Tinkham and T. M. Klapwijk, Phys. Rev. B **25**, 4515 (1982).

[41] T. Kontos, M. Aprili, J. Lesueur, X. Grison, and L. Dumoulin, Phys. Rev. Lett. **93**, 137001 (2004).

[42] P. Dubos PhD Thesis, U. J. Fourier, Grenoble (2000).

[43] P. W. Brower and C. W. J. Beenakker, Phys. Rev. B **52**, 16772 (1995).

[44] A. Altland and M. R. Zirnbauer, Phys. Rev. B **55**, 1142 (1997).

[45] J. Trbovic, N. Minder, F. Freitag and C. Schönenberger, Nanotechnology **21**, 274005 (2010).

[46] Habilitation à diriger les recherches (HDR) Sophie Guéron (2009).

[47] M. V. Feigel'man. M. A. Skvortsov and K. S. Tikhonov, JETP Letters **88**, 747 (2008).

[48] B. M. Kessler, Ç. Ö. Girit, A. Zettl and V. Bouchiat, Phys. Rev. Lett. 104, 047001 (2010).

[49] T. I. Baturina, A. Yu. Mironov, V. M. Vinokur, M. R. Baklanov and C. Strunk, Phys. Rev. Lett. **99**, 257003 (2007).

[50] M. P. A. Fisher, Phys. Rev. Lett. **65**, 923 (1990).

[51] M. P. A. Fisher, G. Grinstein and S. M. Girvin, Phys. Rev. Lett **64**, 587 (1990).

[52] A. F. Andreev, Sov. Phys. JETP **19**, 1228 (1964).

[53] D.B. Haviland, Y. Liu, and A.M. Goldman, Phys. Rev. Lett. **62**, 2180 (1989)

[54] Y. Liu, D.B. Haviland, B. Nease, and A.M. Goldman, Phys. Rev. B **47**, 5931 (1993).

[55] A. F. Hebard and M.A. Paalanen, Phys. Rev. Lett. **65**, 927 (1990).

[56] T. I. Baturina, A. Yu. Mironov, V. M. Vinokur, M. R. Baklanov, and C. Strunk Phys. Rev. Lett. **99**, 257003 (2007), T. I. Baturina and C. Strunk, M. R. Baklanov and A. Satta Phys. Rev. Lett. **98**, 127003 (2007).

[57] From the lectures on electronic transport on graphene given by Jean Nöel Fuchs and Mark Goerbig at Orsay in March 2008.

[58] P. M. Ostrovsky, I. V. Gornyi and A. D. Mirlin, Phys. Rev. B **74**, 235443 (2006).

[59] N. H. Shon and T. Ando, J. Phys. Soc. Jpn. **67**, 2421 (1998).

[60] K. Nomura and A. H. MacDonald, Phys. Rev. Lett. **98**, 076602 (2007).

[61] N. M. R. Peres, F. Guinea and A. H. Castro Neto, Phys. Rev. B **73**, 125411 (2006).

[62] S. Adam, E. H. Hwang, E. Rossi and S. Das Sarma, Solid State Communications **149**, 1072 (2009).

[63] S. Adam and S. Das Sarma, Phys. Rev. B **77**, 115436 (2008).

[64] S. Adam, E. H. Hwang, V. M. Galitski and S. Das Sarma, PNAS **104**, 18392 (2007).

[65] C. Jang, S. Adam, J. H. Chen, E.D Williams, S. Das Sarma and M. S. Fuhrer, Phys. Rev. Lett. **101**, 146805 (2008).

[66] L. A. Ponomarenko, R. Yang, T. M. Mohiuddin, M. I. Katsnelson, K. S. Novoselov, S.V. Morozov, A. A. Zhukov, F. Schedin, E.W. Hill, and A. K. Geim, Phys. Rev. Lett. **102**, 206603 (2009).

[67] D. A. Abanin and L. S. Levitov Phys. Rev. B **78**, 035416 (2008).

[68] J. R. Williams, D. A. Abanin, L. DiCarlo, L. S. Levitov and C. M. Marcus Phys. Rev. B **80**, 045408 (2009).

[69] J. Martin, N. Akerman, G. Ulbricht, T. Lohmann, J. H. Smet, K. von Klitzing and A. Yacoby Nature Phys. **4**, 144 (2008).

[70] P. T. Coleridge, R. Stoner and R. Fletcher, Phys. Rev. B **39**, 1120 (1989).

[71] A. H. Castro Neto, F. Guinea, N. M. R. Peres, K. S. Novoselov and A. K. Geim, Rev. Mod. Phys. **81** 109, (2009).

[72] D.M. Basko, Phys. Rev. B **78**, 115432 (2008).

[73] J. C. Meyer et al., Nano Lett. **8**, 3582 (2008).

[74] F. Guinea, M. I. Katsnelson, and M. A. H. Vozmediano, Phys. Rev. B **77**, 075422 (2008).

[75] P. R. Wallace, Phys. Rev. **71**, 622 (1947).

[76] Mark O. Goerbig, Pascal Lederer, Lectures on quantum Hall effect and bidimensional electrons in high magnetic fields, Orsay (2006).

[77] A. H. Castro Neto, F. Guinea, N. M. R. Peres, K. S. Novoselov and A. K. Geim Rev. Mod. Phys. **81**, 109-162 (2009).

[78] J. Nöel Fuchs, Mark O. Goerbig, M. Potemski, Images de la physique (2007).

[79] A. Geim and K. S. Novoselov, Nature materials **6**, 183 (2007).

[80] N. D. Mermin, Phys. Rev. **176**, 250 (1968).

[81] K. S. Novoselov, A. K. Geim, S. V. Morozov, D. Jiang, Y. Zhang, S. V. Dubonos, I. V. Grigorieva and A. A. Firsov, Science **306**, 666 (2004).

[82] F. Molitor, D. Graf, C. Stampfer, T. Ihn and K. Ensslin, Adv. in Solid State Phys. **47**, 171 (2008).

[83] F. V. Tikhonenko, A. A. Kozikov, A. K. Savchenko, and R. V. Gorbachev, Phys. Rev. Lett **103**, 226801 (2009).

[84] R. V. Gorbachev, F. V. Tikhonenko, A. S. Mayorov, D.W. Horsell, and A. K. Savchenko, Phys. Rev. Lett. **98**, 176805 (2007).

[85] G. Sambandamrthy, L. W. Engel, A. Johansson and D. Shaar, Phys. Rev. Lett. **92**, 107005 (2004).

[86] M. Monteverde, C. Ojeda-Aristizabal, R. Weil, K. Bennaceur, M. Ferrier, S. Guéron, C. Glattli, H. Bouchiat, J. N. Fuchs, and D. L. Maslov, Phys. Rev. Lett. **104**, 126801 (2010).

[87] C. Ojeda-Aristizabal, M. Monteverde, R. Weil, M. Ferrier, S. Guéron, and H. Bouchiat, Phys. Rev. Lett. **104**, 186802 (2010).

[88] C. Ojeda-Aristizabal, M. Ferrier, S. Guéron, and H. Bouchiat, Phys. Rev. B **79**, 165436 (2009).

[89] A. Chepelianskii, P. Delplace, A. Shailos, A. Kasumov, R. Deblock, M. Monteverde, C. Ojeda-Aristizabal, M. Ferrier, S. Guéron, and H. Bouchiat, Phys. Rev. B **79**, 235418 (2009).